THE UNIVERSITY
of EDINBURGH

Earthquake nucleation: small signals from Big Data

Roseanne Clement

THE UNIVERSITY
of EDINBURGH

Thesis for the degree of Doctor of Philosophy

The University of Edinburgh

2020

Abstract

Catastrophic failure events, such as earthquakes, volcanic eruptions and landslides, are linked by material failure processes. Seismicity and strain data can be used to track the failure processes that might be occurring before large events, and which may be used to provide forecasts of event magnitude and time. This is often unsuccessful possibly due to missing key elements of the processes occurring before a large event, notably from earthquake catalogues built by traditional methods based on manual picking of events. Some studies have suggested that automated waveform based cross-correlation methods can identify multiple sets of additional small seismic events with high waveform similarity - multiplets - where their similarity indicates that their source locations are restricted to a localised spatial zone. If multiplets occur prior to failure then they may provide more information that can be used to test between competing hypotheses for pre-rupture processes, and to evaluate the degree to which forecasting power can be improved.

A set of multiplets may occur on their own, or be followed by larger catastrophic events. If so, this may be due to (a) accelerated nucleation of the larger rupture from the edge of a growing local slipping patch, often associated with local creep-type deformation or (b) a cascade of sequentially triggered events of increasing size, involving ruptures that are not associated with a creep signal, and may not be so closely co-located, despite their similarity. These two hypotheses have very different implications for probabilistic earthquake forecasting using earthquake catalogue data, respectively the debate on (a) the existence of nucleation-related earthquake precursors and (b) the extent to which models based on triggering of seismicity describe the process - and hence determine the forecasting power - better. Other possibilities also exist, notably (c) triggering of large aftershocks with no accelerating cascade and (d) random occurrence as a null hypothesis. The problem with finding multiplets is that they are often small, obscured in ambient noise, and sometimes only picked up by one seismometer.

I have developed an optimised detection and analysis technique to extract a catalogue of multiplets and determine their temporal evolution in different seismic datasets. I discover new similar events automatically by enhancing the common STA/LTA event detection method with a moving cross-correlation window in an iterative template matching approach. Subsequent analysis of these events then allows me to examine their occurrence and to better resolve or place constraints on the processes taking place and to test the alternate hypotheses described above. The algorithm's success in finding events amongst realistic noise is evaluated statistically in synthetic tests by comparing the catalogue of events found through template matching to official catalogues based on more traditional manual phase picking methods.

My method works significantly more successfully than the common STA/LTA triggering approach alone, with more (generally smaller) events found and more accurate pick times. It is particularly useful for sparse seismic networks, where such signals may only be detectable on the nearest station. Other studies have used multiple seismic stations to determine specific location of events, but commonly only test for one hypothesis for failure, and they often neglect to quantify the success rate for finding new events or missing known events from official event catalogues. Here I use single station data to compare sets of multiplets found across several different types of failure sequences, quantify the success of the method in synthetic data with realistic noise, and use the results to infer the processes taking place in each case.

I applied this method to two significant tectonic earthquake sequences - the M_W 6.0 Parkfield, USA sequence in September 2004 and the M_W 8.2 Iquique, Chile sequence in April 2014. I also examined a seismic swarm with no clear mainshock that occurred near Diemtigen, Switzerland in April 2014. Finally I considered two further applications with the 2004 eruption of Mount St. Helens Volcano, USA and the June 2017 landslide in Nuugaatsiaq, Greenland.

The results show that the eventual failure of the M_W 6.0 Parkfield earthquake was

preceded by an episode of repeated rupture of the small locked patches, consistent with the occurrence of slip nucleation and creep on the fault. Alternatively, transients associated with aftershocks of previous earthquakes were the only clear pattern observed in the two weeks preceding the M_W 8.2 Iquique earthquake, rather than any precursory behaviour. The events detected through the multiplet matching method in the Nuugaatsiaq landslide sequence showed behaviour consistent with transient, steady-state and accelerating stages in the approach to catastrophic failure driven by underlying creep processes.

In contrast, my method also worked well in detecting events in cases which did not end with catastrophic failure, such as the seismic swarm at Diemtigen. This swarm was very spatially constrained, allowing my method to pick up many more events due to their similar waveforms. An underlying stationary or steady-state process was also observed after an initial transient during the Diemtigen seismic swarm, consistent with a process driven by localised creep in response to a stress perturbation. The evolution of multiplets at Mount St. Helens showed a relatively stationary event rate involving a deceleration trend analogous to a primary creep process.

In summary, my developed method significantly improved the catalogues with many new event detections for the five separate case studies considered in this thesis. These results prove that it can be utilised to detect candidate nucleation events even on sparse networks, such as those often used to monitor landslide or volcanic activity. The new data discovered by the template matching technique has helped in developing understanding and placing constraints on what happens prior to, or accompanying failure in a number of different scenarios. In the long term these new data will also help quantify the probabilistic forecasting power of seismicity prior to a variety of extreme events.

Lay summary

Ground motion is continuously recorded at seismic stations. When there is significant motion, the oscillations can be isolated and we consider individual earthquakes as events in a seismic dataset. Many events which have small amplitudes and similar shaped waveforms have been observed prior to catastrophic failure, such as large tectonic earthquakes, volcanic eruptions or landslides. The similarity in the shape of the events indicate that they come from the same location. Hence, detecting and analysing these small events has the potential to reveal patterns and relationships with larger failure events. Understanding the small event behaviour can therefore improve failure forecasts. The problem with identifying these small events, however, is that they are often hard to find as they are hidden within the seismic data.

I have developed a technique to extract the similar events and determine if there are any patterns in groups of similar events in different scenarios. By enhancing the established methods, I can discover these small signals in large seismic datasets based on their similarity. Subsequent analyses of these events then allows me to examine their relationship to physical processes. I measure success of my method by comparing the number of events found to official datasets, which are based on more traditional methods for finding events.

My method is significantly more successful, with more precision and accuracy in finding events, than the common approach on its own. Other studies have used multiple seismic datasets to determine specific locations of the similar events, and neglect to quantify the success rate of finding or missing known events. I instead use individual seismic datasets to compare sets of similar events found in different situations, quantify the success of the method in synthetic data, and use the results to infer the processes taking place in each case.

I applied my method to two large earthquake sequences, a swarm sequence, where many small earthquakes without a large event, during an active volcanic period, and prior to a large landslide, as these had all known occurrences of multiplets in literature. The results showed that my method detected many new small events in each case. These events could then be attributed to the slow rock movement on a fault prior to one large earthquake, and no pattern prior to the other large earthquake. The similar events detected before the landslide exhibited behaviour that is typically seen in a model of slow, then accelerating movement.

My method also worked well in cases which did not end with a large event, such as in the swarm dataset, which revealed behaviour also typical of slow rock movement. The similar events during the active volcanic period instead illustrated a scenario where the process causing the events was decelerating. The similarity between events also decreased as time went on, indicating that the location of the event was moving.

Overall, the method found many new events for the five separate case studies considered in this thesis. These results prove that my method can be utilised to detect small similar events even in areas with small data coverage, such as those often used to monitor landslide or volcanic activity.

In summary, the new data discovered by the technique described in this thesis has helped in developing understanding on what happens prior to, or accompanying failure in a number of different scenarios. In the long term these new data will also help quantify the forecasting of seismicity prior to a variety of events.

Acknowledgements

Firstly, thanks to my supervisors Ian Main and Andy Bell. Ian provided continuous support, patience, motivation, and enthusiasm, particularly during the writing stage. Thank you both for answering those countless emails and being supportive of all the conferences, internships and teaching I have been able to do during my time. Also, to the E3 DTP team (particularly Stephanie). You have always answered all my many queries and have given me so many opportunities during my PhD. The past few years have been hard, but I believe that I am leaving academia very prepared.

I would like to thank my wonderful family and friends for their ongoing support through the making of this PhD. Eleri, Lauren, Ben and Rob - you guys have always been a great source of fun with many games nights, and for always being there to listen and help.

To my amazing husband, Jack. Thank you for putting up with what has been a particularly super stressful time (why did we arrange the wedding during writing up again?), especially during the pandemic through these corrections. Your support throughout all of this has meant everything. You are my biggest cheerleader and I could not have done this without you.

Last, but not least, thank you to everyone in the attic - your regular coffee breaks, motivational oranges and cake Fridays have always been very welcome. Special mentions to my corner bestie James, who always had a coffee ready for me in the morning (before he left me for the high-life of industry), Lyss - for all the coffee, Huel, corrections, and deciphering code chats, and Megan - for encouraging me on those Raptor runs and being there for chats. Also to the earthquake girls of Gina, Sophie, Rachel and Kirsty, for all the PhD rants, thesis/plot formatting, corrections and helping me learn about seismology 101 for 4 years.

Contents

Chapter 1

Introduction

1.1 The research problem

The deterministic prediction of earthquakes has been the goal of seismology for many decades (Meissner, 1982). This would allow for not only their time of occurrence, but also location and magnitude to be predicted in advance, with small margins of error, and in a reasonable timeframe (Main, 1999). One of the main reasons that deterministic prediction has not been possible, is that we do not fully understand the processes of rupture initiation and growth, a process known as earthquake nucleation (Ohnaka, 1992; Iio, 2009). Laboratory studies show that a nucleation process occurs in a localised space prior to rupture, and involves precursory stable slip on a nucleation patch (Dieterich, 1992; Ohnaka, 1992). If such nucleation processes can be detected, this could have significant potential to improve earthquake forecasting if the results scale to tectonic source lengths and timescales (Ohnaka and Kuwahara, 1990; Yamashita and Ohnaka, 1991; Ohnaka, 1992).

The nucleation of an earthquake occurs by a build up of localised, mostly aseismic, slip at the mainshock hypocentre (Lapusta and Rice, 2003). It can be associated with, or inferred from, repeated localised seismic slip from small events, which would indicate

the preslip model (Ellsworth and Beroza, 1995; Nadeau and Johnson, 1998). Events with similar waveforms ('multiplets') indicate that they come from a similar source location, to within a quarter of a wavelength (Geller and Mueller, 1980). Their presence has often been observed in the seismic signal prior to several large tectonic earthquake sequences (Bouchon et al., 2011; Kato et al., 2012), as well as volcanic eruptions (Thelen et al., 2010; Bell et al., 2018) and landslides (Yamada et al., 2016; Poli, 2017; Bell, 2018).

There are two main models to explain the occurrence of multiplets prior to mainshocks: the preslip model described above and the alternative cascade model of Ellsworth and Beroza (1995) and Gomberg (2018). Multiplets which are part of an ongoing process towards failure indicate the preslip model, whereas the cascade model is instead if the failure has been preceded by multiplets that have been inferred to be triggered. Both models would then enter a breakaway phase to the eventual dynamic rupture of a mainshock (Beroza and Ellsworth, 1996). These two models are not also mutually exclusive, partly due to the subjective nature of their definition and the diagnostics used to detect them, hence the applicability of both models is still up for much debate (Gomberg, 2018). In some settings, it is also possible to have a mixture of both the preslip and cascade models due to different underlying processes (Udias et al., 2014). Finally, the null hypothesis would be that there is no causal pre-slip or cascade, and the mainshock occurrence time is the outcome of a random process, as commonly assumed in probabilistic seismic hazard analysis (Reiter, 1991).

In the preslip model, as defined by Ellsworth and Beroza (1995), an earthquake is preceded by slow (aseismic) slip over a limited region, which involves a combination of stable creep-type deformation and some seismic rupture, and accelerates until the critical point for the slipping patch is reached. Beyond this point, the system becomes unstable and the main dynamic rupture occurs beyond the region (Ellsworth and Beroza, 1995). This model has the deterministic view that the underlying processes that cause the slip would then determine the size of the main rupture (Kilb and Gomberg, 1999; Gomberg, 2018).

The cascade model instead suggests that small earthquakes trigger a stochastic cascade of increasingly neighbouring larger events until the eventual large main earthquake occurs (Gomberg, 2018). This differs from the preslip model, as the earthquakes themselves are providing the mechanism that triggers the failure of the next event and the process involves a significant stochastic component (Gomberg, 2018).

It is also possible to have two competing hypotheses for the same sequence (Gomberg, 2018). For example, Bouchon et al. (2011) interpreted the repeating events in the foreshock sequence prior to the 1999 M_W 7.6 İzmit, Turkey earthquake as being driven by aseismic fault slip, therefore indicating the preslip model. Alternatively, Ellsworth and Bulut (2018) studied the same sequence and found that the stress of the surrounding rocks was reduced in a small radius from each foreshock. Outwith this area, there was an increase in the stress, which would trigger another foreshock, eventually resulting in the mainshock (Ellsworth and Bulut, 2018). Hence, the cascade model was more appropriate as there was no indication of a slow-slip-driven trigger, and the foreshocks instead appeared to trigger one another until the eventual failure.

These models can also be used to describe multiplets found prior to other catastrophic failures, such as volcanic eruptions and landslides. In such events, the catastrophic failure has been preceded by seismicity that has been inferred to be triggered (the cascade model) or occurs as part of an ongoing process (the preslip model) (Voight, 1988; Main, 2000; Rubinstein et al., 2007; Bell and Kilburn, 2012; Kilburn, 2018; Bürgmann, 2018).

Multiplets often have a small amplitude with respect to the background noise and so their frequency of occurrence, and thus significance are often missed in conventional catalogues based on the manual phase picking of events (Ross et al., 2019). There have been several techniques developed in recent years to detect these events by the similarity of their waveforms (Anstey, 1964; Harris, 2006; Gibbons and Ringdal, 2006; Brown et al., 2008; Yoon et al., 2015). This is important, as identifying multiplets in the

seismic signal has the power to improve the understanding of the processes described above and therefore the associated forecasting power (Ross et al., 2019). The current methods to identify multiplets within seismic datasets, however, have drawbacks. For example, some require an event to be detected on multiple stations in order to pass selection criteria for an event. This criterion does not always work well in sparse network areas.

1.2 Scope of work

I have developed an optimised detection and analysis method based on the template matching approach used in Green and Neuberg (2006) to extract catalogues of multiplets from several seismic datasets for single stations. I expand upon the method in Green and Neuberg (2006) by adding further iterations to discover new multiplets automatically in a dedicated high Random-Access Memory supercomputer from single seismic station data, finding small signals in relatively large datasets. This simple approach has the potential of rapid processing times compared to multiple station networks in a real-time forecasting scenario.

Firstly, I benchmarked the method on synthetic datasets before applying it to different failure scenarios of earthquakes sequences, during a period of volcanic activity, and a landslide, to test the versatility of the method. This benchmarking procedure is not widely used in the development of similar methods, however it was important to quantify the success rate of finding, or missing, known events for different types of sequences. Once established, I then tested the method on real datasets chosen to cover a wide variety of seismic sequence types. The data was freely available to download, and there were several comparative studies to compare my results to. The datasets I chose to study included two significant earthquake sequences - during the M_W 6.0 Parkfield, USA sequence in September 2004 and during the M_W 8.2 Iquique, Chile sequence in

April 2014. I also included seismic swarms from near Diemtigen, Switzerland in April 2014, during a volcanic eruptive period at Mount St Helens volcano, USA on 15th-18th December 2004 which exhibited a clear repeating pattern, and prior to the Nuugaatsiaq, Greenland landslide on 17th June 2017.

The multiplets were then examined as a time series of events, and reviewed with different statistical techniques to test the hypotheses of pre-slip nucleation, triggered cascades, and random occurrence. The results were compared to those from independent catalogues from sources such as the United States Geological Survey (USGS) to assess the confidence in the detection of the newly found events, and to assess the performance of the method. In some cases, the method did find new events, at the expense of missing large events in the ground-truth event catalogues. Thus the method could be used to expand, rather than replace the known event catalogues.

The detection and identification of events allowed for a significant improvement on the numbers of events in current earthquake catalogues for the five different case studies. In particular, the number of low-magnitude events in the catalogues greatly increased, with a more representative population of seismic events. The new data changed both the ratio of low-magnitude to high-magnitude events and the time between events, providing new diagnostics for the discrimination of the competing hypotheses described above. The analysis of the event catalogue properties also provided new insight into the understanding of the time-dependent behaviour associated with deformation processes prior to extreme events for the different types of failure sequences.

1.3 Thesis structure

This thesis will first examine the physics of catastrophic failures, e.g. earthquakes, volcanic eruptions and landslides, and how they are currently forecast. I will also

discuss the background and role of multiplets in this scenario, and the current detection approaches.

Next, I will discuss in chapter 3 the background methods which were already defined in literature prior to my study, including the common triggering functions used for automatically picking events, techniques for finding similar events and different statistical metrics that I will use to analyse event catalogues. I then develop the background methods to introduce an optimised technique that detects multiplets in seismic data. I describe how I built synthetic seismograms with known event catalogue properties, such as their time of occurrence and magnitude, to then confidently assess the ground-truth of the method. I then introduce a step-by-step guide of how my method can be used to find multiplets within the synthetic dataset. Performance tests of the method analogous to clinical trials in medicine with 'hits', 'misses' and 'false alarms', are presented in chapter 4.

Chapter 5 presents and discusses the results of using the introduced method on the 2004 M_W 6.0 Parkfield, USA and the 2014 M_W 8.2 Iquique, Chile earthquake datasets, which have both exhibited repeating earthquakes prior to their mainshocks (Thurber et al., 2006; Kato and Nakagawa, 2014). In chapter 6, the method is applied to the 2014 Diemtigen, Switzerland seismic swarm (i.e. no large event occurred) that was reported to have many co-located earthquakes (Diehl et al., 2015), Mount St Helens volcano, USA on 15th-18th December 2004 during a period of repetitive volcanic seismicity (Thelen et al., 2008) and the repeating seismic pattern observed prior to the 2017 Nuugaatsiaq, Greenland landslide (Poli, 2017; Bell, 2018), and their results discussed.

Lastly, chapter 7 presents a discussion of the thesis results and implications, as well as specific ideas for future work.

Chapter 2

Literature Review

2.1 Motivation

There is an increase in the evidence that similar waveforms have been observed in the seismic signals prior to catastrophic failures, e.g. significant earthquakes (Bouchon et al., 2011; Kato et al., 2012, 2016a), volcanic eruptions (Moran et al., 2008b; Thelen et al., 2011; Bell et al., 2018) and landslides (Yamada et al., 2016; Poli, 2017; Bell, 2018). These events that have similar waveforms are known as 'multiplets'. Multiplets are caused by a repeating process which leads to waveforms that correlate highly with one another. The high correlation means they have been most likely caused by the same initial process and have travelled along the same path, hence leading to very similar seismic signals being recorded on the seismometer. Multiple sets of multiplets can also be grouped further into 'families', which are groups of higher similarity often seen in volcanic studies (Green and Neuberg, 2006; Neuberg et al., 2006; Hammer and Neuberg, 2009; Bell et al., 2017). The presence of multiplets in the preceding seismic signal can help better understand the processes which are occurring, and has implications for the forecasting of the failure and reduction of the risk. However, the frequency of

multiplets prior to different types of catastrophic failure is currently unknown, hence it is important to evaluate their occurrence.

This chapter will examine the current understanding behind models and processes associated with the lead-up to catastrophic failure. The precursory signals which are sometimes found prior to these failures are also examined, as well as how the failures are currently forecast.

2.2 The physics of catastrophic failure events

In order to improve forecasting and evaluate the potential hazard of catastrophic failure events (such as earthquakes, volcanic eruptions and landslides), we have to first understand the physics of the failure. This will therefore allow us to interpret the recorded surface observations and thus infer the processes happening within the Earth's lithosphere. In this section, I discuss the range of proposed theories for rupture growth and earthquake triggering. I also present some of the different statistics used in earthquake analysis and their application to volcanic eruptions and landslides.

2.2.1 Earthquake nucleation and triggering models

There is an increasing amount of evidence that failure is preceded by a nucleation phase starting from an initiation of the rupture, past an equilibrium point, to eventual rupture growth (Yamashita and Ohnaka, 1991; Ohnaka, 1992; Iio, 2009; Main, 2017; Vasseur et al., 2017). In the context of an earthquake, the rupture initiates with quasi-static growth, until reaching instability at the equilibrium point and the rupture grows outward. The rupture velocity accelerates and the system shifts from quasi-static to a dynamic state. The process from rupture initiation to rupture growth is called 'the nucleation process' (Iio, 2009). In order for an earthquake to occur, this

rupture progresses from a locked state to slip and propagates spontaneously along a fault (Ellsworth and Beroza, 1995). Understanding the nucleation associated with earthquakes can help better understand the processes taking place in this time prior to the failure (Mignan, 2014).

There are two conceptual models that involve a causal-relationship to large earthquakes, the cascade model and the preslip model (Ellsworth and Beroza, 1995), which are illustrated in Figure 2.1.

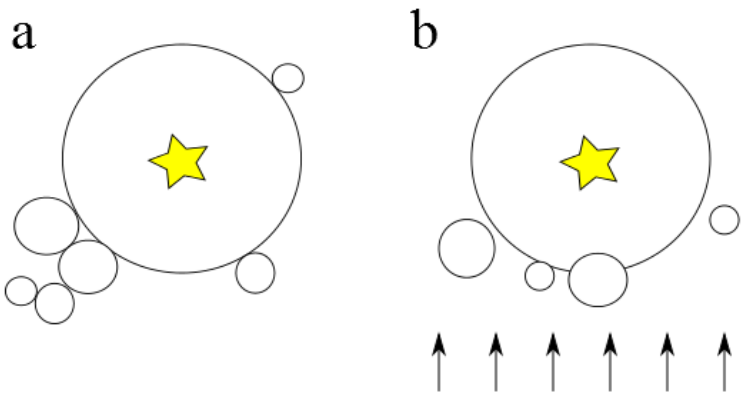

Figure 2.1: Illustration of the two main conceptual models for the occurrence of multiplets prior to earthquakes, inspired by Iio (2009); Mignan (2014); Gomberg (2018). The circles represent events (with size relative to magnitude), with the star demonstrating the mainshock. The left diagram shows a cascade nucleation, where the smaller events have triggered larger events resulting in the large mainshock. The right diagram illustrates a preslip nucleation model, with events occurring on the edge of a slipping patch (represented by the arrows), resulting in a large mainshock. The cascade model has events that are less likely to be located close to each other, and does not involve precursory aseismic creep.

The cascade model (Figure 2.1a) involves small earthquakes triggering a cascade of

increasingly larger events, until the eventual large main earthquake occurs. This model makes no differentiation between the beginnings of small and large earthquakes.

Alternatively, in the preslip model (Figure 2.1b), an earthquake is preceded by aseismic slip in the local region. In contrast to the cascade model, this model differentiates between the beginnings of small and large earthquakes. The failure is induced by an episode of slow and stable aseismic slip which accelerates until the slip area reaches a critical level where it is no longer stable, causing high velocity propagation to the main earthquake event. The two can be distinguished by the fact that preslip nucleation would involve a precursory creep to failure signal in data such as total number of events or strain inferred from geodetic data or the total seismic moment. In contrast the cascade model does not require aseismic preslip, and events are less likely to be co-located or to cluster closely together on the edge of a slip patch. The events associated near areas of slow slip (also called aseismic slip or fault creep), such as in subduction zones, are called slow slip events (Obara, 2002; Rogers and Dragert, 2003; Ide et al., 2007). They have been observed prior to large interplate earthquakes in subduction zones when studied in retrospect (Kato et al., 2012; Kato and Nakagawa, 2014; Ruiz et al., 2014; Socquet et al., 2017), and could be the triggering mechanism for these larger events due to stress loading of the fault (Rogers and Dragert, 2003; Ruiz et al., 2014; Socquet et al., 2017), or conversely, can relieve the stress thus reducing the coseismic slip (Radiguet et al., 2012; Dixon et al., 2014). Both of these causes can exist; slow slip events may reduce the long-term risk of earthquakes by limiting the rupture area, but may also elevate the short-term probability of earthquakes from stress perturbations (Voss et al., 2018). Thus, identifying episodic slow slip events can help analyse the spatio-temporal evolution of fault slip and hence better understand what is happening during the nucleation process (Bürgmann, 2018).

The onset of the earthquake nucleation process for the cascade model is from the first event that creates the cascade of events triggering nearby ruptures to the mainshock (Ellsworth and Beroza, 1995; Beroza and Ellsworth, 1996). The end-member of the

preslip model results in a large event being triggered by processes such as aseismic slip at an asperity, suggesting that these processes could determine the size of the large event, hence this model holds importance for the forecasting implications of the event (Beroza and Ellsworth, 1996).

As discussed in Gomberg (2018), both models have been recently used to describe different accelerating earthquake sequences. Ellsworth and Bulut (2018) proposed that the cascade model fit the behaviour of the foreshocks prior to the 1999 İzmit earthquake, whereas a previous study of this same sequence interpreted it as being driven by aseismic fault slip, indicating the preslip model (Bouchon et al., 2011). However, Gomberg (2018) discussed how Ellsworth and Bulut (2018) showed that the progression of eastward foreshocks prior to the İzmit earthquake could be interpreted as propagating slow slip, resulting in a different interpretation of the nucleation processes taking place. The preslip model was favoured by Tape et al. (2018) for central Alaskan earthquakes occurring in 2016 because of the accelerating foreshock sequence accompanied by slow slip. Gomberg (2018), however, noted that the authors proposed the Alaskan earthquakes could instead be from a swarm of other small earthquakes triggered by another process. This is again a different interpretation of the nucleation. The subjectivity of nucleation interpretations is further demonstrated by Mignan (2014), who completed a meta-analysis on several foreshock sequences to examine their nucleation processes. Mignan (2014) showed that a minimum magnitude less than 3 magnitudes below the mainshock for a seismic event catalogue was paramount for the interpretation of the nucleation process (i.e. for an earthquake sequence with a mainshock magnitude of 7, a minimum magnitude less than 4 is recommended for a more accurate nucleation interpretation). This conclusion and the discussion in Gomberg (2018) highlight how data selection and having sufficient data are paramount to be able to make inferences about the nucleation processes in any case.

There is clearly debate on the precise definition of the preslip and cascade models. Here I take the preslip model to define repeated rupture on the edge of a localised

slip patch, which may involve genuinely precursory aseismic creep, and which acts as a nucleation point for the future rupture. In contrast the cascade model involves local triggering of closely-neighbouring ruptures with no associated creep signal and where the main event is triggered by the smaller ones. Both are causal models, but only the first represents classical nucleation. These two end-members form the two main hypotheses to be tested in this thesis. The preslip nucleation hypothesis is favoured if events are more strictly co-located and if the cumulative event number and cumulative seismic moment show evidence of two or more phases of creep (primary, secondary and tertiary), whereas the cascade triggering hypothesis is more consistent with the absence of a creep signal and evidence of events that are close to each other but not strictly co-located. In addition to these hypotheses, I also test the null hypothesis of no causal signal prior to the mainshock.

2.2.2 Volcanic seismicity

Magmatic volcanic eruptions can be classified as either effusive (passive emission of lava) or explosive (dominated by eruption of pyroclastic material) (Francis and Oppenheimer, 2004). Eruptions can also be steam-driven (phreatic), where fluid is rapidly heated below the surface before expanding and exploding. Phreatic activity has also been seen to precede larger magmatic eruptions (Stix and de Moor, 2018). External force mechanisms can also trigger eruptions, such as earthquakes and landslides (Kanamori and Given, 1982; Chesley et al., 2012). It is also possible for several mechanisms to be at play, as seen by the 1980 Mount St. Helens eruption, which was preceded by several phreatic explosions, seismicity and a landslide before the strong lateral explosion (Kanamori and Given, 1982; Chouet and Matoza, 2013).

Through the monitoring of volcanoes, we can infer many of the volcanic process that are occurring. By measuring the gas emissions, deformation and seismicity we can estimate the current state of unrest at volcanoes thus allowing us to make more

accurate forecasts. For example, the seismicity recorded can be caused by the brittle failure of rock allowing us to track the movement of magma to help better understand the volcanic processes taking place (Thelen et al., 2013). Effusive eruptions in particular often have precursors associated with accelerating seismic event rate because of the stress required for the magma body to exert a large enough stress to propagate a new fracture (Kilburn, 2003; Bell et al., 2018). Although seismic signals are often seen to precede volcanic eruptions (Benoit and McNutt, 1996), their presence does not always mean an eruption is imminent (Moran et al., 2011; Newhall et al., 2017).

There are many seismic signals that are measured at volcanic sites and thus they can be broken down into sub-categories of events, discussed in a comprehensive review in Chouet and Matoza (2013). I discuss two of the main sub-categories that are most frequently measured, Volcanic-Tectonic (VT) and Long Period (LP, also called Low Frequency) events. The VT events often occur due to brittle failure and have spectral frequency contents of 5-15 Hz. They are recognisable due to their sharp onset and rapid decay. The waveforms alone are often indistinguishable from tectonic earthquakes (Lahr et al., 1994; Chouet and Matoza, 2013). They often occur as a result of brittle rock failure from the stress changes associated with the magma ascent, but can also be due to the injection and transport of magma at shallow depths (Lahr et al., 1994). However, there is often a challenge to distinguish VT swarm seismicity from tectonic seismicity. A large proportion of small-magnitude to large-magnitude events (see also section 2.3.2), and also no clear mainshock are characteristic of volcanic seismicity (McNutt, 2002).

The LP events (0.5-5 Hz) are emergent and lack a clear P and S wave, with a tail of a harmonic coda (Chouet and Matoza, 2013). They occur from the ascent or injection of magma into the surrounding rocks (Chouet and Matoza, 2013; Bell et al., 2017). Their emergent P and S waves are related to their triggering mechanisms (e.g. pressure changes) and the coda is due to the resonance in a fluid or ash filled crack (Neuberg, 2011; Chouet and Matoza, 2013). Their occurrence is a part of several processes that do not necessarily indicate imminent eruption (Neuberg, 2011).

Other than VT and LP earthquakes, there are also Hybrid, Very Long Period (VLP, also called Very Low Frequency) and Tremor. Hybrid earthquakes have high frequency onsets followed by a low frequency ringing (Harrington and Brodsky, 2007). VLP events (0.01-0.5 Hz) occur from the elastic response of the conduit walls from a mass transport process (Chouet and Matoza, 2013; Waite et al., 2008; Pagliuca et al., 2009). Tremor is a type of continuous LP signal lasting anything from minutes to months (Chouet and Matoza, 2013). It can generalised into harmonic tremor and non-harmonic tremor. Harmonic tremor has a steady amplitude and is fairly uniform in period, whereas non-harmonic tremor has irregular signals with a higher frequency (McNutt, 2002). Tremor commonly occurs due to unstructured, random background noise caused by magma movement (Schick, 1981; Neuberg, 2011) or the superposition of many LP events which are too close together to be resolvable (Neuberg et al., 2000; Neuberg, 2011).

Swarm activity consisting of VT earthquakes is a common element used in eruption forecasting (Kilburn, 2003; Bell and Kilburn, 2012; Boué et al., 2015; Bell et al., 2018). By analysing the patterns of multiplets in the VT swarms, one of the models described in section 2.2.1 could be used to explain whether the multiplets were to mirror the repeated rupture behaviour of the same asperity (preslip), or were due to local triggering (cascade). Observing tertiary creep in the seismic energy release rates and strain could also imply that the material were degrading and thus a critical weakening could occur, leading to the runaway phase of failure (De la Cruz-Reyna and Reyes-Dávila, 2001). This observation would then allow for the time to failure to be calculated from field data (discussed further in section 2.4.2).

In late 2004, Mount St. Helens began to have seismic swarms containing VT earthquakes occurring regularly near the surface (Moran et al., 2008a; Chouet and Matoza, 2013). The growth of these seismic swarms signalled that Mount St. Helens was in the vent clearing phase, and therefore experiencing unrest (Moran et al., 2008a; Major et al., 2005; Scott et al., 2008). As these repeating signals in the swarms were

likely a part of another process of stresses on the edge of cracks around the conduit (Thelen et al., 2011), it mirrors the seismicity behaviour in the preslip model.

Bell and Kilburn (2012) attributed swarm behaviour to magmatic events which were triggered by transient episodes of elevated rates of aseismic flank movement for several eruptions and intrusions at Kilauea, Hawaii. From the definitions made above, this behaviour follows the cascade model.

Therefore, understanding the different seismic signals associated with volcanoes, particularly the events occurring during swarms, can help in better understanding the underlying processes taking place prior to, and during, an eruption.

2.2.3 Landslides

Landslides occur due to the change in stability on a natural or artificial slope causing the slope to fail under the influence of gravity (Sidle et al., 2006). Several external triggering mechanisms have been observed to cause landslides, such as excessive rainfall (Dhakal and Sidle, 2004; Gariano and Guzzetti, 2016) and larger earthquakes (Lin et al., 2006), but large landslides are more commonly preceded by an accelerating creep of the material failure (Voight, 1978). Kilburn and Petley (2003) used a model to show that the accelerating creep seen in landslides can be described by the nucleation, growth and merging of a fractal crack system prior to the failure. Multiplets could be seen here if the propagation paths from the cracks were within one-quarter of a wavelength, i.e. the difference between the waveforms would be indistinguishable from each other (Geller and Mueller, 1980). The Kilburn and Petley (2003) model demonstrated that shallow landslides were likely associated with the movement of loose material (such as previously fractured rock) and hence only require a small perturbation to trigger failure. In constrast, catastrophic landslides tend to require slow rock cracking (aseismic slip) that accelerates the deformation towards failure (Kilburn and Petley, 2003). Monitoring

this transition from aseismic slip to catastrophic failure in landslides is critical in understanding their complex behaviour (Handwerger et al., 2016). Seismic signals are radiated during this process to failure, thus it is possible to understand the complexity of landslides through seismicity (Ekström and Stark, 2013; Whiteley et al., 2019).

2.2.4 Similarities between catastrophic failure processes

There are similarities between how a catastrophic failure occurs in tectonic earthquakes, volcanic eruptions and landslides. Simply put, tectonic earthquakes occur because of a stress change in the rock causes a fault to slip. The failure associated with VT earthquakes is caused by the rock cracking near a volcano, which tends to happen in areas of crustal weakness where the mass of the volcano adds to the regional stress (Cailleau et al., 2007). Alternatively, landslides are a large failure that happens due to a change in the slope stability. Often an earthquake can occur with no prior seismicity indicating an impending failure, however volcanic eruptions and landslides are typically preceded by seismicity associated with their underlying nucleation processes. They can all be triggered or be a part of another ongoing process. The physics of these failures is similar, thus it can be modelled empirically from observational data together.

All of these failures that I have mentioned here have been observed to have been preceded (or accompanied) by seismic signals and more importantly, multiplets, that are either from a triggering mechanism or as part of a process that is ongoing. To relate these events to the models discussed in section 2.2.1, a failure event which is associated with a local creep-type deformation is more like the preslip model, and a failure due to a cascade of triggered events involving failures that are not associated with a creep signal and are not too close spatially (despite their waveform similarity) is more like the cascade model. Finally, there is also the case that the multiplets are the outcome of a random process not associated with the failure. However, the similarity in the seismic signals that are produced from these three failures can be exploited to examine their

occurrence with the same statistics and theory with the method that I develop in this thesis.

2.3 Forecasting catastrophic failure with statistics

Catastrophic failure events are often seen to result from a positive feedback of the failure process resulting in a critical point of a finite-time singularity (Sammis and Sornette, 2002; Sornette, 2002). This singularity could be caused by a stress transfer or the lowering of the local elastic stiffness, which would make forecasting feasible (Main, 2000; Sammis and Sornette, 2002; Main and Naylor, 2012). However, their occurrences are also meaningful outliers (also called 'dragon-kings'), as they are found to occur outwith the governing power laws (Sornette, 2002, 2009; Main and Naylor, 2012). Self-organised criticality dynamics play a critical role in many dragon-king systems, such as catastrophic failures, whereby they are in an open dissipative system with many metastable states, and are driven by a slow driving process (Bak et al., 1988; Sornette, 2002). To forecast these events, we need to better understand their processes.

2.3.1 Earthquake magnitude behaviour

An empirical way of comparing earthquakes to one another, is through their magnitude. The use of the moment magnitude (M_W) (Hanks and Kanamori, 1979),

$$M_w = \frac{2}{3} log(M_o) - 10.7, \tag{2.1}$$

is preferable as it is based on its seismic moment (M_o),

$$M_o = \mu * \text{rupture area} * \text{slip length}, \tag{2.2}$$

where μ is the shear modulus (Hanks and Kanamori, 1979). However, local magnitudes (M_L),

$$M_L = log(A) + 2.56log(D) - 1.67, \tag{2.3}$$

are simpler to use in real-time as they are based on the maximum amplitude A of the ground shaking and distance D between station and event (Richter, 1935; Kendall et al., 2019). The M_L typically underestimates the strength of distant, deep and strong earthquakes due to attenuation and thus is not well suited for large earthquakes (Kanamori, 1983). However, M_L and M_W should be roughly equivalent for events between M_L =3-7 (Hanks and Kanamori, 1979). When M_L <3, the difference between M_W and M_L increases as the size of the event decreases, thus Kendall et al. (2019) recommended to use M_L to infer M_W and M_o when dealing with small events.

2.3.2 Frequency-magnitude distributions

The total number of earthquakes N with magnitude M which are reliably recorded, can be related to the Gutenberg-Richter Law (Gutenberg and Richter, 1944) as,

$$\log_{10} N = a - b(M - M_c), \tag{2.4}$$

where a is a constant related to the total seismicity in the region, and b is a constant that describes the ratio of small events to large events. The threshold for the minimum magnitude above which all earthquakes are reliably recorded is the magnitude of completeness, M_c. Usually in tectonic settings, $b \approx 1$, but in cases such as volcanic seismicity, a higher b-value (anywhere between 1.1-3.5) can sometimes occur (Roberts et al., 2015). An example of a frequency-magnitude distribution for a synthetic catalogue sampled from an underlying Gutenberg-Richter distribution can be seen in Figure 2.2.

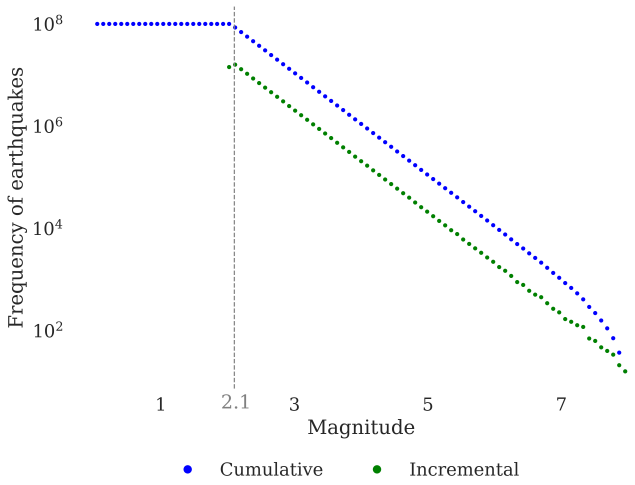

Figure 2.2: Frequency-magnitude distribution for a synthetic catalogue with $N = 10^8$ events and $b = 1$ shown as incremental (green dots) and cumulative (blue dots) frequencies. The minimum magnitude in this synthetic example is 2.0 and the completeness magnitude M_c is set to be 2.1, shown by the grey dashed line.

When the frequency of earthquakes are plotted on a log-linear plot, as in Figure 2.2, the constants a and b can be estimated; a as the y-intercept and b as the gradient of the line. As these constants describe the seismicity of a region, the frequency-magnitude distribution of Equation 2.4 is used to estimate seismic hazard (Baker, 2013).

If we are able to determine the total average magnitude, $\overline{M}$, the magnitude of completeness, M_c, and the magnitude uncertainty (bin size) ΔM for a catalogue, then an estimation of b ($\hat{b}$) can be calculated using the maximum likelihood method (MLE) (Aki, 1965),

$$\hat{b} = \frac{\log_{10}\mathrm{e}}{\overline{M} - (M_c - \Delta M/2)}. \tag{2.5}$$

The uncertainty can be estimated with (Shi and Bolt, 1982; Marzocchi and Sandri, 2003),

$$\sigma_{\hat{b}} = 2.30\hat{b}^2\sqrt{\frac{\sum_{i=1}^{N}(M_i - \overline{M})}{N_c(N_c - 1)}}, \tag{2.6}$$

where N_c is the number of events above M_c, which for this synthetic example gave a

$\hat{b}$-value of 1.0 ± 0.00010, as expected from the input of a Gutenberg-Richter distribution with a true b-value of 1.0.

The MLE method is preferred over a simple linear least squares regression for calculating the estimated b-value ($\hat{b}$) as it takes into consideration the significance that the many smaller magnitude events have over the fewer larger magnitude events, unlike a linear regression which gives equal weighting to all magnitudes (Naylor et al., 2010).

The value for M_c can be reliably calculated by following the workflow in Roberts et al. (2015), as summarised in Figure 2.3, which estimates the best model from the following: the b-Value Stability (BVS), Maximum Curvature (MaxC) and Goodness-of-Fit Test (GFT) methods.

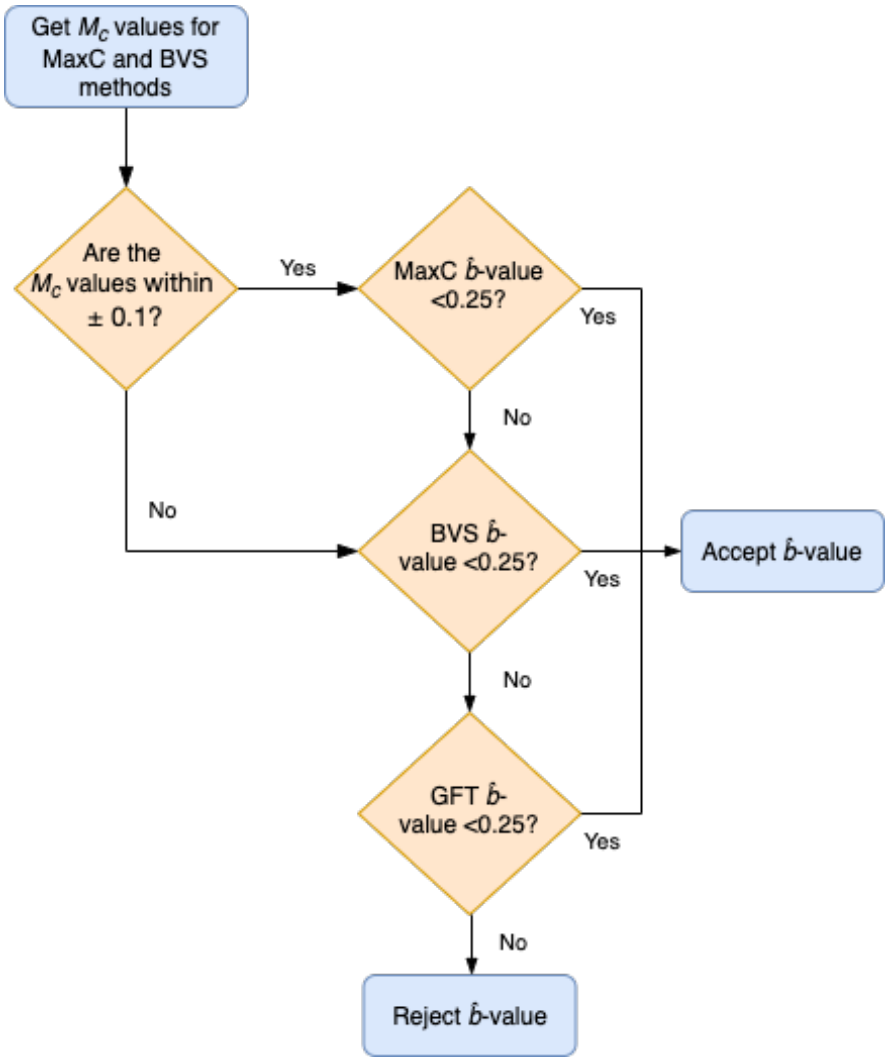

Figure 2.3: Illustration of the workflow in Roberts et al. (2015) for choosing the best model for estimating the b-value ($\hat{b}$) from the magnitude of completeness, M_c.

The decision points are represented as orange diamonds, where the 'yes' and 'no' responses are shown on the arrows, and the blue boxes indicate the initial and end points of the workflow. The first step in Figure 2.3, is to check whether the BVS and MaxC estimate an M_c within $\pm$ 0.1. If so, and the $\hat{b}$-value error of the MaxC method < 0.25, then the MaxC method is chosen. However, if the MaxC $\hat{b}$-value error > 0.25, or the M_c values do not agree within $\pm$ 0.1, then the BVS method is chosen if the BVS

$\hat{b}$-value error < 0.25. If these criteria fail, then the GFT method is tested next. If the GFT $\hat{b}$-value error < 0.25, then the GFT method is chosen. If not, then the $\hat{b}$-value is rejected as the Gutenberg-Richter model is not appropriate.

Roberts et al. (2015) discussed that the BVS method is the preferred method if the distribution of magnitudes is broader, however it does tend to choose higher M_c values than other methods (such as the MaxC or GFT methods, as tested in Woessner and Wiemer (2005)) thus will generally choose higher $\hat{b}$-values due to bias.

The BVS method observes the $\hat{b}$-value as a function of the M_c (Cao and Gao, 2002; Roberts et al., 2015). The BVS method calculates a $\hat{b}$-value from the MLE method (Equation 2.5) while increasing the M_c for the catalogue until a point of stability. The stability is chosen as when the average of the $\hat{b}$-value for five successive M_c falls within the error of the magnitudes (Roberts et al., 2015). The BVS method works under the assumption that the $\hat{b}$-value will increase as M_c increases until this point of stability. The MaxC method instead calculates the M_c as the maximum curvature of the frequency-magnitude distribution (Wiemer and Wyss, 2000), whereas the GFT method (from Wiemer and Wyss (2000)) calculates the M_c for when 90% of the catalogue can be described by a power-law fit.

Alongside sequences with magnitudes that follow Gutenberg-Richter statistics, it is also possible for the magnitudes to follow other types of distributions in the time series. Bouchon et al. (2011) showed accelerating magnitudes in the foreshock sequence prior to the 1999 M_W 7.6 İzmit, Turkey earthquake. An acceleration of magnitudes was also seen in the interplate foreshock sequences in the North Pacific area between 1999 - 2011 Bouchon et al. (2013). Poli (2017) previously showed that the seismic events preceding the Nuugaatsiaq landslide on 17th June 2018 also accelerated in magnitude before the failure.

2.4 Temporal earthquake behaviour

Inter-event times (also known as waiting times) are the times between two consecutive events, i.e. if event 1 occurred at 20:30:20 (format hh:mm:ss) and event 2 occurred at 20:30:55, the inter-event time between these two events would be 35 seconds.

Earthquakes can be described by a Poisson distribution when aftershocks are removed (Gardner and Knopoff, 1974). The Poisson distribution is appropriate for discrete events occurring independently of one another in time (i.e. randomly) as,

$$P(n,t,\lambda) = \frac{(\lambda t)^n}{n!} e^{-\lambda t}, \quad t = 1, 2, 3.., \tag{2.7}$$

which states that the probability of n earthquakes occurring in the time interval $(0,t)$, where there is an underlying rate λ (related to the average recurrence time τ by $\tau = \frac{1}{\lambda}$), is exponential. The probability that at least one earthquake ($n > 1$) would occur in the time interval $(0,t)$ is then,

$$P(n > 1, t, \lambda) = e^{-\lambda t}. \tag{2.8}$$

Thus, the time to the next event t_f and the time since the previous event t_b follow the same exponential distribution as the waiting time τ between any two consecutive events,

$$P(t_f < t) = P(t_b < t) = P(\tau < t) = 1 - \exp^{-\lambda t}. \tag{2.9}$$

If the inter-event times follow an exponential distribution, it is diagnostic of a Poisson distribution, implying events are occurring independently. If there is no deviation from Poisson statistics prior to a mainshock, that infers that there is no precursory seismic activity.

Touati et al. (2009) showed that the inter-event time distribution can also be described as a bimodal mixture of gamma and exponential distributions. The gamma

distribution arises due to correlated event pairs, such as those belonging to the same aftershock sequence, and the exponential distribution from the uncorrelated events at longer times (Touati et al., 2009). In some areas, the aftershock sequences may even overlap which could hide the underlying triggering behaviour by mixing different aftershock sequences which are independent of each other (Touati et al., 2009).

Periodic inter-event times have sometimes been observed in volcanic seismicity, and are often termed 'drumbeats' due to their unique pattern of swarms of small regularly repeating events (Kendrick et al., 2014). Highly periodic drumbeat seismicity have been observed at the Tungurahua volcano, Ecuador in 2015 (Bell et al., 2017), the Soufrière Hills volcano, Montserrat in 2003 and at the Mount St Helens volcano, USA in 2005 (Kendrick et al., 2014). The periodicity of the inter-event times indicates that the failure is under an approximately constant load, which could occur if the source is in a steady-state mode (Nadeau et al., 1995). Also, the short inter-event times (which are often seen in drumbeat seismicity), imply that rapid healing, loading, and reactivation of the source is required, indicating a much more complex system (Chouet and Matoza, 2013; Bell et al., 2018).

2.4.1 Inter-event time model comparison

The comparison between models, such as the exponential and gamma models for inter-event times, can be achieved using two penalised-likelihood criteria: the Akaike Information Criterion (AIC, in Equation 2.10) from Akaike (1974) and the Bayesian Information Criterion (BIC, in Equation 2.11) from Schwarz (1978),

$$AIC = 2k - 2\ ln(\hat{L}), \tag{2.10}$$

$$BIC = k\ ln(n) - 2\ ln(\hat{L}). \tag{2.11}$$

These two criteria aim to evaluate a model based on its likelihood $\hat{L}$, number of free parameters k, and number of observations n, where the model with the lower result is the preferred model. The difference between the AIC and BIC, is in the penalisation term for k. The AIC is considered better for prediction, however it can sometimes cause over-fitting, whereas the BIC allows for a consistent estimation of the underlying data generating process (Burnham and Anderson, 2004). The BIC is also considered more reliable for datasets larger than 46 (Main et al., 1999), however it is preferred to use both criteria for model selection (Burnham and Anderson, 2004).

2.4.2 Time to failure

The Failure Forecast Method (FFM) is a technique based on the empirical relationship between the geophysical rate of change of a given precursor $\dot{\Omega}$, to the failure rate of materials $\ddot{\Omega}$ (Voight, 1988),

$$\ddot{\Omega} = K\dot{\Omega}^{\alpha}, \tag{2.12}$$

with K and α as constants derived empirically from observational data to describe how the rate changes with time. Solutions generally applied to earthquakes show that changes in the seismic event rate $n(t)$ ($\dot{\Omega}$ in Equation 2.12), may indicate changes in underlying processes such as aftershock triggering, which follows the empirical modified Omori-Utsu formula (Utsu et al., 1995),

$$n(t) = \frac{K}{(t+c)^{p}}, \tag{2.13}$$

where t is the time since occurrence of the mainshock, K in this case is the productivity of the aftershocks counted in $n(t)$, c is a constant and the exponent p is the decay rate, usually around 1. In this case, the rate of aftershocks is inversely proportional to the time since the mainshock. The aftershocks described in Equation 2.13 can also be reflected in the Epidemic-Type Aftershock Sequence (ETAS) model, which describes

earthquake sequences as consisting of a series of independent background events and their own aftershocks, where any event can generate its own aftershocks with some probability (Ogata, 1988, 1992).

The Omori-Utsu law (Equation 2.13) results from a critical branching process or cascade of causally-related events (Vere-Jones, 1976). In the case of nucleation, physical models based on damage mechanics predict a reverse-time Omori law in the general case of $\alpha > 1$ in Equation 2.12, following a power-law increase in the mean rate of precursory signals from,

$$n(t) = \frac{K}{(t_f - t)^{p'}}, \tag{2.14}$$

where t_f is the failure time and $p' = \frac{1}{(\alpha-1)}$ (Voight, 1988; Cornelius and Voight, 1994; Main, 1999, 2000; Bell et al., 2011; Bell and Kilburn, 2013; Bell et al., 2018). Detecting a change in event rate ($n(t)$ in Equation 2.14 and $\dot{\Omega}$ in Equation 2.12) provides an improved insight into the pre-failure physical processes and gives the potential for a quantitative measure that can be used in the FFM to calculate the time to failure (Bell et al., 2011; Boué et al., 2015). To identify such changes, Bell et al. (2011, 2018) used an information criterion to test competing hypotheses of accelerating versus stationary seismicity, and if accelerating, whether this took the form of an exponential increase or an inverse power law, such as Equation 2.14.

2.5 Triggering and interaction processes

An earthquake can trigger another earthquake in both the near-field and far-field distances due to stress changes, which can either induce or impede seismic activity in the surrounding region (static triggering), or induce events at larger distances (dynamic triggering). Thus, estimating the stress changes helps to understand the underlying triggering mechanisms to better assist in seismic hazard (Freed, 2005).

2.5.1 Coulomb triggering

The Coulomb failure criterion explains how the stress changes that can induce/impede local seismicity (static triggering) occurs due to the Coulomb failure stress (σ_c), where earthquakes can occur when the shear stress (τ) is large enough to overcome the normal stress (σ_n) that would usually keep the fault from slipping, also taking into consideration the pore fluid pressure (p) and the coefficient of friction (μ) (Freed, 2005; Jaeger et al., 2007),

$$\sigma_c = \tau - \mu(\sigma_n - p). \tag{2.15}$$

Dynamic triggering is instead a transient change in the Earth's stress field, where the stress from one earthquake propagates and triggers a secondary earthquake (Hill et al., 1993; Freed, 2005; Prejean and Hill, 2011; Shelly et al., 2011).

Measuring stress in the field is more difficult than in the small-scale laboratory setting, however an effective coefficient of friction (μ') can be substituted in as $p \propto \Delta\sigma_n$ (Cocco and Rice, 2002). The coseismic Coulomb stress (σ_c) can then be inferred from how the change in τ ($\Delta\tau$) and σ_n ($\Delta\sigma_n$) are affected on a fault (Reasenberg and Simpson, 1992) as,

$$\Delta\sigma_c = \Delta\tau - \mu'\Delta\sigma_n. \tag{2.16}$$

This then helps calculate whether a fault is closer to, or further from failure. The perturbation associated with these two types of triggering are represented by the change in σ_c (Belardinelli, 2003).

2.5.2 Induced seismicity

Earthquakes can also be caused by anthropogenic sources such as geothermal injection, waste-water disposal wells, and hydraulic fracturing causing the fluid pressures to increase within the fault and more likely to rupture (Ellsworth, 2013; Goebel and

Brodsky, 2018), in which case they are 'induced'. Induced seismicity differs from tectonic seismicity due to a higher rate of background events and repeating events, a larger proportion of small clusters, a greater distance between parent and event, and also a faster temporal decay of events (Zaliapin and Ben-Zion, 2016).

Induced seismicity has been the cause of several moderately-sized events in the US, e.g. the 2011 M_W 4.0 earthquake in Youngstown, Ohio (Kim and Das, 2013), 2011 M_W 4.7 in Guy-Greenbrier, Arkansas (Yoon et al., 2017) and the 2016 M_W 5.1 earthquake in Fairview, Oklahoma (López-Comino and Cesca, 2018).

An important characteristic of induced earthquakes is their magnitude, as this is used to assess the strength of the seismic events. In order to minimise the risk of large events and eliminate the potential for damage, mitigation strategies for induced seismicity associated with fluid injection operations is closely monitored (Bommer et al., 2006; Petersen et al., 2015; Kendall et al., 2019; Porter et al., 2019). A previous study by Kendall et al. (2019) emphasised the importance of assigning accurate estimates of micro-earthquake magnitudes in real time for cases like this.

2.5.3 Rate and state friction

An amplification effect based on the rate-and-state-variable friction law (also known as the Dietrich-Ruina or 'slowness' law) (Dieterich, 1979; Ruina, 1983; Scholz, 1998), says that earthquake triggering can occur due to the sudden change in the normal stress across faults. This law describes the relationship between the shear stress (τ), effective normal stress (σ), sliding velocity (V) and steady-state friction (μ_0),

$$\tau = \left[\mu_0 + a \ln\left(\frac{V}{V_0}\right) + b \ln\left(\frac{V_0 \theta}{L}\right)\right]\sigma, \tag{2.17}$$

where constants a and b are proportionality constants to represent material properties, V_0 is a reference velocity, with the 'state' variable (θ) and critical slip distance (L)

scaling as,

$$\frac{d\theta}{dt} = 1 - \frac{\theta V}{L}. \tag{2.18}$$

The small-scale failure due to the sub-critical propagation of cracks may represent the main mechanism of creep observed, once scaled to seismic lengths (Main, 2000; Sheldon and Micklethwaite, 2007). Relating this directly to earthquakes, the driving of time-dependent sub-critical cracking processes can be attributed to this rock fracture (Dascalu et al., 2009; Brantut et al., 2013). For a critically stressed rock, where τ is near the strength limit for brittle failure to occur, the maximum stress level that can be supported is limited by the frictional strength of pre-existing faults (Townend and Zoback, 2000; Scuderi et al., 2017). Whether the slip will be seismic or aseismic however, relies on the frictional stability, which in turn depends on the local elastic stiffness around a fault. To look at the fault stability empirically, the velocity-dependence when μ is at a steady-state (μ^{ss}), i.e. when $\theta \propto L/V$, can be assessed in terms of the material property constants $a - b$,

$$a - b = \frac{\partial \mu^{ss}}{\partial[\ln(V)]}, \tag{2.19}$$

which is also illustrated in Figure 2.4, where μ begins in a steady state (μ^{ss}).

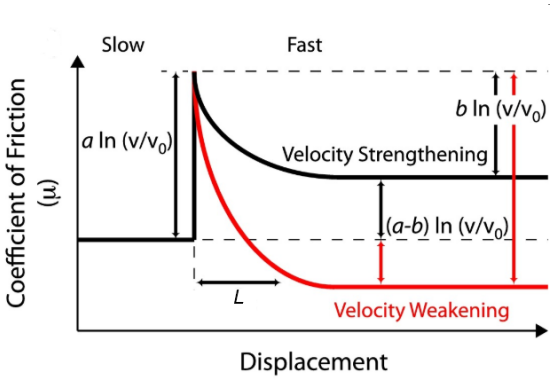

Figure 2.4: Illustration how the sliding velocity V can cause an immediate increase in frictional stress μ past the critical slip distance L, evolving to either a velocity weakening (red line) or velocity strengthening (black line) state depending on the material property constants a and b, impacting the stability of the system (Image edited from Scuderi et al. (2017)).

Figure 2.4 illustrates that if $(a-b) \geq 0$ the slip is stable and velocity strengthening takes place, which leads to aseismic slip. If $(a-b) < 0$, velocity weakening occurs, which leads to the nucleation of a seismic instability if the weakening rate of $(b-a)/L$ is sufficient (Ruina, 1983; Scuderi et al., 2017; van den Ende et al., 2018).

Analysing seismic signals associated with landslides along with field measurements also enables the physical parameters, such as V or μ, to be obtained to estimate their dynamic behaviour, as the source time function is equivalent to the inertial force of the sliding mass (Kanamori and Given, 1982; Petley et al., 2005; Moretti et al., 2012; Allstadt, 2013; Yamada et al., 2013, 2018).

2.5.4 Creep-to-failure

The presence of a creep type signal is a key diagnostic in discriminating between the competing hypothesis in Figure 2.1. Main (2000) showed a classic 3-stage creep-to-failure evolution from the damage associated with time-dependent, sub-critical crack

growth in the brittle field, starting with a primary phase of deceleration, a steady-state secondary phase, and then a third accelerating creep phase (Figure 2.5).

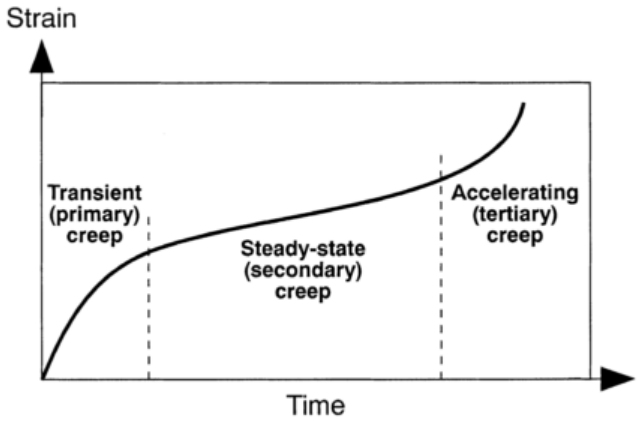

Figure 2.5: Illustration of the three phases of creep: transient, steady-state and accelerating. Image from Main (2000).

The creep model in Figure 2.5 is supported by the observations already made in a controlled laboratory setting by Heap et al. (2009, 2011), illustrating that a similar signal is also seen in the cumulative number of events and with cumulative seismic moment. This model of creep in earthquakes can also be applied to volcanic activity, such as dyke propagation, where the dynamic failure is preceded by a slower mechanism of large fractures which extend their growth and merge with smaller cracks around their tips (Main, 2000; Kilburn and Petley, 2003). Accordingly, in this thesis I will examine evidence for two or more phases of creep as a diagnostic in favour of the preslip nucleation hypothesis.

2.5.5 Precursory signals

What happens before an earthquake, and why precursors may or may not occur, is still poorly understood. Cicerone et al. (2009) and Hough (2010) wrote comprehensive reviews on some of the most popular candidate precursors. These include (but are not

limited to) changes in: animal behaviour prior to an earthquake (Lott et al., 1981; Li et al., 2003; Grant and Halliday, 2010; Berberich et al., 2013; Yamauchi et al., 2014), the Earth's electric or magnetic field (Varotsos et al., 1988, 1993; Uyeda et al., 2009; Sobisevich et al., 2017), geochemical (Tsunogai and Wakita, 1996), geodetic (Borghi et al., 2016), geoelectrical (Rodriguez et al., 2004), hydrological (Viesca and Rice, 2012) and thermal (Silver and Valettesilver, 1992) variations, among others. Many of these are attributed as being unusual phenomena associated with earthquakes rather than acting as a precursory signal (Hough, 2010; Woith et al., 2018). Foreshocks, however, have been frequently seen to precede large earthquakes, and have been long thought of as one of the most promising ways to forecast earthquakes (Papazachos, 1975; Jones and Molnar, 1979; Oskin, 2013). The difficulty lies in the retrospective labelling - an earthquake event is not known as foreshock until the mainshock has occurred. Nonetheless, there have been cases where there have been earthquakes which have been correctly forecast from their foreshocks, but mostly retrospectively.

The case of the 1975 Haicheng, China earthquake is an example of how foreshocks were reportedly identified prior to the mainshock, and so led to the evacuation of the city prior to the earthquake. The scientists who were analysing this area from 1970 predicted the earthquake in incremental stages, narrowing in on both location and time with different prediction timeframes (Raleigh et al., 1977; Wang et al., 2006; Chen and Wang, 2010). Unfortunately, this method was not subsequently developed reliably due to the inaccuracy found in the reporting of the predictions, and the unusually pronounced foreshock activity (Wang et al., 2006; Chen and Wang, 2010). This is apparent by the 1976 M_W 7.8 Tangshan, China and the 2008 M_W 7.9 Wenchaun, China earthquakes where there were no foreshocks flagged as significant before these earthquakes, and thus no alarm (Chen and Wang, 2010).

A case of retrospective analysis of foreshock sequences was completed by Bouchon et al. (2013) using seismic catalogues of the North Pacific area. The authors analysed the foreshock sequences prior to all earthquakes in this region with a magnitude of at least

6.5 and at depths shallower than 50 km, occurring between 1999 - 2011, amounting to 72 events. From their analyses it was found that interplate earthquakes were preceded by accelerating seismic activity (foreshocks) in the months to days before the mainshock, whereas this was infrequently the case for intraplate earthquakes. This was deduced by analysis that at plate boundaries (therefore interplate), the interface slowly slips before the rupture, thus causing a long precursory phase.

2.5.6 Probabilistic forecasting

Probabilistic forecasting of earthquakes produces a likelihood of an event of a given size occurring for a region of interest within a given time period (Baker, 2013). Forecasting enables building design implementation, determination of insurance policies, and emergency preparedness (Petersen et al., 2007; Jordan et al., 2014; Wang and Rogers, 2014). These types of forecasts can be split into two main types: time-independent and time-dependent methods.

Time-independent forecasting follows a Poisson distribution of earthquake occurrences (i.e. only the average earthquake recurrence time is required), and assumes that the earthquakes occur independently of one another in time, thus the probabilities of future events are independent of earthquake history (Petersen et al., 2007; Jordan et al., 2011).

Time-dependent forecasting instead uses recent earthquake occurrences in an elastic dislocation model which follows the hypothesis that the probability of an earthquake event increases with time as the stress on the fault increases, thus the probabilities depend on the information available at time when the forecast is made (Petersen et al., 2007; Jordan et al., 2011).

The latter forecasting type can be used in Operational Earthquake Forecasting (OEF), which provides a short-term time-dependent seismicity for use in forecasts

(Jordan et al., 2011). The probability of an earthquake event occurring is based on the observed tendency of earthquakes to cluster in space and time. It can be estimated by the use of the earthquake history and geology of the area in statistical and physical models, such as the ETAS model. As the ETAS model defines the clustering of foreshocks, mainshocks and aftershocks by the same seismic triggering mechanism, it therefore assumes that earthquakes are dependent on one another (i.e. earthquakes trigger other earthquakes) (Helmstetter and Sornette, 2002; Felzer et al., 2004; Jordan et al., 2004, 2011). These models can then be used to forecast the time, space and magnitude dependence of the seismic triggering involved in generating the subsequent events to estimate the future probability of earthquakes in the area (Jordan et al., 2011). Following on from this, the information can be portrayed in a seismic hazard map which is a forecast of how the seismicity would affect a region. Recently, these seismic hazard maps also began to incorporate suspected non-tectonic activity, such as induced seismicity, in order to include events triggered by oil and gas exploration (Petersen et al., 2015).

Seismic risk is instead a forecast that incorporates the hazard with the societal damage, from the resilience, exposure and vulnerability of a community in a region (Jordan et al., 2011). Risk is often written as the simplistic notation of risk = hazard $\times$ exposure $\times$ vulnerability $\div$ resilience (Jordan, 2009). The resilience is the capacity that a region would cope and recover from the hazard (Cutter et al., 2014; Jordan, 2009). The exposure is a measure of who and what is affected, and the vulnerability is what makes a community, individual, or asset particularly susceptible to a hazard (Field et al., 2005; Jordan et al., 2011).

The International Commission on Earthquake Forecasting (ICEF) report in Jordan et al. (2011) discusses how there is no reliable method at present that can provide a deterministic earthquake prediction. At present, scientists can identify particular areas of earthquake risk and at most make a probabilistic forecast. Deterministic earthquake prediction is still the goal, as it would allow for the prediction that an earthquake will

occur within a specific geographical region, time window and magnitude range, with a high probability and low error rates (Jordan et al., 2011; Main and Naylor, 2012).

2.5.7 Role of repeating earthquakes

Repeating earthquakes have been seen prior to large earthquakes, volcanic eruptions and landslides, however, it is also possible to have repeating seismic patterns with no catastrophic failure, such as within a seismic swarm or in volcanic settings (Power and Lalla, 2010). Mesimeri and Karakostas (2018) demonstrated many repeating signals in seismic swarms in the Western Corinth Gulf in Greece during 2008-2014 which were attributed to aseismic slip along the brittle-ductile boundary layer. Yamaguchi et al. (2018) showed that many small repeating events emerged and subsequently disappeared on a geological fault in a gold mine in South Africa, likely due to fault creep. De Meersman et al. (2009) also showed multiplets occurring in oilfield microseismicity likely due to fluids in the area, that did not culminate in any large event. Although repeating earthquakes are mostly looked at in relation to catastrophic failure, there are several studies showing their relationship with other features. Thus, even with no catastrophic failure, the underlying processes causing the repeating signals in different settings can be better understood.

2.6 Identifying repeating earthquakes

In practice, the terms 'multiplets' are used interchangeably with 'repeating earthquakes,' and thus they are defined clearly here. When multiple sets of events have high waveform similarity, they are called 'multiplets'. For waveforms to be sufficiently similar to one another, their propagation path should not differ by more than one-quarter of a wavelength, i.e. the events would be < 400 metres from each other (Geller and Mueller, 1980). If the multiplets are determined to have the same origin, fault area

and slip geometry, they are called 'repeating earthquakes' (Ellsworth, 1995; Uchida and Bürgmann, 2019).

Multiplets are important to find as they have often occurred prior to numerous catastrophic failure events, e.g. large earthquakes (Bouchon et al., 2011; Kato et al., 2012; Kato and Nakagawa, 2014; Kato et al., 2016a), landslides (Yamada et al., 2016; Poli, 2017; Bell et al., 2018) and volcanic eruptions (Green and Neuberg, 2006; Moran et al., 2008a).

Kato et al. (2012) studied the foreshock sequence to the 11th March 2011 M_W 9.0 Tohoku-Oki, Japan earthquake, and found an additional 1,416 similar events which were relocated to the same location as other events in the known event catalogues. Their evolution showed a migrating slow slip, however, this does not necessarily mean that we can infer the preslip nucleation model (section 2.2.1), as there was no rupture growth or accelerating occurrence of foreshocks prior to the mainshock.

Kato and Nakagawa (2014) and Kato et al. (2016a) retrospectively studied seismic clusters prior to the M_W 8.2 Iquique, Chile earthquake on 1st April 2014 to identify many similar events (called repeating earthquakes in Kato et al. (2016a)). The presence of the events in the foreshock sequence indicated several slow slip events along the plate boundary fault.

Bouchon et al. (2011) studied the seismicity prior to the 1999 M_W 7.6 İzmit, Turkey earthquake, to identify four large foreshocks with increasing magnitude, originating at the eventual nucleation point. This indicated a very localised and short nucleation phase for this event. Bouchon et al. (2011) identified this precursory activity as accelerating slow slip occurring at the base of the brittle crust, which likely led to the main rupture. However, the study in Ellsworth and Bulut (2018) of the same sequence of foreshocks showed that they occurred as a triggering cascade prior to the mainshock, rather than a slow slip process.

Mount St. Helens exhibited increased seismic swarms, with highly repetitive VT events occurring roughly once a minute, started in 2004 (Moran et al., 2008a; Chouet and Matoza, 2013). These types of highly similar and repetitive waveforms are often referred to as 'drumbeat' earthquakes due to their resemblance of the sound pattern that is produced from the beating of a drum (Moran et al., 2008a).

The cause of the drumbeat earthquakes have been attributed to either a resonating fluid-filled crack (Waite et al., 2008), or a stick-slip motion of a conduit plug interacting with the walls during magma ascent (Iverson et al., 2006; Iverson, 2008; Anderson et al., 2010). The drumbeats were followed by a series of solid lava spines extruding at the surface (Scott et al., 2008) and that initiated a rapid phase of dome growth (Chouet and Matoza, 2013) until the volcano returned to a state of rest in late January 2008 (Dzurisin et al., 2015).

The occurrence of LF multiplets at the Soufrière Hills volcano on Montserrat, has been suggested to be an indicator of magma ascent (Hammer and Neuberg, 2009), as significant dome collapses have been preceded by an acceleration of magma ascent and thus earthquake swarms (Miller et al., 1998). The 1997 LF seismic swarm was analysed by Green and Neuberg (2006) and found to have many multiplets occurring in several different families, attributed to a depressurisation process at the volcano. Neuberg et al. (2006) studied the same sequence and suggested that the swarms were triggered by brittle failure of magma due to the high viscosity gradients and strain rates near the conduit walls of the volcano.

Bell et al. (2018) looked at the similarities between accelerating rates of LP events before the Tungurahua, Ecuador volcanic eruption in 2013, using the Failure Forecast Method outlined in section 2.4.2. The authors previously found the activity levels of different families of multiplets were related with changes in rate, amplitude, and periodicity of events (linking to Equation 2.14). The authors suggested that the accelerating LP event rates and increasing amplitude were likely from an accelerating

magma ascent and high gas pressures. By applying the Failure Forecast Method, the authors were able to provide reliable and informative retrospective analyses of the preceding activity to the eruption, and attribute the underlying processes that were associated with the events.

Landslides have also shown the precursory activity of similar waveforms, likely due to the stick-slip of small patches on the base or lateral surfaces of the slope (Uchida and Bürgmann, 2019). Yamada et al. (2016) previously reported that there were several repeating earthquakes recorded before the Rausu landslide in Japan, on 24 April 2015. Poli (2017) and Bell (2018) previously showed that the seismic signal preceding the Nuugaatsiaq landslide on 17th June 2018, contained many similar waveforms that accelerated in time before the failure.

Analysing multiplets has the potential to reveal underlying processes such as the nucleation of large events, or stable repeated slip, and hence could improve probabilistic forecasts (e.g. OEF in section 2.5.6) of the likelihood of different catastrophic events. The problem with finding multiplets, however, is that they are often small, and so are often missed in event catalogues.

2.6.1 Using cross-correlation to assess waveform similarity

Cross-correlation is a method frequently used in signal processing to quantitatively compare how similar two signals, $f(t)$ and $g(t)$ are to one another as a function of the lag τ of one signal to the other. The cross-correlation will output a function which will quantify how much one signal has to move with respect to another signal to get the best match. To calculate the cross-correlation of two signals, we use

$$(f \star g)(\tau) \equiv \int_{\infty}^{-\infty} f^*(t)\, g(t+\tau)\, dt, \tag{2.20}$$

where the left hand side of the equation is the cross-correlation ($\star$) of signal $f(t)$ with signal $g(t+\tau)$, where τ is the lag. On the right hand side, $f^*(t)$ is the complex conjugate of $f(t)$.

High similarity between two signals leads to high cross-correlation coefficients $(f \star g)(\tau)$, and those with lower similarity have low cross-correlation coefficients. Often, the degree of similarity is indicated by $f \star g$ at optimum lag τ_{opt}, which is the lag time at highest $f \star g$. The output is commonly normalised, so that values of 1 show exact correlation, -1 with exact correlation but opposite phase, and those with values close to 0 show very little similarity between the signals.

2.6.2 Template matching methods

Cross-correlation can also be used to find new events below the noise threshold from a 'template' provided by the seismogram of a known detected event, in a technique called 'template matching'. Template matching (also known as matched filter) is a method frequently used in seismology due to its ability to pick out known signals in seismic data (Anstey, 1964). It uses a known template waveform and finds similar waveforms in a longer time series of data with a moving window cross-correlation. Thus, every part of the continuous signal is compared with the template waveform by cross-correlation to assess similarity. If two separate events are found to have a high cross-correlation coefficient, this indicates a candidate set of multiplets, as it means the two events have a similar waveform. As discussed in section 2.6.1, complete correlation results in a cross-correlation coefficient of 1. Multiple sets of multiplets can also be grouped further into 'families', which are groups of higher similarity often seen in volcanic studies (Green and Neuberg, 2006; Neuberg et al., 2006; Hammer and Neuberg, 2009; Bell et al., 2017). Template matching is a powerful technique which can find weak and undetected waveforms, similar to the template waveform, in noisy data (Gibbons and Ringdal, 2006). A particular limitation of this technique is the threshold to define how similar

an event needs to be to be considered a multiplet. The choice for this event threshold is varied in literature, but tends to be associated with the Median Absolute Deviation (MAD) of the seismogram, as it gives a measure of statistical dispersion and is resilient to outliers (Shelly et al., 2007; Kato et al., 2016b; Vuan et al., 2018).

2.6.3 Other approaches

There are several other techniques similar to template matching, such as the Fingerprint And Similarity Thresholding (FAST) method (Yoon et al., 2015). Firstly, the waveforms are compressed into 'fingerprints' to maintain only their vital information in a binary file. Then, Locality-Sensitive Hashing (LSH) is used to sort the fingerprints into different groups depending on their similarities. The FAST method has the advantage that a known template waveform is not required as the method tests every part of the time series against every other part, hence, it is a great tool to use when a catalogue of template events is not available, or in addition to template matching to complement it (Yoon et al., 2017). However a current disadvantage to the FAST method is that it has trouble scaling to large datasets without domain-specific optimisation techniques due to the vast amount of data that is being tested against itself (Rong et al., 2018).

There is also the auto-correlation technique (Brown et al., 2008), which requires no template, but instead uses a brute force search for similar waveforms in continuous data. Although it is a blind search, it can detect events with previously unknown waveforms effectively. However, due to its 'proof by exhaustion' type approach, it does not scale well with the size of the dataset.

Subspace detection (Harris, 2006; Barrett and Beroza, 2014; Chambers et al., 2017) is also a viable method which generalises common features of waveforms and reduces the seismic signal to a linear combination of orthogonal basis waveforms. The method requires sets of events with similar waveforms to create a 'subspace', or orthonormal

base, for each set. This design set of earthquakes representing intended events of interest are then compared to the seismic signal to identify waveforms which contain similar characteristics. This method has the disadvantage that it does still require some prior knowledge of waveform signatures to create the design set.

Template matching and the methods mentioned above, are powerful tools in finding many small events within an earthquake sequence. Having a more complete catalogue of events allows for a better understanding of the seismicity occurring, particularly in a foreshock sequence.

2.7 Outstanding research questions

Multiplets (events with similar waveforms), have been observed to be associated with, or precede, tectonic earthquakes, volcanic activity and landslides. Multiplets are usually not detected with classic triggering methods as their amplitude is often too small to be seen clearly above the background noise. Their presence is important, as it can help better understand the processes driving these failures, which leads to improving the possibility of forecasting them. It is first important to discover how general the presence of multiplets are in different types of failure sequences. It is also essential to assess how their statistical properties can be linked to the nucleation models to understand the underlying processes taking place.

Methods currently used to detect multiplets are often optimised for use in finding multiplets prior to tectonic earthquakes, rather than also testing on volcanic and landslide datasets with the same methodology. They also tend to have a strict criteria for the event to be detected on multiple seismic stations. This criteria is, however, not often met, as failures often occur in sparse network areas, particularly in volcanic and landslide settings. Thus, the accuracy of the method performance in different failure sequences based on the data from one seismic station will be evaluated.

In this thesis I will show how including multiplets in the analysis of synthetic and natural datasets from different processes and separate regions can provide significant new insight into the processes leading up to large events of different types, and in particular allows for the discrimination of the competing preslip nucleation and triggering cascade models for accelerating signals prior to failure.

Chapter 3

Method: Finding Repeating Events in Synthetic Data

Building on the established work discussed in chapter 2, I designed a new algorithm based on the template matching method which finds repeating events in earthquake data, even on sparse seismic networks. In particular, repeating events or 'multiplets' are identified by their similar waveforms at a single station. This is often a realistic scenario in sparse seismic networks used for monitoring, but the method could in principle be extended to two or more stations in the future. The similarity of the waveforms implies the source location is the same as that of the parent template event within one quarter of a seismic wavelength, and that the focal mechanism is also similar, given the same relative amplitudes of the different phases as they sample different parts of the focal sphere.

Section 2.6.2 discussed how template matching has been commonly used due to its ability to pick out repeating signals in seismic data (Gibbons and Ringdal, 2006; Bouchon et al., 2011; Thelen et al., 2011; Kato et al., 2016a). However these analyses often neglect to examine the pattern of evolution of events found or their implications

for the underlying physical processes involved, and do not always quantify explicitly the success rate of finding or missing known events ('*Hits*' or '*Misses*').

This chapter introduces a reliable method of finding multiplets and analysing their temporal evolution in the approach to catastrophic failure, in order to better understand the underlying processes taking place. The method is automated to be used for any seismic dataset, including tectonic seismicity, landslides and volcanic eruptions to date. Most methods in the literature are designed for use with one particular type of failure rather than testing different kinds, or use multiple stations for the determination of repeating events (Moran et al., 2008b; Kato et al., 2012, 2016a). The method develops a simple approach to identify multiplets with rapid processing times compared to multiple station networks. This rapid analysis is a particular advantage in a real time forecasting scenario.

This chapter will introduce and discuss the method that I built to find the repeating events. I could not use a 'real' seismic dataset to develop the method, as there could have been unknown events present. Instead, I built 'synthetic' seismograms with known event properties, such as when the events occurred and their magnitude, to develop and confidently assess the method with a known 'answer'. This chapter also introduces a variety of event picking methods before introducing a step-by-step guide of the method I developed to identify multiplets in waveform data in the presence of realistic seismic noise, and with varying signal-to-noise ratios. This exercise provided a suitable validation of the approach, and informed the design of the final algorithm, prior to its application in real data later in the thesis.

3.1 Synthetic seismograms

To build a method for finding multiplets within seismic data, it was necessary to first create synthetic seismograms. This had the advantage of controlling parameters in the

catalogue, such as background noise level, time between repeating events (inter-event times) and the magnitude distribution of events, to better understand the circumstances for when the method succeeded or failed to identify all candidate repeating events. By using synthetic seismograms, the multiplet locations in time were known for every catalogue created, allowing for the accuracy of the method for finding multiplets to be determined confidently. Knowing the success of the method on synthetic data meant that I could then apply the method to real data to look at the occurrence of multiplets for different types of catastrophic failure.

I constructed synthetic seismograms from three main components: background noise, inter-event times and magnitude of the events. The background noise for the synthetic seismogram is based on a stochastic realisation of the background noise measured from a real seismic station. Next, I added event waveforms distributed temporally which followed four different types of inter-event time distributions often observed in real cases. Finally, I assigned three different types of frequency-magnitude distributions to the repeated events in the synthetic seismograms. The aim of creating these synthetic seismograms with various inter-event time and magnitude distributions was to emulate likely scenarios to test if the multiplet matching method recovered the known input events and their parameters accurately, or not.

This section discusses each of these synthetic seismogram components, which are outlined below,

1. Background noise.
    (a) Characterising real seismic noise.
    (b) Creating realistic synthetic seismic noise.
2. Incorporating different types of inter-event time distributions (described in section 2.3.1):
    (a) Poisson (random) distributed,

(b) Periodic,

(c) Accelerating

(d) and clustered.

3. Using different magnitude distributions (described in section 2.3.1):

(a) Sampling from a stationary Gutenberg-Richter distribution,

(b) The same 'characteristic' magnitude,

(c) and a non-stationary Gutenberg-Richter distribution with amplitude increasing with respect to time.

3.1.1 Background noise

First, I characterised noise from a real seismogram to be recreated for the synthetic seismograms. I used a relatively long time window with no visible or known seismic events in order to get representative sample of the noise.

3.1.1.1 Characterising real noise

Firstly, to characterise noise from a real dataset, a 'quiet' day from the RETU seismic station on the Ecuador seismic network (EC) near the Tungurahua volcano, Ecuador on 22nd January 2015 was examined, as this dataset was openly available. The seismic data was measured on a short period vertical component seismometer, with a corner frequency of 1Hz. Short period instruments were chosen as they are better at detecting higher-frequency signals, such as multiplets from small source ruptures (Sović et al., 2013).

As illustrated in Figure 3.1, it is clear that there were no visible events occurring in the time window selected, and that the noise itself is relatively stationary. Both criteria

are important because the dataset was going to be resampled at many different points to create realistic synthetic stationary background noise.

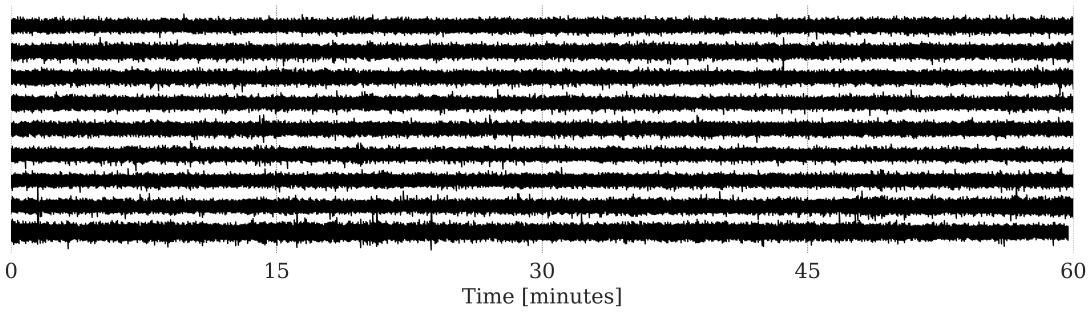

Figure 3.1: A seismic recording taken from the RETU seismic station near the Tungurahua volcano, Ecuador, with no known or visible events. Each horizontal line represents 60 minutes of seismic recording. Total shown here is almost 9 hours.

Figure 3.1 shows that the dataset behaves, more or less, as a stationary stochastic process, i.e. the statistical properties are time invariant for the dataset.

3.1.1.2 Creating synthetic seismic noise

Next, 20 different de-trended, de-meaned and normalised two minute segments of seismic signal from the Tungurahua dataset, sampled at 100Hz, were extracted to create a two minute synthetic noise segment. The choice of two minute segments were so that this process could be scaled to be dependent on the event duration, i.e. if a noise sequence lasting 10 minutes was required, this process could be repeated five times. I also did not want to take too long a segment from the recording in case of any signal inconsistencies, such as random low frequency fluctuations of signal.

Next, the seismic signal was 'cleaned' by de-trending and de-meaning to remove any non-stationary trend and take away the sample mean, leaving an ideal seismic noise

signal with zero mean. To reproduce stationary noise, each segment was normalised to its maximum amplitude.

Subsequently, these noise segments were then converted to the Fourier domain through a Fast Fourier Transform (FFT) algorithm to observe their amplitudes at different frequencies. Next, the average of the segments was taken to obtain a noise segment that was not affected by any fluctuations in the data in an individual sample. To further smooth the data, a moving average of the averaged noise frequency with a window size of 20 samples (or 0.2 seconds) was taken, as illustrated in Figure 3.2. The noise is very broad band, with a steep power law decay at low frequencies (Brown noise), a characteristic peak at a few Hz, and a flat trend or gentle decay at high frequencies ('pink noise').

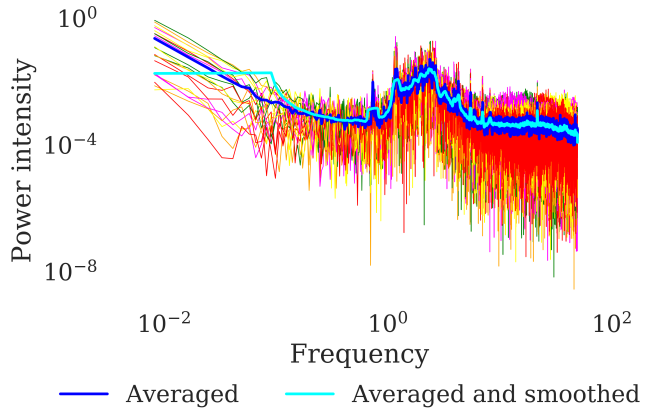

Figure 3.2: Illustration of 20 de-trended, de-meaned and normalised seismic noise segments from a seismic station near the Tungurahua volcano, with the averaged (blue) and the smoothed averaged (cyan) in the Fourier domain.

Next, the product of the smoothed spectrum and normalised white noise in the Fourier domain was taken to obtain a realistic stationary sample of synthetic noise. Multiplying by white noise ensured the noise was random and uncorrelated. The FFT of the synthetic noise, alongside the white and real noise, are shown in Figure 3.3 for comparison.

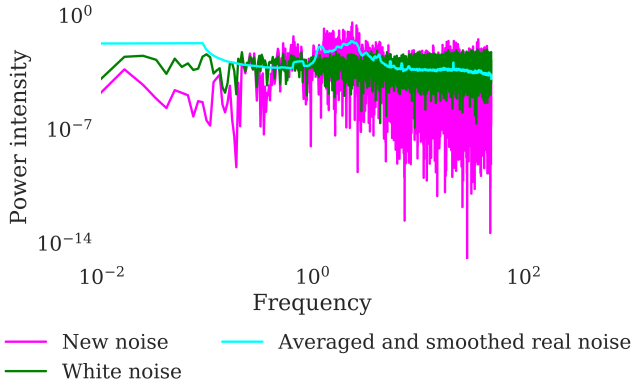

Figure 3.3: Illustration of the de-trended, de-meaned and normalised white (green), real (cyan) and new synthetic (pink) noise in the Fourier domain.

Finally, the inverse Fast Fourier Transform (IFFT) was taken to convert the synthetic noise back into the time domain. The spectrograms for the real and synthetic noise (Figure 3.4) confirm that the method reproduced the character of the observed noise very well. The synthetic noise showed some slightly stronger signals around the 1Hz band, due to the 1Hz corner frequency in the signal from the real noise being amplified by the multiplication involved in the convolution with random-phase white noise.

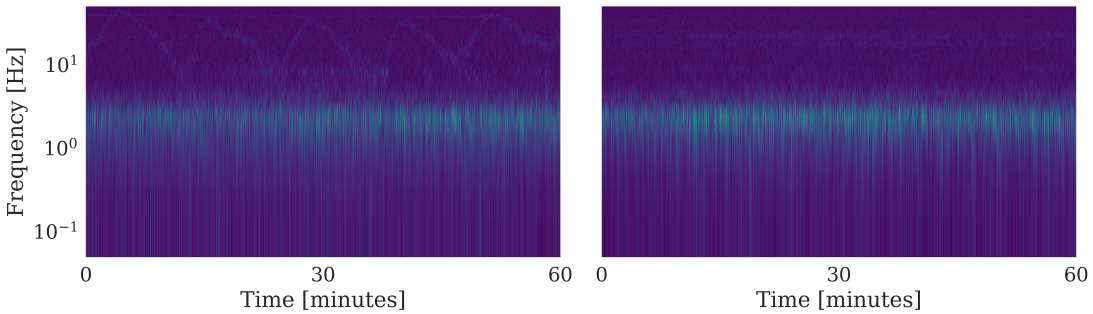

Figure 3.4: Hour long spectrograms of real (left) and synthetic (right) noise.

This process is then repeated for however long a noise segment is required (i.e. a 10 minute seismogram will require the process to be repeated five times). The synthetic noise can be scaled to any Signal-to-Noise Ratio (SNR), which is used as a measure of the amount of the desired signal to the amount of background noise. The SNR

is calculated based on the ratio of the power (P) of the signal (i.e. the normalised repeating event which is going to be used) to the power of the noise,

$$SNR = \frac{P_{signal}}{P_{noise}}, \tag{3.1}$$

where P is defined as the root mean square of the amplitude data (x),

$$P_x = \sqrt{\frac{\sum^{N} x^2}{N}}, \tag{3.2}$$

with $x = signal\ amplitude$ to calculate P_{signal} and $x = noise\ amplitude$ to calculate P_{noise}, for the data of length N. Amplitude in this case are the arbitrary units from the datasets.

3.1.2 Creating a synthetic signal

The template event chosen in this case was taken from the HSR seismic station on the Pacific Northwest Seismic Network (PNSN) operated by the University of Washington (UW), located on the south ridge of the Mount St. Helens volcano, USA. The noise between events in this dataset had similar frequency components to the noise at Tungurahua used earlier to simulate the synthetic background noise. However there was not enough of a continuous period of uninterrupted noise in the Mount St. Helens dataset to use as the basis for synthesising the noise. This particular dataset was chosen as it exhibited clearly defined highly repetitive seismicity in a high signal-to-noise ratio setting during December 2004 and was openly-accessible. The template event used in this example is illustrated in Figure 3.5.

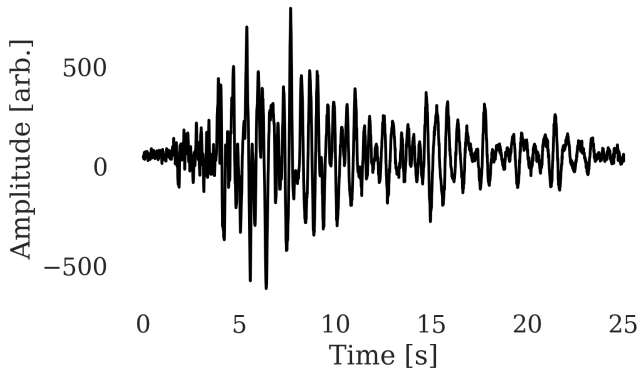

Figure 3.5: Illustration of the template event used in creating the synthetic seismograms. This data was taken from the HSR seismic station on the Pacific Northwest Seismic Network at the Mount St. Helens volcano, USA during a period of highly repetitive seismicity in December 2004.

This event was added on top of the noise at random times sampled from the inter-event time and amplitude distribution chosen. An example of this is illustrated in Figure 3.6, where three events of equal amplitude in this case in the top diagram, were added to the background noise lasting ten minutes in the middle diagram to create the synthetic seismogram shown in the lower diagram.

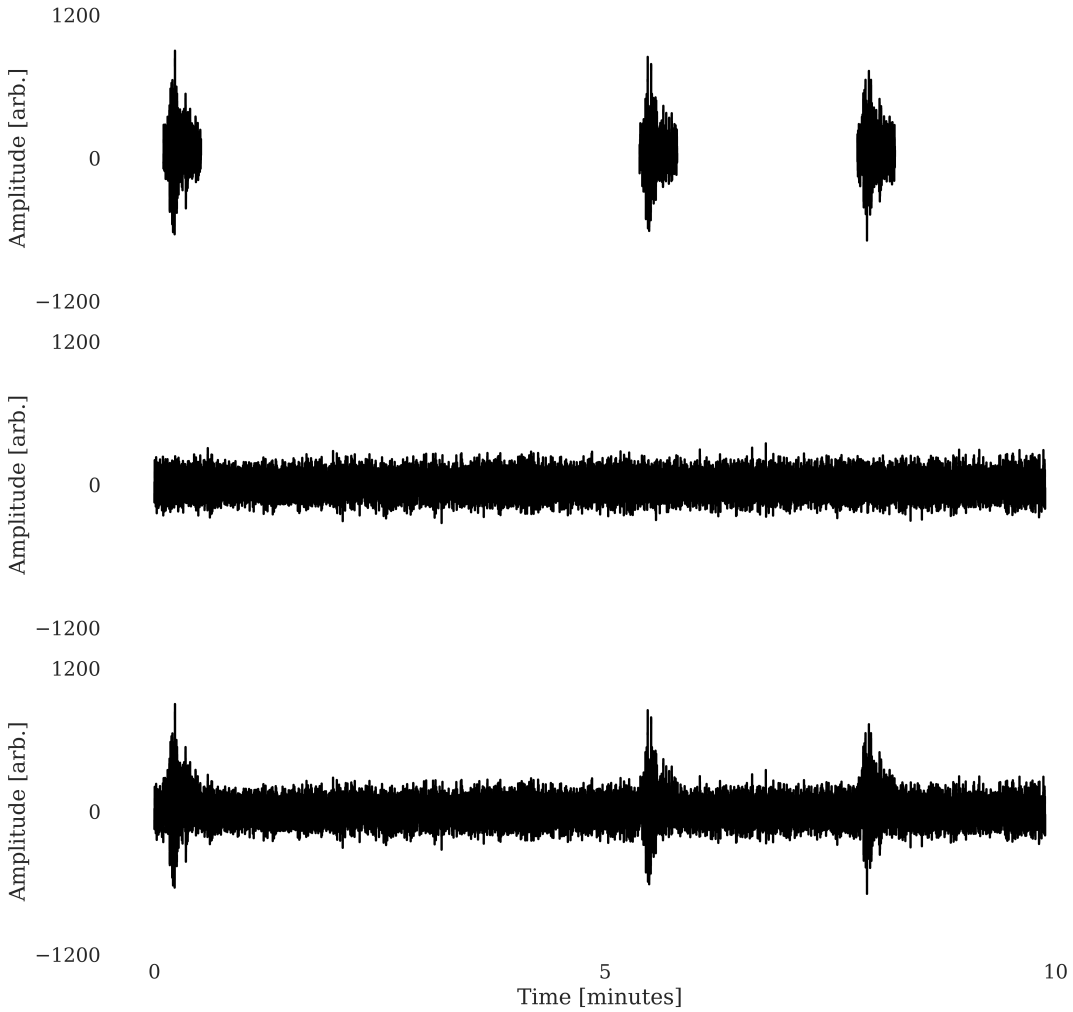

Figure 3.6: Illustration of the three events (top) and the noise (middle) making up a synthetic seismogram (bottom).

There are slight differences between the resultant events amplitudes as the noise addition will alter the waveform by interference, by an amount depending on the SNR chosen (here SNR = 1.2, as calculated from Equations 3.1 - 3.2) and the random phase of the noise.

The full seismogram for 100 events from the synthetic inter-event time distribution of Figure 3.7 is shown in Figure 3.8. This example was for an ideal Poisson process of randomly occurring independent events of equal amplitude.

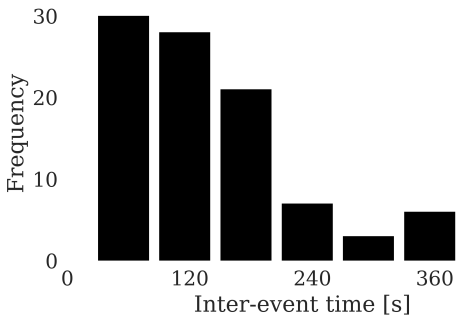

Figure 3.7: Input inter-event time distribution for events in the synthetic seismogram shown in Figure 3.8, where events were spaced as a Poisson distribution ($\lambda = 0.01$).

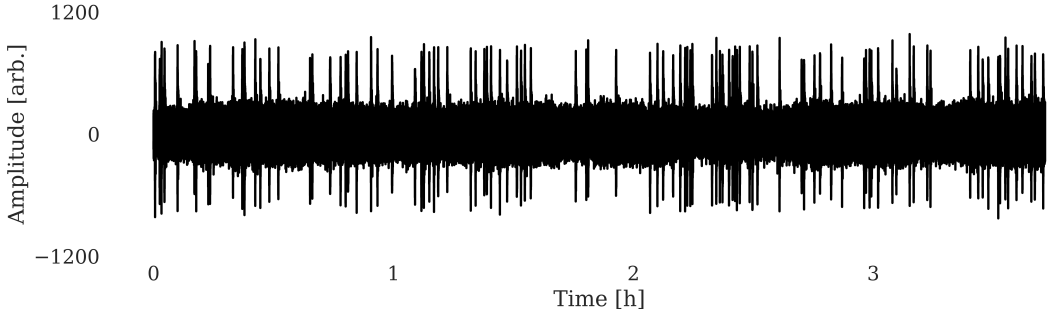

Figure 3.8: Synthetic seismogram with 100 events from inter-event time distribution in Figure 3.7.

Periodic inter-event times have sometimes been observed in volcanic seismicity, therefore examples of synthetic seismograms with periodic inter-event times were also generated here. Specifically I chose 100 events of equal amplitude repeating 300 seconds apart, as expected from a periodic distribution (Figure 3.9). This distribution is then used to generate the synthetic seismogram in Figure 3.10.

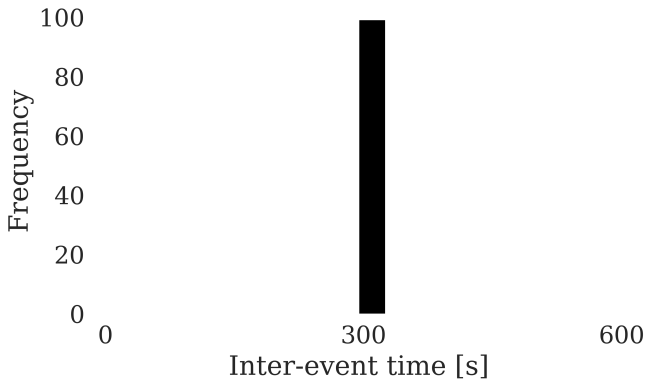

Figure 3.9: Inter-event time distribution for synthetic seismogram shown in Figure 3.10. All events are occurring 300 seconds apart.

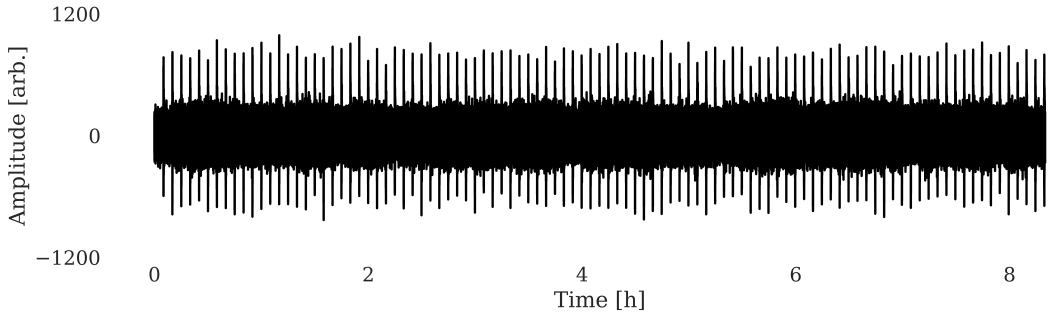

Figure 3.10: Synthetic seismogram, with 100 events spaced periodically (every 5 minutes) from the inter-event distribution from Figure 3.9.

Bouchon et al. (2011) showed inter-event times getting smaller as catastrophic failure approached, prior to the 1999 M7.6 İzmit, Turkey earthquake, associated with an acceleration in event rate. Poli (2017) and Bell et al. (2018) found a similar inter-event time distribution prior to the 2017 Nuugaatsiaq, Greenland landslide. Hence I included an inter-event time distribution reflecting an accelerating event rate of power-law form, where the time of the event t is related to the number of the event n by,

$$t_n = n^2 \quad n = 100, 99, .., 1. \tag{3.3}$$

as illustrated in Figure 3.11. The time between events was ordered so that the events were closer together at the end of the synthetic seismogram than those at the start (i.e. the first inter-event time is 100^2, the second inter-event time as 99^2, etc.).

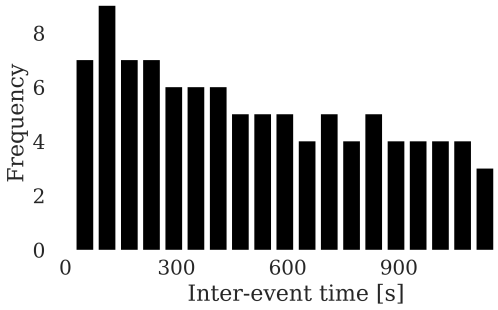

Figure 3.11: Inter-event time distribution for an accelerating event rate following the power-law of Equation 3.3, for events in synthetic seismogram in Figure 3.12.

Figure 3.11 shows that the inter-event time frequency decays only gently with respect to inter-event time in this case, with somewhat more smaller inter-event times than large. This is a consequence of the input of an accelerating event rate where the events get closer together as time goes on. This systematic change in the inter-event time for 100 events is shown in the synthetic seismogram in Figure 3.12.

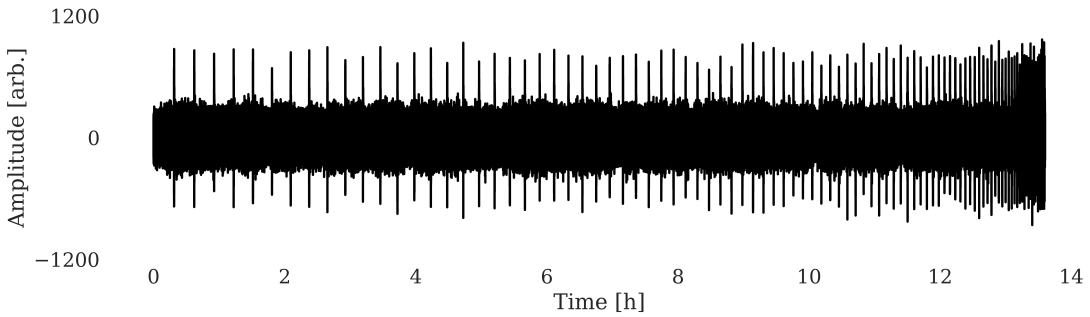

Figure 3.12: Illustration of a synthetic seismogram with the inter-event times drawn from the accelerating distribution following a power law, shown in Figure 3.11.

Next, a distribution representing a swarm-like event pattern was introduced by

increasing the rate of earthquakes at different points. The aim of this exercise was to test how the method would pick up events which did not follow a simple trend, and to examine how the method would deal with events which were very close, or even overlapping. Conceptually, this could also be thought of as switching between two Poisson distributions, as there are two event rates being used in the inter-event time distribution shown in Figure 3.13. One Poisson rate for background events ($\lambda = 0.0005$), and another Poisson rate for those events within the swarm ($\lambda = 0.005$).

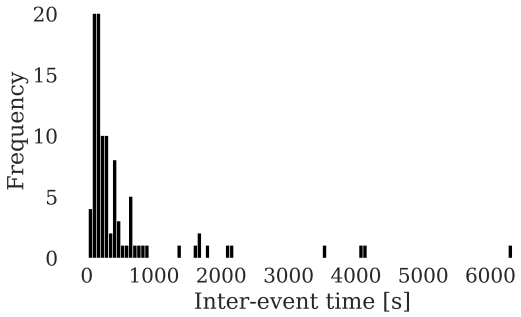

Figure 3.13: Inter-event time distribution for two Poisson distributions of different rates. There are 20 events at a Poisson rate of $\lambda = 0.0005$ to signify events at the start of a swarm, and then four further events in each swarm with a Poisson rate of $\lambda = 0.005$. This distribution of inter-event times is then the input to obtain the synthetic seismogram in Figure 3.14.

The inter-event time distribution in Figure 3.13 highlights the difference in the two rates used. The larger inter-event times indicate the start of a new swarm, and the smaller inter-event times for those events within the swarm. The very small inter-event times (those within the first bin of 60 seconds) indicate that some of these events within the swarm were overlapping, as an exponential distribution would otherwise be expected from using a single Poisson rate.

The distribution of inter-event times in Figure 3.13 was used as an input for the synthetic seismogram, as illustrated in Figure 3.14.

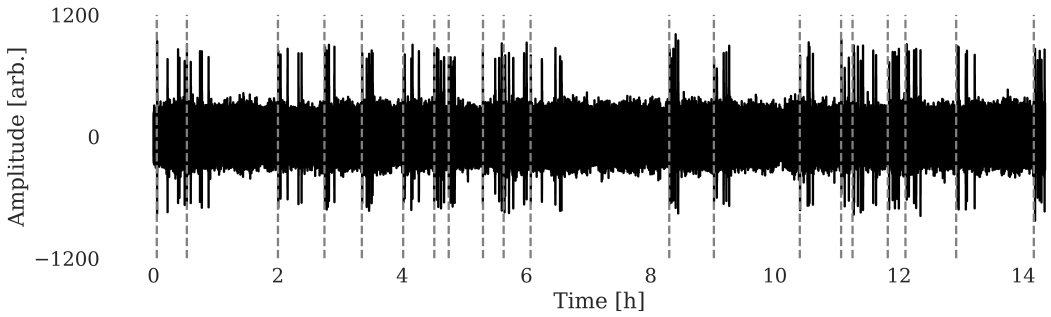

Figure 3.14: Synthetic seismogram, with 100 events spaced with swarm-like inter-event times (20 swarms), shown in Figure 3.13. The start of the swarms are indicated by the grey dashed vertical line.

3.1.3 Magnitude distribution

Next, I incorporated different magnitude distributions in the synthetic seismograms to better represent realistic seismic behaviour. Here, I created a distribution of scaling factors to have relative amplitudes rather than magnitudes, as the seismograms had arbitrary amplitude units. The scaling between the relative amplitudes and the magnitudes is given explicitly in section 3.4.

Frequency-magnitude distributions are used to estimate seismic hazard (Baker, 2013), most commonly with the Gutenberg-Richter law (Equation 2.4). Thus I modelled magnitudes with an underlying Gutenberg-Richter distribution where $b = 1$ and the minimum magnitude (or scaling factor) is 1, as illustrated in the normalised frequency-magnitude distribution of events in Figure 3.15.

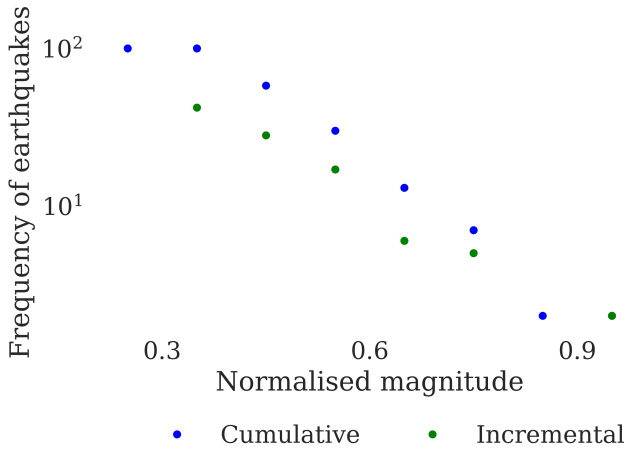

Figure 3.15: Magnitude distribution of input events in synthetic seismogram shown in Figure 3.16, which had an underlying Gutenberg-Richter magnitude distribution ($b = 1.0$).

These events were the input to obtain the synthetic seismogram shown in Figure 3.16.

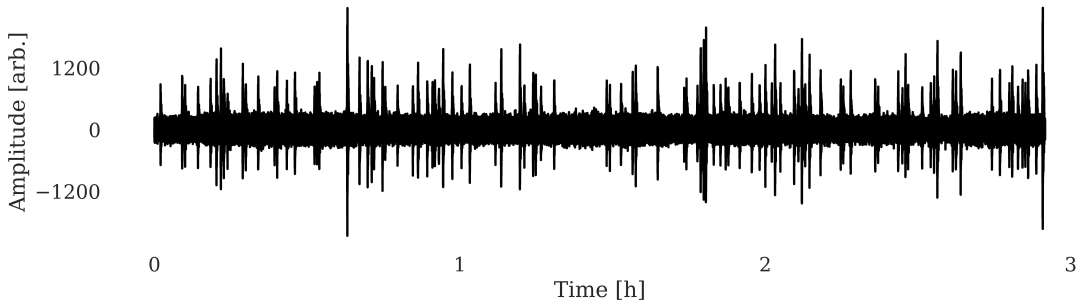

Figure 3.16: Synthetic seismogram with Gutenberg-Richter distributed magnitudes input from distribution shown in Figure 3.15 ($\hat{b} = 1.0 \pm 0.10$. Poisson spaced events: $\lambda = 0.01$).

I used the maximum likelihood estimation (MLE) method (Aki, 1965), (discussed in section 2.3.1 and shown in Equation 2.5) to find the estimated b-value ($\hat{b}$) from the synthetic data. The MLE method calculates the synthetic catalogue shown in Figure 3.16 to have $\hat{b}$-value=1.0 $\pm$ 0.10, consistent with the input of b-value=1.0, i.e. in this case there was no bias due to the addition of seismic noise.

Accelerating magnitudes have been seen in some precursors prior to catastrophic failure (Bouchon et al., 2011; Poli, 2017). Therefore I also developed a synthetic time series for magnitudes which increased in time by sorting the randomly-sampled catalogue from the lowest to the highest amplitudes. The frequency-magnitude distribution for this case is illustrated in Figure 3.17, showing that the events still follow a Gutenberg-Richter frequency-magnitude distribution, where $\hat{b}$=0.98 $\pm$ 0.080 is still equal to the underlying b-value=1.0 within the stated error.

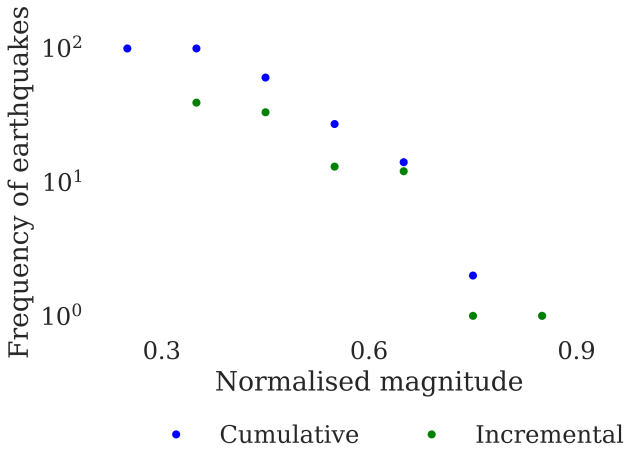

Figure 3.17: Frequency-magnitude distribution of events used in synthetic seismogram in Figure 3.18, which had an underlying Gutenberg-Richter magnitude distribution ($\hat{b}$ = 0.98 $\pm$ 0.080), ordered in time from lowest to highest.

The synthetic seismogram of Figure 3.18 was created by randomly sampling the frequency-magnitude distribution of Figure 3.17 and then reordering the magnitudes in time from lowest to highest.

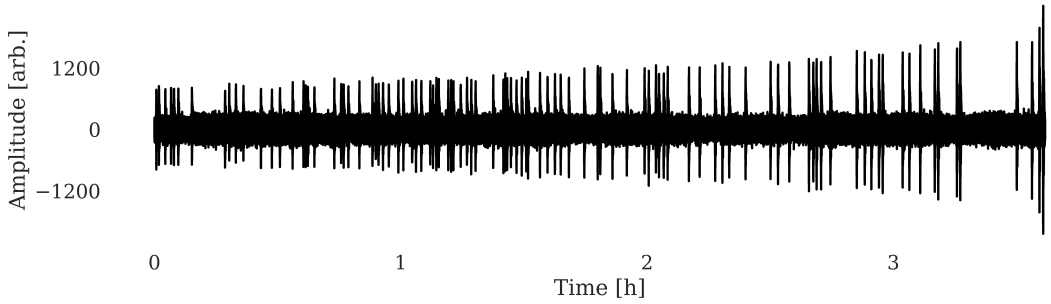

Figure 3.18: Synthetic seismogram, with random inter-event times accelerating Gutenberg-Richter magnitudes ($\hat{b} = 0.98 \pm 0.080$, Poisson spaced events: $\lambda = 0.01$), ordered in time from lowest to highest.

In summary, I demonstrated in this section how I built synthetic seismograms by creating synthetic noise and adding in identical events with various inter-event time and magnitude distributions as an input. This was necessary as in section 4.1, I will be testing the method for finding repeating events in synthetic seismograms with realistic statistical properties to provide ground-truth for finding repeating events where the solution is known. The next section begins to describe the modifications I made to the established methods in the previous chapter for building the method, based on the experience gained in creating the synthetic seismograms described above.

3.2 Event picking methods

In order to achieve the project aims, it was necessary first to design an algorithm which finds repeating events in earthquake data. Having found the events, it was then necessary to analyse their temporal evolution to better understand the underlying processes taking place, and to relate these to the possible existence of nucleation-related earthquake precursors.

Here, I discuss the common methods used for picking events through triggering

algorithms, the standard and adapted approaches for finding repeating events using their similarity identified by the cross-correlation method, as well as how I define a threshold for an event.

3.2.1 Standard triggering method

The most common way of finding events in continuous earthquake recordings is through the Short-Time-Average/Long-Time-Average (STA/LTA) ratio method (Withers et al., 1998; Trnkoczy, 2012). This approach picks out events based on the ratio of short- to long-time average amplitudes of the signal. It continuously calculates the cumulative sum of the absolute amplitude of the seismic signal in two moving time windows of different length. The data in one of these windows is used to calculate the STA, which measures the average short-time amplitude, and the other to calculate the LTA, which measures the average long-time amplitude, and is normally dominated by the seismic noise. The STA/LTA ratio is then the ratio of the average amplitude in the smaller window to that in the larger one. Once this exceeds a user-defined threshold, it triggers the detection of an event above the noise. Once the STA/LTA ratio falls below another user-defined threshold value, it is then 'detriggered', meaning the event is deemed to be over. This then allows the user to identify multiple events above the triggering threshold.

There are many triggering functions available within the Obspy library (Beyreuther et al., 2010; Megies et al., 2011; Krischer et al., 2015). Here, I compare two triggering functions from within this library; the classic STA/LTA method and the z-detect method. Both are in common use in earthquake seismology (Berger and Sax, 1980; Earle and Shearer, 1994; Wong et al., 2009; Schaff, 2010).

The STA and LTA are calculated from seismograms expressed as a time series of amplitude x_j, where j is the index of the window for the time index i, using Equations

3.4 and 3.5 below (Withers et al., 1998; Wong et al., 2009),

$$STA = \frac{1}{N_S} \sum_{j=i-N_S}^{i} x_j^2, \tag{3.4}$$

$$LTA = \frac{1}{N_L} \sum_{j=i-N_L}^{i} x_j^2, \tag{3.5}$$

where N_S and N_L are the sizes of the window for the short-time and long-time averages, respectively. These two equations imply it is strictly an energy (amplitude squared) that is being used as a detection metric rather than amplitude itself. Nevertheless, I retain the convention to refer to the metrics as STA or LTA respectively.

The classic STA/LTA function takes the ratio of these two quantities, i.e. STA_j/LTA_j. This created a characteristic function based on this trigger, where a threshold is set to indicate an event. This process is illustrated in Figure 3.19. I tested the triggering algorithm on a 2.5 minute signal taken from a seismometer near the Mount St. Helens volcano, USA, which contained 2 events, as shown in plot a. Following Equations 3.4 and 3.5, the cumulative sum of the squared seismic data for a short-time and long-time window is shown in plot b as a green and orange line, respectively, alongside the cumulative sum of the data with no window applied in purple. The short-time and long-time average incremental amplitudes defined by the window are then normalised by their window size, as illustrated in plot c. The ratio of the STA/LTA is shown in plot d, alongside the trigger on threshold, here set as 1.8, meaning the ratio of STA/LTA needs to be 1.8 to signify an event has started, shown by the horizontal red dashed line on plot d. The trigger off threshold (to represent the event is over) is set as 0.5 for this example, shown as the horizontal blue dashed line in plot d. The times of these thresholds in the signal is illustrated by the corresponding red and blue vertical lines in plot e.

It is clear that the definition of an event is very sensitive to the choice of trigger threshold. If it were lowered too much, it would begin to contain false events from

random correlations in the noise, and if it were too high it would begin to miss events visible to the eye. As the event often begins prior to the trigger on threshold, the window defining an event is then expanded to include areas before and after the triggering threshold, so that the onset of the event is clear and the reader can visualise the preceding noise (Figure 3.19e).

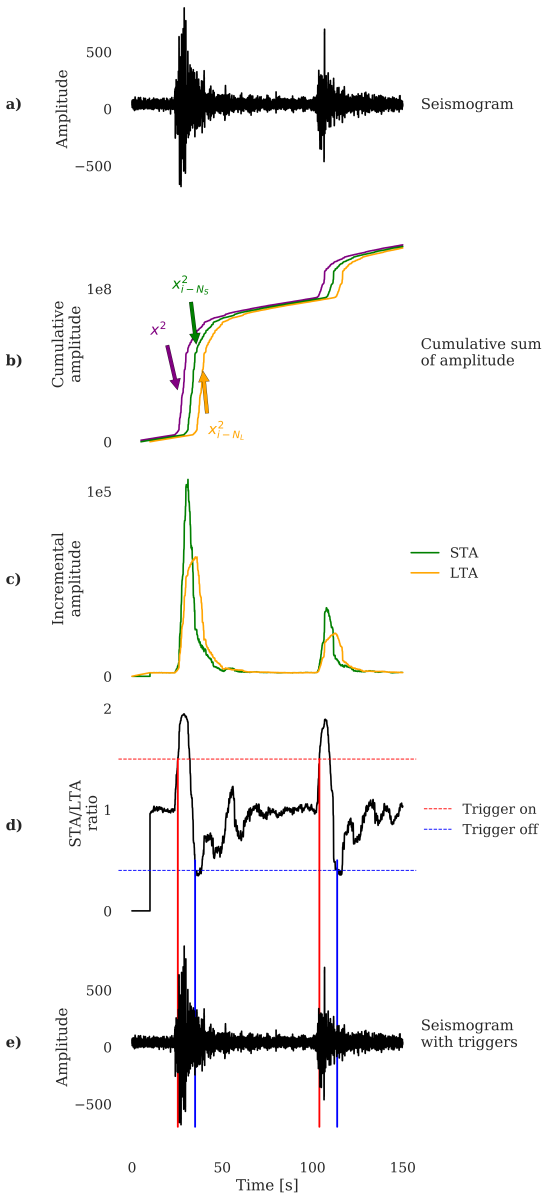

Figure 3.19: Illustration of the classic short-time-average/long-time-average (STA/LTA) ratio trigger method for a 2.5 minute seismogram taken from a seismometer near the Mount St. Helens volcano, USA in December 2004. Plots show a) the original seismogram, b) the cumulative sum of the squared signal (purple), STA_j (green) and LTA_j (orange) window amplitudes, c) the STA_j and LTA_j incremental amplitudes normalised by their window size, as defined by Equations 3.4 and 3.5. Plot d) illustrates the STA_j/LTA_j ratio, where the horizontal dashed lines illustrate where an event is triggered on (red) and deemed over (blue). Plot e) shows the original seismogram with the times of these thresholds as vertical lines for the start of the event (red) and when it was over (blue).

I also tested the z-detect trigger method, which continuously calculates a standardised variable (Z) which quantifies how much the seismograms, expressed as a time series of amplitude x_j, where j is the index of the window for the time index i, differs from the mean (μ), and normalised by the standard deviation (σ), following Equation 3.6 (Withers et al., 1998),

$$Z = \frac{1}{\sigma} \sum_{j=i-N_S}^{i} x_j^2 - \mu. \tag{3.6}$$

This is done for each window (of size N_S) of the data to create the Z-statistic function. A trigger threshold is set for when the value of Z-statistic corresponds to the detection of a triggered event.

An example of how the z-detect triggering method picks events is shown in Figure 3.20, which follows the same protocol as Figure 3.19. Figure 3.20a shows the same signal as Figure 3.19a. Figure 3.20b illustrates the cumulative sum of the window as a green line, alongside the cumulative sum of the data with no window in purple. As in Equation 3.6, the Z variable is calculated by de-meaning the incremental amplitude defined by the window (green line in Figure 3.20b) and normalised by the standard deviation, as illustrated in Figure 3.20c. An event is picked when the Z variable (Figure 3.20c) is above the horizontal dashed red threshold line, set here as 0.6, and stops when below the horizontal dashed blue threshold line, set in this example as 0.05. These thresholds were chosen as it was where the STA/LTA ratio noticeably differed at the times of events. The times of these thresholds are illustrated in the signal by the corresponding red and blue vertical lines in Figure 3.20d.

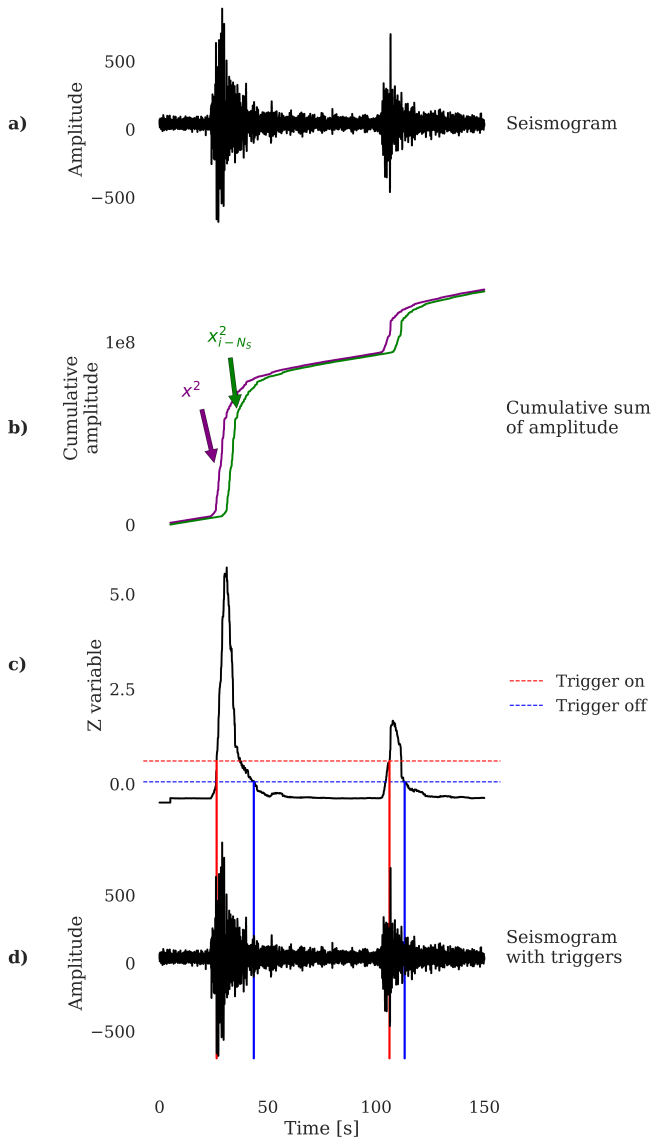

Figure 3.20: Illustration of the Z-detect triggering method for a 2.5 minute seismogram taken from a seismometer near the Mount St. Helens volcano, USA in December 2004. Plots show a) original seismogram, b) the cumulative sum of the seismogram and short windowed seismogram amplitudes, c) Z-variable with red and blue horizontal dashed lines for the trigger on and off points, d) original seismogram with vertical red and blue lines showing trigger points.

Comparing Figure 3.19 and Figure 3.20, the z-detect triggering function has several

advantages over the typical STA/LTA method. First, due to the Z variable being normalised by standard deviation, it allows for automatic adjustments for variance fluctuations in the dataset. Second, the characteristic function looks a lot smoother during the time when no events were occurring in the dataset. This minimises the rate of false alarms compared to the classic STA/LTA method that could be generated from too low a threshold line. Finally, the thresholds for event detection and cessation can be much smaller as a proportion of the maximum amplitudes for Z than STA/LTA as a metric. Hence for these reasons, the z-detect method is used in the rest of this thesis.

3.2.2 Standard cross-correlation method

As discussed in section 2.6.1 and 2.6.2, waveform cross-correlation (also known as template matching) is a technique used where a template (or candidate earthquake event) is cross-correlated with the rest of the seismic signal (e.g. the daily seismogram), to uncover any similar events within the seismic signal. I adopted this approach in the method used later in this thesis to detect multiplet events, so it is important to evaluate the technique here.

Cross-correlation can be computationally expensive when being used for template matching, e.g. if there were 200 templates used for template matching, the cross-correlation process would need to be repeated 200 times, because cross-correlation scales with the amount of templates used. As cross-correlation is used several times in the method, it was paramount for its implementation to be optimised.

In this thesis, I used cross-correlation first to compare events that have already been detected by the triggering algorithms described above. They are cross-correlated with one another to quantify the similarity between conventionally-detected events. Cross-correlation is then used to find new events below the noise threshold set by the automatic detection algorithms, from a 'template' provided by the seismogram of a known detected

event. If the two separate events are found to have a high cross-correlation coefficient, this indicates a candidate set of repeating events, because it means the two events have a near-identical waveform. An example of two events analysed in this way can be seen in Figure 3.21.

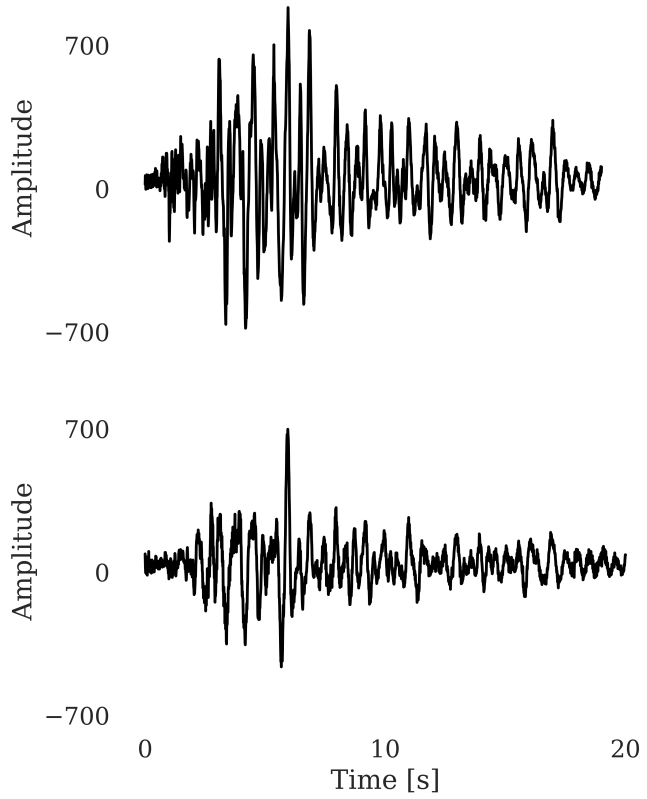

Figure 3.21: Seismograms for two events taken from a seismometer near the Mount St. Helens volcano, USA, in December 2004, used to determine the cross-correlation function. These two events resulted in a cross-correlation value of 0.74 at a lag of zero.

The two events shown in Figure 3.21 are the same as those shown in Figures 3.19 and 3.20. In this case the start of the windows shown have been both reset from Figure 3.19 and 3.20 to zero, indicating the start of the event window set by the automatic detection algorithm. When these two events are compared by cross-correlation with no lag, they obtain a cross-correlation value of 0.74, indicating a similar waveform at zero lag, as expected in this case. This is consistent with the underlying similarity of the

events known to occur in this dataset, despite the presence of significant background noise.

To illustrate the detection of an optimal lag, and hence the time of occurrence of similar events, I also used cross-correlation to compare the seismogram $f(t)$ of a picked event with the entire seismic signal $g(t)$ at all possible lags τ, as illustrated in Figure 3.22. In this illustrative case, both f and g contain the same event. This created the cross-correlation function $(f \star g)(\tau)$, as shown in lower diagram of Figure 3.22. The window which creates the largest cross-correlation value then indicates the optimum lag where the picked event has highest similarity to the seismic signal. In this case, we would expect a maximum in $(f \star g)(\tau)$ of 1 at optimum lag τ being the start of the window.

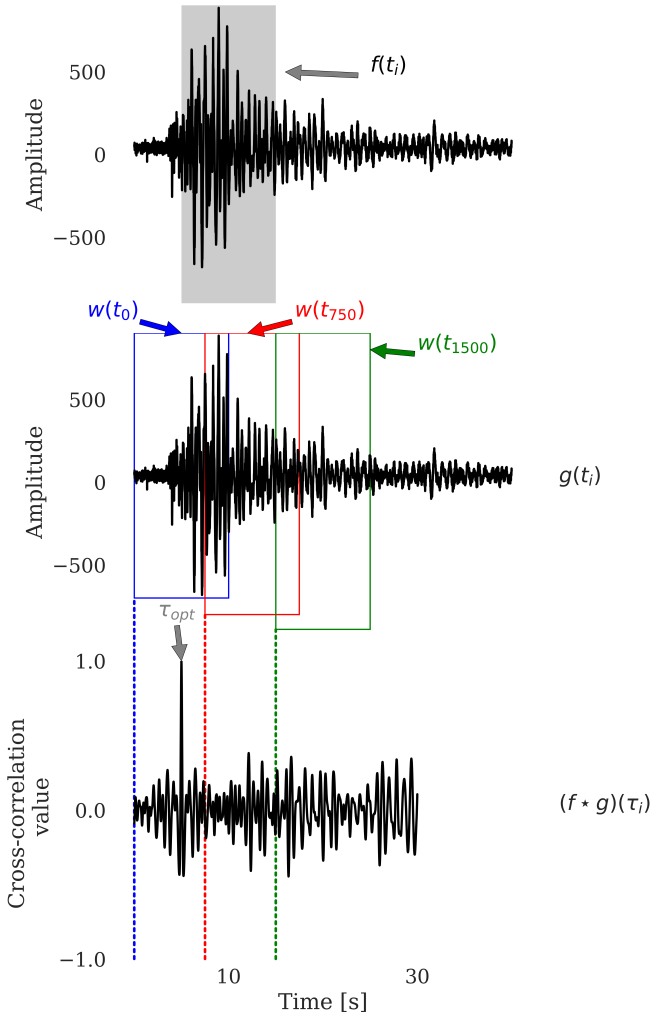

Figure 3.22: Moving window cross-correlation example. The top plot shows picked event (grey box) from entire signal. The middle plot shows the 0th, 750th and 1500th windows used in cross-correlation. The cross-correlation function is shown in the bottom plot.

In Figure 3.22, the picked event $f(t_i)$, defined by the grey box in the top plot is cross-correlated with the seismic signal with a window of the same size in the middle plot, denoted $g(t_i)$. This will output a cross-correlation value $(f \star g)(\tau)$, shown in the lower plot. This is the same method as in Figure 3.21 where the cross-correlation outputs one value at lag τ, and is a measure of the similarity of the two signals at lag τ. The window is then moved along by one sample, $\tau \rightarrow \tau + 1$, and the process is repeated through

the entire signal to create a cross-correlation function, $(f \star g)(\tau)$. As the signal $g(t)$ in this case is 40 seconds long, and is sampled at 100Hz, this means that the time series $g(t)$ has 4000 samples. The 'template' event $f(t)$ that I have used for cross-correlation is 1000 samples long (10 seconds), so the cross-correlation function $(f \star g)(\tau)$ is 3000 samples long. As the cross-correlation value is shown at the start of the window, the cross-correlation signal is always a little shorter than the sample (depending on window size). Hence the cross-correlation function is shorter than the initial seismogram in the upper plot of Figure 3.22. For clarity, I have only shown 3 windows in this example (shown by the different colours) in the middle plot. These represent the 0th, 750th and 1500th windows as examples corresponding to the lag times τ indicated by the dashed coloured lines on the lower plot, when really there will be 3000 windows in this example. Figure 3.22 shows a clear optimum lag of ≈ 7 seconds, with an ideal cross-correlation value of 1.0 in this case.

3.2.3 Cross-correlation method used

I investigated two different cross-correlation techniques: Obspy's cross-correlation in the time domain (OTD) through a moving window and Scipy's cross-correlation in the frequency domain (SFD).

The OTD technique has been described above in section 3.2.2. It is used to quantify the similarity between detected events, and can be used with a moving window to find new events below the noise level. If the two separate events are found to have a high cross-correlation coefficient, this indicates a candidate set of repeating events because it means the two events have a near-identical waveform.

The accuracy of the OTD technique was tested on a 7.5 hour synthetic seismogram of 200 events (Poisson distributed inter-event times) with SNR=1.5. This technique gave an accurate measure of similarity when comparing two events to one another,

but when used with the template matching approach (i.e. using a sliding window to compare an event with the full seismic signal), it took around 80 seconds of CPU time to find all 200 events. However, it had the advantage that it normalises the output accordingly, and so it is preferred for comparing several cross-correlation functions to one another. As expected, doing this type of calculation is slow in the time domain, hence the same technique was investigated in the frequency domain.

The convolution theorem states that cross-correlation function $f \star g$ is the same as convolving ($*$) one signal $f(t)$ with another complex conjugated time-reversed signal $g(-t)$ in the frequency-domain $\mathcal{F}$,

$$f \star g = \mathcal{F}\{f(t) * g^*(-t)\}. \tag{3.7}$$

Hence, I tested convolution with the SFD technique from the Scipy library on the same synthetic seismogram as before. While this technique was extremely fast, taking <1 second to find all 200 events, there is not a simple expression for normalising the cross-correlation amplitude in the frequency domain (Lewis, 1995). The cross-correlation should not just be divided by the highest value in the cross-correlation function between candidate repeater events, as the amplitude of this ratio should only be equal to 1 for auto-correlation (cross-correlation of f with itself, not a slightly different waveform).

Within Obspy's library of cross-correlation functions, there is also one cross-correlation technique which takes place in the frequency domain. However this has the same issue as the SFD technique of Scipy, i.e. it did not normalise the amplitude of the cross-correlation function correctly. Thus, a new approach was adopted for this thesis, using a moving window technique, carried out in the frequency domain (FDW).

The FDW approach implemented starts by time reversing the template trace. Next, this signal is convolved in the frequency domain with a window from the full seismic

signal, and then converted the result back to the time domain through IFFT to obtain the cross-correlation coefficient for that window.

The cross-correlation functions of the FDW method (green) is compared to the OTD (blue) method for finding the same event in a synthetic seismogram, to evaluate the accuracy of FDW, as illustrated in Figure 3.23.

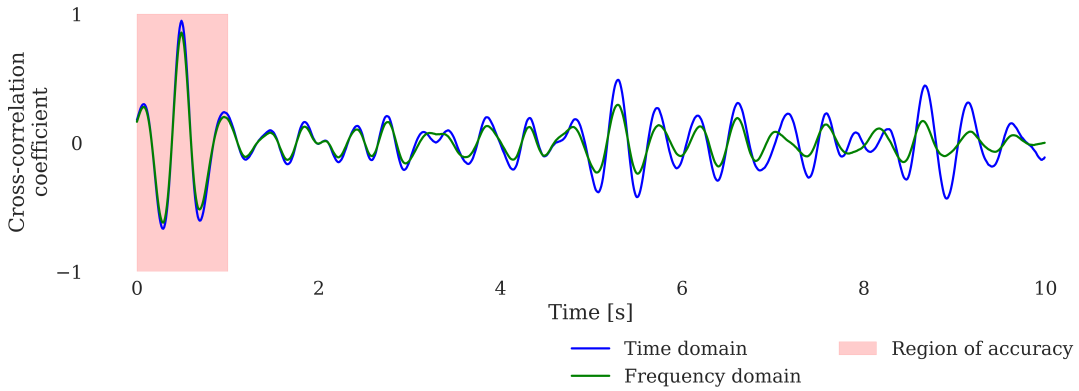

Figure 3.23: Comparison of two cross-correlation methods by their cross-correlation functions of a template trace with a synthetic seismogram; Obspy's time domain method (OTD in blue) and a frequency domain method (FDW in green). The region deemed accurate between the two methods is shown by a red box.

Figure 3.23 illustrates that the cross-correlation functions of the OTD (blue line) and FDW (green) methods begin to diverge after several seconds. The divergence occurs due to the FDW approach taking place in the frequency domain, therefore it is being based on an infinite length of discrete time signals. This creates a circular cross-correlation (rather than linear cross-correlation), meaning the signal wraps around at the ends. In Figure 3.23, the FDW method works well in the one second window, but degrades in amplitude while retaining phase. Hence, the cross-correlation function becomes less accurate as time goes on due to the mixed convolution between $f(t)$ and $g(-t)$ from time-aliasing. Thus I adopted the 'overlap save and discard' technique from digital signal processing (Proakis and Manolakis, 1996) and saved a region of accuracy

of a one second window for the FDW method where the FDW and OTD are the same, shown by the red box in Figure 3.23, and discarded the rest.

Next, the FDW method is performed again in a similar technique to the OTD method where a moving window is used. The window is moved along by one second (100 samples in 100Hz data) as this is the size of the region of accuracy in Figure 3.23, and repeated for the remainder of the seismic signal. A cross-correlation function is then built up by combining together all the saved regions of accuracy for the full seismogram.

An illustration of how the FDW technique performs once the windowing method has been implemented, in comparison to the OTD technique is shown in Figure 3.24.

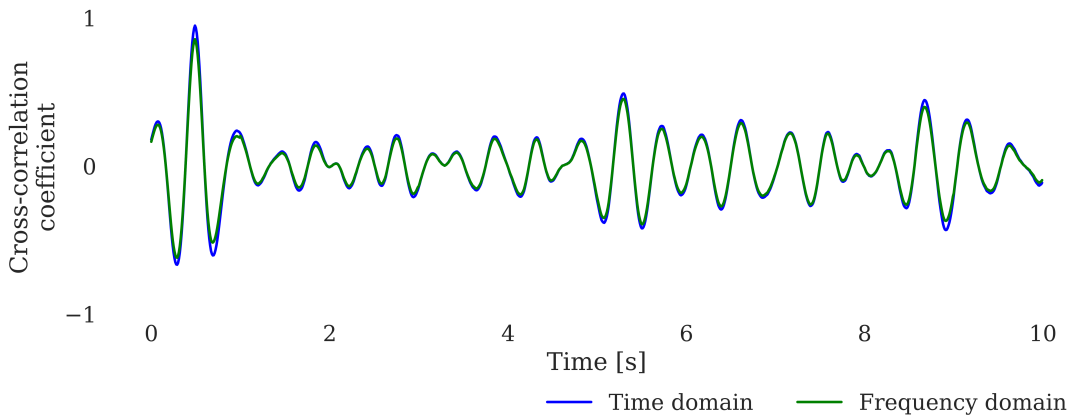

Figure 3.24: Comparison of two cross-correlation methods by their final cross-correlation functions; Obspy's time domain method (OTD in blue) and a frequency domain method using a moving window (FDW in green), for the event found through cross-correlation in a synthetic seismogram.

The FDW method was very fast, only taking 6 seconds to complete. Figure 3.24 highlights that the results of the FDW method are very similar to the ground-truth OTD method for finding an event in a synthetic seismogram.

A flowchart of the method used for the FDW approach can be seen in Figure 3.25, where the domain changes points are annotated.

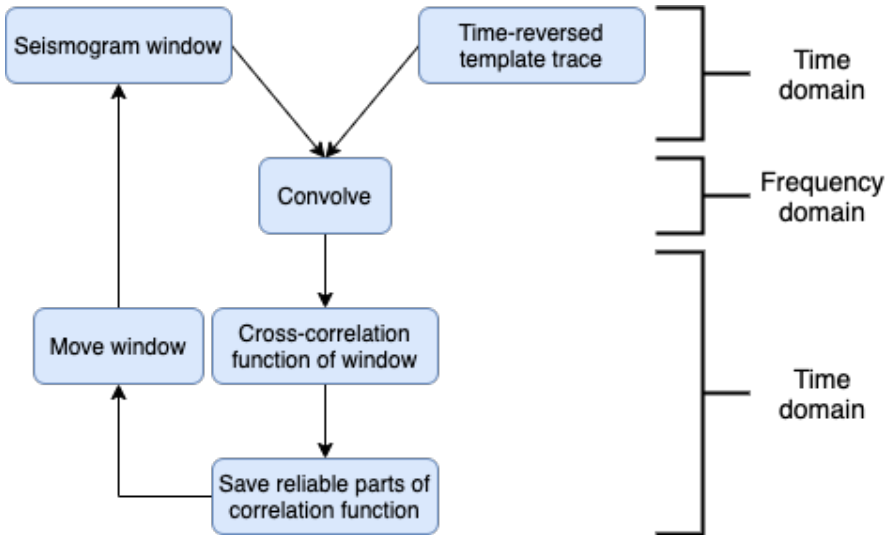

Figure 3.25: Summary of windowed cross-correlation approach in the time and frequency domain. The points at which the domain changes are annotated for further clarity.

The three techniques discussed above to speed up the cross-correlation are summarised, along with an evaluation of their performance in terms of accuracy and speed in Table 3.1. The OTD technique was taken as ground-truth, so I measured the accuracy of the FDW and FD techniques by quantifying the similarity of their resultant cross-correlation functions to the OTD cross-correlation function.

	OTD	**FDW**	**FD**
Accuracy [%]	100	99.9	86.0
Speed [s]	80	6	<1

Table 3.1: Summary of cross-correlation methods for the Obspy's Time Domain (OTD), Frequency Domain Window (FDW) and Frequency Domain (FD) techniques and their performance with a synthetic seismogram sampled at 100Hz and 7.5 hours long. Accuracy is measured through the similarity between cross-correlation functions when compared with the OTD approach, and speed for however long the method takes on a standard local computer.

With reference to Table 3.1, the OTD method was the most accurate, as it produced a cross-correlation function that was normalised correctly, therefore gave a reliable measure of the similarity between signals. Hence the OTD technique will be used when directly comparing one event to another event in order to yield the most accurate results. However, it was the slowest for comparing an event to the rest of the seismic signal (template matching), for a dataset that is not considered large.

The SFD was very quick, but was the least accurate due to there being no normalisation procedure for the cross-correlation function output. Therefore, using a combination of these two methods culminated in the FDW method. This method was very fast and had an accurate normalisation procedure for comparing one event to the rest of the seismic signal, hence the developed FDW method was used when using a template matching approach in the method.

3.2.4 Event threshold

I defined a new multiplet event as occurring when a threshold value of the cross-correlation coefficient was exceeded. The higher the threshold, the more similar the events were, but the risk of missing events would also increase. If the threshold is too low, false alarms may start to appear.

The Median Absolute Deviation (MAD) is often used as it gives a measure of statistical dispersion and is resilient to outliers, making it an ideal candidate for setting a threshold. Vuan et al. (2018) reported that typical thresholds are between 8 and 15 times the MAD of the cross-correlation function where an event has occurred, and chose 9 times the MAD for finding repeating earthquakes prior to the 2009 M6.3 L'Aquila, Italy earthquake. Shelly et al. (2007) used 8 times the MAD of the summed cross-correlation coefficients across several stations to identify repeating non-volcanic tremor in Japan. Kato et al. (2016b) set a threshold of 10 times the MAD of the average cross-correlation coefficients across all stations used for finding repeating earthquakes prior to the 2014 M8.2 Iquique, Chile earthquake. Based on this, I set the threshold for defining an event to default to 8 times the MAD to be significant enough of a statistical dispersion. However this threshold can be increased if a higher precision of similarity is needed.

The 'trigger onset' function was used within Obspy to output event times which exceeded the threshold. However, this function picked the first point at which the cross-correlation function reached the threshold. It was necessary to alter the trigger onset function, as the time that should be recorded is when the cross-correlation coefficient is at its maximum. This is the point of highest similarity, rather than the first point the cross-correlation coefficient exceeds the threshold. Therefore, this point is adjusted by selecting the time at which the highest cross-correlation coefficient (i.e. the local maximum) is reached within a 5 second window of the triggered point. The need

for this adjustment is demonstrated in Figure 3.26, which illustrates how the trigger onset function picked the trigger point slightly earlier than the maximum in the cross-correlation coefficient, which in turn represents the event onset time, τ_{opt}.

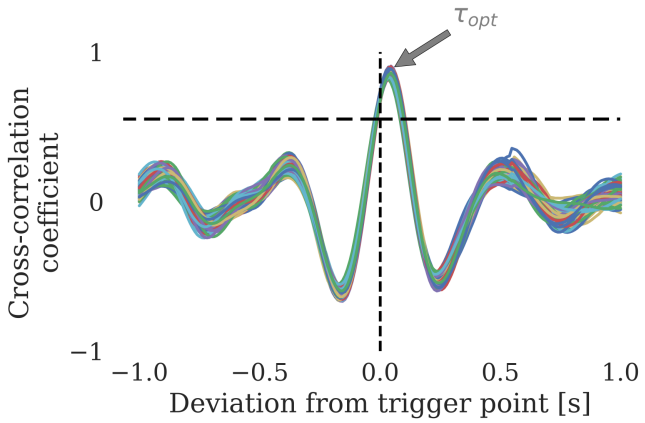

Figure 3.26: Cross-correlation coefficients for a 2 second window around all cross-correlation at the triggered event points. The vertical black dashed line represents the trigger time (at 8 times the Median Absolute Deviation of the day correlation), which is systematically earlier than the time when the highest similarity occurs. The different colours represent the different cross-correlation functions.

With the reviewed modifications to the standard cross-correlation techniques described in this section, I have demonstrated a fast and accurate way of picking events within a seismic signal through a moving window that works within the frequency domain. I also detailed the simple implementation to adjust the trigger point in order to obtain the time which had the highest similarity to the template trace, rather than the point that it passed the threshold. These approaches discussed above went directly into the new multiplet matching method, which is examined in the next section.

3.3 Multiplet matching method

Here, I describe the method built using a combination of cross-correlation techniques described in the previous section to find repeating events in a seismic signal, based on the method of Green and Neuberg (2006). As I am finding repeating events with similar waveforms, I will refer to the method herein as the '*multiplet matching method*'.

I describe how the method finds multiplets in an example with a synthetic seismogram sampled at 100Hz, with 200 repeating events spaced by a Poisson inter-event time distribution, with magnitudes following a Gutenberg-Richter distribution (b-value=1), and SNR=1.2, as defined by Equations 3.1 - 3.2. This meant that the ratio of the maximum signal amplitude to the maximum noise amplitude is still quite high.

3.3.1 Detailed description of method

The multiplet matching method can be used either with a pre-determined catalogue of starting template events, or with no prior information. It is based on the method of Green and Neuberg (2006), but modified to include an adapted first pass (Step 1), and Steps 7-9. The method described here also includes termination points if no multiplets were found.

In the case of a pre-existing catalogue of template events, the method begins from Step 4 and is applied for each of the templates to culminate in multiplets found for each template event. Thus, if there were a catalogue that contained three template events, the method would be repeated three times to result in a new updated catalogue. In the case of no prior information, it is necessary to start at Step 1, whereby events are picked based on the automatic triggering z-detect method, for reasons outlined in section 3.2.1.

In this step-by-step guide, I examine the synthetic seismogram assuming that there is no prior information of known events, i.e. the most general case.

3.3.1.1 Step 1: Identify template events

In Green and Neuberg (2006), the first pass involved a manual pick of events. However, in the multiplet matching method, the first pass uses the z-detect method to create a set of seismograms for a catalogue of picked events.

I set the trigger threshold where an event has begun when the Z-variable, shown on the lower plot of Figure 3.27, exceeds 1.0, and is lower than 0.8 for when the event is deemed to be over. The thresholds are important because it is necessary to find events, but avoid false alarms. This Step is illustrated in Figure 3.27, where red horizontal dashed lines on the bottom plot represent the triggering threshold being exceeded thus signifying an event, and the blue horizontal dashed lines for when the event is deemed over. The times at which the Z-variable has exceeded these horizontal thresholds are shown by the corresponding vertical lines in the top diagram. I have also added in grey dashed vertical lines in the lower diagram to highlight to the reader where the events are.

The events picked from the triggering algorithm shown in Figure 3.27 create a set of template seismograms for a new catalogue of events for input into Step 2.

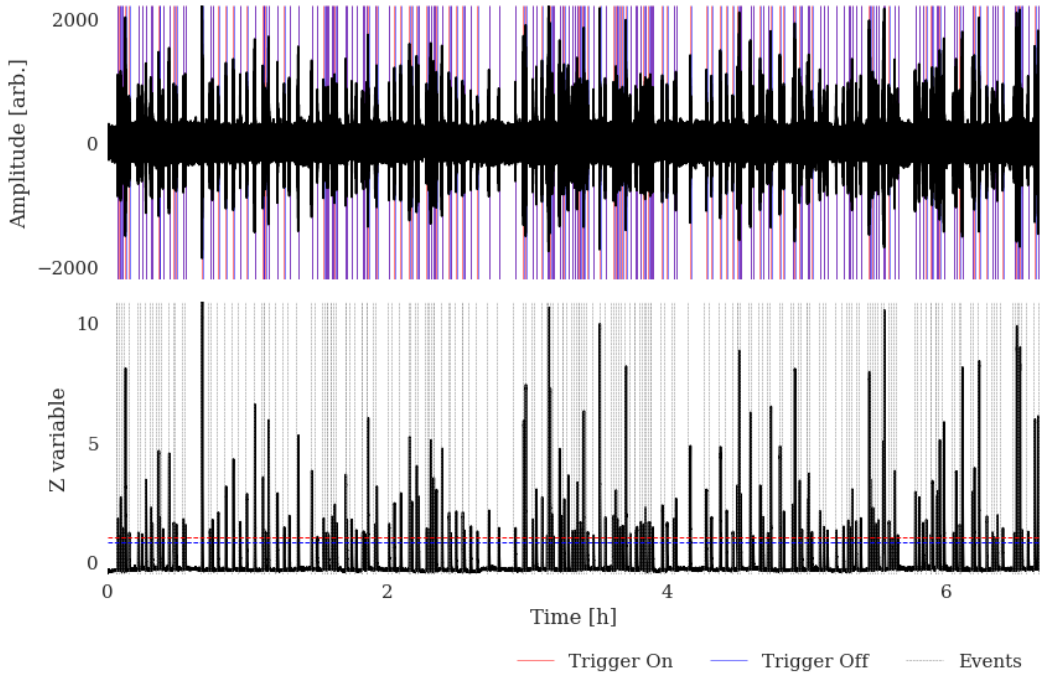

Figure 3.27: Illustration of the z-detect triggering method for a synthetic seismogram for the first pass of the multiplet matching method. Upper diagram shows original seismogram with vertical red and blue lines showing trigger points. The lower diagram shows the Z-variable with red and blue horizontal dashed lines for the trigger on and off points, and grey dashed vertical lines for the known event times.

3.3.1.2 Step 2: Compare events

Next, all of the events above the threshold from Step 1 are cross-correlated to every other event to create a cross-correlation matrix (ccm). A ccm is a matrix that contains the cross-correlation values of every event with every other event, as shown in Equation 3.8,

$$CCM = \begin{bmatrix} CC_{00} & CC_{01} & \cdots & CC_{0n} \\ CC_{10} & CC_{11} & \cdots & CC_{1n} \\ \vdots & \vdots & & \vdots \\ CC_{n0} & CC_{n1} & \cdots & CC_{nn} \end{bmatrix}. \tag{3.8}$$

Each individual element contains the cross-correlation coefficient, CC, where the subscripts represent the row and column. Therefore, CC_{10} contains the cross-correlation coefficient of event 1 with event 0. A ccm is symmetric around the diagonal, as the cross-correlation coefficient of event 1 with event 0 (CC_{10}) will be the same as event 0 with event 1 (CC_{01}), therefore only one half of the diagonal is actually calculated. The diagonal will always have cross-correlation coefficients of 1, as this is auto-correlation (the comparison of an event with itself, e.g. CC_{00} is the cross-correlation of event 0 with event 0).

199 events were found from the first pass, so a ccm of 199 x 199 is created in Figure 3.28, showing a large range of cross-correlation values.

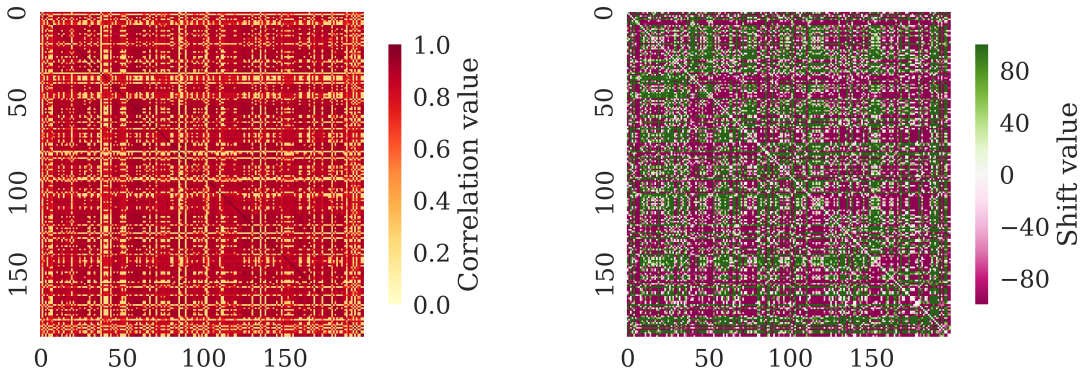

Figure 3.28: Comparison of cross-correlation (left) and shift (right) values for the triggered events from the first pass in Figure 3.27. The darker red colours indicate a high correlation (very similar) and a light yellow indicate a low correlation (not similar). Shift values which are white show accurate pick times, with non-white showing inaccuracies.

The cross-correlation method used here is to cross-correlate picked event 1 (window of 5 times the sampling rate before and 10 times the sampling rate after) to compare to picked event 2 of the same window size as in the OTD method explained in section 3.2.2, with a small lag window included. As this data is sampled at 100Hz, this means that the event has a window of 15 seconds.

A lag shift value matrix is also shown to the right in Figure 3.28 as this can be used as a metric in how accurate the event was picked. A 0 shift (white) meant that the code had picked out the event at the point of highest cross-correlation similarity, whereas a purple or green colour show that there was significant lag needed for maximum correlation to occur.

The first pass z-detect found 192/200 events (Hits) and had 7 false alarms. False alarms occurred where the picking approach has triggered to signify an event, but there were no events there. This can also be inferred from the yellow stripes in the left diagram of Figure 3.28, which highlights areas of low correlation. I investigate this further by observing the distribution of cross-correlation values for one template event (i.e. inspecting one row or column), as seen in Figure 3.29.

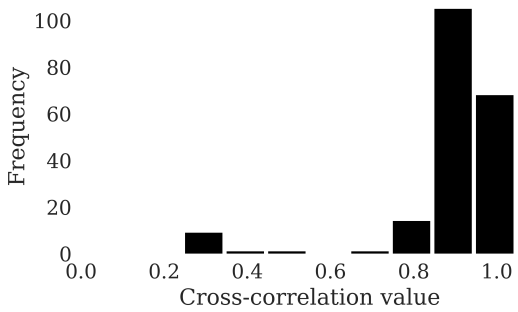

Figure 3.29: Illustration of the distribution of cross-correlation coefficients for events detected by the z-detect method. Identical similarity has a cross-correlation value of 1, and closer to 0 shows little to no similarity.

It is clear in Figure 3.29 that most of the z-detected events had a high correlation with the chosen template event but there are several with very low correlation. The reason for this could be either that the picking approach had picked the wrong part of the signal (e.g. only the tail of the event), or that they were not real repeating events (i.e. false alarms).

The picking approach also missed 8 events due to their amplitude being below

the triggering threshold. This highlights the trade-off involved in choosing the picking threshold. If I lowered the threshold, more false alarms could be picked, but if I increased the threshold, I could miss more events.

The non-zero values (shown as non-white) in the shift value matrix in the right diagram of Figure 3.28 highlight the inaccuracy of the z-detect method in finding the start time of the event. The starting time defined by the z-detect method gave different start times than that optimal time defined by the peak correlation in 3.28. The shift value would be 0 for the highest correlation, which is represented by a white pixel. This highlights one advantage of the cross-correlation method, which finds the optimum lag time with the highest cross-correlation value.

3.3.1.3 Step 3: Find families

Next, I grouped the multiplets found in the first step, to better understand and attribute the processes causing them. To do this, I classify multiplets into 'families', i.e. groups of higher similarity, using the cross-correlation matrices illustrated in Figure 3.29.

In order to group the multiplets into families, it was necessary to first choose a parent event (also known as a dominant event), which signified the event that had the most similarity to the other events in a family. Petersen (2007) chose the parent event by taking the average cross-correlation value for each event within the ccm (i.e. taking the average of all cross-correlation values per row). Green and Neuberg (2006) used a similar method when analysing the 1997 seismic swarms at Soufrière Hills volcano, Montserrat. The latter authors chose their parent event as the event that had the highest number of cross-correlations above 0.7, and then removed those events from their ccm. They repeated this method across all events until they were all in separate families.

I chose a threshold similar to Green and Neuberg (2006) and selected the parent

event by summing all the cross-correlation values above 0.5 in each row. This Step calculates the total maximum cross-correlation values for all events above a cross-correlation value of 0.5. I chose 0.5 so as not to rule out too many possibilities at an early stage, as a cross-correlation value of 0.5 is considered the minimum for cross-correlated variables to be moderately correlated (Mukaka, 2012) in any case. Next, I chose the event which had the highest amount of correlations, and then removed that event and those correlated to it above this threshold. This created the first 'family' of similar events. I repeated this procedure for the remainder of events until all events were grouped into the other families.

As in Green and Neuberg (2006), I then averaged the events in family 1 to eliminate any small fluctuations between events to create a new master template trace, as shown in Figure 3.30.

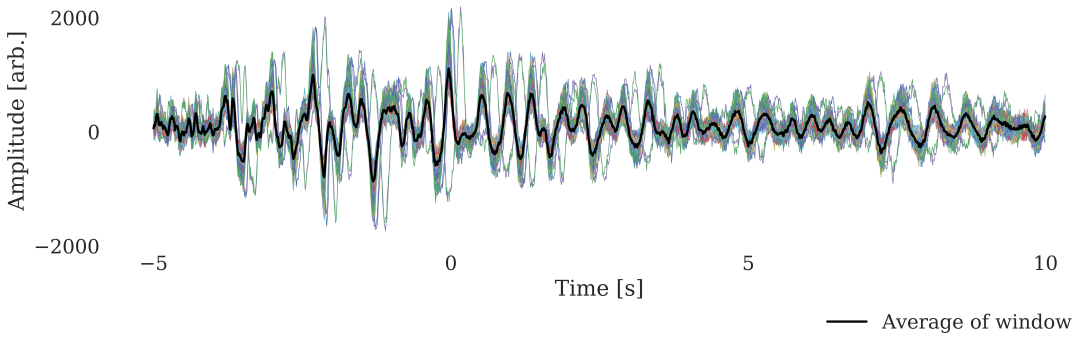

Figure 3.30: Overlay of seismograms of family 1 events from Figure 3.28, with the thicker black line signalling the average waveform, which becomes the new master template trace.

3.3.1.4 Step 4: Cross-correlate with template trace (start here when prior knowledge known)

Next, I used a similar method as in Green and Neuberg (2006), who used the new master template trace (the average of the first family) and cross-correlated it with the rest of the seismogram to pick any previously missed events. It is expected that events

that are similar to the new master template trace will be detected here. Figure 3.31 shows the result of this cross-correlation, which picked up waveforms similar to the template trace in Figure 3.30. The threshold level is set as the lower between 8 times the Median Absolute Deviation (MAD) from the day trace, or 0.5 in order to pick up as many events as possible. I have set a maximum threshold level of 0.5 so that it will not be automatically set too high by the MAD in datasets where there are many highly repeating events. Anything which is above the threshold level is considered to be a triggered event of the first family.

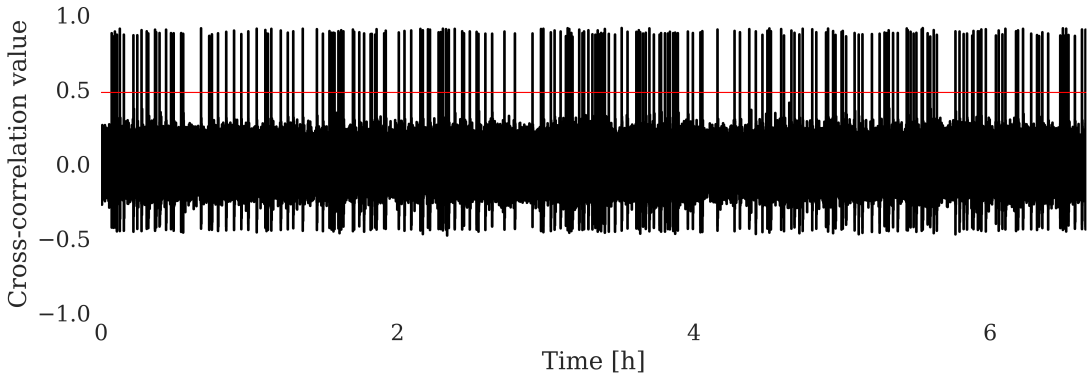

Figure 3.31: Cross-correlation function of the new template trace (average family trace shown by black line in Figure 3.30) and the entire seismogram. The red line shows the cross-correlation threshold level. Cross-correlation values which exceed this threshold are considered as triggered events.

3.3.1.5 Step 5: Compare events in the second pass

Here, I repeated Step 2 of the first pass procedure, i.e. where triggered events are compared to each other by cross-correlation, but this time not with a parent event, but instead with the new master template trace, as shown in Figure 3.32. These events are clearly much more similar than in the first pass, as seen by the dark red colours in the left diagram of the cross-correlation matrix in Figure 3.32, and are picked in time very accurately, as seen by the entirely white shift value matrix in the right diagram. Thus,

the new master trace is a much more representative parent for the dominant family. Additionally, 200/200 events were successfully found, with no false alarms.

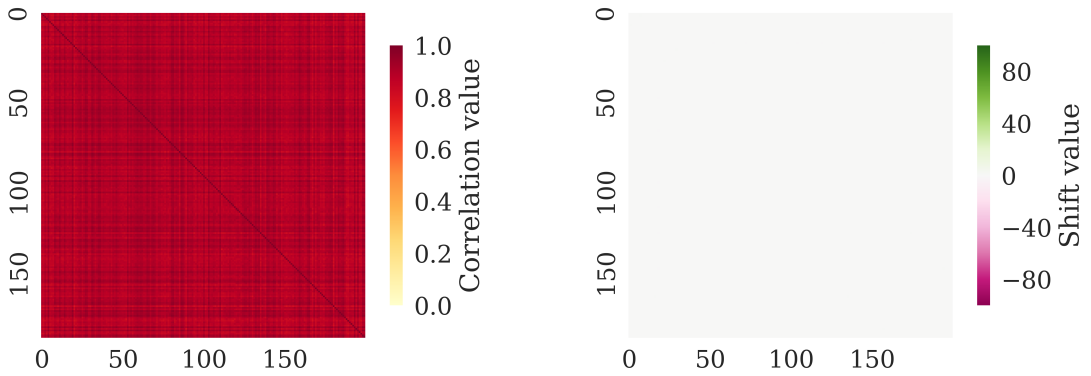

Figure 3.32: Comparison of cross-correlation and shift values for the triggered events from second pass in Figure 3.31. The shift values are all near zero, resulting in a flat white fill in this case.

I further analysed the cross-correlation coefficients by observing their frequency distribution in Figure 3.33. All events have a cross-correlation coefficient of at least 0.9, therefore these are very likely to be repeating events rather than false alarms. Comparing Figure 3.33 to Figure 3.29 shows the increase in cross-correlation coefficients of the found events to being between 0.9 and 1.0, highlighting the efficacy of this technique for finding repeating events.

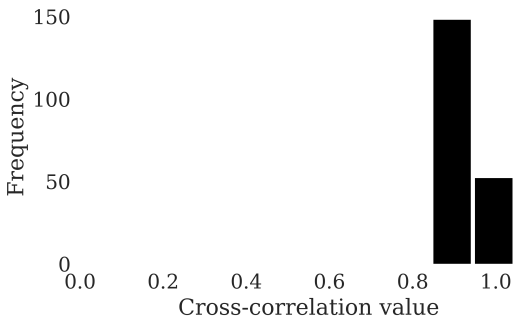

Figure 3.33: Distribution of cross-correlation values for the parent event in Figure 3.32 from triggered events from Figure 3.31.

3.3.1.6 Step 6: Find families

I repeated Step 3 here where I grouped the events found in Step 5 into their families. At the start all 200 of the input 200 repeating events had been successfully found (with no false alarms).

A final pass was not necessary in this described example, but it is included in case of any missed repeating events in other synthetic or real datasets which are tested. In the method of Green and Neuberg (2006), the workflow would terminate here.

3.3.1.7 Step 7: Cross-correlation with a template trace

Here, I expand upon the method from Green and Neuberg (2006) and obtain the family average from Step 6 which creates a new master template trace. This is then cross-correlated with the rest of the seismogram (repeating Step 4).

3.3.1.8 Step 8: Compare events from third pass

All triggered events are then compared to each other again by cross-correlation (repeating Steps 2 and 5). The goal of this third and final pass is to improve cross-correlation values further as seen in Figure 3.34. Although the events are the same as before, their cross-correlation coefficients have improved further due to the average trace picking them more accurately than a single seismogram.

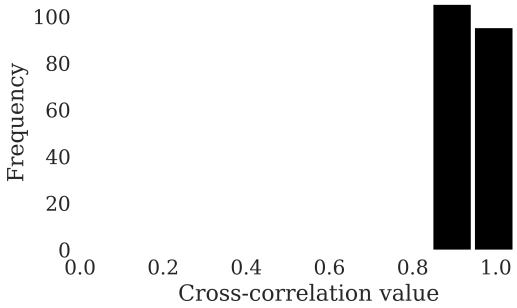

Figure 3.34: Distribution of cross-correlation values for parent event with every other triggered event found from Step 7.

3.3.1.9 Step 9: Find families

Families are then found in the same way as Steps 3 and 6 from the new correlation matrix of triggered events over the threshold level of 8 times the MAD of the day trace, or 0.5 (whichever is lower). In this illustration of the method, I found no extra events, and so all 200/200 events are deemed to be within the same family, as expected from the known input in this example.

3.3.2 Summary of method and outstanding issues

Section 3.3.1 demonstrated a simple step-by-step example of how I used cross-correlating techniques to find all 200 multiplets in a synthetic seismogram that I made. This method is based on Green and Neuberg (2006), modified to include a different first pass (Step 1), and Steps 7-9, as well as automatic termination points in the case of no multiplets found. Testing this method on a synthetic seismogram with a known solution allowed for an accurate measure of how well multiplets are picked, and whether they were hits, misses or false alarms. In this example, the final hit rate was 100% with no misses or false alarms. In a real example, this is unlikely to be the case.

The method described can be summarised in the flowchart shown in Figure 3.35. The method by Green and Neuberg (2006) does not include a third pass, and terminates after the second pass (i.e. after the second iteration at Step 3).

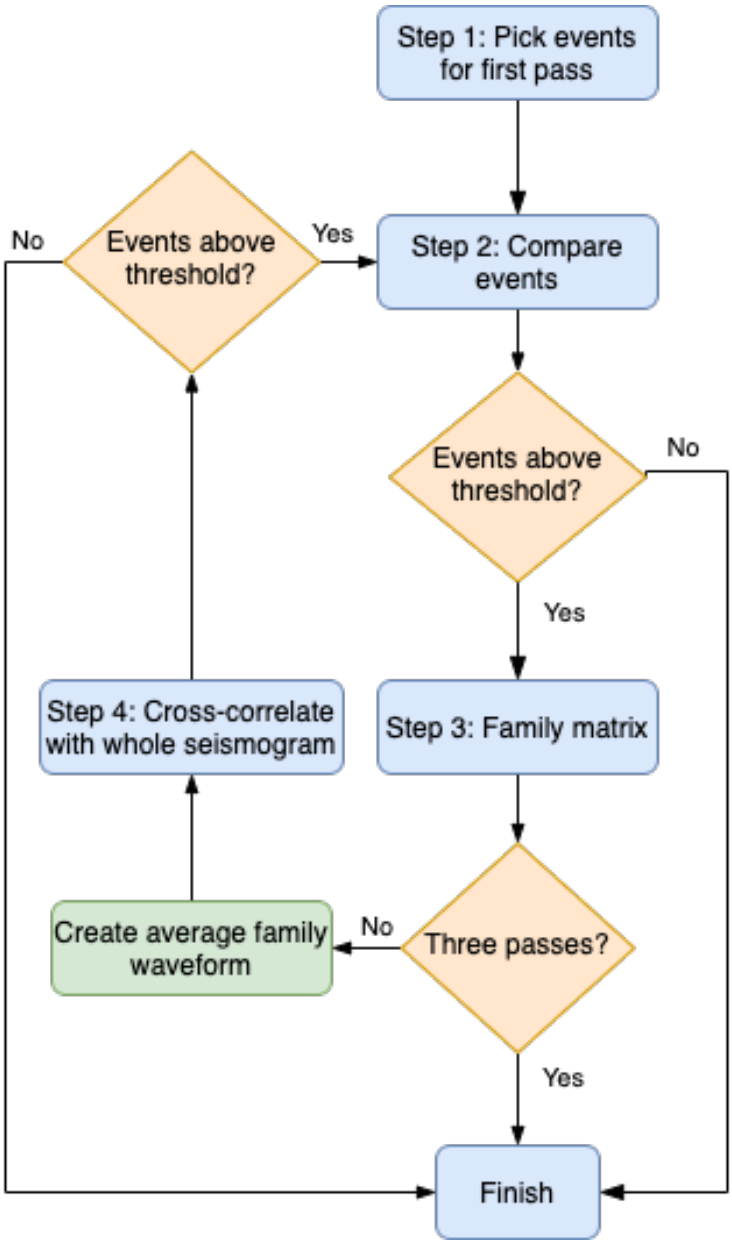

Figure 3.35: Summary of method based on Green and Neuberg (2006) to identify multiplets, labelled by steps that correspond to those in section 3.3.1. Described Steps are labelled within the blue boxes, and green boxes describing minor developments within Steps. Decision boxes in orange are annotated for the outcomes to found event responses, or number of passes.

The main weaknesses of the argument to this point is that I have made several

assumptions in this example, notably the high SNR, which is not always possible in real datasets. This has resulted in a perfect hit rate. Accordingly, I will test this method further on synthetic seismograms with lower levels of SNR in chapter 4. Moreover, I have also used only a single multiplet that repeats in the synthetic seismogram, when in real datasets there could be several different types of multiplets from different families that correspond to different processes occurring at different places. Although this method separates the events into families based on their similarity (Steps 3, 6 and 9), the iterative nature of this method focusses on the most dominant family in the seismogram. It is possible to explore the other families in a case-by-case basis, however this is not included here.

As the multiplets tested here overlapped slightly in some cases, this highlighted a risk in the detection of multiplets from different families in real cases. This is not an issue here as the multiplets are known to be from the same family. However I introduce an additional 'cleaning' step to remove all events within a certain time window of each other when testing for real cases. This time window will be based on an optimum to avoid any bias in a catalogue from multiple detections of single events.

Additionally, there could also be real events with no repetitive nature to them, and so no multiplets. These would not be picked up in this method unless they were selected as template events at Step 1. Accordingly, the method may work best as an additional procedure for catalogues starting with template seismograms for known events.

3.4 Scaling for magnitude

To compare events found by the template matching method to those in the official catalogues (from sources such as the USGS), I assigned magnitude estimates to the new events. As I have designed this method to work even on sparse networks, I was using data from only one seismometer. In the case of similar waveforms, it is possible to

neglect the effect of the radiation pattern so that it is possible to use a simple amplitude ratio to estimate the magnitude of the events (Gibbons and Ringdal, 2006; Rubinstein and Ellsworth, 2010). Having found clusters of repeating events from a given template event, I used the more general scaling relationship of Shelly et al. (2016a) to determine the magnitude of the new event (M_{new}) discovered by the cross-correlation technique even in the case that the waveforms are not too dissimilar (Ellsworth, 2018). This calculation uses the template event magnitude ($M_{template}$), a scaling constant (c) and the ratio of event amplitudes (α), shown in Equations 3.9 and 3.10.

$$M_{new} = M_{template} + c \log_{10}(\alpha), \tag{3.9}$$

where

$$\alpha = \frac{v(2)}{v(1)}, \tag{3.10}$$

with $v(1)$ and $v(2)$ are specifically the elements of the eigenvector $\mathbf{v}$, which corresponds to the largest eigenvalue of the covariance matrix of the template waveform and the new waveform. This allows for the calculation of new event magnitudes from the template event. This means that I can use results obtained from only one seismometer to work out magnitudes of all the same family of repeating events. This is done through scaling rather than requiring the source location and focal mechanism calculation from phases picked from multiple stations and corrected for epicentral distance.

I calibrated c in Equation 3.9 using events which have already had a local or duration magnitude assigned by conventional methods, so 'M_{new}' is known. I then calculated the covariance matrix for the cross-correlated waveforms and extracted parameters $v(1)$ and $v(2)$ from the result. The best estimate of c is then determined from the known 'M_{new}' and $M_{template}$.

The results of this calibration for the magnitude scaling relationship are shown in Figure 3.36 for the Parkfield earthquake dataset, collecting families for every separate template event. The estimated magnitudes for the new events were determined from

Equation 3.9 and the values of α determined from the covariance matrix of the two waveforms. Several test values of c are shown, with the value of c that best fit the dataset was 0.80 shown as the overlain data points.

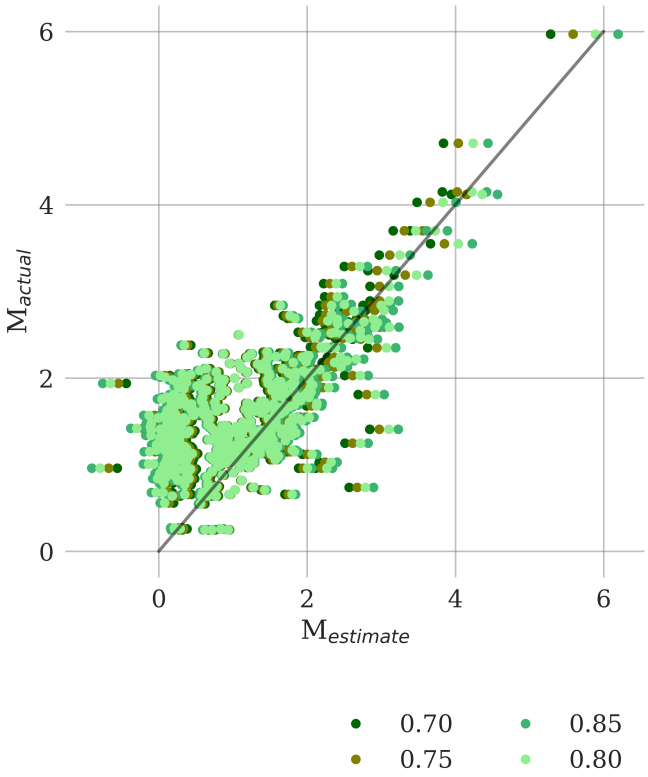

Figure 3.36: Scaling relation c between the estimated magnitude $M_{estimate}$ and the actual magnitude M_{actual}, for calculating the new event magnitude from the earthquake catalogue for the 2004 Parkfield earthquake sequence. Several tests run showing results with different c values, shown by the colour. The $y = x$ line is shown in black for reference. In this case it is a best fit line at $c = 0.80$, shown by the light green dots. Other test values of c are shown with varying colours of green.

Having established the value of c for this dataset, I assigned an estimated magnitude to actual new events discovered by cross-correlation. The majority of events in catalogues are local magnitudes rather than the preferred moment magnitudes (section

2.5), thus, the magnitudes estimated assigned with this technique are to extend the catalogue, rather than replace the known magnitudes (Shelly et al., 2016a).

Next, I examined how estimated magnitudes of the repeating events evolve temporally prior to catastrophic failure. An example of this is shown in Figure 3.37, which illustrates two events from the 2004 Parkfield earthquake dataset: a new event (blue window) found through cross-correlation techniques, and a known template event from the USGS catalogue (green window).

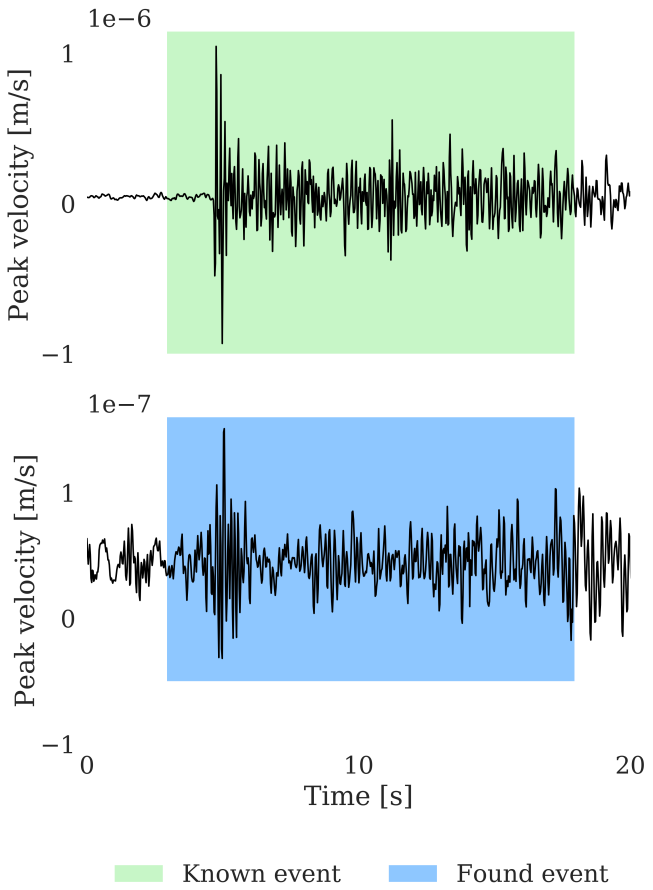

Figure 3.37: Example of a known event (green window) from the 2004 Parkfield earthquake catalogue and a new event (blue window) identified by cross-correlation within the same dataset. The magnitude of the second is related to the first by Equation 3.9 resulting in a simple amplitude scaling (reflected in the scale of the y-axis), albeit degraded by background noise.

The magnitude of the new event, M_{new}, is calculated from Equation 3.9, with c as 0.65 (as set from Figure 3.36). Here, $M_{template}$ is 2.0 (a local magnitude as assigned from the USGS catalogue), which gives an estimated M_{new} of 0.9 for the new event. This example encapsulates the thesis title of *'finding small signals in Big Data,'* as the small event in Figure 3.37 has been found by using a larger event within a seismic signal lasting several weeks, and would not have been detected with simple phase-picking methods as in section 3.2.1.

3.5 Scaling up

I tested the multiplet matching method on a relatively short example of 9 hours, but it is often necessary to work with many days worth of seismic data as multiplets could occur over several days. I implemented the method in the form of a simple script so it could be easily edited to run on the Edinburgh Compute and Data Facility (ECDF), or Eddie. The programme can also be run on a specific computer within the Eddie cluster, called the Terracorrelator, which is a NERC funded computer comprising of two large 2TB high random-access-memory nodes, sharing 300TB of local storage. Creating these scripts to run the method remotely for processing freed up local space to be available for other work, and allowed for the method to be applied to many different datasets in parallel, both considerable advantages for processing large datasets.

I tested the timings of the multiplet matching method on a local computer, the Terracorrelator and on Eddie with 3 days worth of 'drumbeat' (quasi-periodic) seismicity at Mount St. Helens, USA sampled at 100 Hz. These timings, itemised by which step of the method is taking place, are shown in Figure 3.2.

Pass	Step	Local	TC	Eddie
First pass	1	4:57:56	0:04:58	0:02:13
	2	0:00:08	0:00:25	0:00:13
	3	0:00:00	0:00:00	0:00:00
Second pass	4	0:00:55	0:02:56	0:01:23
	5	0:40:10	1:58:39	1:01:32
	6	0:00:01	0:00:01	0:00:00
Third pass	7	0:00:55	0:02:56	0:01:23
	8	0:47:56	2:20:54	1:12:56
	9	0:00:01	0:00:01	0:00:00
	Total	6:28:05	4:30:54	2:19:45

Table 3.2: Timings per step for the processing of out Mount St. Helens dataset on a local computer, Terracorrelator (TC) and Eddie supercomputer. Timings are given as HH:MM:SS.

As almost 4000 repeating events were found, 16 million cross-correlations were taking place, thus making this a slow computation. On a local computer (purchased in 2015), this took about 6.5 hours to complete, whereas it only took 4.5 hours on the Terracorrelator (purchased in 2013) and 2 hours 20 minutes on the Eddie supercomputer using more recent hardware.

Some steps are faster on the local computer than on the supercomputers, and vice versa (Table 3.2). For example, Step 1 (the picking events step) was 99% slower on a local computer than Eddie as it took almost 5 hours to complete, with Eddie only taking 2 minutes. However, Steps 5 and 8 (the comparison of events to one another through cross-correlation) were 66% and 34% faster on the local computer than the Terracorrelator and Eddie, respectively. The reason for these particularly memory-

intensive Steps being slow on the Eddie supercomputer is that this was only run on one core with a memory limit of 2GB (local computer has memory limit of 8GB). The Eddie supercomputer is better designed for speed, and has massive potential for parallelising code, however it does not have the same storage facilities as the Terracorrelator, which was built for a large storage space rather than speed. Hence, although the Terracorrelator is slower for this cross-correlation step, it is able to hold more data in its 2TB random-access-memory, as anticipated in its procurement. Thus, when there are many more template events being cross-correlated with one another than in this case, the Terracorrelator is preferred.

From this analysis on a large dataset, it seems that the code works optimally if run on a local computer if I miss the first pass, i.e. if I do not need to pick events. This would only be appropriate if a template trace were already available. However, if I do not have a starting template trace, it is best to use Eddie as I would then require the first pass in order to find the events. This is also only applicable if I have one template trace to test. If I have numerous template traces, such as to obtain a more complete catalogue by finding repeating events similar to all the defined pre-mainshock events, it is always preferable to use a supercomputer to run the method in parallel. When dealing with many repeating events, the Terracorrelator is favoured due to its large memory nodes which are ideal for running many cross-correlation calculations.

3.6 Methodological developments summary

A new method based on that in Green and Neuberg (2006) was developed for finding multiplets within seismic data, using known template seismograms and the control over parameters such as noise level, inter-event times and magnitude distribution. This allowed for an evaluation of its performance with a known solution. Synthetic seismograms with known multiplets were generated to form an ideal synthetic seismogram,

and inverted by cross-correlation using the new method. This allowed the accuracy of the method for finding multiplets to be determined with confidence. Having optimised this approach on the ECDF supercomputer, the next chapter applies the same method to more synthetic seismograms to further test its performance with different parameters.

Chapter 4

Performance tests

As described in section 3.1, I created several synthetic seismograms in order to test how the multiplet matching method of Figure 3.35 (section 3.3) worked under several conditions. This had the advantage of being able to control the parameters of the synthetic catalogue and the background noise. In this chapter, I show results from a more comprehensive set of performance tests used to check the effectiveness of the algorithm used to identify multiplets with the multiplet matching method for different inter-event time and frequency-magnitude distributions, as well as various background noise levels. I also demonstrate the effect of different sampling rates for the seismogram, and the sensitivity of the event detection threshold to highlight the importance that these parameters hold for identifying a multiplet accurately. Testing the success of the method on synthetic data in this way provides more confidence in analysing real data to look at the occurrence of multiplets for different types of catastrophic failure.

4.1 Success of the method under different conditions

The performance tests described here test the limits of how well the method works under noisy conditions (i.e. when Signal-to-Noise Ratio, SNR, is low) for each of the

passes described in the multiplet matching method (section 3.3). To quantify the success of the method, I used a metric where 'Hits' represents found events which are known multiplets, 'Misses' for when the pass has missed the known multiplet, and 'False alarms' for when the pass has identified an event which is not a 'real' multiplet, as represented in Table 4.1. There is also a metric for 'Correct rejection' for when the method correctly identifies no multiplet, however I will not measure this in my performance tests.

		Known multiplet	
		Yes	**No**
Found repeating event	**Yes**	*Hit*	*False alarm*
	No	*Miss*	*Correct rejection*

Table 4.1: Summary of outcomes for method performance tests for finding multiplets.

Here, I tested the multiplet matching method on a synthetic seismogram where 200 otherwise identical multiplets (or repeating events in this case) were placed randomly in time as in a Poisson process following a Gutenberg-Richter distribution ($b = 1$), and at different noise ratios, as illustrated in Figure 4.1. Plot a illustrates the timings of the events in plots b-d with the peak amplitudes from plot b taken as an example of the distribution of amplitudes. The seismogram in plot b represents a relatively clear signal with a SNR of 1.2, plot c with a SNR of 0.8, and plot d represents a noisy environment with a SNR of 0.4.

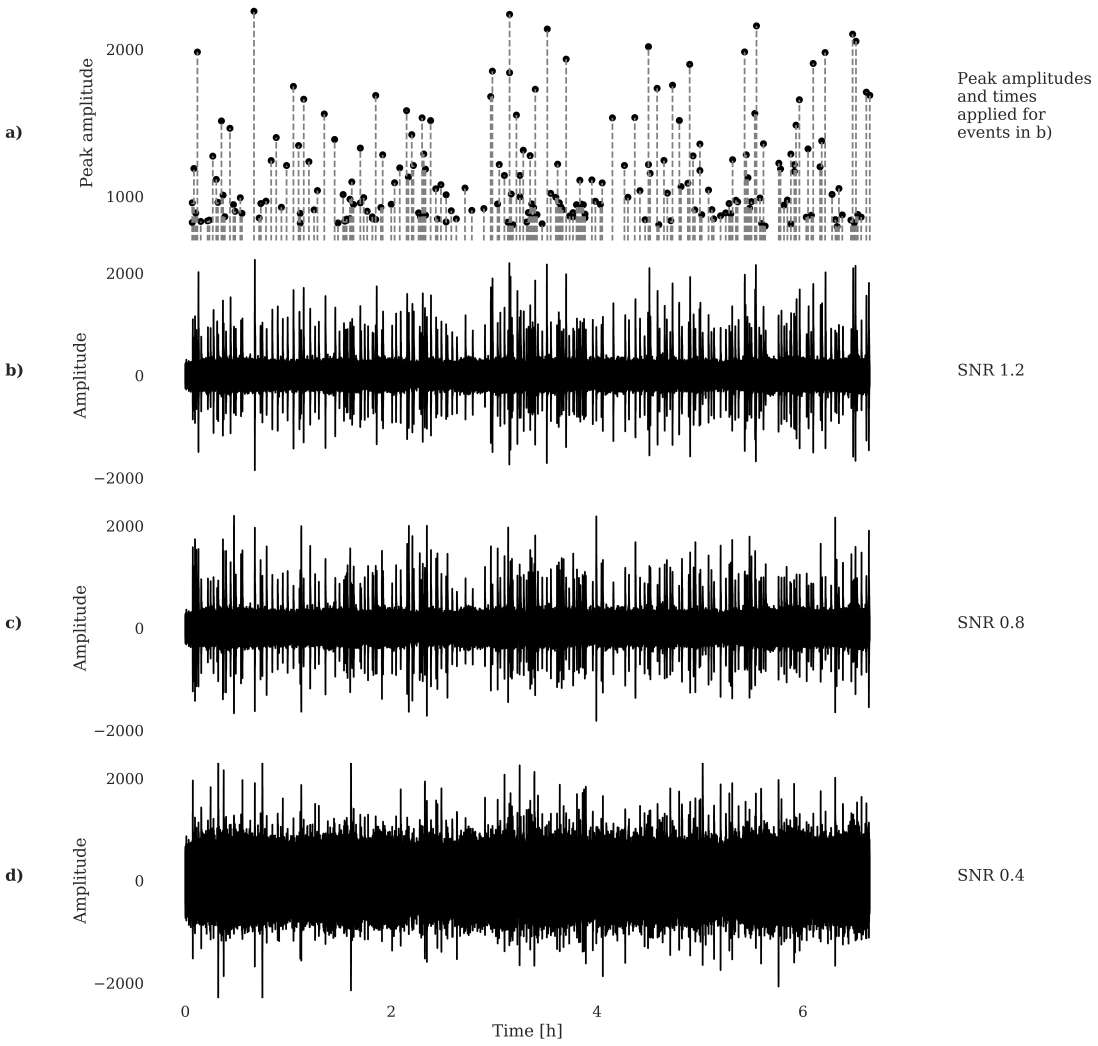

Figure 4.1: Case 1 - Synthetic seismograms with Poisson distributed inter-event times and a Gutenberg-Richter distribution of magnitudes, for a Signal-to-Noise Ratio (SNR) of 1.2 (b), 0.8 (c) and 0.4 (d). Plot a illustrates the times of the events in the three examples, with the peak amplitudes taken from plot b.

The success of the method in finding 'true' multiplets in the seismograms shown in Figure 4.1, is displayed in Table 4.2.

Pass	Success	SNR 1.2	SNR 0.8	SNR 0.4
First pass	Hits	180	186	144
	Misses	20	14	56
	False alarms	19	14	25
Second pass	Hits	200	200	200
	Misses	0	0	0
	False alarms	0	0	0
Third pass	Hits	200	200	200
	Misses	0	0	0
	False alarms	0	0	0

Table 4.2: Case 1 - Success rate for different Signal-to-Noise Ratios (SNRs) for each pass of the multiplet matching method on a synthetic seismogram with Poisson distributed inter-event times and a Gutenberg-Richter distribution of magnitudes.

Table 4.2 shows that the first pass (the z-detect picking method) found many of the events, with success rates of 90%, 93% and 72% for SNRs 1.2, 0.8 and 0.4, respectively. Despite reporting promising success rates for the first pass, there were also many false alarms, particularly for noisy conditions. The locations of the events which were successfully detected (hits) and those that were not detected (misses) in the first pass are shown in Figure 4.2.

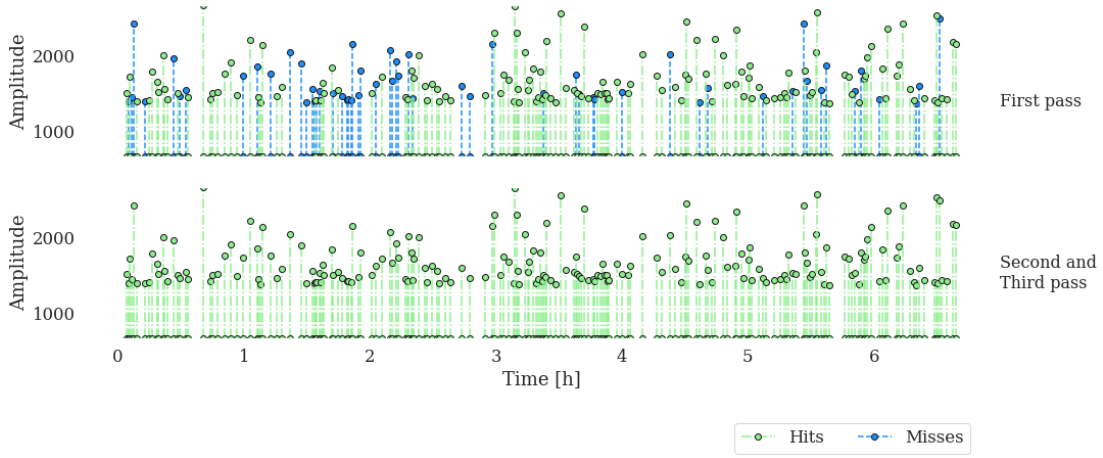

Figure 4.2: Peak amplitudes and times of correctly identified events (hits - green dashed line) and missed events (blue dot-dash line) for case 1 (Poisson distributed inter-event times and a Gutenberg-Richter distribution of magnitudes) for a Signal-to-Noise Ratio of 0.4 (d in Figure 4.1). The first pass is shown in the upper, and the second and third pass together in the lower as they had the same result.

The upper of Figure 4.2 shows that there was no relationship between the rate or amplitude of events and the missed events (shown as blue dot-dashed lines) in the first pass. Instead, the failure was due to the first pass picking too many incorrect events (false alarms) due to the low SNR, thus missing where the correct events were. For example, this could happen if the z-detect method triggered on from a noise fluctuation but did not then trigger off for some time. Thus, then the z-detect picking method in the first pass could easily miss the real events, as the real event would then be overlapping/within with the false alarm.

Fortunately, the implementation of the second pass (cross-correlation with averaged template from previous pass) found 100% of multiplets successfully by the multiplet matching method, even in the very noisy conditions. This is shown by all the hits (green dashed lines) in the lower of Figure 4.2.

Next, I tested an inter-event time distribution of an accelerating event rate to

simulate inter-event times getting smaller as failure approaches. The events also had Gutenberg-Richter distributed magnitudes ($b = 1$), as illustrated in Figure 4.3. Here the time between events is not otherwise random. The events occur periodically, but with a period that decreases in time according to Equation 3.3.

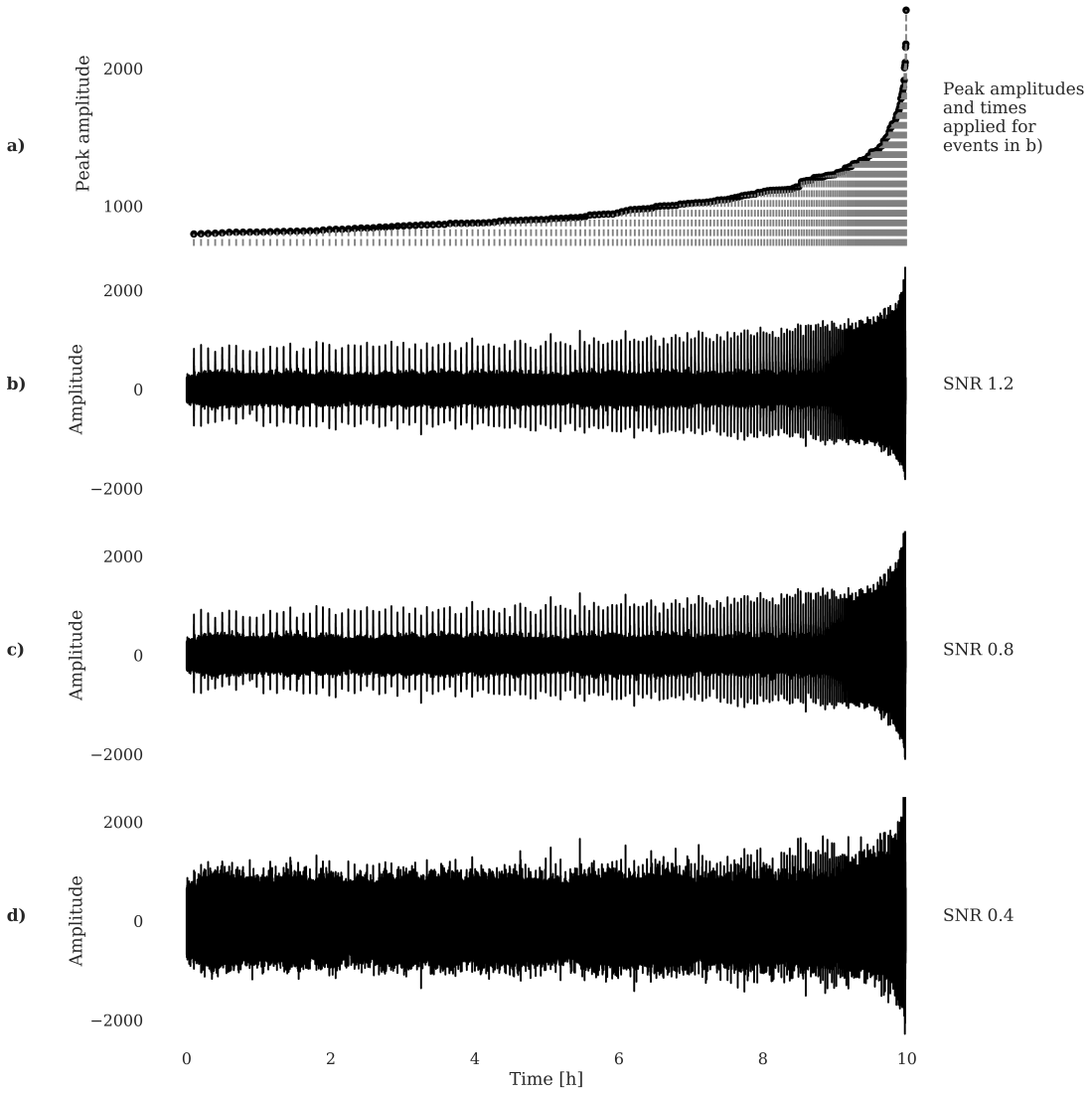

Figure 4.3: Case 2 - Synthetic seismograms with an inter-event time distribution of an accelerating event rate and a Gutenberg-Richter distribution of magnitudes (accelerating with respect to time), for a Signal-to-Noise Ratio (SNR) of 1.2 (b), 0.8 (c) and 0.4 (d). Plot a illustrates the times of the events in the three examples, with the peak amplitudes taken from plot b.

The success of the method in finding the 'true' multiplets in the seismograms in Figure 4.3, is displayed in Table 4.3.

Pass	**Success**	**SNR 1.2**	**SNR 0.8**	**SNR 0.4**
First pass	Hits	192	191	175
	Misses	8	9	25
	False alarms	0	0	79
Second pass	Hits	200	200	23
	Misses	0	0	177
	False alarms	0	0	0
Third pass	Hits	200	200	200
	Misses	0	0	0
	False alarms	0	0	0

Table 4.3: Case 2 - Success rate for different Signal-to-Noise Ratios (SNRs) for each pass of the multiplet matching method on a synthetic seismogram with an inter-event time distribution of an accelerating event rate and a Gutenberg-Richter distribution of magnitudes (accelerating with respect to time).

Table 4.3 shows that the first pass (the z-detect picking method) found ≈96% (192 and 191) multiplets for SNRs of 1.2 and 0.8, respectively. These SNRs also reported very few misses and no false alarms. However, more noisy conditions (SNR 0.4) show that despite correctly identifying 86% (175) of the multiplets, there were also 79 false alarms at this first pass. The second pass was more favourable for SNRs of 1.2 and 0.8, as the method correctly identified 100% of the multiplets with no misses and no false alarms. The SNR of 0.4 did not work well in this pass as it only found 12% (23) of the multiplets, and had an extremely large miss count of 177. Despite not picking up all events at this stage, the method still did not identify any false alarms, highlighting the power of the cross-correlation method for only finding similar events. By the third

pass, all three SNRs conditions found all 200 events successfully. I observed the points in time where these hits and misses occurred in the first and second passes of this case in Figure 4.4.

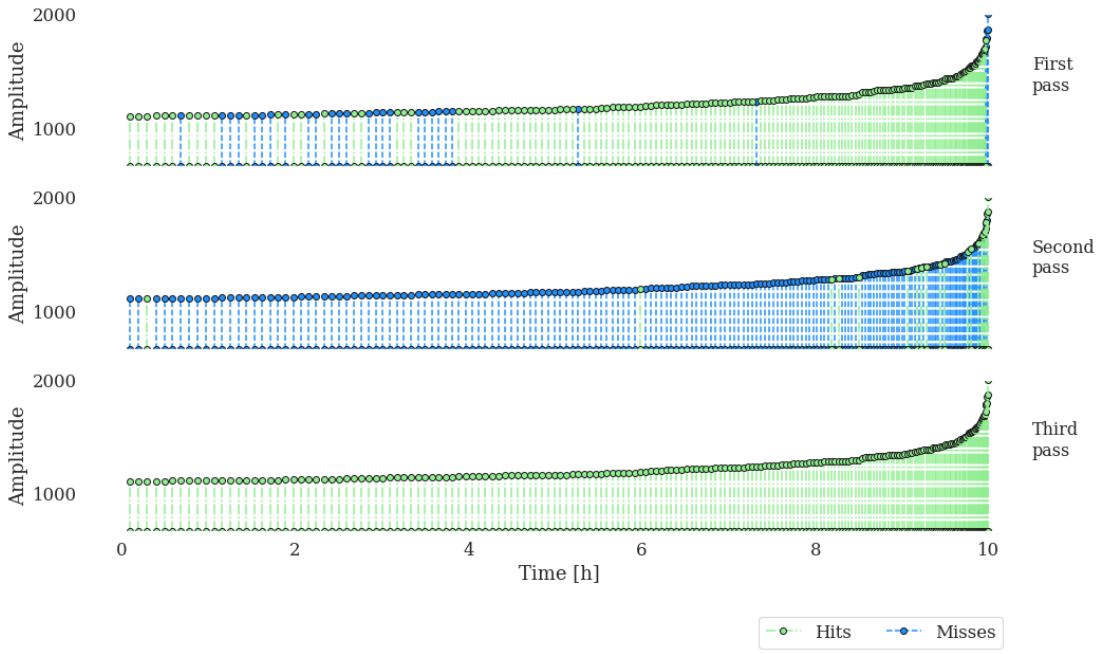

Figure 4.4: Peak amplitudes and times of correctly identified events (hits - green dashed line) and missed events (blue dot-dash line) for the three passes in case 2 (accelerating with respect to time) for a Signal-to-Noise Ratio of 0.4 (d in Figure 4.3).

The upper of Figure 4.4 shows that the first pass missed mainly the smaller-amplitude events at around 1-4 hours (shown by the blue dot-dashed lines), whereas the middle of Figure 4.4 shows that the second pass was only able to successfully identify those near the end of the time period (shown by the green dashed lines). As the first pass was able to successfully detect some of the larger amplitude events, the master trace created from averaging these events was not largely influenced by the false alarms. This then allowed for the second pass to correctly identify those events later in the signal, as the master trace was sufficiently similar to these larger-amplitude events. It is not surprising for the smaller-amplitude events to be missed in this second pass, as the events picked up from the first pass were not well-aligned with one another, and so the

master trace was not sufficiently similar to these smaller-amplitude events (which were more affected by the noise fluctuations). For a SNR of 0.4, the third pass (the lower of Figure 4.4) enabled those 23 events previously found to create a more accurate template trace which was then able to find the other multiplets in the seismogram. Including a third pass was paramount in this case, as otherwise the method would have had an extremely high miss rate for noisier conditions.

Finally, I tested the method on a seismogram created with inter-event times representing a swarm-like event pattern by increasing the rate of earthquakes at different points (initial swarms separated by Poisson rate and a higher Poisson rate for events within the swarm) and Gutenberg-Richter distributed magnitudes ($b = 1$), as shown in Figure 4.5. The top seismogram shows a SNR of 1.2, the middle with a SNR of 0.8, and the lower with a SNR of 0.4.

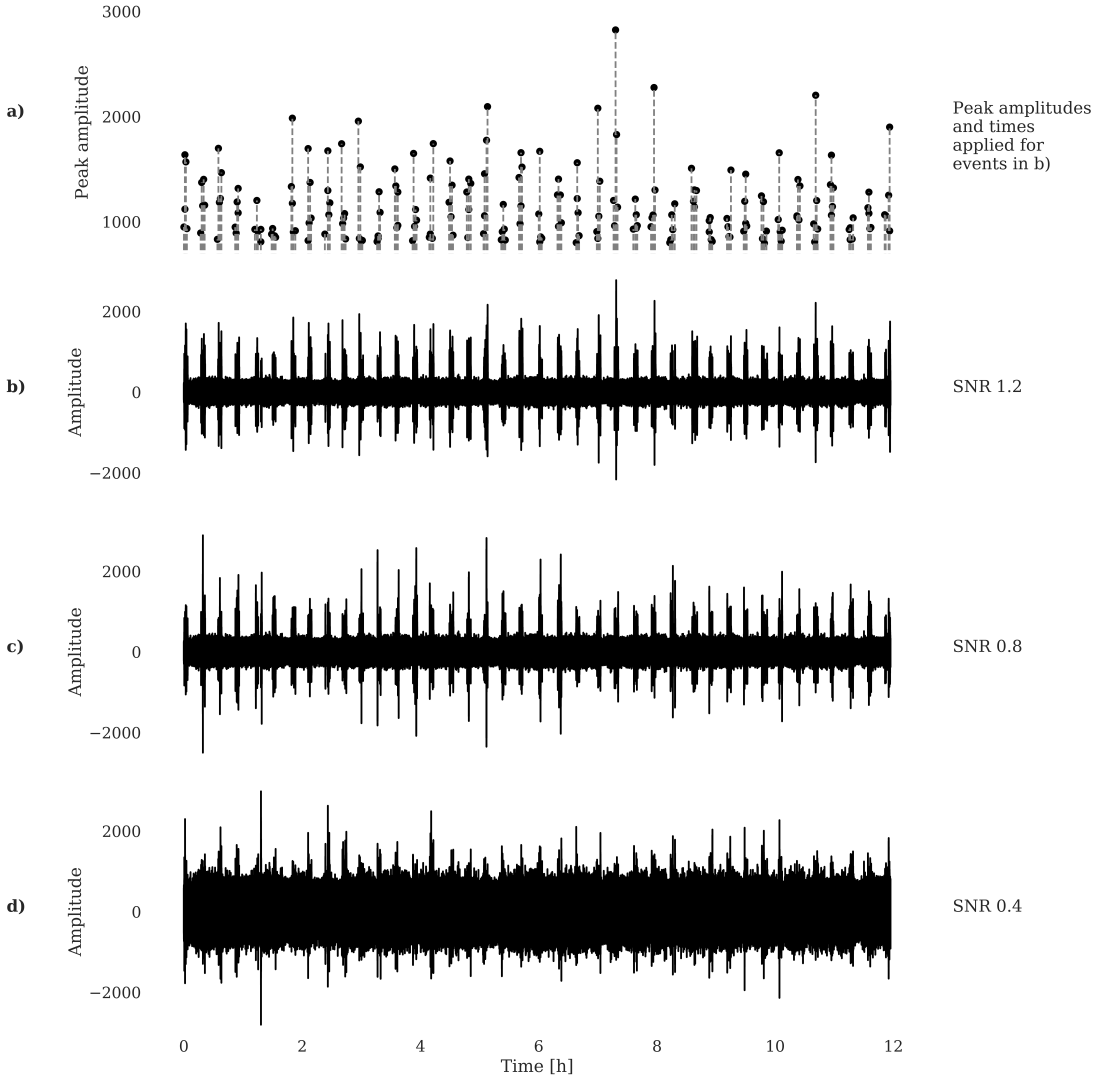

Figure 4.5: Case 3 - Synthetic seismograms with swarm-like inter-event times (40 swarms each containing 5 events) and a Gutenberg-Richter distribution of magnitudes for a Signal-to-Noise Ratio (SNR) of 1.2 (b), 0.8 (c) and 0.4 (d). Plot a illustrates the times of the events in the three examples, with the peak amplitudes taken from plot b.

The inter-event time distribution for the events shown in Figure 4.5a is illustrated in Figure 4.6 to illustrate its form for an underlying swarm-like pattern.

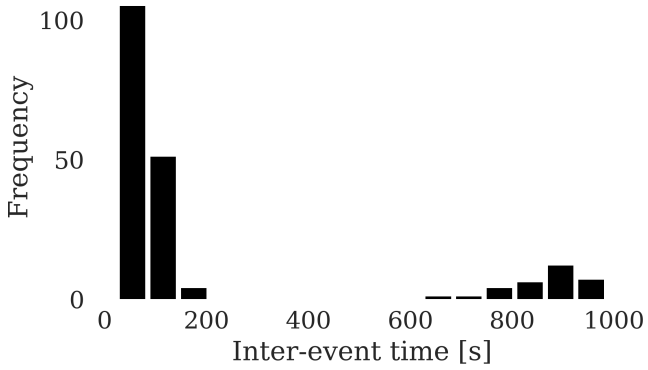

Figure 4.6: Inter-event time distribution of events in Figure 4.5a to illustrate its form for a swarm-like pattern.

The success of the method in finding the 'true' multiplets in the seismograms of Figure 4.5, is displayed in Table 4.4.

Pass	**Success**	**SNR 1.2**	**SNR 0.8**	**SNR 0.4**
First pass	Hits	200	200	185
	Misses	0	0	15
	False alarms	0	0	83
Second pass	Hits	200	200	200
	Misses	0	0	0
	False alarms	0	0	0
Third pass	Hits	200	200	200
	Misses	0	0	0
	False alarms	0	0	0

Table 4.4: Case 3 - Success rate for different Signal-to-Noise Ratios (SNRs) for each pass of the multiplet matching method for a synthetic seismogram with swarm-like inter-event times and a Gutenberg-Richter distribution of magnitudes with b=1.

Table 4.4 shows that for the first pass, all 200 out of 200 multiplets were correctly identified for a SNR of 1.2 and 0.8, with no misses or false alarms. However, a SNR of 0.4 led to the method identifying 92% (185) multiplets correctly, thus missing 18% and picking up 83 false alarms. To investigate further where the method failed in the first pass for a SNR of 0.4, I observed the points in time where these hits and misses occurred in Figure 4.7.

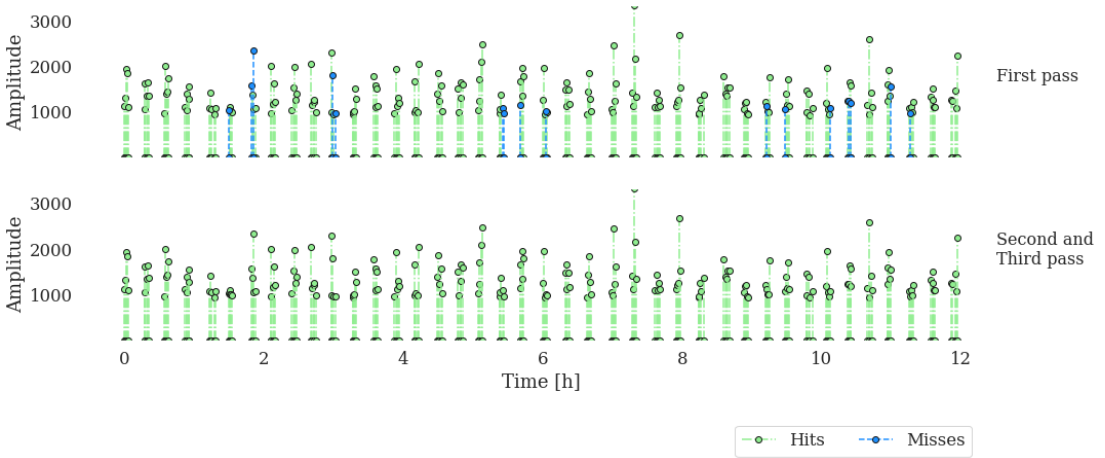

Figure 4.7: Peak amplitudes and times of correctly identified events (hits - green dashed line) and missed events (blue dot-dash line) for the first pass (upper) and second/third pass (lower) of case 3 (swarm-like inter-event times and a Gutenberg-Richter distribution of magnitudes) for a Signal-to-Noise Ratio of 0.4 (d in Figure 4.5).

The upper of Figure 4.7 shows that the first pass failed at different point within different swarms (shown by the missed events, represented by blue dot-dashed lines), rather than say one particular swarm. This indicates that this is again due to the incorrect picking of false alarms over the correct events, and therefore that the method does not deal well with overlapping events for the first pass. The introduction of cross-correlation in the second pass meant that all 200 multiplets were then correctly identified, with no misses or false alarms, as shown in the lower of Figure 4.7. The second and third pass are shown together in the lower of Figure 4.7 as they had the same result.

In summary, Tables 4.2 - 4.4 and the lower of Figures 4.2, 4.4 and 4.7, collectively show that all 200 input (identical) synthetic multiplets were found by the third pass, with no false alarms, in all inter-event time and magnitude distributions tested, for a seismogram sampled at 100Hz. The improvement that the cross-correlation technique has in the second pass for picking an accurate master trace which directly then enables the third pass to detect all events is clear, and in one case the accuracy gets worse in the second pass before it gets better in the third pass. This does not imply that the method is infallible in all cases, but these tests provide a strong benchmark for building confidence in the method at realistic signal-to-noise ratios.

4.2 Effect of different sampling rates

The high sampling rates tested so far can result in significant computation time being required to make the tests. Hence, to see if computation time could be speeded up, I tested the multiplet matching method on different sampling rates. Although using lower sampling rates would be faster computationally, it can also impact the quality of the data. The synthetic seismograms tested in section 4.1 were sampled at 100Hz. Here, I tested this method on the same seismograms, but downsampled to 20Hz to test the method on seismograms of a lower quality. An example of how this changes the quality of the data is illustrated in Figure 4.8, which shows an event sampled at 100Hz (top), 20Hz (middle), and also 10Hz (lower) in a setting with a SNR of 0.4 (therefore a noisy environment).

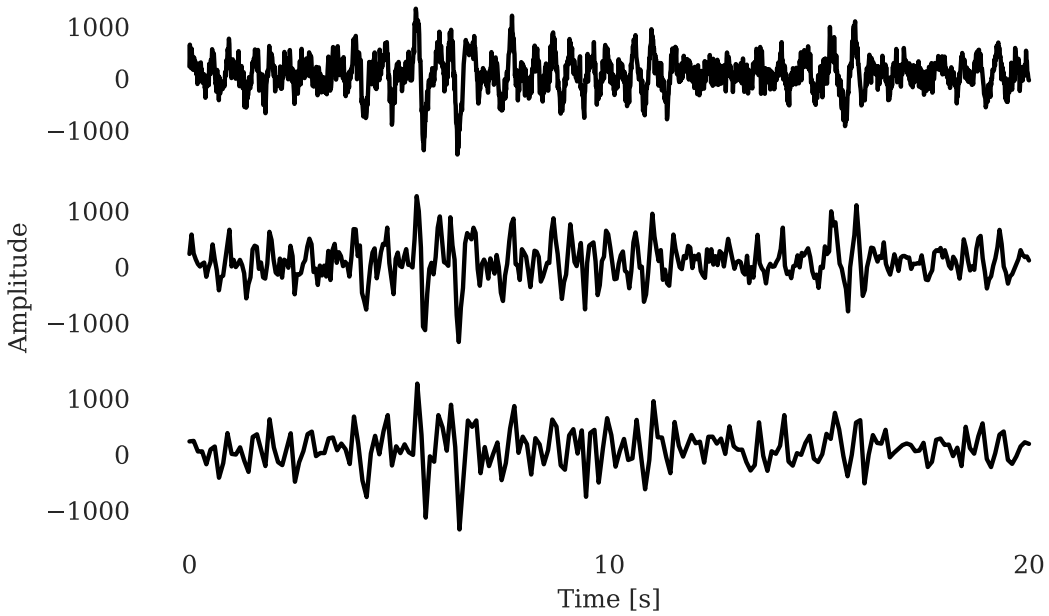

Figure 4.8: Comparison of event signal with a sampling rate of 100Hz (top), 20Hz (middle) and 10Hz (bottom).

The success rate for case 1 (Poisson distributed inter-event times and a Gutenberg-Richter distribution of magnitudes), using the seismograms shown in Figure 4.1 but downsampled to 20Hz, is displayed in Table 4.5.

Pass	**Success**	**SNR 1.2**	**SNR 0.8**	**SNR 0.4**
First pass	Hits	181	187	143
	Misses	19	13	57
	False alarms	17	12	38
Second pass	Hits	200	200	199
	Misses	0	0	1
	False alarms	0	0	0
Third pass	Hits	200	200	200
	Misses	0	0	0
	False alarms	0	0	0

Table 4.5: Case 1 - Success rate for different Signal-to-Noise Ratios (SNRs) for each pass of the multiplet matching method on downsampled seismograms of 20Hz with Poisson distributed inter-event times and a Gutenberg-Richter distribution of magnitudes with an exponent b=1.

Comparing Table 4.2 to Table 4.5 shows that there were only minor differences between success rates in this case. Noticeably, the downsampled seismogram required a third pass in order to successfully identify all 200 multiplets when the SNR was 0.4.

Next, the success rate for case 2 (accelerating event rate and a Gutenberg-Richter distribution of magnitudes that are accelerating with respect to time), evaluated by downsampling Figure 4.3 to 20Hz, is displayed in Table 4.6.

Pass	Success	SNR 1.2	SNR 0.8	SNR 0.4
First pass	Hits	192	189	179
	Misses	8	11	21
	False alarms	0	2	107
Second pass	Hits	195	197	93
	Misses	5	3	107
	False alarms	0	0	0
Third pass	Hits	200	200	200
	Misses	0	0	0
	False alarms	0	0	0

Table 4.6: Case 2 - Success rate for different Signal-to-Noise Ratios (SNRs) for each pass of the multiplet matching method on downsampled seismograms of 20Hz with an accelerating event rate and a Gutenberg-Richter distribution of magnitudes (accelerating with respect to time).

Comparing Table 4.3 to Table 4.6 again shows that there were only minor differences between success rate. However, the third pass was essential for all SNRs to successfully identify all 200 multiplets in the downsampled seismogram, whereas in the 100Hz seismogram, all 200 multiplets were found from the second pass for SNRs of 1.2 and 0.8.

Finally, the success rate for case 3 (40 swarms each containing 5 events, and a Gutenberg-Richter distribution of magnitudes), using the seismograms of Figure 4.5 downsampled to 20Hz, is displayed in Table 4.7.

Pass	**Success**	**SNR 1.2**	**SNR 0.8**	**SNR 0.4**
First pass	Hits	200	200	184
	Misses	0	0	16
	False alarms	0	0	122
Second pass	Hits	200	200	193
	Misses	0	0	7
	False alarms	0	0	0
Third pass	Hits	200	200	200
	Misses	0	0	0
	False alarms	0	0	0

Table 4.7: Case 3 - Success rate for different Signal-to-Noise Ratios (SNRs) for each pass of the multiplet matching method on downsampled seismograms of 20Hz with swarm-like inter-event times (40 swarms each containing 5 events) and a Gutenberg-Richter distribution of magnitudes.

Comparing Table 4.4 to Table 4.7 shows only minor differences between success rate. In the higher quality 100Hz seismograms, all events were found from the first or second pass, however in the downsampled 20Hz seismograms, the second or third pass were needed in order to correctly identify all 200 multiplets.

The computation time in the multiplet matching method decreased from 92 seconds to 22 seconds when using the lower sample rate of 20Hz. This is as expected as the computational time increases linearly with respect to the number of data points. This result is promising, as alongside a decrease in computation time, all events were still found by the third pass.

Testing the limits of the method was an important step to explore the balance between computation time and seismogram quality. To investigate this further, I tested

downsampling the same seismograms to the lower sampling rate of 10Hz, as shown in Tables 4.8 - 4.10 below. Downsampling the data to 10Hz decreased the computational time marginally to 21 seconds.

Pass	**Success**	**SNR 1.2**	**SNR 0.8**	**SNR 0.4**
First pass	Hits	183	186	153
	Misses	17	14	47
	False alarms	15	12	41
Second pass	Hits	200	200	197
	Misses	0	0	3
	False alarms	0	0	0
Third pass	Hits	200	200	196
	Misses	0	0	4
	False alarms	0	0	0

Table 4.8: Case 1 - Success rate for different Signal-to-Noise Ratios (SNRs) for each pass of the multiplet matching method on downsampled seismograms of 10Hz, with Poisson distributed inter-event times and a Gutenberg-Richter distribution of magnitudes.

Pass	**Success**	**SNR 1.2**	**SNR 0.8**	**SNR 0.4**
First pass	Hits	191	189	179
	Misses	9	11	21
	False alarms	0	2	129
Second pass	Hits	187	182	2
	Misses	13	18	198
	False alarms	0	0	0
Third pass	Hits	200	200	164
	Misses	0	0	36
	False alarms	0	0	0

Table 4.9: Case 2 - Success rate for different Signal-to-Noise Ratios (SNRs) for each pass of the multiplet matching method on downsampled seismograms of 10Hz, with an accelerating event rate and a Gutenberg-Richter distribution of magnitudes that are accelerating with respect to time.

Pass	Success	SNR 1.2	SNR 0.8	SNR 0.4
First pass	Hits	200	200	187
	Misses	0	0	13
	False alarms	0	0	147
Second pass	Hits	200	200	191
	Misses	0	0	9
	False alarms	0	0	0
Third pass	Hits	200	200	198
	Misses	0	0	2
	False alarms	0	0	0

Table 4.10: Case 3 - Success rate for different Signal-to-Noise Ratios (SNRs) for each pass of the multiplet matching method on downsampled seismograms of 10Hz, with swarm-like inter-event times and a Gutenberg-Richter distribution of magnitudes that are accelerating with respect to time.

In this case, Poisson distributed inter-event times (case 1) resulted in 2% of events being missed (98% success) after the third pass for the SNR of 0.4. For swarm-like inter-event times, 18% were missed (82% success) and for accelerating times, 1% events were missed (99%), by the third pass in the noisiest setting of SNR 0.4. In contrast there were no false alarms in the second or third passes. For the SNRs of 1.2 and 0.8, 100% of events were found successfully by the third pass in all cases.

Downsampling signal data can cause distortion in the waveform (aliasing) if the frequencies of interest are above the Nyquist frequency. The Nyquist frequency is the maximum frequency before aliasing, according to the Nyquist-Shannon sampling theorem which says the sampling rate must be at least twice the maximum frequency of the signal of interest (Nyquist, 1928; Shannon, 1998). The original event signal used in the synthetic seismograms (Figure 3.5) was sampled at 100Hz, therefore a Nyquist

frequency of 50Hz. From observing the spectrogram of the event signal, the frequencies of interest can then be selected, as illustrated in Figure 4.9.

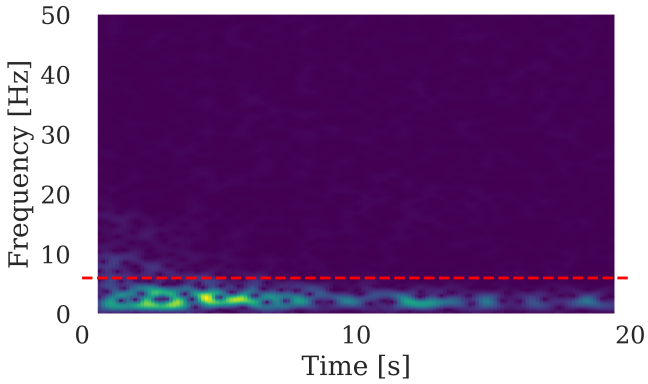

Figure 4.9: Spectrogram of the original event signal, with the red dashed line showing the maximum frequency of interest.

The frequencies of interest (defined by the spectrum of the original template seismogram) are mostly within 6Hz (as shown by the red dashed line in Figure 4.9), thus the sampling rate must be at least 12Hz to satisfy the Nyquist-Shannon sampling theorem. As the signal is downsampled in integer increments, it is possible to downsample the signal to 20Hz, hence the downsampled signal will have a Nyquist frequency of 10Hz. Therefore, as the Nyquist frequency is above the frequencies of interest the waveforms should be retrieved accurately, and there should be an associated reduction in computation time compared to a higher sampling rate.

4.3 Event threshold sensitivity

As discussed in section 3.2.4, an event is defined when the cross-correlation value exceeds a threshold. The importance of setting this threshold is demonstrated in one of the missed events from the 10Hz dataset tested in section 4.2, compared to the other sampling rates where it had been correctly identified, in Figure 4.10.

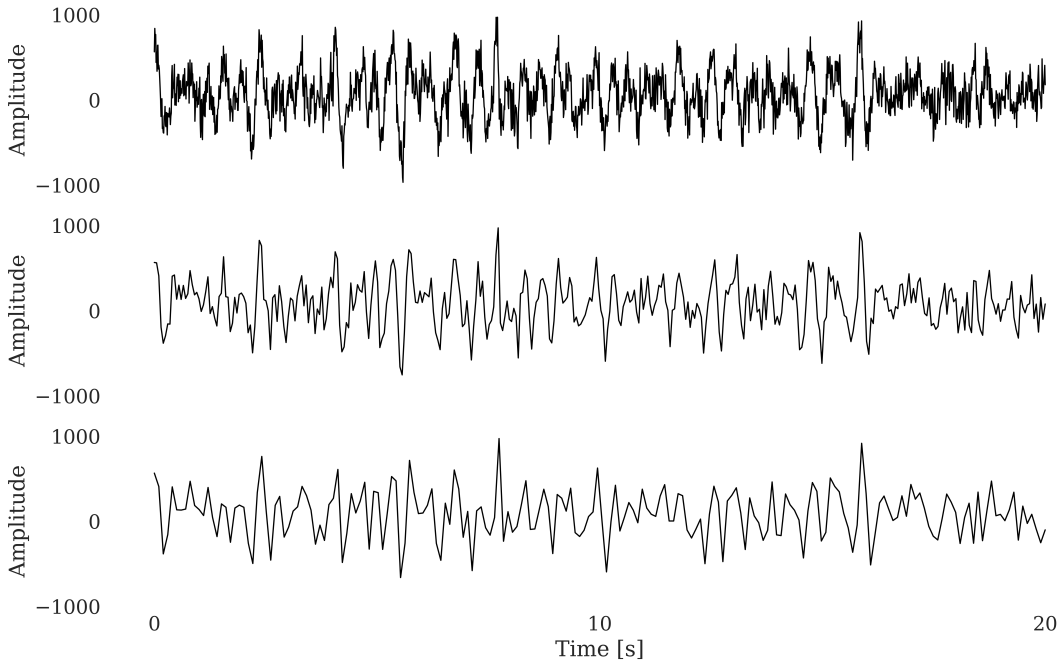

Figure 4.10: Comparison of event signal with a sampling rate of 100Hz (upper), 20Hz (middle) and 10Hz (lower). The event was not detected with the multiplet matching method in the 10Hz dataset.

It is clear in Figure 4.10 that some aliasing has taken place within the peaks and troughs of the 10Hz waveform as these parts require sampling above the Nyquist frequency. The low sampling rate has filtered out some key features which are needed for successful cross-correlation based on similarities between waveforms. This can also be observed in the spectrograms of the event with the different sampling rates from Figure 4.10, in Figure 4.11.

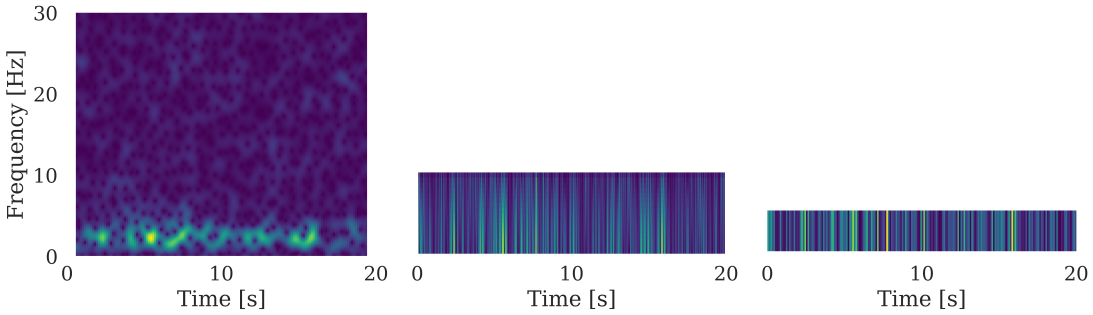

Figure 4.11: Comparison of the spectrograms for the event signal when sampled at 100Hz (left), 20Hz (middle) and 10Hz (right). The event was not detected with the multiplet matching method in the 10Hz dataset.

The cross-correlation function around this event in the 10Hz dataset is shown in Figure 4.12, where the red lines show different thresholds. This event, annotated as A, was 0.03 below the cross-correlation threshold shown by the red solid line of 8 times the Median Absolute Deviation (MAD), which is why it was not detected as an event at this point. This is compared to another event, annotated as B in Figure 4.12, which was successfully detected with the initial threshold.

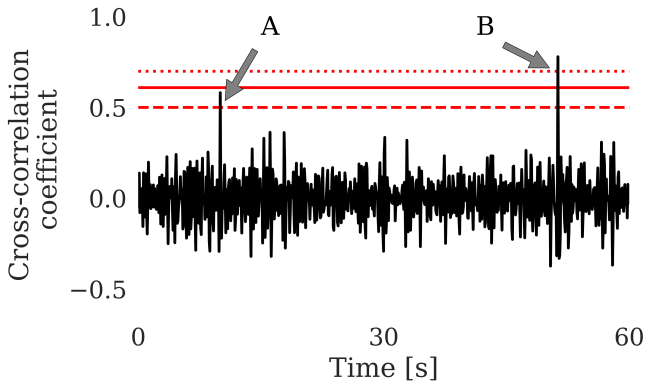

Figure 4.12: Section of cross-correlation of template trace with signal, to show a missed event (annotated as A) not passing the cross-correlation threshold level if set at 8 times the Median Absolute Deviation (MAD), shown by the red solid line. This is compared to the threshold level of 0.5 (red dashed line), 0.7 (red dotted line), and another event (B) which passed all tested thresholds.

As discussed in section 3.3, I chose 8 times the MAD as a threshold (red solid line in Figure 4.12), as this is a quantity that takes into account the general correlation trend of the data to isolate those which are significantly different. This is compared with a more inclusive cross-correlation threshold of 0.5 (red dashed line in Figure 4.12), as some datasets have many highly similar events, and can produce very large threshold values based on the MAD alone, as demonstrated in Figure 4.12. This is the non-general case, as most times the threshold of 8 times the MAD will be sufficient. To ensure that similar events will not be missed in all cases, the cross-correlation threshold is set to the lower of a cross-correlation value of 0.5, or 8 times the MAD. With the updated threshold of 0.5, event A in Figure 4.12 would be deemed a multiplet by the method, despite the waveform degradation.

It is important to find a balance in this threshold. If the similarity is too high, more misses could be obtained in the final catalogue due to small variations in the waveform translating to larger differences in the cross-correlation coefficient, which

are subsequently not above threshold level. If the application requires extremely high similarity events to be found, a higher threshold can be selected, for example to only accept events above a cross-correlation coefficient of 0.7 (dotted line on Figure 4.12).

4.4 Multiple families of multiplets

The performance tests described so far in this chapter have used a single multiplet that repeated in synthetic seismograms. In real datasets however, there could be several different types of multiplets from different families that correspond to different processes occurring at different places.

The tests performed here present a situation where the propagation path of the waveforms did not differ by more than one-quarter of a wavelength (Geller and Mueller, 1980), thus were sufficiently similar to one another. Grouping multiplets into families can be a subjective choice, similar to how the cross-correlation threshold is chosen (section 3.2.4), as it is again based on a threshold value.

The multiplet matching method focuses on events which have at least a cross-correlation value of 0.5 as this is the appropriate level to be considered as moderately correlated (Mukaka, 2012). I chose to concentrate on the most dominant family of multiplets which were moderately correlated to one another to attribute their occurrence to a limited set of processes and locations. However it is certainly possible to expand this testing to examine all families in future work.

4.5 Performance test summary

The accuracy of the multiplet matching method for finding the dominant family of multiplets from synthetic seismograms under various conditions has been tested successfully for a number of realistic scenarios.

The failure in reliable event detection associated with the overlapping events was observed during the z-detect picking method in the first pass of the performance tests shown here. This highlighted a weakness in the multiplet matching method with how overlapping events are detected. This could be an issue when dealing with real events, as events could appear to be overlapping in time when examined on a seismometer. The multiplet matching method removes events within an overlap region to avoid multiple detections of the same event, as their occurrence could lead to bias in event catalogues. As a false alarm is considerably more misleading than a missed event in this case, I chose to keep this preferential removal of overlapping events within the multiplet matching method, however it is considered as a limitation and a current weakness to the workflow.

The performance tests also showed that different sampling rates and the sensitivity of the event detection threshold both have an influence on identifying a multiplet accurately. The results provide guidance for setting such sampling rates and detection thresholds that can be used with confidence in detecting multiplets in real seismograms before band-pass filtering to isolate the frequencies of interest. These frequency bands will be chosen from observing several of the spectrograms of known events in each sequence. The next chapter applies the method on real datasets to look at the occurrence of multiplets for different types of catastrophic failure sequences.

Chapter 5

Applications to earthquakes prior to a large mainshock

5.1 Introduction

In the previous chapters, I presented a new cross-correlation method (chapter 3) to find multiplets and then performed a series of performance tests (chapter 4) to assess its reliability.

In this chapter, I demonstrate the application of the multiplet matching method, combined with further statistical analysis, to two significant earthquake sequences, the 2004 M_W 6 Parkfield, USA earthquake and the 2014 M_W 8.2 Iquique, Chile earthquake. The overall aim is to demonstrate the utility of the multiplet matching technique, and then to examine whether the new catalogue is an improvement on pre-existing earthquake catalogues around the times of these events, and whether the results provide any new insights into the processes associated with such events. I will also examine the extent of the improvements via analysis of the time series of events, and statistical properties such as the frequency-magnitude relation, inter-event time distributions, and the temporal evolution of multiplets with respect to the mainshock.

5.2 Parkfield

5.2.1 Introduction

The Parkfield sequence was chosen for this first analysis as it is a well examined seismically active area between a creeping and locked segment of the San Andreas fault in California (Peng and Zhao, 2009). This area is key to a long-term earthquake research project for the purpose of better understanding the physics of earthquakes (Hickman and Langbein, 2004). Several $M \approx 6$ earthquakes have occurred with an average interval of 22 years between 1857 and 1966 in this area (Bakun and Lindh, 1985). Due to the characteristic nature of these earthquakes, there were predictions that the next earthquake of a similar magnitude would occur by 1993, thus several measuring instruments were deployed to capture the predicted future earthquake (Bakun and McEvilly, 1984; Bakun and Lindh, 1985). In 1987, the USGS installed 18 stations as part of a permanent seismic network within 25km of Parkfield (Bakun et al., 1987).

The next large earthquake occurred in Parkfield at 17:15 UTC on 28th September 2004 at a depth of 8km, with a M_W 6.0 event, which was well recorded by these stations. This earthquake was associated with several other smaller earthquakes occurring in the same area. Therefore, I chose to start this catalogue on the 20th September 2004, as this is when the rate of M>0 earthquakes increased from <2 to >3 per day in this region, and to end the time window examined on 29th September 2004, so as to include a representative number of the aftershocks from the M_W 6.0 event. The locations of the earthquakes from the USGS catalogue for this time period are shown in Figure 5.1, where the colour of the dots denotes the time and the size corresponds to magnitude.

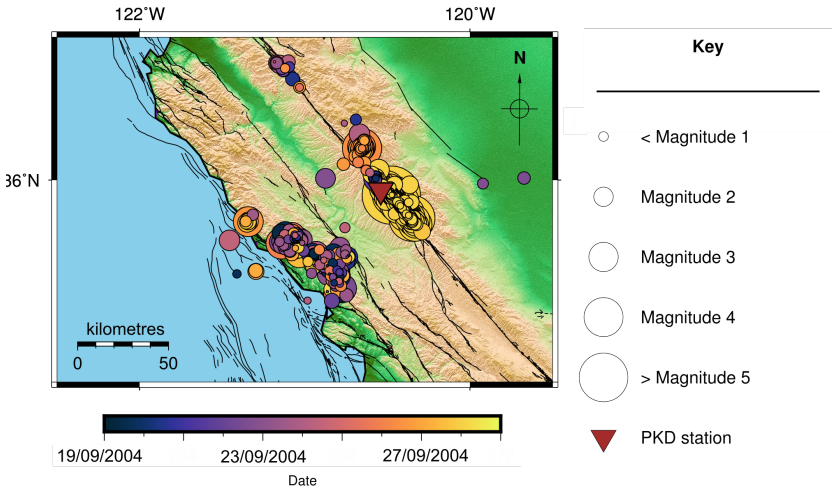

Figure 5.1: Illustration of the locations of the 561 earthquake events in the USGS catalogue for the M_W 6.0 earthquake sequence in Parkfield, USA from 20th - 29th September 2004. The M_W 6.0 earthquake occurred at 17:15 UTC on 28th September 2004. The location of the seismic station used in this analysis is shown by the brown triangle.

I downloaded waveform data for this time period from the Berkeley Seismology Lab's Bear Valley Ranch seismometer (station PKD, shown in Figure 5.1 as a brown triangle) from the Incorporated Research Institutions for Seismology (IRIS). I chose this particular broadband station as it was openly available, and close to both the small earthquakes leading up to the mainshock, and the mainshock itself. Next, I observed the spectrograms of known earthquake events in this catalogue, and as they were <14Hz, I band-pass filtered between 1Hz and 14Hz to and downsampled the data to 40Hz.

The seismogram for this chosen earthquake sequence is illustrated in Figure 5.2, with the y-axis clipped at a velocity of $\pm 10^{-4}$ m/s to better show the smaller seismic signals prior to the mainshock, whose arrival time is shown by a red vertical dashed line.

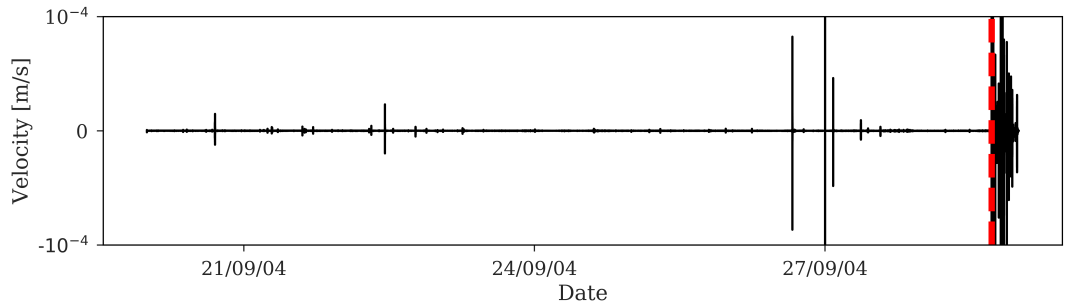

Figure 5.2: Illustration of the M6.0 earthquake sequence in Parkfield, USA from 20th - 29th September 2004, with the mainshock occurring at 17:15 UTC on 28th September 2004, denoted by the vertical red dashed line. This illustration has been clipped at $\pm 10^{-4}$ m/s in order to better show the smaller signals in this sequence.

5.2.2 Method

The USGS catalogue contained a total of 561 events in this time period for this region, as was shown in Figure 5.1. All 24 local earthquakes above M 2.7 associated with this M 6.0 event, as well as the M 6.0 event itself, were used as templates for finding more earthquakes with the multiplet matching method (described in section 3.3). The runtime of the method on this dataset was approximately 6 hours on the supercomputer.

The threshold of M 2.7 was chosen as a minimum where local events could be clearly distinguished in the examined signal above the background noise. Events below this threshold were more difficult to identify as they may have occurred further from the station of choice, in which case the template would not have been as clear. I chose a 15-second window for the template waveforms, as this contained the main characteristics of the templates.

Four of the template events used from the USGS catalogue are illustrated in Figure 5.3, with a green box indicating the window used to define the template window.

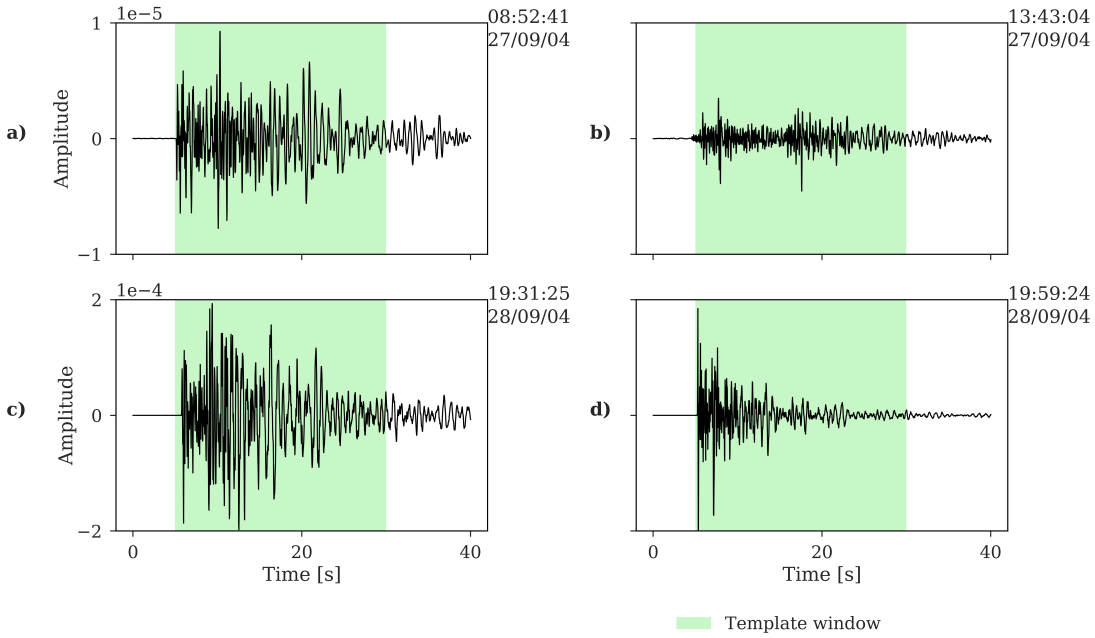

Figure 5.3: Illustration four different templates used in examining the M6.0 earthquake sequence in Parkfield, USA from 20th - 29th September 2004. The UTC start-time and the date of each template is displayed in the upper right of each window. These templates show two events which occurred prior to the mainshock (17:15 UTC on 28th September 2004), and two after. These were identified in the USGS catalogue, and adjusted in time to when they appeared on the seismometer used.

The earthquake events in Figure 5.3a and Figure 5.3b occurred prior to the mainshock, and both had a M_d=2.84 in the USGS catalogue. The events in Figure 5.3c and Figure 5.3d both occurred in the time after the mainshock, and had M_d=4.02 and M_d=3.19 in the USGS catalogue, respectively.

For this earthquake sequence, I will compare the multiplet matching and USGS catalogues to two other catalogues published by Thurber et al. (2006) and Peng and Zhao (2009). The multiplet matching catalogue will contain the template events from the USGS catalogue if they successfully found multiplets. If no multiplets were found from a template, this event was removed from the multiplet matching catalogue. Thus

the multiplet matching catalogue will only contain events which are multiplets. The USGS catalogue is determined by standard phase picking methods, whereas the Thurber et al. (2006) catalogue records only high-quality waveforms from standard picking methods, and Peng and Zhao (2009) catalogue uses template matching techniques.

The Thurber et al. (2006) catalogue contained many events between 1984 - 2005, 259 of whom occurred in the time period used in this chapter. The events for this time period are compiled from the picked events from the Northern California Earthquake Data Center (NCEDC) archive (which is a subsidiary of the USGS and the Berkely Seismological Laboratory), and the Parkfield Area Seismic Observatory (PASO) array. As this catalogue was for the purpose of relocating events, they were filtered based on locations. The events had to occur on at least 8 stations, and interevent distances were to be between 0.5 and 15 km so that differential times were easier to resolve. This meant that the Thurber et al. (2006) catalogue only contained events with high-quality waveforms, and so is not as complete as the USGS catalogue alone. Herein, the Thurber et al. (2006) catalogue will be referred to as the 'standard' catalogue, as the events are originally found through conventional techniques.

The Peng and Zhao (2009) catalogue uses the full catalogue of Thurber et al. (2006) from 1984 - 2005 as a starting point, and then applies template matching through three-day continuous recordings from 28th - 30th September 2004, to detect many additional events, which are predominantly aftershocks of the M6.0 mainshock. From cutting this to the same period as the other catalogues, the Peng and Zhao (2009) catalogue contained 2,769 events, however it should be noted that this method will contain events found from templates outwith the time period studied here. The method used in Peng and Zhao (2009) requires that the template event used in each template matching iteration, be recorded on at least four out of the 13 stations in the region, with a minimum Signal-to-Noise Ratio of five to ensure that the template was clear. This resulted in many new events being discovered, which were classified as a detection when the cross-correlation amplitude between each template and the seismogram exceeded

nine times that of the MAD of the mean cross-correlation trace for each template event. Herein, the Peng and Zhao (2009) catalogue will be called the 'template matching' catalogue, to distinguish it from the 'multiplet matching' catalogue determined in this thesis.

The multiplet matching catalogue initially detected 4,428 events, from 21 of the templates chosen from the USGS catalogue, with a detection threshold of eight times the MAD of the cross-correlation coefficient. Three of the templates did not detect any similar events in this sequence. The locations of the template events which did find multiplets are shown in Figure 5.4, where the size of the dots corresponds to the magnitude of the event, and the colour shows the time of the event (different scale to Figure 5.1).

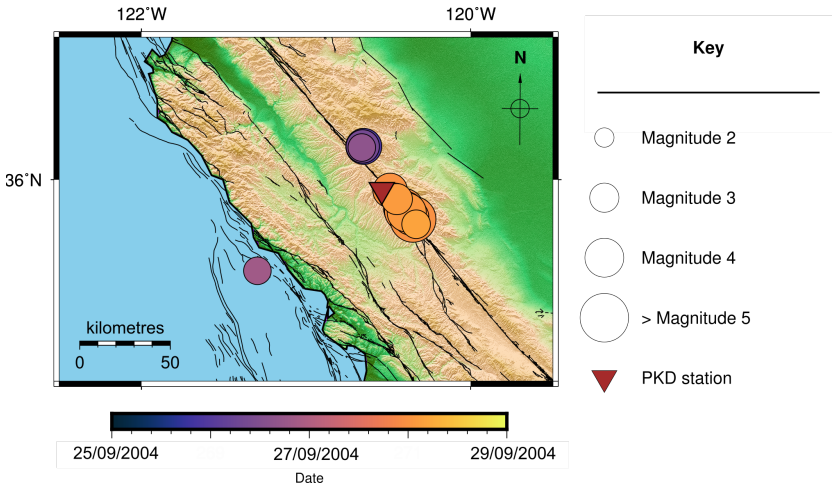

Figure 5.4: Illustration of the locations of the 21 template earthquake events in the USGS catalogue for the M_W 6.0 earthquake sequence in Parkfield, USA from 20th - 29th September 2004. The location of the seismic station used in this analysis is shown by the brown triangle.

Many of the multiplets found from the templates were either duplicates (where two different templates pick up the same similar event), or they overlapped in some way, so

an additional 'cleaning' step was introduced to remove all events within 30 seconds of each other, resulting in 1,913 unique multiplets, including the 21 templates. This has the risk of ignoring several events which would be close together (particularly in the aftershocks sequence), representing a pragmatic optimum that avoided any bias in too large a catalogue from multiple detections of single events.

As a comparison between these catalogues, the multiplet matching catalogue contained 376 events which were also in the template matching catalogue, 191 in the standard catalogue, and 326 in the USGS catalogue, as shown in Table 5.1. The other 235 events from the USGS catalogue were not detected by the multiplet matching method, indicating that these 235 events were either dissimilar and/or within the overlap range. The multiplet matching method also missed some events present in the other catalogues due to a combination of the finite threshold amplitude for the templates, or events that were too dissimilar to the templates used, as shown by the missing events quantities in Table 5.1. The template matching catalogue is more complete in the aftershock sequence, and contains more events that are close in time than the multiplet matching catalogue due to the finite threshold defined to avoid overlapping events. There were also a number of 'new' events found in the multiplet matching catalogue (i.e. those that are not within the other catalogues), as shown in Table 5.1.

Events	**Multiplet matching**	**USGS**	**Standard**	**Template matching**
Found	1,913	561	259	2,769
Matching	-	326	191	376
Missing	-	235	68	2,393
New	-	1,587	1,722	1,537

Table 5.1: Summary of the found, matching, missing and new events in the multiplet matching, USGS, standard (Thurber et al., 2006) and template matching (Peng and Zhao, 2009) catalogues.

Once the events were identified by the multiplet matching method through visual analysis, they were assigned estimated magnitudes using Equations 3.9 - 3.10, that I will refer to as M^e. The c value in Equation 3.9 was calculated using the data from the events in the USGS catalogue which had a magnitude assigned by conventional methods, i.e. 'M_{new}' was known, and comparing them with the known magnitudes (M_{known} in Equation 3.9). I tested several values of c to find which gave the best estimation of the known magnitude, as illustrated in Figure 3.36 in chapter 3 where I discussed the method. In this example, $c = 0.8$ gave the best estimate of the known magnitudes.

An example of the original and final template events and some newly found multiplets are shown in Figure 5.5.

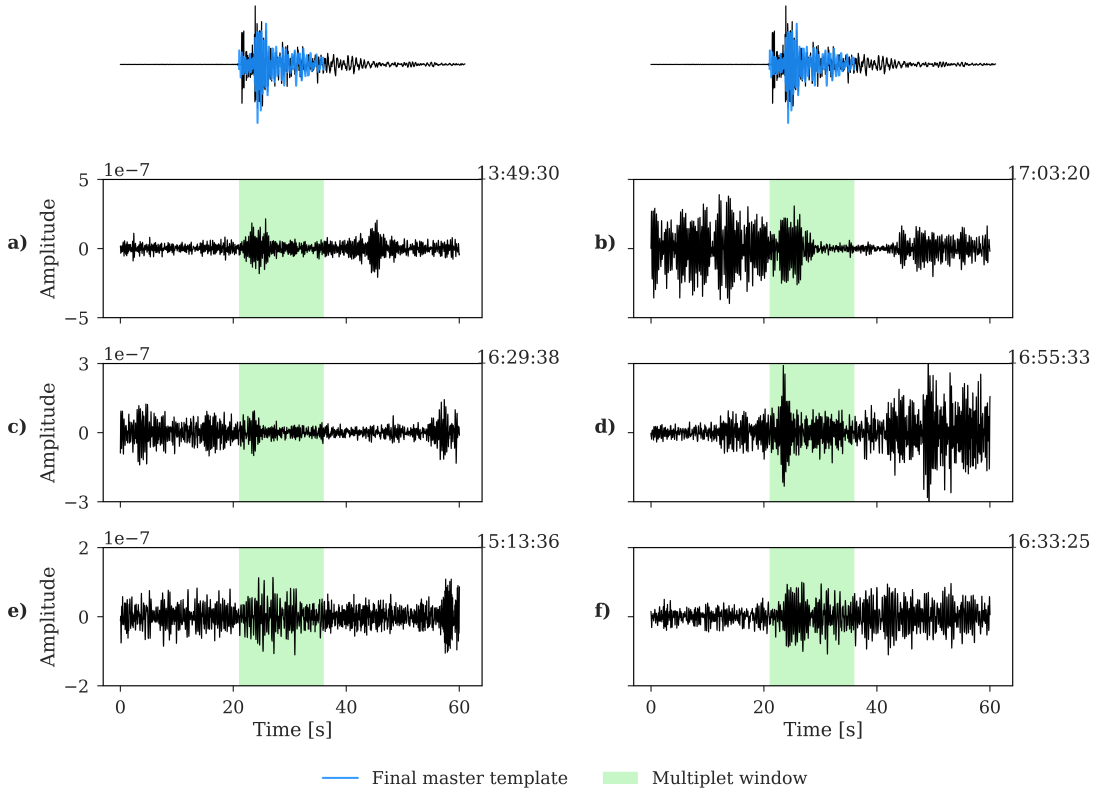

Figure 5.5: Illustration of original template and final master template events (upper) to the newly found multiplets from the multiplet matching method. The horizontal waveforms in a-f are multiplets of one another, and are scaled to the same y-axis. The starting time of each multiplet on 28/09/04 is shown in the upper right of each plot. All the multiplets shown here occurred prior to the mainshock at 17:15, and were found by the template in the upper plots.

In the two upper diagrams, the original template event is compared to the final master template event (blue) used in the multiplet matching method (from Step 7 of section 3.3.1). This template event was recorded as M_d=2.8 in the USGS catalogue, and occurred at 18:45 on 28/09/04, with an epicentre at -120.4°, 35.85° (4.6km from the mainshock epicentre). The multiplets found by the final master template event are shown in Figure 5.5a-f, where the green box indicates the multiplet window, which is

aligned with the upper templates. I chose to show these particular sets of multiplets as the horizontal waveforms are deemed similar to one another as they have a cross-correlation value >0.5.

The multiplet in Figure 5.5a had an estimated M^e=0.81, and another multiplet in Figure 5.5b occurred over three hours later, with an estimated M^e=0.90, with a cross-correlation value between the two seismograms of 0.50. In the second set of multiplets shown in Figures 5.5c and 5.5d, the former had an estimated M^e=0.66 and the latter M^e=0.87, and a cross-correlation value between the two seismograms of 0.57. Finally, the third set of multiplets illustrated in Figures 5.5e and 5.5f had an estimated M^e=1.24 and M^e=0.90, respectively, with a cross-correlation value between the two seismograms of 0.52.

5.2.3 Statistical Analysis

Here, the statistical metrics for the events associated with the Parkfield sequence will be presented and discussed. This will be in the form of time series for the point process, frequency-magnitude distributions, inter-event times, event rate and a temporal view at how the magnitude and inter-event times of the events change with respect to the mainshock. This will be completed to a similar analysis for the USGS, standard, template matching and multiplet matching catalogues. In the relevant figures, these will be denoted by corresponding colours of green, purple, orange and blue, respectively.

First, I show the temporal evolution of the multiplets found by the method in Figure 5.6, denoted by blue circles, with the known events from the USGS catalogue shown in green triangles. The template matching and standard catalogues are also shown by the orange squares and purple diamonds, respectively. The inter-event times in the upper plot of Figure 5.6 are an indication of whether the events are exhibiting any particular

pattern prior to the catastrophic failure. The peak amplitude is shown in the middle as a check on the precision of the magnitudes in the lower plot.

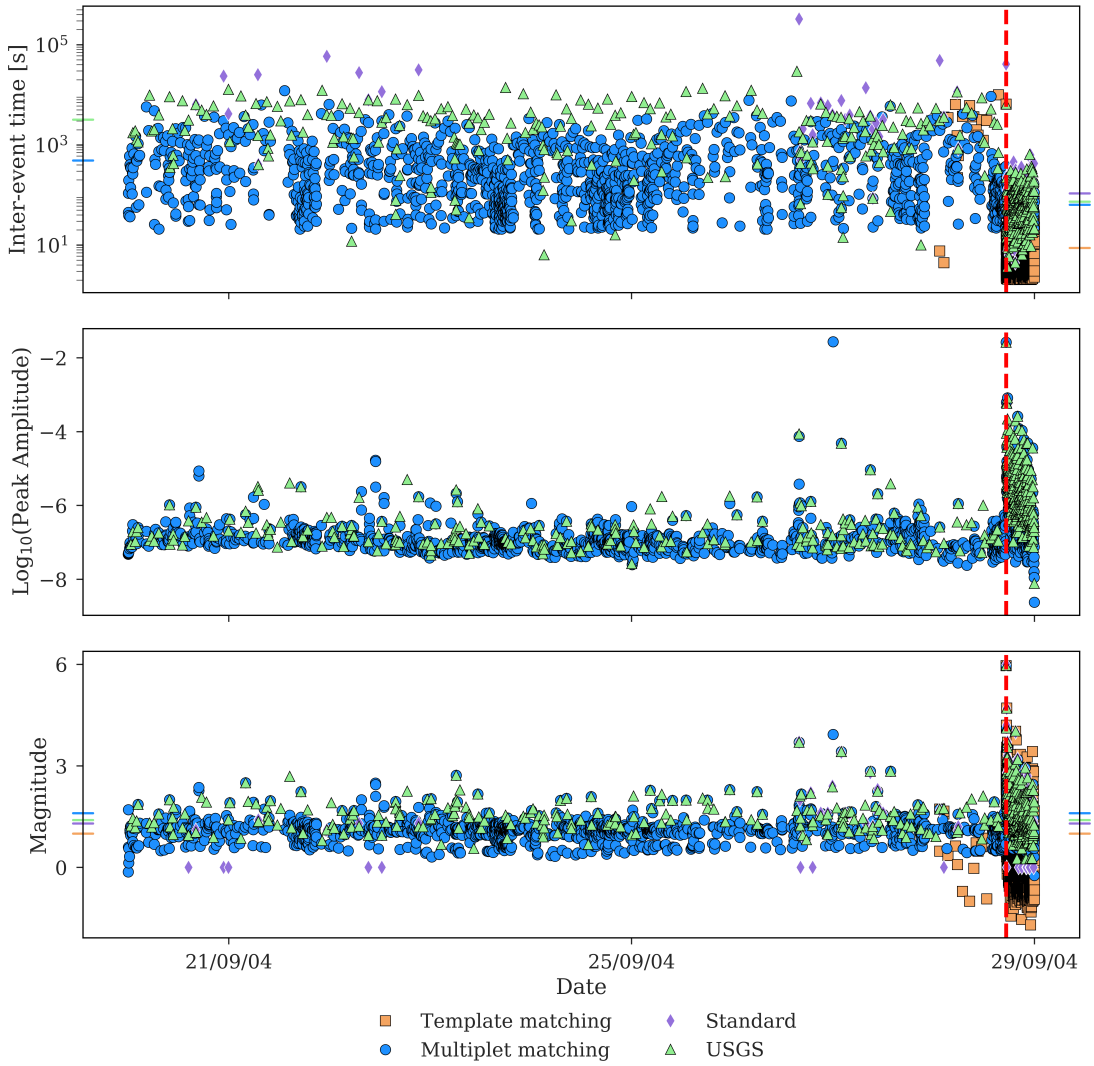

Figure 5.6: Time evolution of the USGS (green triangles), template matching (orange squares), standard catalogues (purple diamonds) and events found by multiplet matching (blue circles), of their inter-event times (upper) amplitudes (middle) and magnitude (lower). The M6.0 earthquake origin time is shown by a red vertical dashed line on both plots. Coloured horizontal tick lines on the two y-axes show average inter-event time (upper), and the magnitude of completeness, M_c, (lower) for before and after the mainshock, per catalogue.

The average inter-event times for before and after the origin time of the mainshock (red vertical dashed line) are shown by the coloured tick marks on the left (before) and right (after) of the upper plot in Figure 5.6, where the colour corresponds to the catalogue. The template matching and standard catalogues did not contain enough events prior to the mainshock to obtain a reliable average inter-event time, therefore the average for these catalogues are only shown for after the mainshock. Prior to the mainshock, the USGS catalogue has a higher average inter-event time than the multiplet matching catalogue because it contains fewer events. The template matching catalogue has the lowest average inter-event time after the mainshock as it contains many aftershocks which are closer together. The three other catalogues have a roughly similar average inter-event time after the mainshock.

The middle plot of Figure 5.6 displays the peak amplitude of the multiplet matching and USGS events. This is used as a check that the magnitudes calculated in the lower plot of Figure 5.6 are accurate, as amplitudes at a given station should be proportional to magnitude for an event from the same location. The lower plot shows the time series for the assigned magnitudes. The M_c for each catalogue is shown by the coloured tick marks on the two y-axes, where the colour represents the catalogue.

Figure 5.6 confirm visually that there are many new events found through the multiplet matching method which have a lower magnitude than the USGS events. The standard catalogue is very sparse, but does contain some lower magnitude events. The template matching catalogue only begins on the day of the mainshock, so does contain many aftershocks. As the template matching catalogue uses many stations, there are many more events picked up within these aftershocks as they have been able to discriminate between events which are close together in time.

To observe the lead-up to catastrophic failure in more detail, a zoomed in version of the twelve hours prior to, and three hours after the M6.0 mainshock, is illustrated in Figure 5.7, following the same protocol as Figure 5.6.

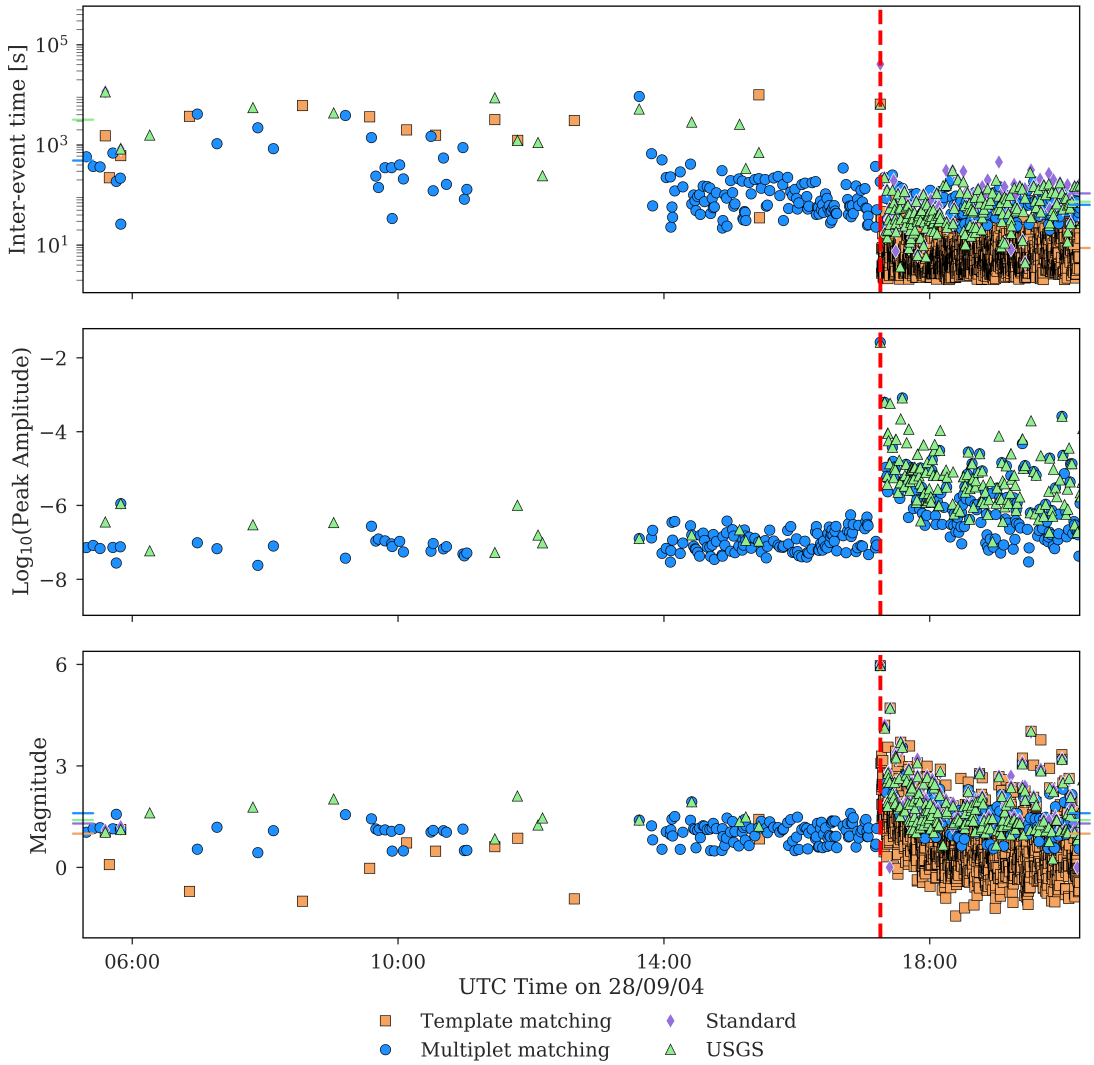

Figure 5.7: Time evolution of USGS (green triangles), template matching (orange squares) and standard catalogues (purple diamonds) and events found by multiplet matching (blue dots), of their inter-event time (top) and magnitude (lower) 12 hours before and three hours after the M6.0 mainshock (vertical red dashed line). Coloured horizontal dashed lines show average inter-event time, and the magnitude of completeness, M_c, for before and after the mainshock, per catalogue.

Figure 5.7 shows that the multiplet matching catalogue had a dramatic increase in events found in the three hours prior to the mainshock, which was not present in the

other catalogues. These low-magnitude events dropped to below the average inter-event time for before the mainshock significantly, and occurred at a stable rate until the M6.0 mainshock. This is an important finding, as it is consistent with the occurrence of a creep event on the fault.

Next, I created a frequency-magnitude distribution of the multiplet matching event catalogue (Figure 5.8a in blue), the USGS catalogue (Figure 5.8b in green), the template matching catalogue (Figure 5.8c in orange), and the standard catalogue (Figure 5.8d in purple).

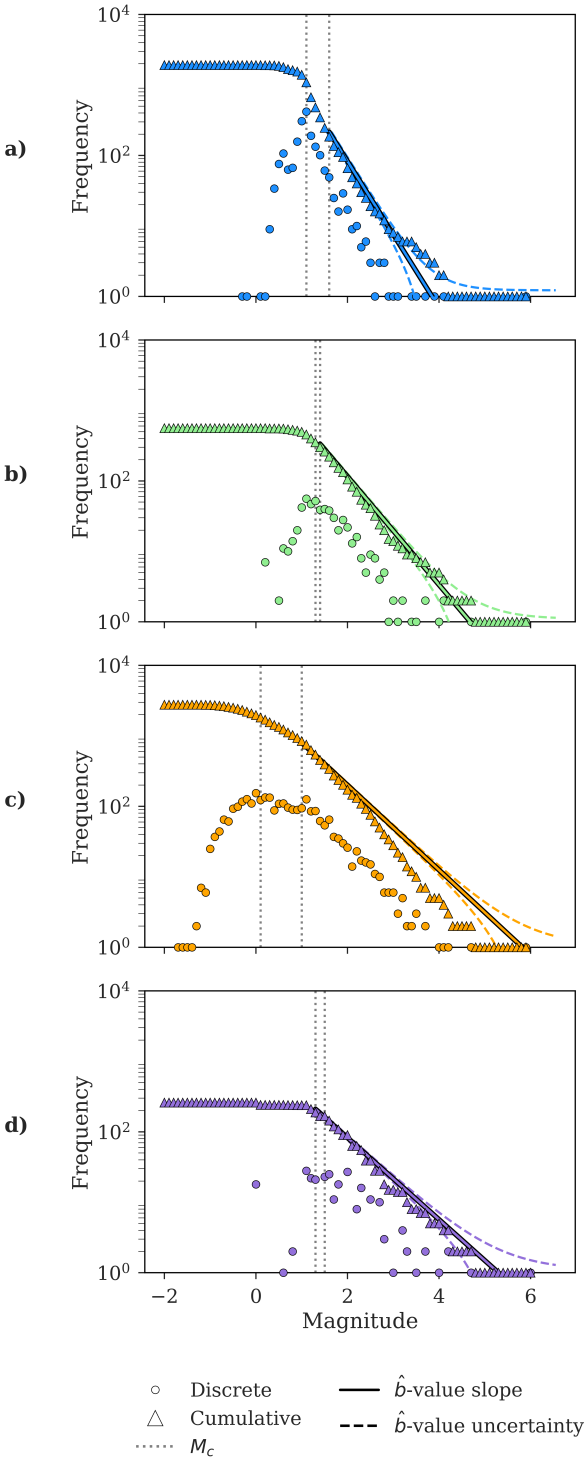

Figure 5.8: Comparison of the frequency-magnitude distributions for events in the multiplet matching (a), USGS (b), template matching (c) and standard (plot d in purple) catalogues. The discrete (filled circles) and cumulative (filled triangles) frequencies are shown for each catalogue. The $\hat{b}$-value corresponding to each catalogue is shown by the filled line, where the colour matches the catalogue, and the dashed lines show the uncertainties on the slope of the line. The grey dotted lines illustrate the different values of M_c calculated.

The grey dotted lines in Figure 5.8 represent the different values for the magnitude of completeness, M_c, which were estimated through the b-value stability (BVS) method and maximum curvature (MaxC) method (section 2.3.1), for each catalogue. These two methods were used as the multiplet matching catalogue (Figure 5.8a) had a sharp peak, and the others (Figures 5.8b-d) had a much broader peak.

The $\hat{b}$-value and its uncertainties estimated from the chosen M_c in MLE method from Equations 2.5 - 2.6, are shown for each catalogue in Figure 5.8, by the solid line on each plot. The dashed lines show the bounds of the uncertainty on the slope of the $\hat{b}$-value.

As discussed in section 2.3.1, the MaxC method calculates the M_c as the maximum curvature of the frequency-magnitude distribution, whereas the BVS method calculates M_c as when the average of the five successive b-values are within one error of the b-value. Plots for the BVS method for the four catalogues are shown in Figure 5.9.

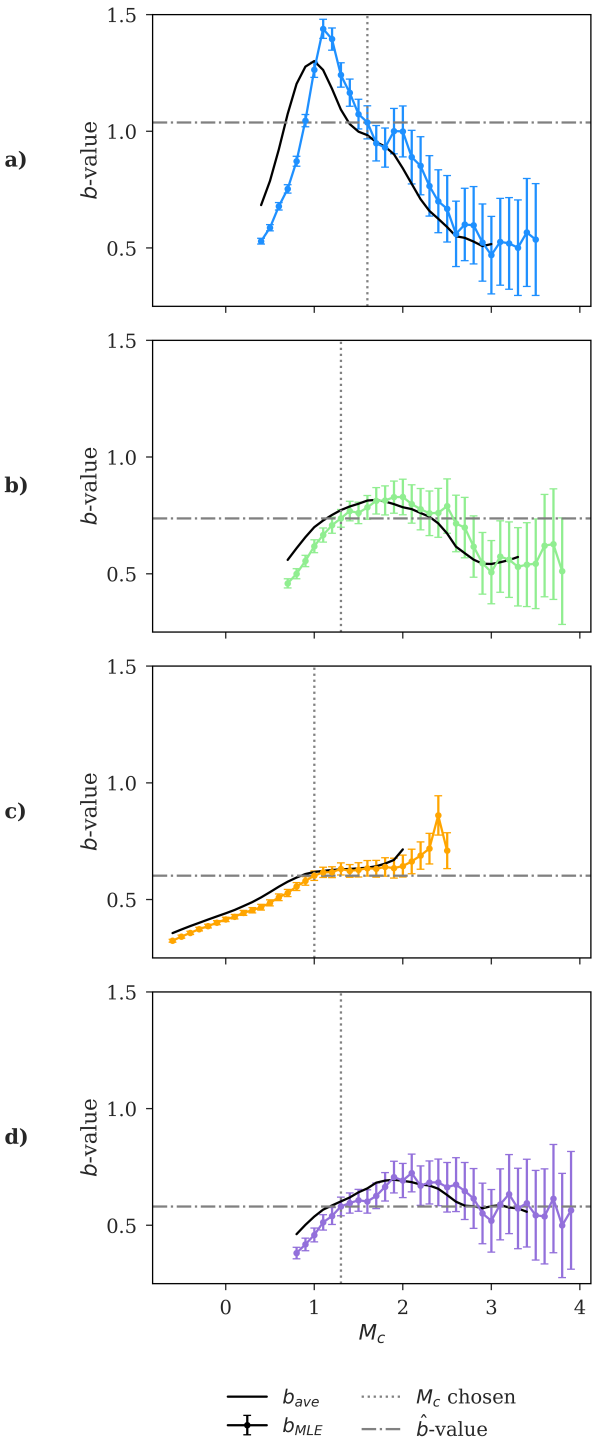

Figure 5.9: Comparison of b-value stability curves, showing the b-values for each magnitude of completeness, M_c, for the multiplet matching (a), USGS (b), template matching (c), and the standard (d) catalogues. The vertical dotted line shows the chosen M_c from this method, and the horizontal dashed line shows the b-value at this point. The M_c is chosen as when the average of the five successive b-values (black line) are within one error of the b-value.

The BVS method shown in Figure 5.9 illustrates how the b-value stabilises when b_{ave} (the average for the next five successive $\hat{b}$-values) lies within the error of the b_{MLE}. At this point, the M_c is chosen, and is shown by the vertical dotted line. The b-value at this M_c is illustrated as the horizontal dot-dashed line.

A summary of the M_c and $\hat{b}$-value results from the discussed methods are shown in Tables 5.2 - 5.5.

	BVS	**MaxC**
M_c	1.6	1.1
$\hat{b}$-value	1.0 ± 0.086	1.4 ± 0.050

Table 5.2: The magnitude of completeness, M_c, for the b-value stability (BVS) and Maximum Curvature (MaxC) methods, and the $\hat{b}$-value plus uncertainty from the MLE (Maximum Likelihood Estimation) method (Equations 2.5-2.6), for the multiplet matching catalogue in Figure 5.8a for each estimate of M_c.

	BVS	**MaxC**
M_c	1.3	1.4
$\hat{b}$-value	0.74 ± 0.037	0.77 ± 0.042

Table 5.3: The M_c calculated from the BVS and MaxC methods, and the $\hat{b}$-value plus uncertainty from the MLE method (Equations 2.5-2.6), for the USGS catalogue in Figure 5.8b for each estimate of M_c.

	BVS	**MaxC**
M_c	1.0	0.10
$\hat{b}$-value	0.60 ± 0.017	0.43 ± 0.0070

Table 5.4: The M_c calculated from the BVS and MaxC methods, and the $\hat{b}$-value plus uncertainty from the MLE method (Equations 2.5-2.6), for the template matching catalogue in Figure 5.8c for each estimate of M_c.

	BVS	**MaxC**
M_c	1.3	1.5
$\hat{b}$-value	0.58 ± 0.037	0.61 ± 0.044

Table 5.5: The M_c calculated from the BVS and MaxC methods, and the $\hat{b}$-value plus uncertainty from the MLE method (Equations 2.5-2.6), for the standard catalogue in Figure 5.8d for each estimate of M_c.

Following the workflow in Figure 2.3 of Roberts et al. (2015), the BVS method is accepted for the multiplet matching catalogue as the M_c's from the BVS and MaxC methods do not agree within ± 0.1, and the error is less than 0.25, resulting in a M_c = 1.6, and a $\hat{b}$-value of 1.0 ± 0.086. The USGS catalogue instead accepts the MaxC method as the best method for calculating the M_c as the M_c's are within 0.1 of each other, hence the M_c = 1.4, with a $\hat{b}$-value calculated as 0.77 ± 0.042. The frequency-magnitude distribution for the template matching catalogue is very broad, therefore the MaxC approach failed, whereas the BVS method calculated M_c = 1.0, with a $\hat{b}$-value of 0.60 ± 0.017. This low $\hat{b}$-value reflects the occurrence of many mid-sized aftershocks in this catalogue. Lastly, the standard catalogue yielded a M_c = 1.3, with a $\hat{b}$-value of 0.58 ± 0.037. These M_c values and $\hat{b}$-values were used to plot the best fit lines and the uncertainty ranges for the frequencies in Figure 5.6 and Figure 5.7.

Although a lower M_c was expected for the multiplet matching catalogue from finding many small-magnitude events, the BVS method chose a higher M_c value and hence a higher $\hat{b}$-value (which is a known caveat of the BVS method (Woessner and Wiemer, 2005; Roberts et al., 2015)). However the multiplet matching and USGS $\hat{b}$-values are typical for a seismically-active area such as Parkfield, where commonly b=1. Furthermore, the template matching and standard catalogues yielded anomalously low $\hat{b}$-values, likely due to differences in productivity for different magnitudes, as for example occurs in the ETAS model (Godano et al., 2014).

The M_c from the multiplet matching method is the highest of the four catalogues because of the amplitude threshold chosen and the use of a single station. However, it still contains important information on new low magnitude events. The reason a higher M_c was chosen was because it is only multiplets, i.e. this catalogue only contains similar waveforms. Events which are not similar to at least one another are not present in this catalogue, hence it is missing out on some of the higher magnitude events, and this is likely why the $\hat{b}$-value is higher. Therefore, a combination of these two catalogues would be the best method for lowering the M_c and having a more complete catalogue in this case. On the other hand, the amplitude ranges for the differences are quite similar (Figure 5.10). Thus, the difference in M_c is likely due to the higher likelihood of event detection when using all stations, some of which will be closer to the source than others.

The M6.0 event and its aftershocks dominate the distribution in Figure 5.8, and hence the $\hat{b}$-values in Tables 5.2 - 5.5. Therefore I also show the same catalogue but with events split into prior to (left), and after (right), the M6.0 mainshock in Figure 5.10, following the same protocol as Figure 5.8. This isolates the seismicity with respect to the time of the mainshock.

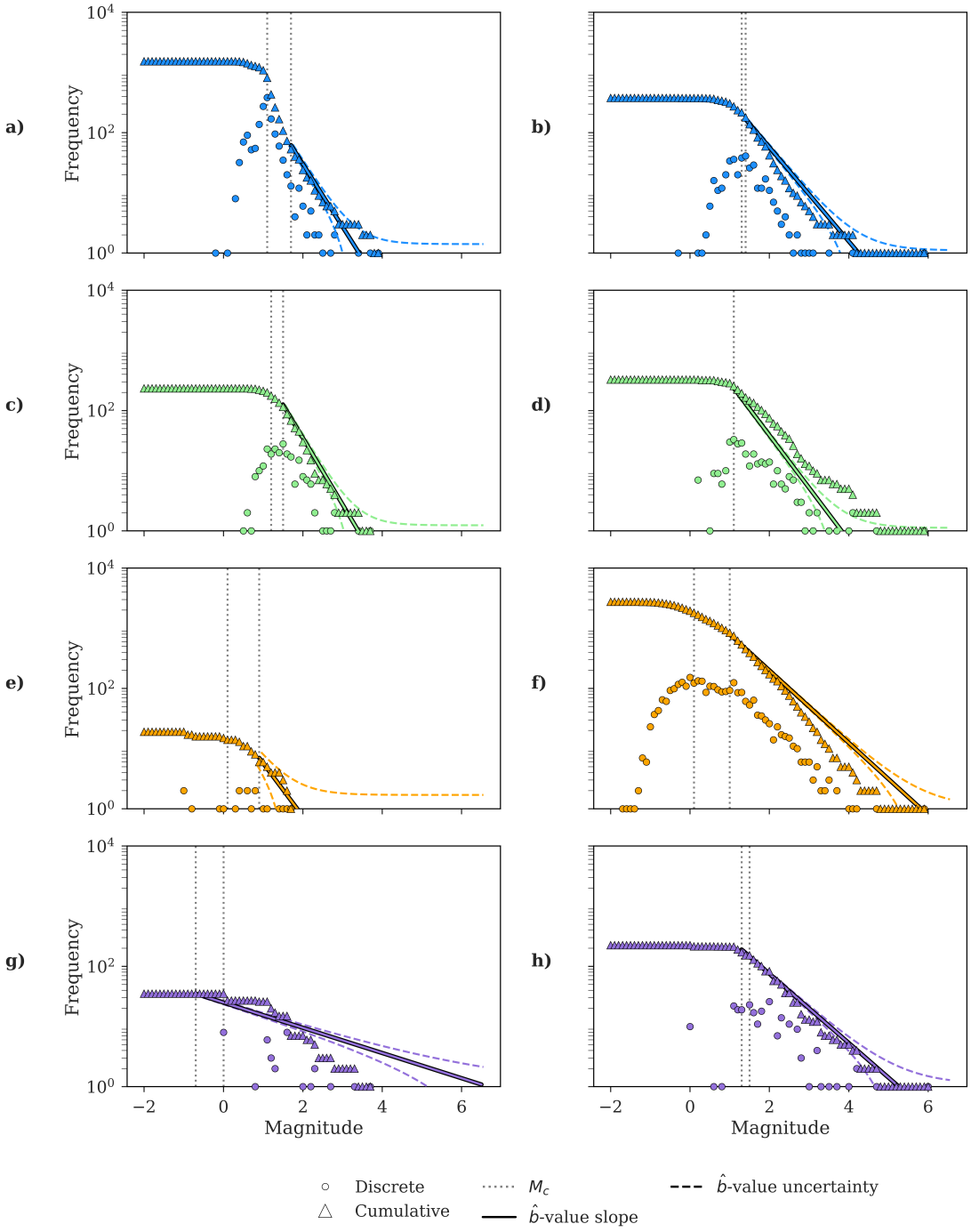

Figure 5.10: Comparison of the multiplet matching (a and b), USGS (c and d), template matching (e and f) and standard (g and h) catalogues discrete (points) and cumulative (lines) frequency-magnitude distributions. These distributions are shown for before the mainshock on the left, and after the mainshock on the right.

The M_c for the separate catalogues in Figure 5.10 for before and after the mainshock were estimated as before with the MaxC and BVS methods (section 2.3.1). These M_c and corresponding b-values are shown in Tables 5.6 - 5.9 for before the M6.0 mainshock, following the same protocol as Figure 5.9.

	BVS	**MaxC**
M_c	1.7	1.1
$\hat{b}$-value	1.0 ± 0.15	1.9 ± 0.076

Table 5.6: The magnitude of completeness, M_c, for the b-value stability (BVS) and Maximum Curvature (MaxC) methods, and the $\hat{b}$-value plus uncertainty from the MLE (Maximum Likelihood Estimation) method (Equations 2.5-2.6), for the multiplet matching catalogue in Figure 5.10a for each estimate of M_c, before the mainshock.

	BVS	**MaxC**
M_c	1.5	1.2
$\hat{b}$-value	1.1 ± 0.093	0.87 ± 0.050

Table 5.7: The M_c calculated from the BVS and MaxC methods, and the $\hat{b}$-value plus uncertainty from the MLE method (Equations 2.5-2.6), for the USGS catalogue in Figure 5.10c for each estimate of M_c, before the mainshock.

	BVS	**MaxC**
M_c	0.90	1.6
$\hat{b}$-value	0.88 ± 0.23	3.7 ± 1.1

Table 5.8: The M_c calculated from the BVS and MaxC methods, and the $\hat{b}$-value plus uncertainty from the MLE method (Equations 2.5-2.6), for the template matching catalogue in Figure 5.10c for each estimate of M_c, before the mainshock.

	BVS	**MaxC**
M_c	-0.7	0.0
$\hat{b}$-value	0.21 ± 0.016	0.32 ± 0.037

Table 5.9: The M_c calculated from the BVS and MaxC methods, and the $\hat{b}$-value plus uncertainty from the MLE method (Equations 2.5-2.6), for the standard catalogue in Figure 5.10c for each estimate of M_c, before the mainshock.

Following the flowchart in Figure 2.3, the BVS method is again accepted for the multiplet matching catalogue, resulting in a $M_c = 1.7$, and a $\hat{b}$-value of 1.0 ± 0.15. The USGS catalogue also accepts the BVS method with a $M_c = 1.5$, and a $\hat{b}$-value of 1.1 ± 0.093 for before the mainshock. These are expected $\hat{b}$-values for this type of tectonically-active area (Schorlemmer et al., 2004). While the standard and template matching catalogues are included in Figure 5.10e and g, there were very few events prior to the mainshock in these cases, and so the M_c and $\hat{b}$-value reported in Tables 5.8 - 5.9 are rejected because of their anomalous values based on sparse data.

The high $\hat{b}$-value for the multiplet matching catalogue prior to the mainshock agrees with the observation that the multiplets found originate from the creeping part of the San Andreas fault just north of Parkfield, known to have high b-values (Wiemer and Wyss, 1997; Amelung and King, 1997). This indicates that the multiplets found may have resulted from small unstable patches embedded within the creeping section of the fault (Nadeau et al., 1995).

Next, I examined the inter-event times of the multiplet matching (Figure 5.11a), the USGS (Figure 5.11b), template matching (Figure 5.11c) and standard (Figure 5.11d) catalogues of the full sequence. These were then compared with known statistical distributions to better understand the processes of the events in the time prior to catastrophic failure.

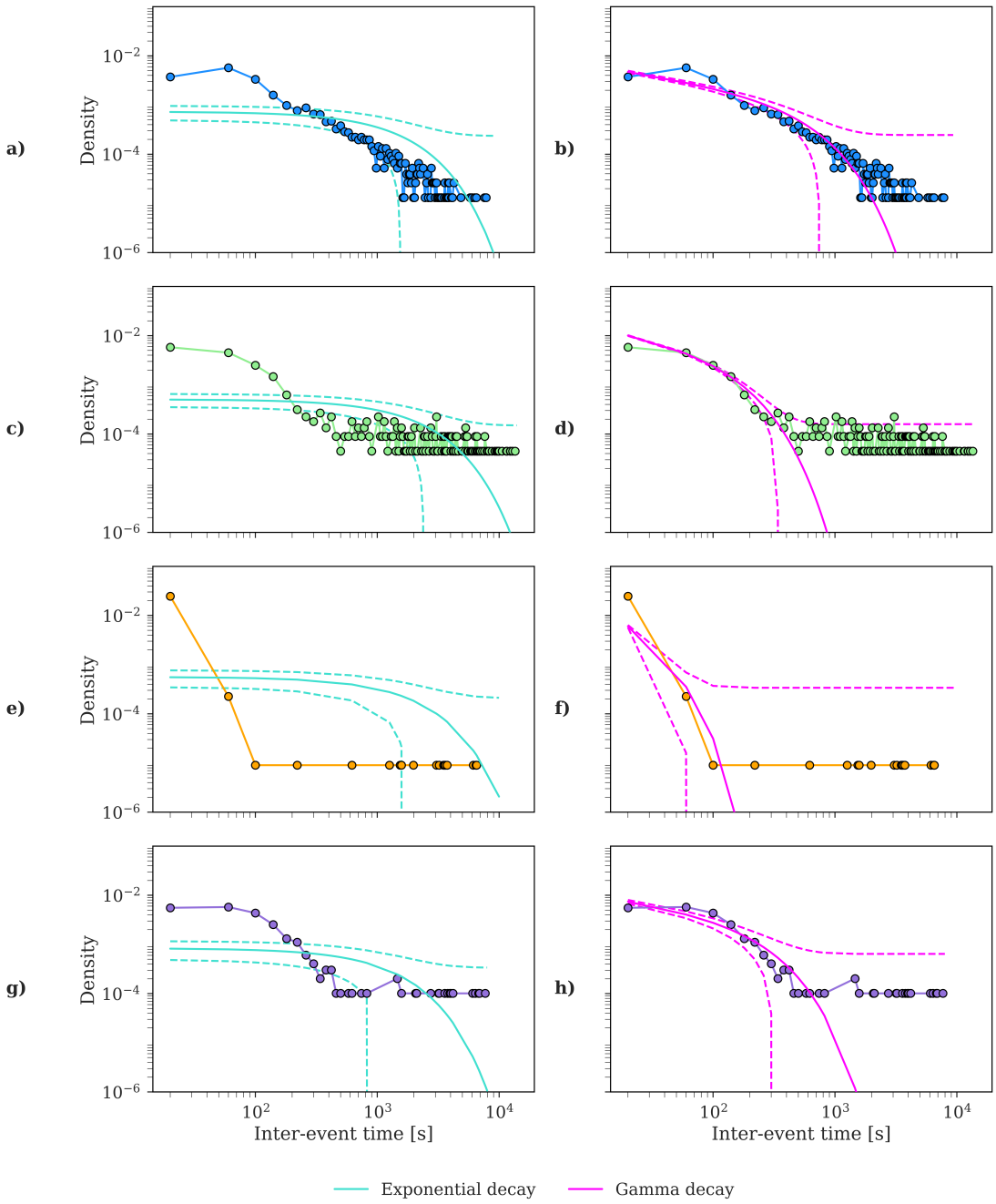

Figure 5.11: Comparison of inter-event times for multiplet matching (a,b), USGS (c,d), template matching (e,f) and standard (g,h) catalogues, with gamma (pink) and exponential (cyan) distributions. Confidence intervals of 95% have been added to both distributions, and are shown by their corresponding colour and boundaries as dashed lines.

As discussed in section 2.3.1, the frequency of the inter-event times of earthquake events generally follow a exponential distribution when the catalogue is declustered to remove aftershocks (Poisson process). The null hypothesis for if there is no causal link between multiplets and the mainshock occurrence time would result in exponential inter-event times. However inter-event times can also have a more general distribution, which is not necessarily exponential. A bimodal mixture of inter-event times could instead follow a gamma distribution between correlated event pairs at short to medium inter-event times, and an exponential distribution for those at longer inter-event times between uncorrelated events, as expected from an ETAS model (Bak et al., 2002; Touati et al., 2009). Therefore, I include both a gamma (pink) and exponential (cyan) fits in Figure 5.11 to the full dataset as hypotheses to be tested. Further to this, the 95% confidence interval of the two distributions are shown in their corresponding colour, with the bounds marked by a dashed line. This confidence interval quantifies the belief of being 95% confident that the true values lie within this interval.

Figure 5.11a shows that the exponential model does not fit the shorter inter-event times of the multiplet matching catalogue well. The fit becomes better when the inter-event times are >200 seconds, with most of the points lying within the confidence bands. This indicates that the events occurring >200 seconds apart may not be correlated to one another. Figure 5.11b shows a better fit of the short inter-event times with the gamma decay function, particularly <1,000 seconds. The gamma fit does not do well between 20 and 100 seconds in this case, with the points here lying outwith the confidence bands. This is likely due to the multiplet matching method removed overlapping events <30 seconds from one another, which lowers the density of the first binned point. These results indicate that the multiplet matching method has picked up some aftershocks at the shorter inter-event times (correlated events), best modelled by a gamma function, as well as independent events at longer inter-event times (uncorrelated events), modelled with an exponential function. The inter-event times between 300 and 1,000 seconds, which fit both the exponential and gamma functions well, could also be

described by a power-law distribution because of the cross-over of these two functions. This result rejects the null hypothesis that these multiplets are the outcome of a random process.

Figure 5.11c shows that the tail end of the USGS catalogue's inter-event time distribution matches an exponential model well from $>$ 1,000 seconds, indicating that the events which are further apart from one another in time are more likely to be independent to one another. Figure 5.11d has a well fitted gamma function for inter-event times $<$ 500 seconds. This is consistent with a catalogue that has not been declustered as it contains predominantly aftershocks, which would contain many correlated event pairs. Hence, the complete USGS catalogue's inter-event time distribution may be best described as a mixture between a gamma for the shorter inter-event times, and an exponential for the larger inter-event times.

The template matching catalogue did not fit the exponential (Figure 5.11e) well for any part of the distribution of inter-event times. The gamma (Figure 5.11f) fit is better overall, and much better for $<$100 seconds. This is because the template matching catalogue contained mostly aftershocks, which all had short inter-event times. The first bin (0-40 seconds) contained 98% of events, therefore the density of this distribution was mostly one sharp peak at the beginning, hence the better apparent fit to a gamma decay function.

Lastly, the standard catalogue fit the exponential (Figure 5.11g) better for inter-event times $>$ 1,500 seconds, and the gamma (Figure 5.11h) better for inter-event times $<$ 1,000 seconds. Again, this is consistent with the standard catalogue having many aftershocks, which causes the density to be larger at the short inter-event times, resulting in a better fit to a gamma function. The exponential fits adequately to the longer inter-event times, however this is quite a sparse catalogue, therefore there is not quite enough data to assess this confidently.

To further analyse which distribution fits the inter-event times the best, I use the Akaike Information Criterion (AIC) from Equation 2.10 and Bayesian Information Criterion (BIC) from Equation 2.11 for both distributions for each catalogue (Table 5.10).

	Multiplet matching method	**USGS**	**Template matching**	**Standard**
$AIC_{exponential-gamma}$	-5	-4	-3	-6
$BIC_{exponential-gamma}$	122	125	7	63

Table 5.10: The Akaike Information Criterion (AIC) from Equation 2.10 and Bayesian Information Criterion (BIC) from Equation 2.11 calculated for the exponential and gamma distributions in Figure 5.11 to measure which fits the inter-event times best.

The results in Table 5.10 indicate that based on the AIC, the exponential distribution best overall fits all the catalogues, whereas the BIC, where the penalty function for the extra parameter also depends on the number of events, favours the gamma distribution. These results indicate that both functions could be used, as some events are best fit by an exponential function, and others by a gamma function. This is consistent with this dataset as there are correlated events and/or aftershocks in all catalogues, mostly at the shorter inter-event times, best modelled with a gamma function. There are also uncorrelated background events with longer inter-event times, modelled with an exponential function.

The AIC is considered better for prediction, as it is roughly equivalent to cross-validation method (which can sometimes cause over-fitting), whereas the BIC allows for a consistent estimation of the underlying data generating process. The BIC is

considered more reliable for datasets larger than 46, as is the case here (Main et al., 1999).

Next, I observed the cumulative rate at which the multiplet matching (blue), USGS (green), template matching (orange) and standard (purple) catalogue events occurred in time, in Figure 5.12, with respect to the M6.0 mainshock (red vertical dashed line).

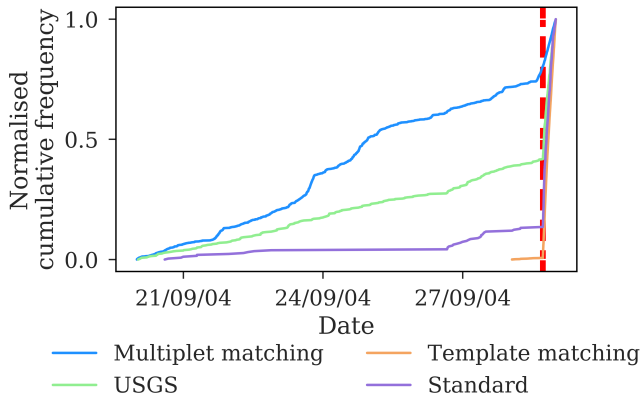

Figure 5.12: Comparison of multiplet matching (blue), USGS (green), Peng and Zhao (2009) (yellow) and Thurber et al. (2006) (purple) normalised cumulative frequency of events to observe event rate. The time of the M6.0 mainshock is shown by the red vertical dashed line.

As there was a large difference between the total number of events in some of the catalogues, the cumulative event rate in Figure 5.12 is normalised for an easier comparison between the four catalogues. The multiplet matching catalogue contains mostly seismicity from before the mainshock, whereas the three other catalogues contain more from after. The multiplet matching catalogue also appears to not follow a consistent pattern, and exhibits alternating periods of increased seismicity and quiescence in the week before the mainshock. The USGS catalogue shows a much more gradual process prior to failure, with a slight increase in slope starting the day before the

mainshock. Both the template matching and standard catalogues contain insufficient data prior to the mainshock to make confident inferences from their behaviour.

Figure 5.12 illustrates that all catalogues had an increased rate of seismicity in the days prior to the mainshock. However, observing the event rate in this way gives equal weighting to the events of all magnitudes, therefore I also observed the cumulative seismic moment M_o, for the four catalogues in Figure 5.13, following the same protocol as Figure 5.12.

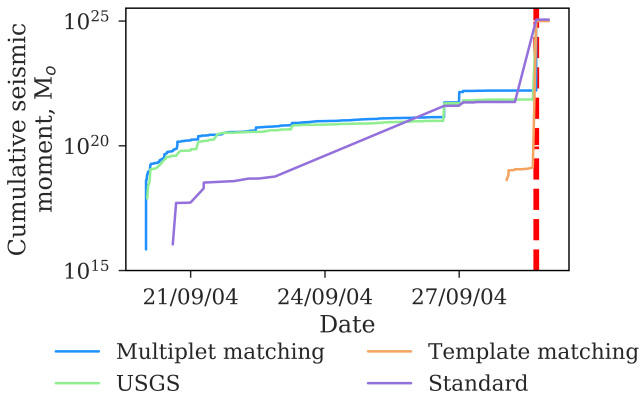

Figure 5.13: Comparison of multiplet matching (blue), USGS (green), template matching (yellow) and standard (purple) catalogues cumulative seismic moment of events. The time of the M6.0 mainshock is shown by the red vertical dashed line.

The results in Figure 5.13 illustrates that there are significant fluctuations in the cumulative seismic moment in the multiplet matching, USGS and standard catalogues in the week leading up to catastrophic failure. The USGS catalogue and the multiplet matching catalogue both show a transient that is increasing at a much slower rate prior to 27/09/04. This is consistent with a partially brittle creep event (Main, 2000; Heap et al., 2009). A more significant increase in the few days leading up to the failure is evident in the multiplet matching catalogue. This could be consistent with a period of active brittle creep associated with an underlying aseismic creep, as seen

in several geodesy studies (Johanson et al., 2006; De Michele et al., 2011). As the multiplet matching catalogue is created by identifying similar waveforms, this increase in seismic moment can be interpreted as the regular failure of the same fault patches forced by the surrounding aseismic slip. This infers that the multiplets were a part of an ongoing local creep-type deformation towards the nucleation of the larger rupture, thus indicating that the preslip model hypothesis is appropriate here. The results here show that having a more complete catalogue could be particularly useful in tracking how the cumulative seismic moment changes, which provides a mechanical support to use the seismic activity (particularly those of small earthquakes) to infer underlying processes such as creep along major faults.

5.3 Iquique, Chile

5.3.1 Summary

I also chose to analyse the Iquique sequence in Chile as a second example, because Kato and Nakagawa (2014) previously showed that there were repeating earthquakes and an increase in seismicity prior to the M_W 8.2 megathrust earthquake at 20km depth on 1st April 2014 at 23:46 UTC, during the period between 1st January 2008 to 31 May 2014 of this region. Subduction earthquakes are common in this area because of the subducting Nazca plate under the South American plate (Angermann et al., 1999). The Iquique earthquake occurred in an area of relatively weak coupling that bounded at least two highly locked segments, as supported by geodesy studies (Métois et al., 2013; Kato and Nakagawa, 2014). It also partially filled the Northern Chile seismic gap, where no major earthquake had occurred since the 1877 M_W 8.6 subduction earthquake (Métois et al., 2013; Kato and Nakagawa, 2014; Cesca et al., 2016).

The largest increase in seismicity occurred due to several large (retrospectively-

designated) foreshocks in the two weeks prior to the mainshock, hence I chose the shorter time period from 15th March - 2nd April 2014 in order to examine the strong foreshock activity prior to the mainshock.

The locations of the earthquakes from the USGS catalogue for this time period are shown in Figure 5.14, where the colour of the dots denotes the time and the size corresponds to magnitude.

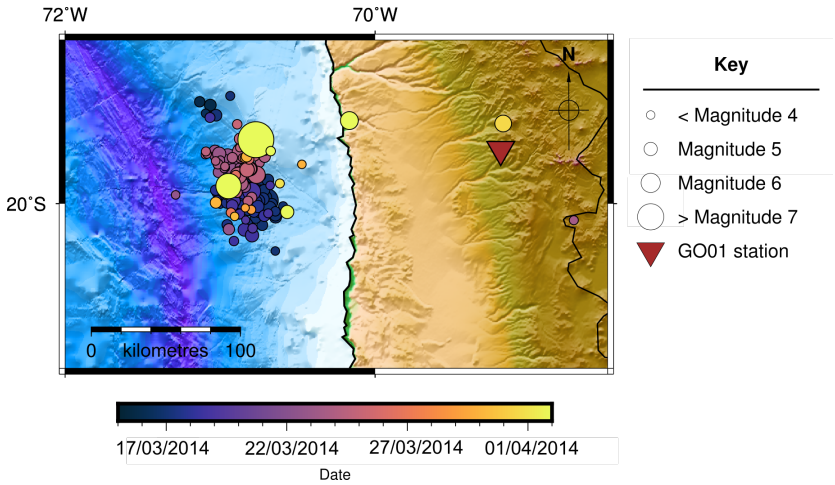

Figure 5.14: Illustration of the locations of the 166 earthquake events in the USGS catalogue for the M_W 8.2 earthquake sequence in Iquique, Chile from 15th March - 2nd April 2014. The M_W 8.2 earthquake occurred at 23:46 UTC on 1st April 2014. The location of the seismic station used in this analysis is shown by the brown triangle.

I downloaded the seismic data from the Chusmiza seismometer (station GO01 and network C, shown in Figure 5.14) from the IRIS website, as this was the closest open-access station to the mainshock available. As the events I was interested in had frequencies $<$ 20Hz, I band-pass filtered between 1Hz and 9Hz and downsampled the data to 40Hz. This earthquake sequence is shown in Figure 5.15, with the y-axis clipped at a velocity of $\pm 10^{-3}$ m/s so that the larger earthquakes do not saturate the image. A red vertical dashed line has been added to show the UTC time of the M_W

8.2 mainshock occurring at 23:46, with the multiple thinner red vertical dashed lines showing the equivalent time for earlier earthquakes M>6.0 in this sequence.

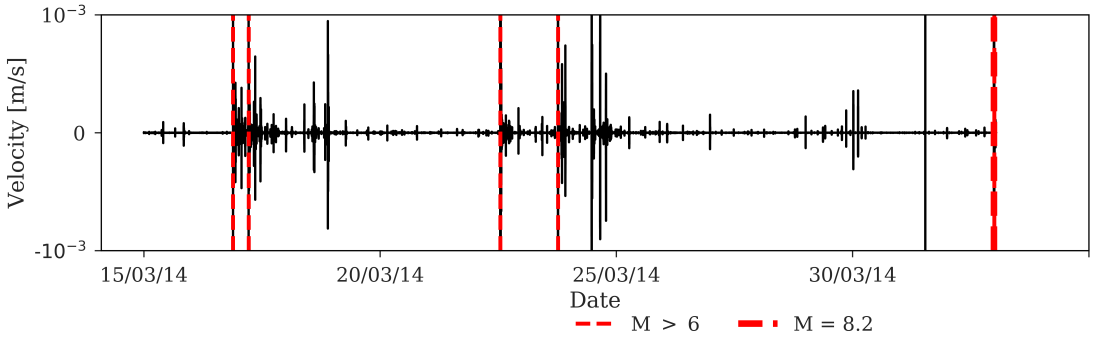

Figure 5.15: Seismogram from near the Iquique mainshock, with light red dashed vertical lines showing notable foreshocks (M_W = 6.7, 6.4, 6.3, 5.6), and the M_W 8.2 mainshock shown by the heavier red dashed vertical line (data downloaded from IRIS). The seismogram has been clipped in the y-axis at $\pm$ 10^{-3} m/s to show the foreshock sequence clearly.

5.3.2 Method

All 166 events from the USGS (locations shown in Figure 5.14) were used as templates in the multiplet matching method (section 3.3) for finding similar events, with the majority of the template events around M_W 4.0. As the minimum magnitude was considerably large here, I did not set a magnitude threshold for templates to maximise the opportunity to capture events. I chose a window size to be 30 seconds long to ensure that the P and S parts of the waveforms would be included within the region studied. The downside of so many templates, was that the runtime in this case was approximately 67 hours on the supercomputer.

Four of the template events used from the USGS catalogue are illustrated in Figure 5.16, with a green box indicating the window used. The UTC start-time and the date of each window for when the event occurred on the Chusmiza seismometer is shown in the upper right of each plot.

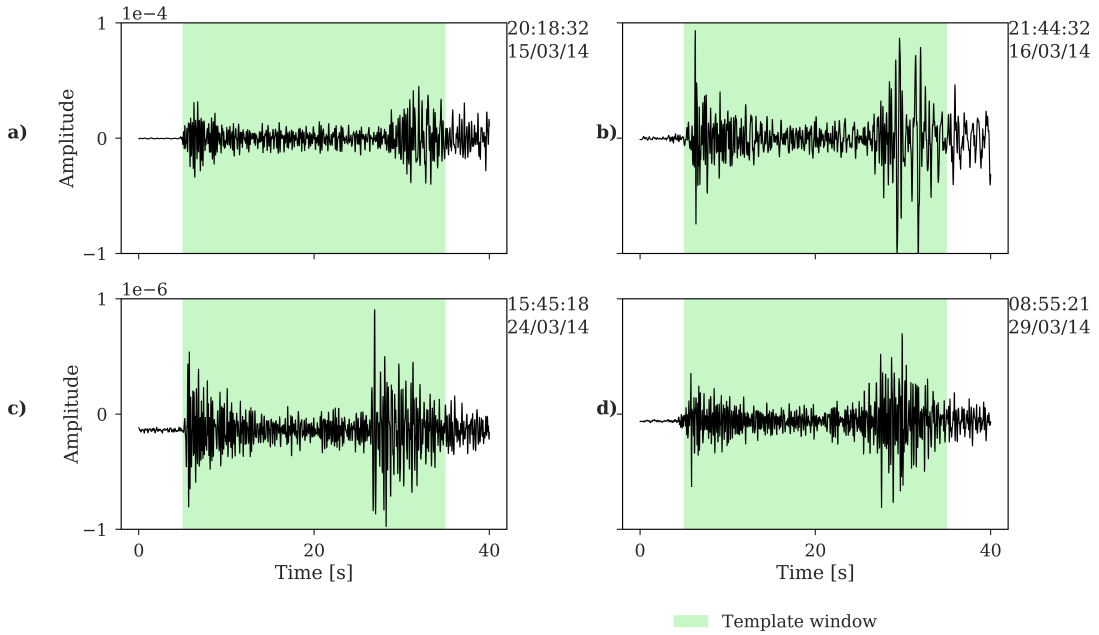

Figure 5.16: Illustration of the four different templates used in the M_W 8.2 earthquake sequence in Iquique, Chile from 15th March - 2nd April 2014. The UTC start-time and the date of each template is displayed in the upper right of each window. These templates show events which occurred prior to the mainshock (23:46 UTC on 1st April 2014). These were identified in the USGS catalogue, and adjusted in time to when they appeared on the seismometer used.

The USGS earthquake events in Figure 5.16a-d are ordered chronologically in time, with moment magnitudes assigned by the USGS in the catalogue as 4.2, 4.6, 5.7 and 3.9, respectively.

The catalogue in Kato and Nakagawa (2014) was compiled through template matching. The template waveforms used were those from the USGS between 1st January 2008 and 1st May 2014 which resulted in 11,690 events for this time period. The threshold for an event detection in the catalogue was set as if the cross-correlation coefficient exceeded at least ten times the MAD of the average cross-correlation coefficient from the ten stations, on the day of interest. The catalogue in Kato and

Nakagawa (2014) was cut to the time period observed here from 15th March - 2nd April, which resulted in 2,447 events. Herein, this catalogue will be referred to as the 'template matching' catalogue for comparison to the USGS and multiplet matching catalogues.

The multiplet matching method initially detected 35,929 multiplets from 79 of the templates from the USGS, however many of these were either duplicates, or were overlapping. The 87 templates that did not find any similar waveforms were mostly due to the larger magnitude of the template events, which had no similar detections. After the catalogue was cleaned and processed by removing any event within 40 seconds of another event, the catalogue finished with 5,897 unique multiplets in their dominant family, including the 79 templates that had similar waveforms. The locations of the template events which did find multiplets are shown in Figure 5.17, where the size of the dots corresponds to the magnitude of the event, and the colour shows the time of the event.

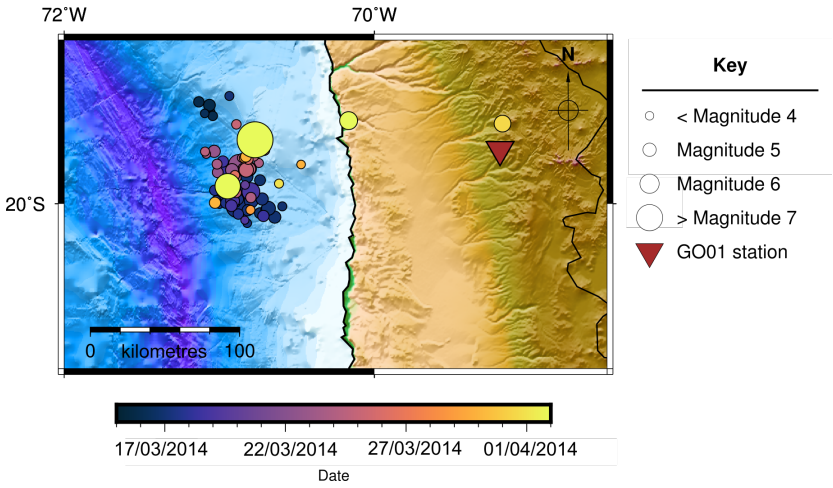

Figure 5.17: Illustration of the locations of the 79 template earthquake events in the USGS catalogue for the M_W 8.2 earthquake sequence in Iquique, Chile from 15th March - 2nd April 2014. The location of the seismic station used in this analysis is shown by the brown triangle.

The multiplet matching catalogue contained 107 from the USGS catalogue and 1,151 of the template matching catalogue, as shown in Table 5.11. The multiplet matching catalogue has an additional 28 events detected from the templates used from the USGS catalogue. As I used the events in the USGS catalogue, it was interesting that the multiplet matching method was also able to pick up some of these. The 28 events did not find any similar events in Step 4 of the method (see Figure 3.35), which terminates the method. However, the 79 templates that did find other events at this Step, successfully then created a new parent trace which was able to detect the 28 additional events which are confirmed in the USGS catalogue at Step 7. The other 59 events from the USGS catalogue were not detected by the multiplet matching method, and did not find any similar events, therefore they were not included in the multiplet matching catalogue, and are shown as missing events in Table 5.11. This indicates that these 59 events did not have any similar events occurring in this earthquake sequence. The missing events between the template matching and multiplet matching catalogues are from the processing stage, whereby any event within 40 seconds is removed.

Events	**Multiplet matching**	**USGS**	**Template matching**
Found	5,897	166	2,447
Matching	-	107	1,151
Missing	-	59	1,296
New	-	5,790	4,746

Table 5.11: Summary of the found, matching, missing and new events in the multiplet matching, USGS and template matching (Kato and Nakagawa, 2014) catalogues.

After the events were identified from the multiplet matching method, they were assigned magnitudes as the same scaling method described in the previous example (using Equations 3.9 - 3.10 from section 3.4). I used the known magnitudes from the

USGS catalogue and found the value of c which gave the best estimate of the known magnitude, as illustrated in Figure 5.18.

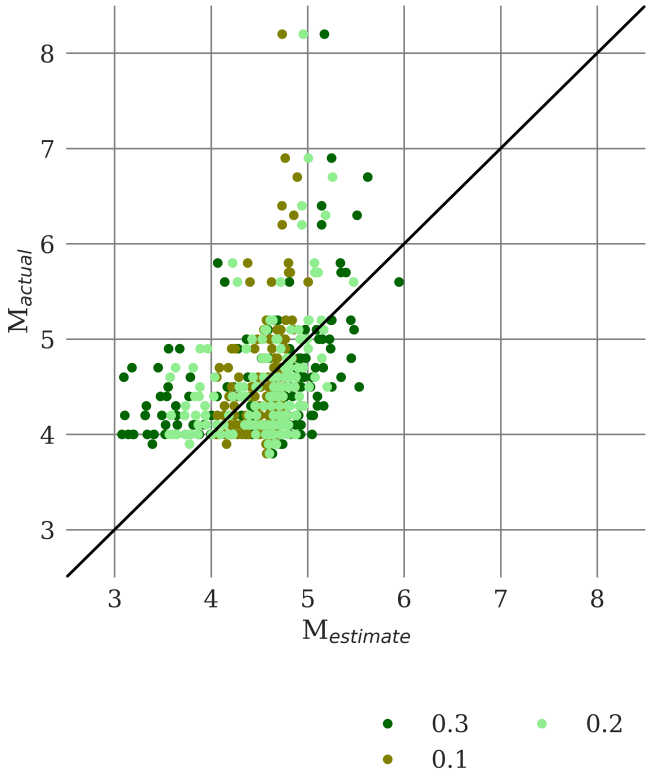

Figure 5.18: Illustration of working out c in Equations 3.9 - 3.10 to best estimate the magnitude of known template events from the USGS catalogue. In this case, the best value of c was deemed to be 0.2.

In this case, the value of $c = 0.2$. This was used with Equations 3.9-3.10 to calculate the estimated magnitudes (M^e) of the new multiplets.

An example of the original and final template events, and some multiplets found in the preceding time to the catastrophic failure, is illustrated in Figure 5.19. I chose to show these particular sets of multiplets as the horizontal waveforms are deemed to be moderately similar to one another as they have a cross-correlation value >0.5.

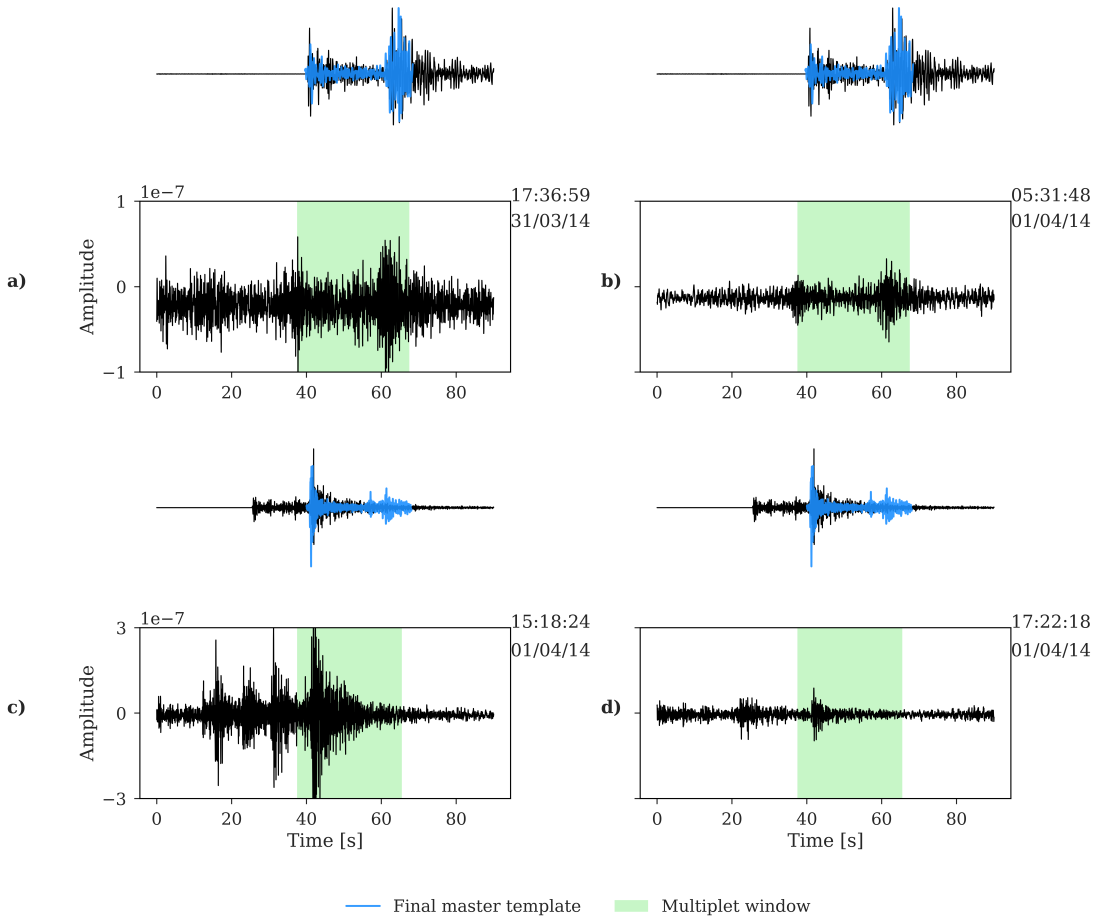

Figure 5.19: Comparison of two sets of two multiplets found from the multiplet matching method. The original template trace and final master template trace (blue) are shown above the multiplets found. The horizontal waveforms are also multiplets of one another, and are scaled to the same y-axis. The window which the multiplet was detected in is shown by a green box. The starting time of each waveform is shown in the upper right of each plot. All the multiplets shown here occurred prior to the M8.2 mainshock at 23:46 on 01/04/14.

The original template trace, and the final master template trace (blue) used in the multiplet matching method (from Step 7 of section 3.3.1) are shown above the new multiplets which were found. The upper original template trace was recorded as M_d=4.1 in the USGS catalogue, and occurred at 06:47 on 17/03/14, with an epicentre

at -19.99, -70.892 (44.1km from the mainshock epicentre). The lower original template trace had a M_d=4.0 in the USGS catalogue, and occurred at 20:43 on 29/03/14, with an epicentre at -19.76, -70.47 (35.5km for the mainshock epicentre). The window which the multiplet was detected is shown by the green box, but the time has been extended to show more of the waveform during this time period. The multiplet in Figure 5.19a had an estimated M^e=2.3, and the multiplet in Figure 5.19b occurred around ten hours later, with an estimated M^e=2.2, and a cross-correlation value between the two seismograms of 0.76. This is a high cross-correlation value, which implies that these two multiplets are highly similar. The multiplets which are detected from the multiplet matching method favour the detection of the S-wave rather than the P-wave (which occurs around 20 seconds before the detected S-wave). Steps 4 and 7 of the multiplet matching method (section 3.3.1) increases this preference for detecting S-waves here as the detected multiplets are being averaged to create a new template trace, where the larger S-wave is then expected to dominate.

The second set of multiplets illustrated in Figures 5.19c and 5.19d had an estimated M^e=3.4 and M^e=3.3, respectively, and a cross-correlation value between the two seismograms of 0.56, implying that these multipelts are moderately correlated. In this example, it is clear that the amplitude of the multiplet does not overly influence the detection, as the method has picked up two similar signals of different amplitudes. Although a longer time window may seem preferable in order to detect more of the P-wave (as seen in Figures 5.19a,b), it could then also pick up more of another signal. In this case in Figure 5.19c, if the window used was larger, this multiplet would have likely not been detected, as there appears to be other events in this time period. This highlights the balance in choosing a window which contains enough of the signal to get a reasonable detection, but not starting to pick up other events.

5.3.3 Statistical Analysis

The statistical analyses of the multiplets found from the multiplet matching method for the Iquique sequence will be presented and discussed here, following the same protocol as the previous section. I will be comparing the results for the multiplet matching catalogue to the USGS and template matching catalogue, herein shown by blue, green and orange colours, respectively.

To summarise these results, I first show the temporal evolution of the multiplets found by the multiplet matching method in Figure 5.20, denoted by blue circles, with the known events from the USGS catalogue shown in green triangles and the events from the Kato and Nakagawa (2014) catalogue illustrated as orange squares, with the inter-event times (upper diagram), peak amplitudes (middle diagram) and magnitudes (lower diagram) shown.

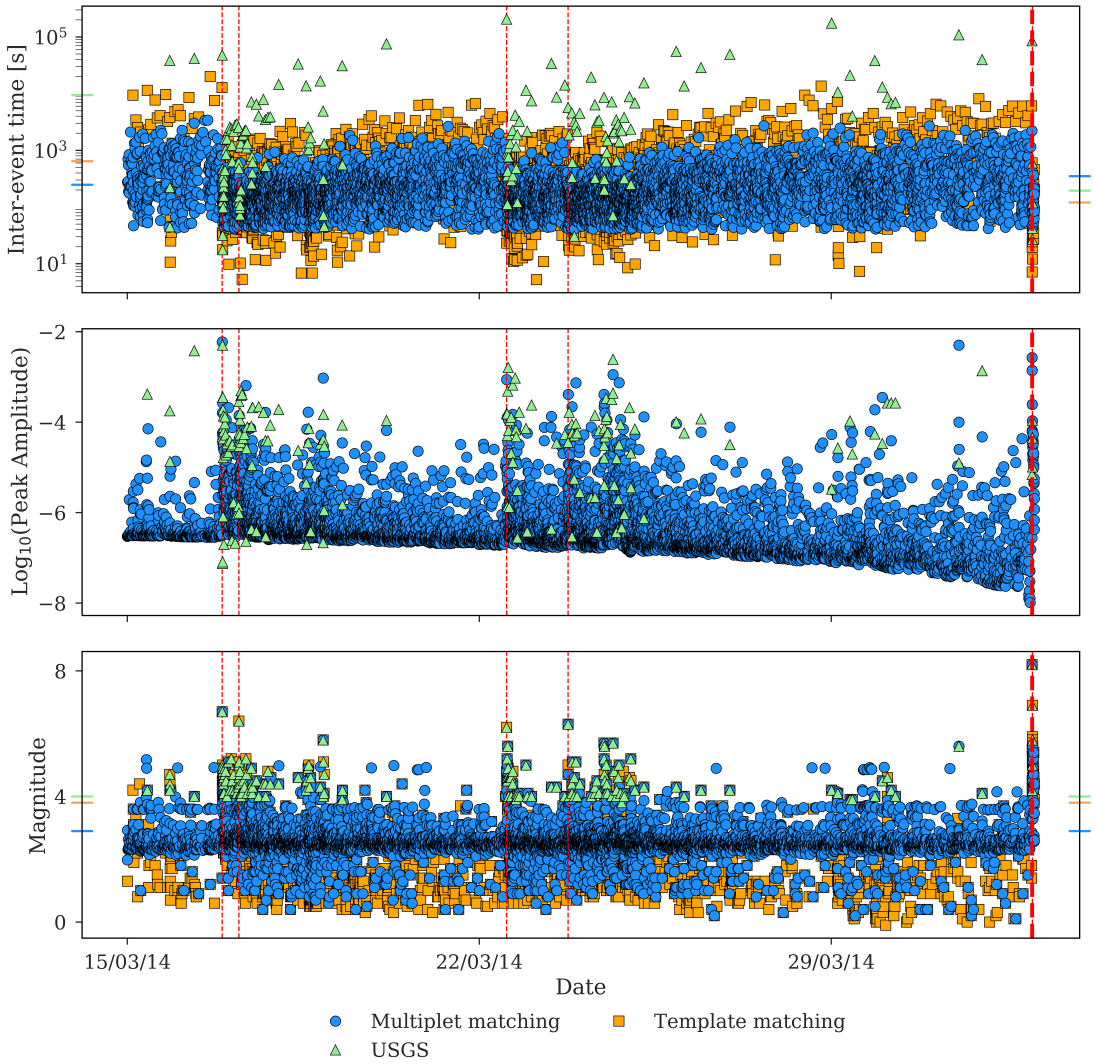

Figure 5.20: Time evolution of USGS catalogue (green triangles), events found by multiplet matching (blue circles) and the template matching catalogue (orange squares), of their inter-event times (upper), amplitudes (middle) and magnitudes (lower). Coloured horizontal tick lines show average inter-event time (upper), and the magnitude of completeness, M_c, (lower) per catalogue.

The inter-event times in the upper plot of Figure 5.20 shows that the multiplets are mostly between 40 seconds and 20 minutes apart, and follow no specific pattern prior to the mainshock, which is shown by the thick red vertical dashed line in Figure 5.20.

The middle plot shows the peak amplitudes of events, as a check on the precision of the magnitudes in the lower plot. The times of the M > 6 events are shown in the upper and lower plots as the thinner red vertical dashed lines for comparison.

The average inter-event times for the events found from the multiplet matching method (blue), USGS catalogue (green) and template matching catalogue (orange) prior to the M_W 8.2 mainshock, are shown by the left coloured tick line in the top diagram, where the colour represents the catalogue in Figure 5.20. The USGS has a large average inter-event time prior to the mainshock as the catalogue was quite sparse, thus the events were further apart. However the template matching and multiplet matching catalogues were much more complete, thus the average inter-event times were lower.

The average inter-event time for after the mainshock is shown by the right coloured tick line in Figure 5.20. These average inter-event times for after the mainshock are much closer together as this will be mostly large aftershocks, which would have been picked up by the three catalogues.

Events with smaller peak amplitudes gradually appear in the multiplet matching catalogue, giving an indication that the multiplets were slowly decreasing in size before the mainshock. This pattern could be due to a number of reasons. The location of the events could be migrating further from the seismic station (but still close enough to the template to be classed as a multiplet), or the templates which are further away from the station are able to detect smaller-amplitude events after the previous aftershock sequence has no longer dominated the signal. This is not to say that smaller events were not happening earlier, but instead that the signal was over-saturated with the larger-amplitude events in the area. Incompleteness after a large event is not uncommon in catalogues with aftershocks due to the detection ability associated with the coda of the large event and the aftershocks being indistinguishable from overlapping (Seif et al., 2017). Lastly, this pattern could also simply be an artefact of the filtering process.

This same pattern is not seen within the magnitude plot of Figure 5.20, thus indicating that the adjustment for magnitude estimations (section 3.4) is not greatly influenced by these artefacts observed.

The values of M_c are calculated later in this section by the MaxC and BVS methods, and are shown by the coloured tick lines on the lower plot of Figure 5.20.

A zoom in of the twelve hours prior to the mainshock and an hour after, is illustrated in Figure 5.21, following the same protocol as Figure 5.20.

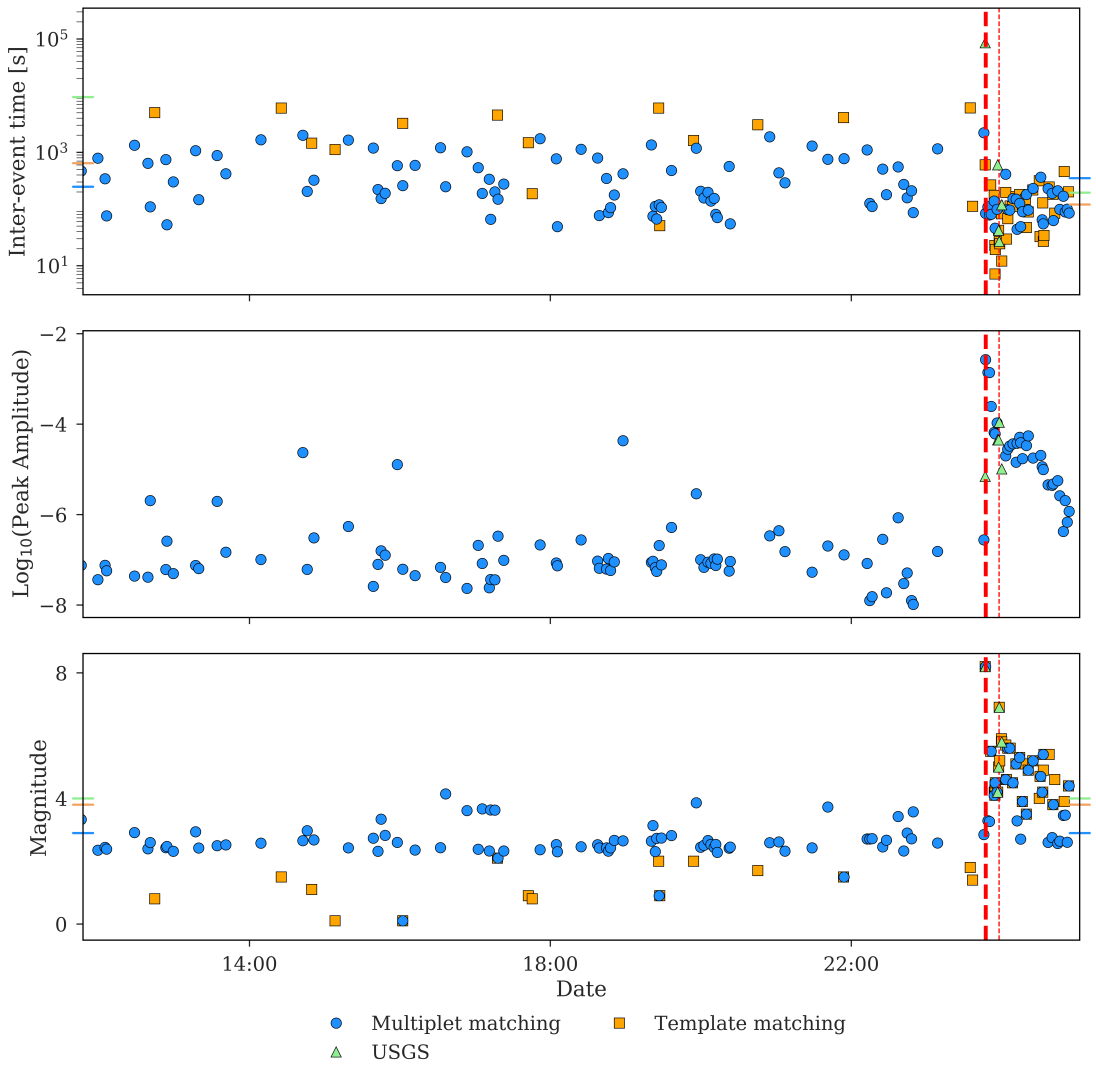

Figure 5.21: Time evolution of USGS catalogue (green), Kato and Nakagawa (2014) catalogue (yellow) and events found by multiplet matching (blue), of their inter-event time (upper) and magnitude (lower) twelve hours before the M8.2 mainshock (thick vertical red dashed line), and some time after. Coloured horizontal dashed lines show average inter-event time, and the magnitude of completeness, M_c, per catalogue prior to the mainshock. The time of a $>$ M_W 6.0 earthquake event which occurred in the M_W 8.2 aftershock sequence is shown by the thinner red vertical dashed line.

Figure 5.21 illustrates again that while this timeframe is seismically active, there is

no particular pattern prior to the mainshock, other than a short gap in the multiplet matching catalogue just before the catastrophic failure. It is also shown that most of the events in this time before failure were below the M_c for all three catalogues.

Next, I created a frequency-magnitude distribution of the multiplet matching event catalogue (Figure 5.22a in blue), the USGS catalogue (Figure 5.22b in green) and the template matching catalogue (Figure 5.22c in orange).

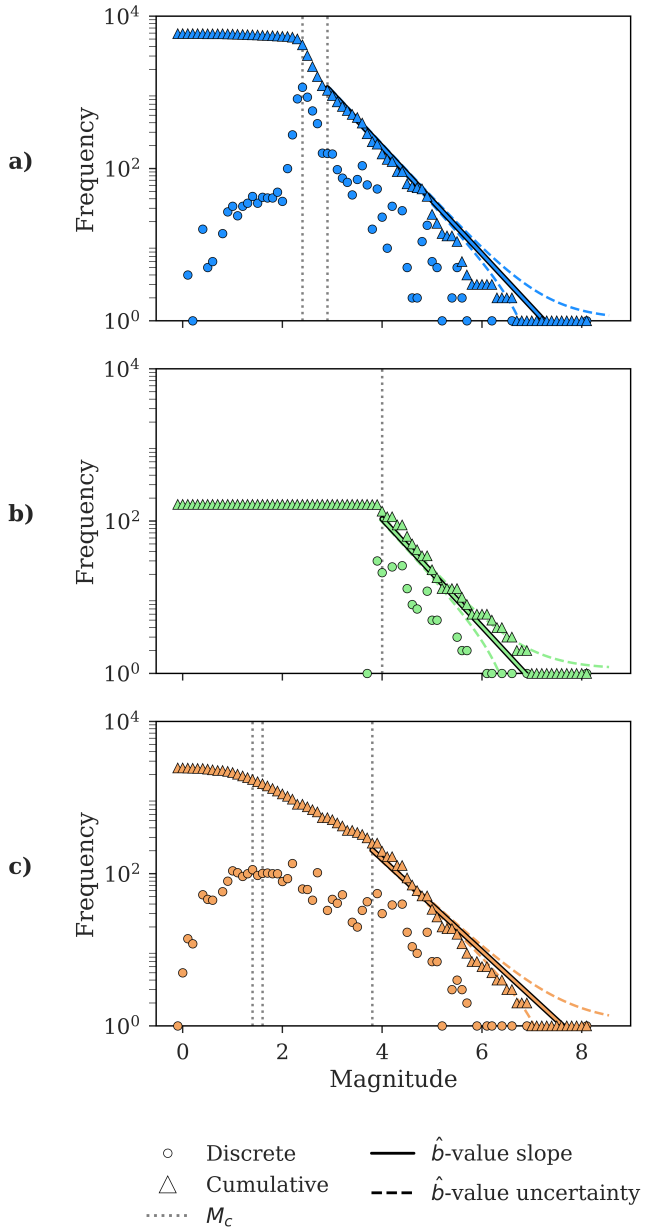

Figure 5.22: Comparison of the magnitudes of events in the multiplet matching (plot a in blue), USGS (plot b in green) and template matching (plot c in orange) catalogues as frequency-magnitude distributions, for the full catalogue. The discrete (filled circles) and cumulative (filled triangles) frequencies are shown for each catalogue. The $\hat{b}$-value corresponding to each catalogue is shown by the filled line, where the colour matches the catalogue, and the dashed lines show the uncertainties on the best fit lines at a 95% confidence. The grey dotted lines illustrate the different values of M_c calculated.

The magnitude of completeness, M_c, was estimated through the b-value stability (BVS) method and maximum curvature (MaxC) method (section 2.3.1), for each catalogue. The values of M_c calculated for these two methods are shown by the grey vertical dotted lines for each catalogue in Figure 5.22. An additional value of M_c is added in Figure 5.22c to illustrate the value quoted in Kato and Nakagawa (2014). The $\hat{b}$-value plus uncertainties, which are estimated from the chosen M_c in MLE method from Equations 2.5 - 2.6, are shown for each catalogue in Figure 5.22, by the solid line on each plot. The dashed lines show the bounds of the uncertainty on the best fit line with the optimal $\hat{b}$-value.

The BVS method for the multiplet matching catalogue is shown in Figure 5.23a, the USGS catalogue in Figure 5.23b, and the template matching catalogue in Figure 5.23c.

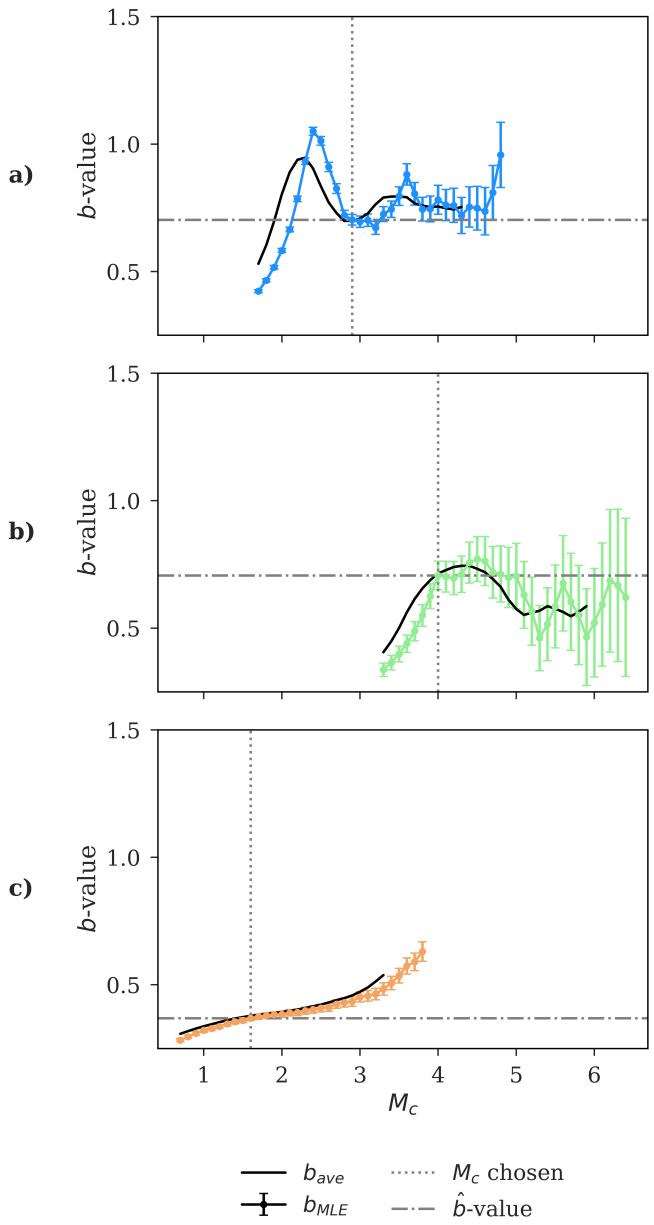

Figure 5.23: Comparison of b-value stability curves, showing the b-values for each magnitude of completeness, M_c, for the multiplet matching (plot a in blue), USGS (plot b in green) and template matching (plot c in orange) catalogues. The vertical dotted line shows the chosen M_c from this method, and the horizontal dashed line shows the b-value at this point. The M_c is chosen as when the average of the five successive b-values (black line) are within one error of the b-value.

The BVS method shown in Figure 5.23 calculates the $\hat{b}$-value using the MLE method while increasing the M_c incrementally. The b-value stabilises when b_{ave} (the average for the next five successive $\hat{b}$-values) lies within the error of the b_{MLE}. At this point, the M_c is chosen, and is shown by the vertical dotted line. The b-value at this M_c is illustrated as the horizontal dot-dashed line.

The BVS method for the multiplet matching catalogue in Figure 5.23a shows that the choice of M_c=2.9 came from when the $\hat{b}$-value began to stabilise at 0.70. The USGS catalogue does not have many low magnitude events in the catalogue, hence the b-value does not stabilise until the chosen M_c of 4.0, also at a $\hat{b}$-value of 0.71. The BVS method of the template matching catalogue in Figure 5.23c shows that the M_c from BVS is very low. This indicates a potential error in the magnitude calibration for this catalogue as it causes the $\hat{b}$-value to be lowered dramatically, inferring that the BVS method is not appropriate for this catalogue.

A summary of the M_c and $\hat{b}$-value results from the discussed methods are shown in Tables 5.12 - 5.14.

	BVS	**MaxC**
M_c	2.9	2.4
$\hat{b}$-value	0.70 ± 0.020	1.1 ± 0.019

Table 5.12: The magnitude of completeness, M_c, for the b-value stability (BVS) and Maximum Curvature (MaxC) methods, and the $\hat{b}$-value plus uncertainty from the MLE (Maximum Likelihood Estimation) method (Equations 2.5-2.6), for the multiplet matching catalogue in Figure 5.22a for each estimate of M_c.

I chose M_c using the method discussed in Roberts et al. (2015), and illustrated in Figure 2.3. For the multiplet matching catalogue, the BVS method was chosen as the best, as the difference between the M_c for the BVS and MaxC methods was greater than 0.1 (as seen in Table 5.15). This resulted in M_c = 2.9, and a $\hat{b}$-value of 0.70 ±

	BVS	**MaxC**
M_c	4.0	4.0
$\hat{b}$-value	0.71 ± 0.057	0.71 ± 0.057

Table 5.13: The M_c calculated from the BVS and MaxC methods, and the $\hat{b}$-value plus uncertainty from the MLE method (Equations 2.5-2.6), for the USGS catalogue in Figure 5.22b for each estimate of M_c.

	BVS	**MaxC**	**Known**
M_c	1.6	1.4	3.8
$\hat{b}$-value	0.37 ± 0.0080	0.35 ± 0.0071	0.63 ± 0.033

Table 5.14: The M_c calculated from the BVS and MaxC methods, as well as the known M_c from Kato and Nakagawa (2014). The $\hat{b}$-value plus uncertainty is calculated from the MLE method (Equations 2.5-2.6), for the template matching catalogue in Figure 5.22c for each estimate of M_c.

0.020. When this $\hat{b}$-value is shown against the data in Figure 5.24a, it appears that it does not fit to the M_W 8.2 mainshock well. This is not surprising because of the inherent selection bias in choosing a catalogue with known large events. Nevertheless, the uncertainty in the best fit $\hat{b}$-value line, shown by the dashed lines in Figure 5.24a, includes most of the data at the larger magnitudes.

The USGS catalogue obtained the same value of $M_c = 4.0$ for both methods, with a $\hat{b}$-value of 0.71 ± 0.057. The best fit $\hat{b}$-value line in Figure 5.24b for the USGS shows that this $\hat{b}$-value fits the data very well, except that it underestimates the likelihood of the largest events, as do the results of the multiplet matching catalogue. Again, this is likely due to selection bias where the M_W 8.2 mainshock is dominating the catalogue, although again not outside the uncertainty ranges shown. Despite the multiplet matching method having a much lower M_c, the $\hat{b}$-values agree within error. Overall, the results from the multiplet matching catalogue agree with those of the USGS catalogue, indicating

the Gutenberg-Richter law extends uniformly to the lower magnitudes revealed by the multiplet matching technique.

Lastly, the template matching catalogue yielded very low $\hat{b}$-values due to having a two-slope frequency-magnitude distribution. The M_c was quoted as 3.8 in Kato and Nakagawa (2014), hence I have included this in Table 5.14.

These low $\hat{b}$-values are not unexpected, as this area exhibited a b-value between 0.6 and 0.8 before the mainshock (Schurr et al., 2014). However, in order to explore the issue of selection bias in choosing times which include a large magnitude event further, I also show the same catalogue but only events prior to the M_W 8.2 mainshock in Figure 5.24, following the same protocol as Figure 5.22.

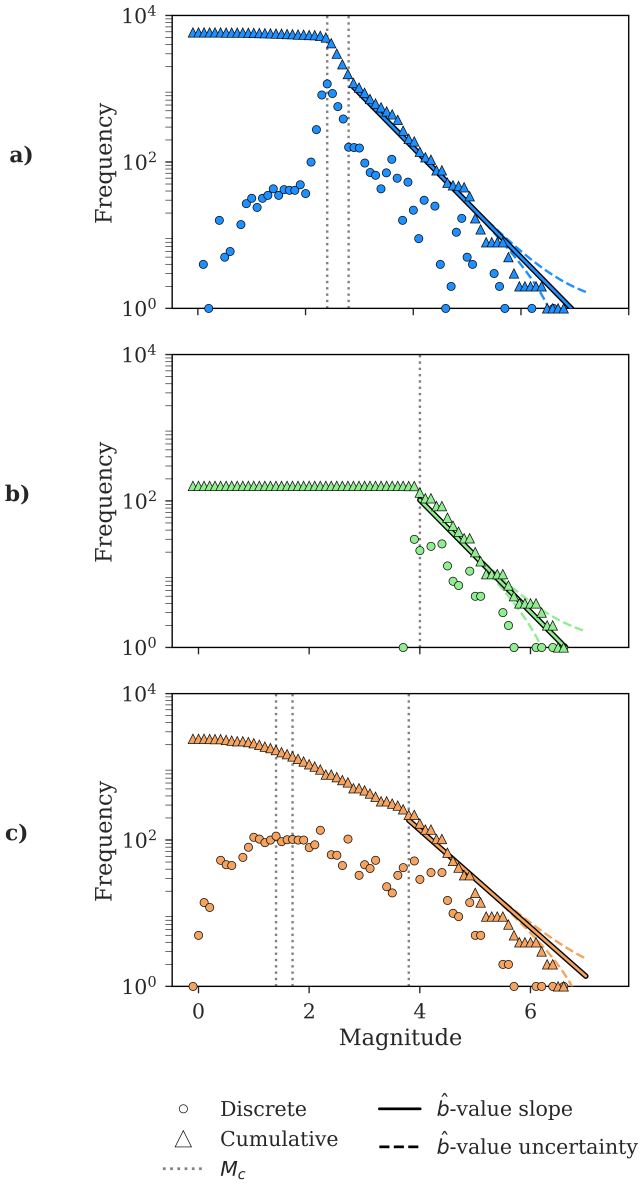

Figure 5.24: Comparison of the magnitudes of events in the multiplet matching (plot a in blue), USGS (plot b in green) and template matching (plot c in orange) catalogues as frequency-magnitude distributions, prior to the mainshock. The discrete (filled circles) and cumulative (filled triangles) frequencies are shown for each catalogue. The $\hat{b}$-value corresponding to each catalogue is shown by the filled line, where the colour matches the catalogue, and the dashed lines show the uncertainties on the slope. The grey dotted lines illustrate the different values of M_c discussed in Tables 5.15 - 5.17.

As before, the M_c was estimated through the BVS method and MaxC methods (section 2.3.1), for before the mainshock. The BVS method applied on the data prior to the mainshock is shown for the multiplet matching catalogue in Figure 5.25a, the USGS catalogue in Figure 5.25b, and the template matching catalogue in Figure 5.25c.

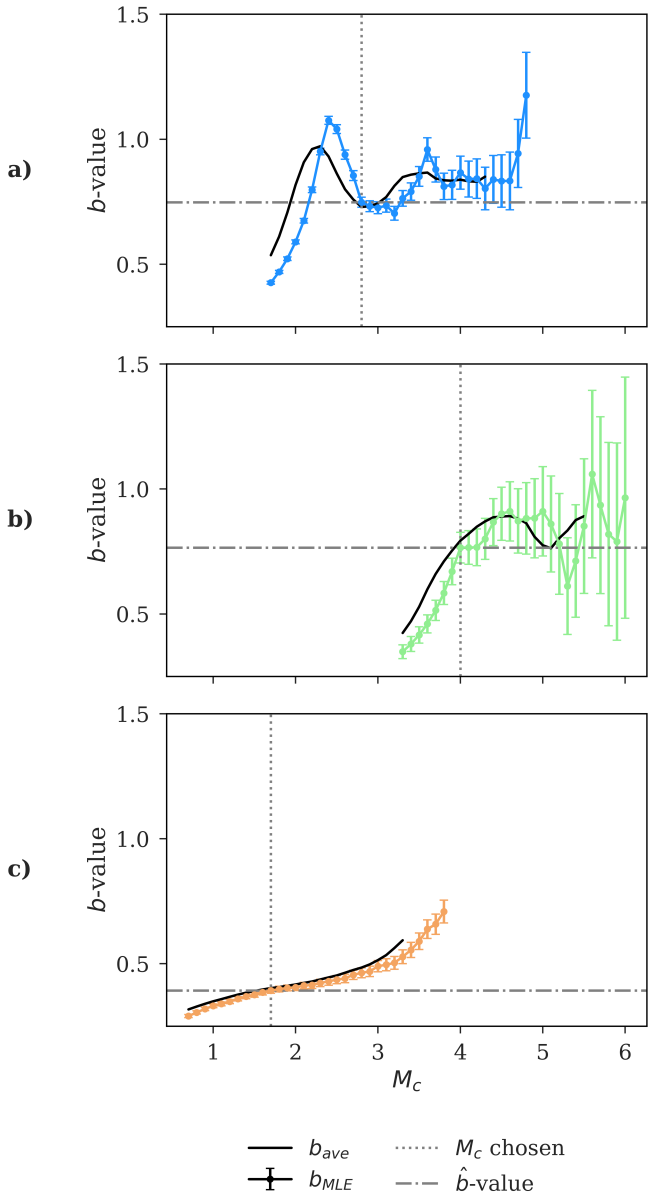

Figure 5.25: Comparison of b-value stability curves, showing the b-values for each magnitude of completeness, M_c, for the multiplet matching (plot a in blue), the USGS (plot b in green), and the template matching (plot c in orange) catalogues, prior to the mainshock. The vertical dotted line shows the chosen M_c from this method, and the horizontal dashed line shows the b-value at this point. The M_c is chosen as when the average of the five successive b-values (black line) are within one error of the b-value.

The multiplet matching catalogue in Figure 5.25a shows the choice of M_c=2.8 when the b-value stabilised at 0.75. This differs from Figure 5.23a with a lower M_c and a higher b-value. The USGS catalogue in Figure 5.25b produces the same M_c as Figure 5.23b of 4.0, but with a higher b-value of 0.77.

A summary of the M_c and $\hat{b}$-value results are shown in Tables 5.15 - 5.17. No analysis is presented for events after the mainshock because the seismic recording ended shortly after the mainshock.

	BVS	**MaxC**
M_c	2.8	2.4
$\hat{b}$-value	0.75 $\pm$ 0.019	1.1 $\pm$ 0.019

Table 5.15: The magnitude of completeness, M_c, for the b-value stability (BVS) and Maximum Curvature (MaxC) methods, and the $\hat{b}$-value plus uncertainty from the MLE (Maximum Likelihood Estimation) method (Equations 2.5-2.6), for the multiplet matching catalogue in Figure 5.24a for each estimate of M_c.

	BVS	**MaxC**
M_c	4.0	4.0
$\hat{b}$-value	0.77 $\pm$ 0.056	0.77 $\pm$ 0.056

Table 5.16: The M_c calculated from the BVS and MaxC methods, and the $\hat{b}$-value plus uncertainty from the MLE method (Equations 2.5-2.6), for the USGS catalogue in Figure 5.24b for each estimate of M_c.

	BVS	**MaxC**	**Known**
M_c	1.7	1.4	3.8
$\hat{b}$-value	0.39 ± 0.0088	0.37 ± 0.0073	0.71 ± 0.037

Table 5.17: The M_c calculated from the BVS and MaxC methods, as well as the known M_c from Kato and Nakagawa (2014). The $\hat{b}$-value plus uncertainty is calculated from the MLE method (Equations 2.5-2.6), for the template matching catalogue in Figure 5.24c for each estimate of M_c.

Following the method for choosing M_c in Roberts et al. (2015) (Figure 2.3) as before, the BVS method (Figure 5.25) was chosen for the multiplet matching catalogue, as the difference between the M_c for the BVS and MaxC methods was greater than 0.1 (as seen in Table 5.15), resulting in $M_c = 2.8$. The $\hat{b}$-value at this M_c was calculated as 0.75 ± 0.019. The $\hat{b}$-value line fits the data in Figure 5.22a better, however a roll-off from the under sampling of the large events is still present. This $\hat{b}$-value is within the range of 0.6-0.8, and close to the M_c estimate of 2.6 in the Schurr et al. (2014) study of pre-mainshock seismicity of the area, indicating that the multiplet matching catalogue appropriately captured the general seismicity.

The USGS catalogue again has a $M_c = 0.4$, with a $\hat{b}$-value of 0.77 ± 0.056, which fits the data well in Figure 5.22b. The $\hat{b}$-values of the USGS and multiplet matching catalogues are again within error.

As discussed earlier, the M_c could not be confidently estimated from the BVS or MaxC methods for the template matching catalogue, therefore I used the M_c in Kato and Nakagawa (2014), where their catalogue had a M_c=3.8, as illustrated in Table 5.17. I used this value to get $\hat{b}$-value=0.71 ± 0.037, which is within error for both the multiplet matching and USGS catalogue. However, as illustrated in Figure 5.24c, there is still a significant bias at high magnitudes, this time over-estimating the actual occurrence. In this case, the bias is significant because the uncertainties in Figure

5.24c do not generally include the occurrence rates of the higher magnitude events. Another cause of this anomaly for the two catalogues could be that the multiplet and template matching catalogues pick up many new events which creates a catalogue that does not necessarily follow the same Gutenberg-Richter characteristics. This could be because the multiplets are, in theory, picking up similar events due to a repeated rupture of the same patch, meaning that this could be a mix between the characteristic and Gutenberg-Richter models. However, there is a risk of over-interpreting the data as the events in the tail of the distributions are probabilistically less likely. Whatever the underlying reason, the results indicate that the $\hat{b}$-value is not very sensitive to the time period chosen, but the best fit line may under- or over-estimate the occurrence at large magnitudes, sometimes outside the formal error bounds.

Next, the inter-event times of these three complete catalogues before the mainshock, were compared with common statistical distributions used to model inter-event times in Figure 5.26, where the multiplet matching catalogue is in the upper plots, a) and b) in blue, the USGS catalogue is shown in the middle as plots c) and d) in green, and the template matching catalogue is shown in lower plots e) and f) in orange.

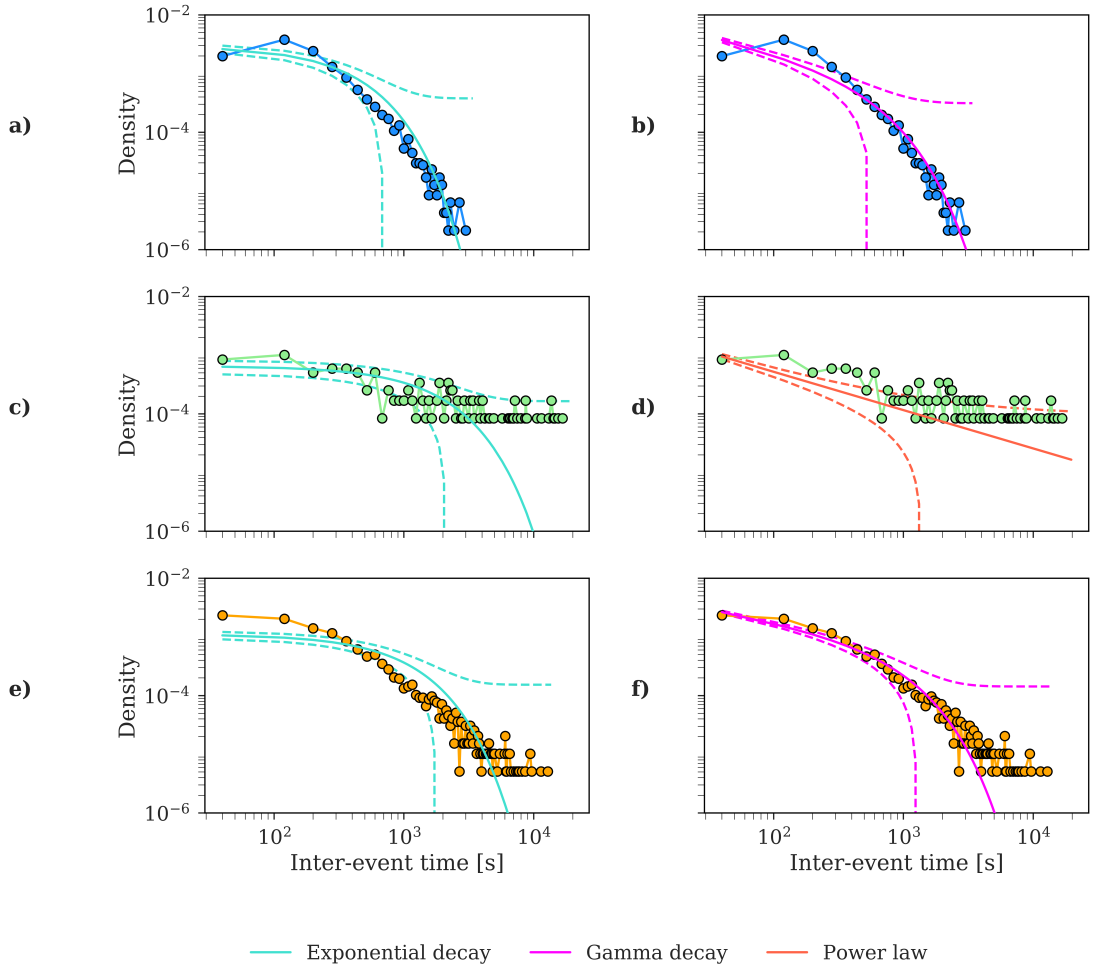

Figure 5.26: Comparison of multiplet matching (blue), USGS (green), and template matching (orange) catalogues inter-event times, shown by filled circles, with the null hypothesis of exponential (cyan) distributions shown in the left plots, and gamma (pink) and power law (orange) distributions in the right plots as solid lines. Confidence intervals of 95% are shown by dashed lines in corresponding colours.

I include exponential (cyan) fits in the left plots of Figure 5.26, and gamma (pink) and power law (orange) fits in the right plots in Figure 5.26 for the three catalogues inter-event times. The counts are normalised in Figure 5.26 to form a probability density, where it is weighted so that the integral of the density over the range, is 1. Further to

this, the 95% confidence interval of the distributions are shown in their corresponding colour, with the bounds marked by a dashed line. The multiplet matching and template matching catalogues both have most of their events occurring at very short intervals, whereas the USGS indicates that their events are more out spread.

As illustrated in Figure 5.26a and Figure 5.26b, the multiplet matching catalogue looks to have a bimodal mixture of both an exponential and gamma fits to describe different parts of the distribution of inter-event times, as observed in aftershock sequences (Touati et al., 2009). This indicates that perhaps the exponential distribution is best for modelling the 'background' events (those not occurring as a direct consequence of another event), and the gamma distribution is the best for the 'offspring' events (those that have been triggered by a preceding event), which are indicative of the temporal correlations observed in aftershock sequences (Corral, 2004; Touati et al., 2009; Naylor et al., 2009). The pure exponential fits generally quite well between 300 and 2,000 seconds, but the gamma fits best in the 600 - 2,000 second region. Neither distribution does well <200 seconds. This is most likely due to the bias from the size of the multiplet window being 28 seconds long, and the removal of any event within 40 seconds of the arrival time of a previous event (i.e. at least 12 seconds between each event) to avoid any events which were close together. Therefore, many events which would have populated this inter-event time would have been removed, so it is not unexpected that the start of the distribution is not well modelled.

The exponential distribution fitted in Figure 5.26c fits the USGS catalogue well <3,000 seconds, with most of the data points occurring within the error bounds. The pure power law (orange line) in Figure 5.26d fits the larger inter-event times better than the exponential and gamma distributions.

The template matching catalogue fits an exponential distribution (Figure 5.26e) well at the larger inter-event times between 3,000 - 6,000 seconds. Whereas the gamma

distribution (Figure 5.26f) fits best at <3,000 seconds. This is consistent with the mixture distribution from the ETAS model as in Touati et al. (2009).

To compare these different distributions, the AIC from Equation 2.10 and BIC from Equation 2.11 were calculated as a statistical measure of which distribution fit these inter-event times the best over the whole range. The null hypothesis is that the exponential (the left distributions in cyan) would fit the data best, as this is indicative of a Poisson process (i.e., independently distributed exponential times). This is compared with a gamma (in Figure 5.26b and Figure 5.26f) and a power law (Figure 5.26d) distribution. These criteria for the inter-event times prior to the mainshock are shown in Table 5.18, where the distributions in Figures 5.26a,c and e are compared with the distributions in Figures 5.26b,d and f, respectively.

	Multiplet matching method	**USGS**	**Template matching**
$AIC_{exponential-gamma/power}$	-1	-1	-24
$BIC_{exponential-gamma/power}$	-29	-24	140

Table 5.18: The Akaike Information Criterion (AIC) from Equation 2.10 and Bayesian Information Criterion (BIC) from Equation 2.11 calculated for the exponential and gamma or power law distributions in Figure 5.26 to measure which fits the inter-event times prior to the mainshock better.

The multiplet matching catalogue in Table 5.18 shows that the AIC and BIC favour the exponential distribution to best approximate the inter-event times of multiplets in this sequence overall. This is deduced as both the AIC and BIC produce a negative score, meaning that the exponential model is better at fitting the whole dataset than the gamma model. This implies that the null hypothesis is not rejected on a first

approximation and that the events are independent, either because there are not many aftershocks, or the aftershocks have been systematically removed from the catalogue. In part, this may be due to the removal of overlapping events at short inter-event times.

If this is the case, it indicates that the null hypothesis cannot be completely rejected here as some events in this catalogue are likely due to random occurrence. However, there is also a confident indication that there are a significant amount of events occurring due to the type of triggering that is commonly observed to be associated with aftershock sequences.

For the USGS catalogue, the AIC and BIC prefer the exponential distribution. This implies the catalogue contains relatively few aftershocks, likely due to the high M_c or a lack of recording of aftershocks of the mainshock.

Alternately, the BIC prefers the gamma distribution as the best fit for the inter-event times of events found using data obtained from the template matching method, whereas the AIC prefers the exponential distribution. This result from the BIC indicates that there are significant numbers of correlated event pairs, most likely due to the lower magnitude threshold obtained, and the presence of multiplets from the same source area.

Next, I observed the normalised cumulative rate at which the multiplet matching (blue), USGS (green) and template matching (orange) catalogues events occurred, as illustrated in Figure 5.27. The UTC times of the M>6.0 events are shown by the orange vertical dashed lines, and the M_W 8.2 mainshock is shown by the red vertical dashed line.

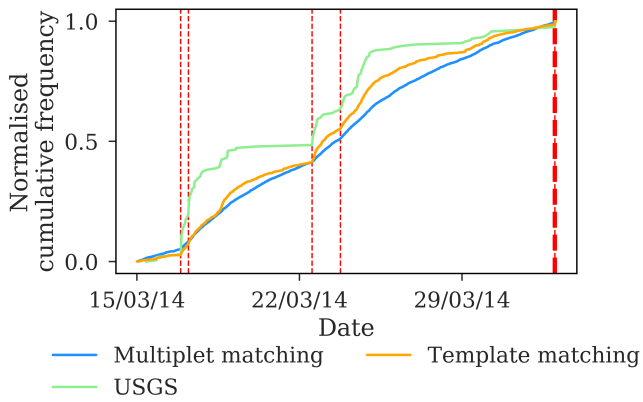

Figure 5.27: Comparison of multiplet matching (blue), USGS (green) and Kato and Nakagawa (2014) (yellow) catalogues normalised cumulative frequency of events to observe event rate. The orange vertical dashed lines show foreshocks with M>6.0, and the M8.2 mainshock is shown by a red vertical dashed line.

Figure 5.27 illustrates that the USGS catalogue contained predominantly the aftershocks of the larger (M>6) earthquakes that occurred prior to the M8.2 mainshock. The template matching catalogue and multiplet matching catalogue show very similar trends in the evolution of the cumulative frequency in Figure 5.27. The template matching catalogue begins to diverge from the multiplet matching catalogue after the M>6.0 earthquakes due to the removal of overlapping events in the multiplet matching method. Hence, the multiplet matching method shows a much more steady slope to failure due to some missing aftershock events.

I also observed the cumulative seismic moment, M_o, for the multiplet matching (blue), USGS (green) and template matching (orange) catalogues in Figure 5.28, with respect to the M_W 8.2 mainshock (heavier red vertical dashed line) and other earthquakes above M_W 6.0 (lighter red vertical dashed lines).

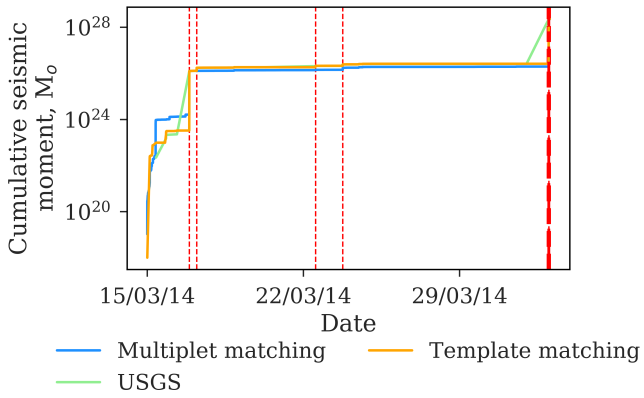

Figure 5.28: Comparison of multiplet matching (blue), USGS (green) and Kato and Nakagawa (2014) (yellow) catalogues cumulative seismic moment of events. The time of the M_W 8.2 mainshock is shown by the red vertical dashed line, and the times of $> M_W$ 6.0 earthquakes are shown by orange vertical dashed lines.

Figure 5.28 illustrates that the largest events have the biggest influence in each of the three catalogues shown here, on the seismic moment and that they all follow the same general trend. This confirms that the main differences in the catalogue are at the lower magnitudes, and these have a low or negligible effect on the total seismic moment.

This dataset has failed to reject the null hypothesis that there is no causal pre-slip or cascade associated with these magnitudes. Instead, the occurrence times and magnitudes of the multiplets indicate that they are the outcome of aftershock processes consistent with ETAS models.

5.4 Results summary

In this chapter I described the results obtained from applying the multiplet matching method to two significant earthquake sequences: the 2004 M_W 6.0 Parkfield and the 2014 M_W 8.2 Iquique earthquakes. From this, I observed the inter-event times, event

rate and magnitudes of the found multiplets and compared these to those obtained in other published catalogues in the approach to a significant mainshock.

The results showed that the events detected through the multiplet matching method in the Parkfield sequence provide new information on the underlying seismicity associated with the preslip model prior to the M_W 6.0 mainshock. There were several cases of an increase in seismic moment, followed by a quiescence between 20th September - 22nd September. This followed a period of quiescence until around 27th September, when the USGS and multiplet matching catalogue detected a significant increase in seismic moment, before levelling out again. However, the multiplet matching method then detected an increase in relatively close together low-magnitude events in the three hours prior to the mainshock, which is consistent with the occurrence of a creep on the fault. As these detected events are multiplets, this means that they are similar events, implying a repeated rupture of the same patch consistent with the preslip model hypothesis. A spatial analysis of the multiplets would be needed to confirm whether the multiplets found are true events. Although the M_c was not lowered significantly in the multiplet matching catalogue, compared to that of the USGS catalogue, the inclusion of these multiplets leads to a higher and possibly more representative $\hat{b}$-value, and a better fit on the inter-event times, that rejected the null hypothesis that the events were a random occurrence. An obvious next step would be to develop methods to combine the two catalogues to develop further understanding.

The events picked up by the multiplet matching method in the Iquique sequence lowered the M_c significantly from 4.0 to 2.9 prior to the M_W 8.2 mainshock. There were many other large earthquakes (M>6.0) prior to this mainshock, therefore there were also some aftershocks of these earthquakes in the sequence examined. This meant that there were many events which overlapped in time, therefore many were removed in the data cleaning stage of the method. In future work, the addition of other stations will allow for these events to not be removed, and therefore the M_c could be lowered even further. This also explains why the inter-event time distribution for this catalogue

does not follow a gamma fit well at the smaller inter-event times, as the event pairs that are correlated in time have been preferentially removed at this stage. There was no particular pattern prior to the mainshock in this sequence in this case, most of which shows the behaviour consistent with transients associated with aftershocks of the previous M>6 earthquakes. Observing this sequence on a longer timescale, both prior to and after the mainshock, might provide more insight. From this analysis, the Iquique multiplet catalogue cannot be confidently described by the preslip or the cascade model as appointed in chapter 2. Instead, the multiplet catalogue behaviour indicates the triggering of large aftershocks with no accelerating cascade, consistent with that of ETAS models.

In the next chapter, I will describe the results of applying the multiplet matching method on three different types of settings: during a seismic swarm with no obvious mainshock, during a volcanic eruptive period, and prior to a large landslide.

Chapter 6

Applications to a seismic swarm, volcanic seismicity and seismicity preceding a landslide

6.1 Introduction

In the previous chapter, I used the multiplet matching method to find multiplets and analyse their temporal evolution in two different earthquake sequences. In this chapter, I demonstrate the further application of the multiplet matching method to a seismic swarm with no clear mainshock (near Diemtigen, Switzerland in April 2014), during a volcanic eruptive period (Mount St Helens volcano, USA in December 2004) and prior to a large landslide (leading up to the Nuugaatsiaq, Greenland landslide on 17th June 2017).

The aims of this are to demonstrate the general applicability of the multiplet matching technique, to examine the improvement on the catalogues and to assess the significance of any new insights for the different types of failure compared to pre-existing

earthquake catalogues around the times of these events. I examine the extent of such improvements by analysing the time series of events, and the statistical properties such as the frequency-magnitude relations and inter-event time distributions, in a similar way as done in the previous chapter.

6.2 Diemtigen, Switzerland

6.2.1 Introduction

Switzerland has a relatively moderate level of seismicity mainly caused by the African plate subducting below the Eurasian plate, as well as from induced origins related to geothermal energy projects (Deichmann and Giardini, 2009) or the construction of tunnels (Husen et al., 2013). The largest historical earthquake in this region has been estimated to have been M_W 6.7 - 7.1 near Basel in 1356 (Fäh et al., 2009), however the seismicity tends to typically be less than M_W 5.

The area near Diemtigen was chosen because there were several seismic swarms during April 2014, with seismic events with local magnitudes reaching up to M_L 2 and a depth of 9km. A swarm can be defined as an extended period of localised activity with no obvious distinct mainshock (Roland and Mcguire, 2009). The seismicity eventually began to decrease by the end of 2014, and then increased again in July 2015, lasting until September 2015 (Diehl et al., 2015). Several earthquakes within these swarms were felt by the local population, with local magnitudes ranging between 2.7 and 3.2 in 2014. Therefore, I chose to start this catalogue on the 13th April 2014 to capture the beginning of the swarm in this region, and to finish the catalogue on 1st May 2014. The locations of the earthquakes from the Swiss Seismological Service (Schweizerischer Erdbebendienst, SED) catalogue for this time period are shown in Figure 6.1, where

the colour of the dots denotes the date and the radius corresponds to magnitude. These events were detected using standard phase-picking methods.

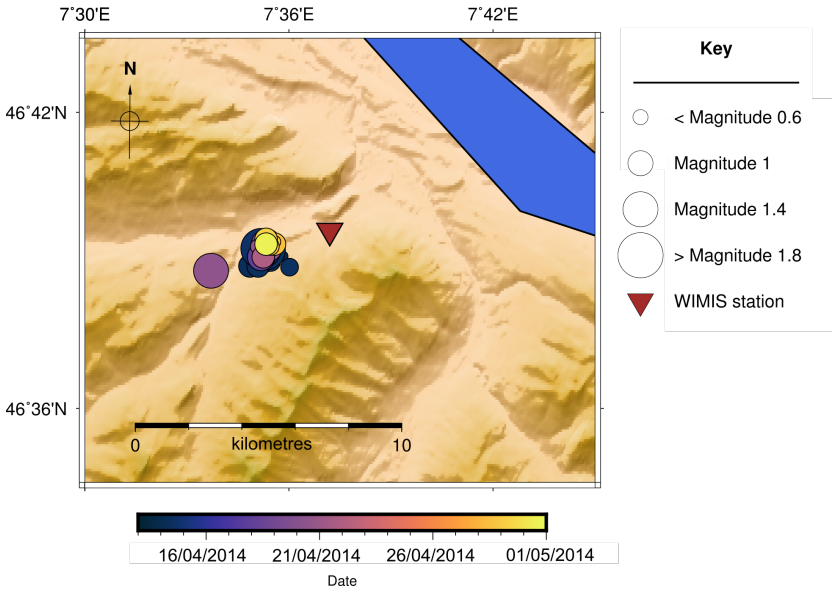

Figure 6.1: Illustration of the locations of the 40 earthquake events in the SED catalogue for the Diemtigen, Switzerland earthquake sequence from 13th April - 1st May 2014.

I downloaded waveform data for this time period from the WIMIS seismometer (location -46.66°, 7.62° in latitude and longitude, respectively) from the open-access website of the Incorporated Research Institutions for Seismology (IRIS), and I applied a band-pass filter between 5Hz and 30Hz to isolate the dominant frequencies in the known events, and downsampled the data to 60Hz. The seismogram for this chosen earthquake sequence is illustrated in Figure 6.2.

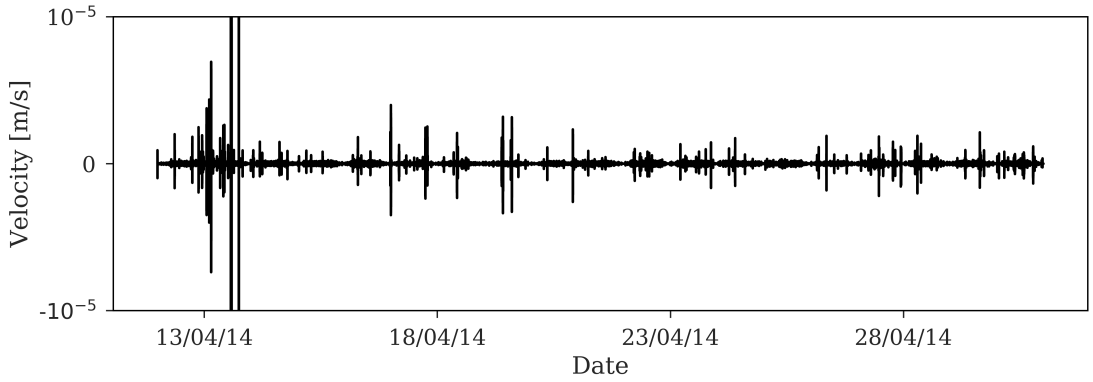

Figure 6.2: Illustration of the seismic swarm sequence in Diemtigen, Switzerland from 13th April - 1st May 2014. This illustration has been clipped at $\pm 10^{-5}$ m/s in order to better show the smaller signals in this sequence.

6.2.2 Method

The SED catalogue contained a total of 40 events in this time period for this region (Figure 6.1). I chose the three highest magnitude earthquakes in this catalogue (local magnitudes of 1.5, 1.6 and 1.6) to be used as templates. The runtime of this dataset with the multiplet matching method was approximately 14 hours.

The locations of the templates are shown in Figure 6.3, with the size of the dots corresponding to the magnitude, and the colour showing the time of the event (different scale to Figure 6.1).

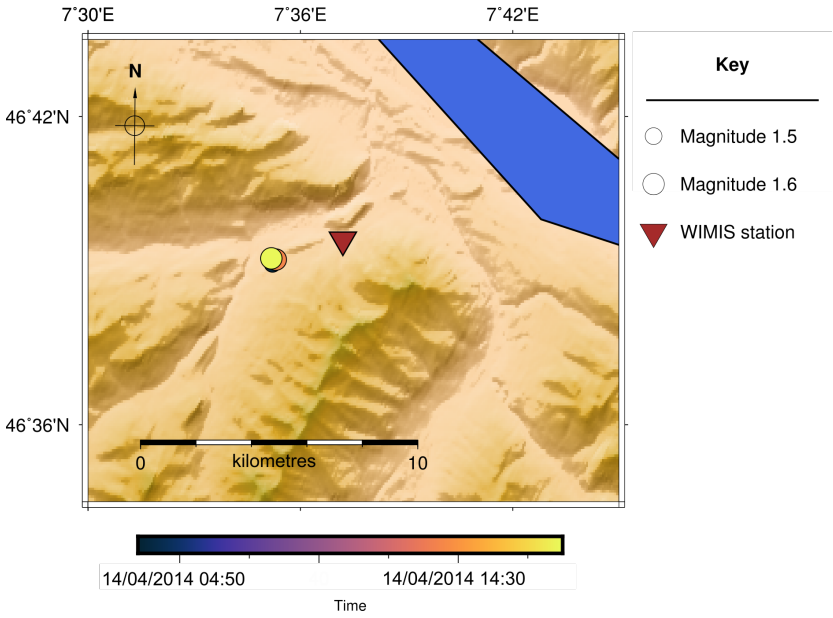

Figure 6.3: Illustration of the locations of the three template earthquake events in the SED catalogue for the Diemtigen, Switzerland earthquake sequence. The WIMIS seismometer used in this study is outwith the bounds, and is stationed at -46.66°, 7.62° in latitude and longitude, respectively.

The threshold of M_L 1.5 was chosen as a minimum, as the three events above this were well recorded on the WIMIS seismometer used, which was located within 3km from their epicentres. The waveforms for these three template events are shown in Figure 6.4a-c, with a green box indicating the time window used. Events slightly below this threshold, like that in Figure 6.4d were still distinguishable, but were not used as templates as they appeared to be visually very similar to one of the three largest template events. Thus it was not necessary to search for multiplets of seismograms such as Figure 6.4d, as the multiplets would be found by the template traces in Figure 6.4a-c.

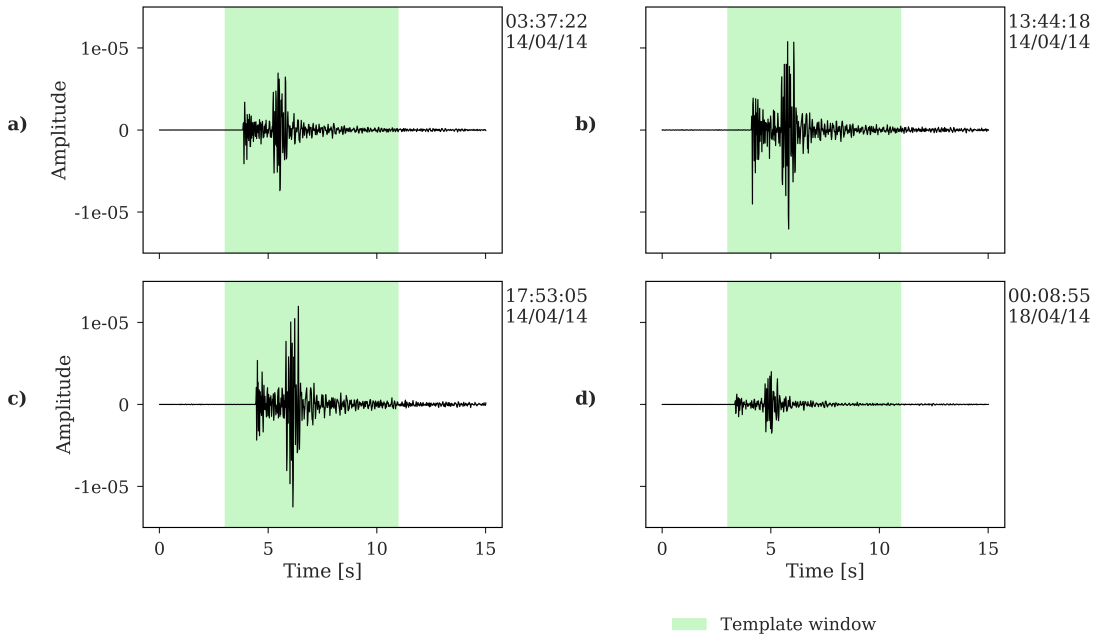

Figure 6.4: Illustration of three templates used (a - c), and another smaller event (d) in the Diemtigen earthquake sequence in Switzerland from 13th April - 2nd May 2014. The UTC date and start-time of each template is displayed in the upper right of each window. These were identified in the SED catalogue, and adjusted in time to when they appeared on the seismometer used.

The earthquake event in Figure 6.4a had a M_L=1.5, the events in Figure 6.4b and c had the same magnitude, M_L=1.6, and occurred early on in the sequence. The smaller event in Figure 6.4d had a M_L=1.1, and occurred several days after the events in Figure 6.4a-c.

The multiplet matching catalogue detected 1,466 unique multiplets from the three templates from Figure 6.4a-c, which were at least moderately correlated (cross-correlation coefficients > 0.5). An example of those found in the moderately correlated catalogue are illustrated in Figure 6.5, which shows the 1,333 multiplets found with the first template (6.4a) in a 'stack plot', which is a 2d greyscale image in the lower diagram, where each point of the waveform is converted into a discrete level of grey.

The stack (i.e. the sum) of all these waveforms is shown in the upper diagram. The other 133 unique multiplets for this catalogue were found by the other two template traces (Figure 6.4b,c).

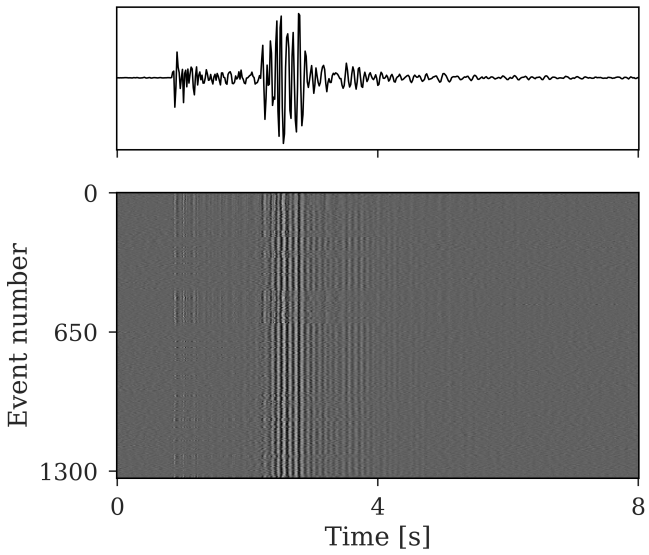

Figure 6.5: Normalised stack of 1333 repeating events in family 1 found through the multiplet matching method from the first template, with a cross-correlation threshold of 0.5. The summed waveform is shown in the upper plot, with the lower plot showing a greyscale image of all waveforms.

The wave attributes are well aligned particularly for the S-waves at around the three second mark in Figure 6.5. The waves are well aligned as a result of the cross-correlation technique in the multiplet matching method, which synchronises the signals to the point in time where there is a maximum similarity between the signals. As the S-wave has the largest amplitude, the cross-correlation function adjusts the time to get the best fit around this part of the sigal. The P-waves (around one second) and the coda waves (> four seconds) are not as clearly defined in the lower plot of Figure 6.5 due to these events only being moderately similar (cross-correlation coefficients > 0.5). This means that events which are not as similar are being included in this catalogue.

The dissimilar coda waves indicate that these events are in a slightly different location to each other (as this part of the wave is most sensitive to relative location).

I then ran the multiplet matching method with a higher cross-correlation threshold of 0.7, thus detecting only events which are considered highly correlated. This reduced the runtime to approximately 5 hours on the supercomputer. The multiplet matching method found a total of 220 unique multiplets (cross-correlation coefficients > 0.7) from this second run. The stack plot for the higher similarity catalogue in Figure 6.6 shows the 150 multiplets found with the first template in a stack plot. The other 70 unique multiplets were found by the second and third templates.

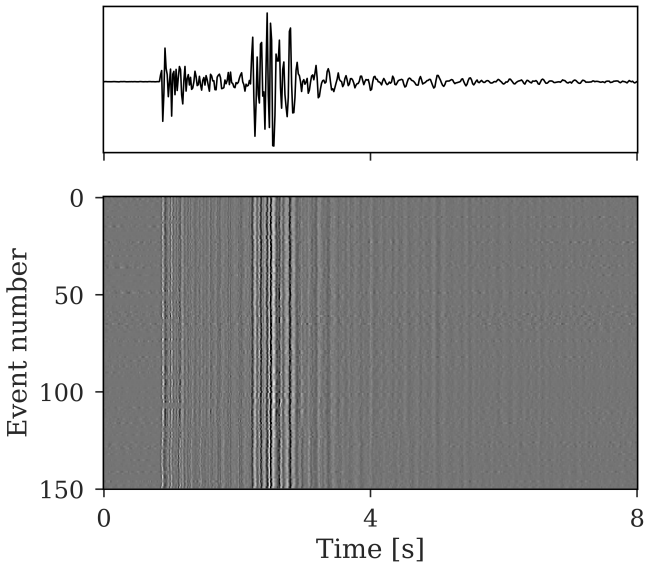

Figure 6.6: Normalised stack of 150 repeating events in family 1 found through the multiplet matching method from the first template, with a cross-correlation threshold of 0.7. The summed waveform is shown in the upper plot, with the lower plot showing a greyscale image of all waveforms.

Figure 6.6 shows a much clearer alignment of all parts of the wave (P, S and coda), indicating a much more localised area in which these multiplets were occurring. As there is a considerable difference between the moderately correlated (cross-correlation

threshold = 0.5) catalogue in Figure 6.5 and the highly correlated (cross-correlation threshold = 0.7) catalogue in Figure 6.6, I chose to analyse only the multiplets found in the highly correlated catalogue from here. This highly correlated multiplet matching catalogue contained 26 of the 40 events featured in the original SED catalogue, thus missing 14, as summarised in Table 6.1.

Events	**Multiplet matching**	**SED**
Found	150	40
Matching	-	26
Missing	-	14
New	-	124

Table 6.1: Summary of the found, matching, missing and new events in the highly correlated multiplet matching and SED catalogues.

The events were missed because they were below the finite detection threshold for highly similar templates. Some of the missed events present in the SED catalogue were also within the overlap range used to reduce the multiplet matching catalogue by removing events within 15 seconds of one another (for reasons studied in section 3.3.2).

Once the highly correlated events were identified, I estimated their magnitudes using Equations 3.9 - 3.10 (described in section 3.4). Figure 6.7 illustrates several values of the scaling parameter c, where each known template event from the SED catalogue is used to calculate the other known template events in the catalogue. The value of c which I judged to estimate the known magnitude the best was $c = 0.9$, which is shown as the light green dots in Figure 6.7. This value of c was then used in Equations 3.9 - 3.10 to calculate the estimated magnitudes (M^e) of the new multiplets.

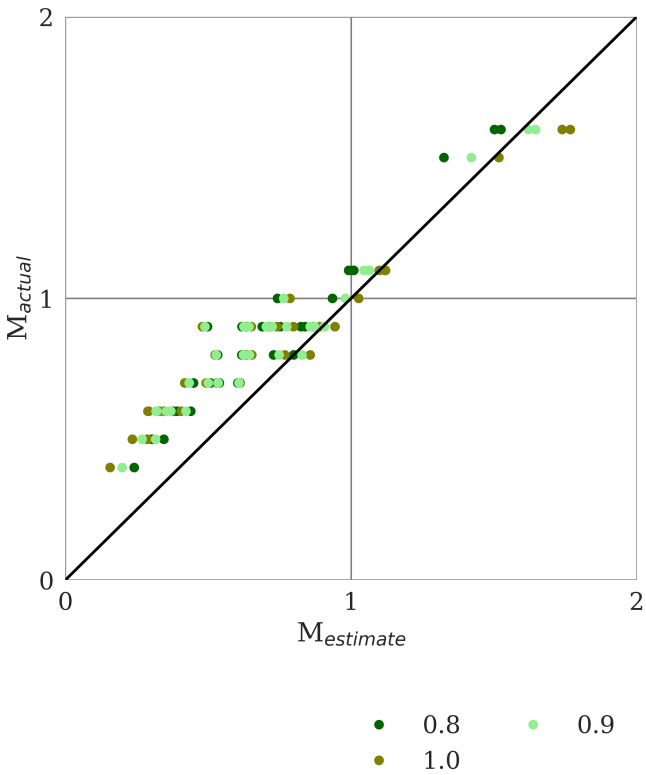

Figure 6.7: Illustration of working out c in Equations 3.9 - 3.10 to best estimate the magnitude of known template events (M_L) from the SED catalogue.

An example of the original and final master (composite) templates, and six new multiplets found with the multiplet matching method are shown in Figure 6.8.

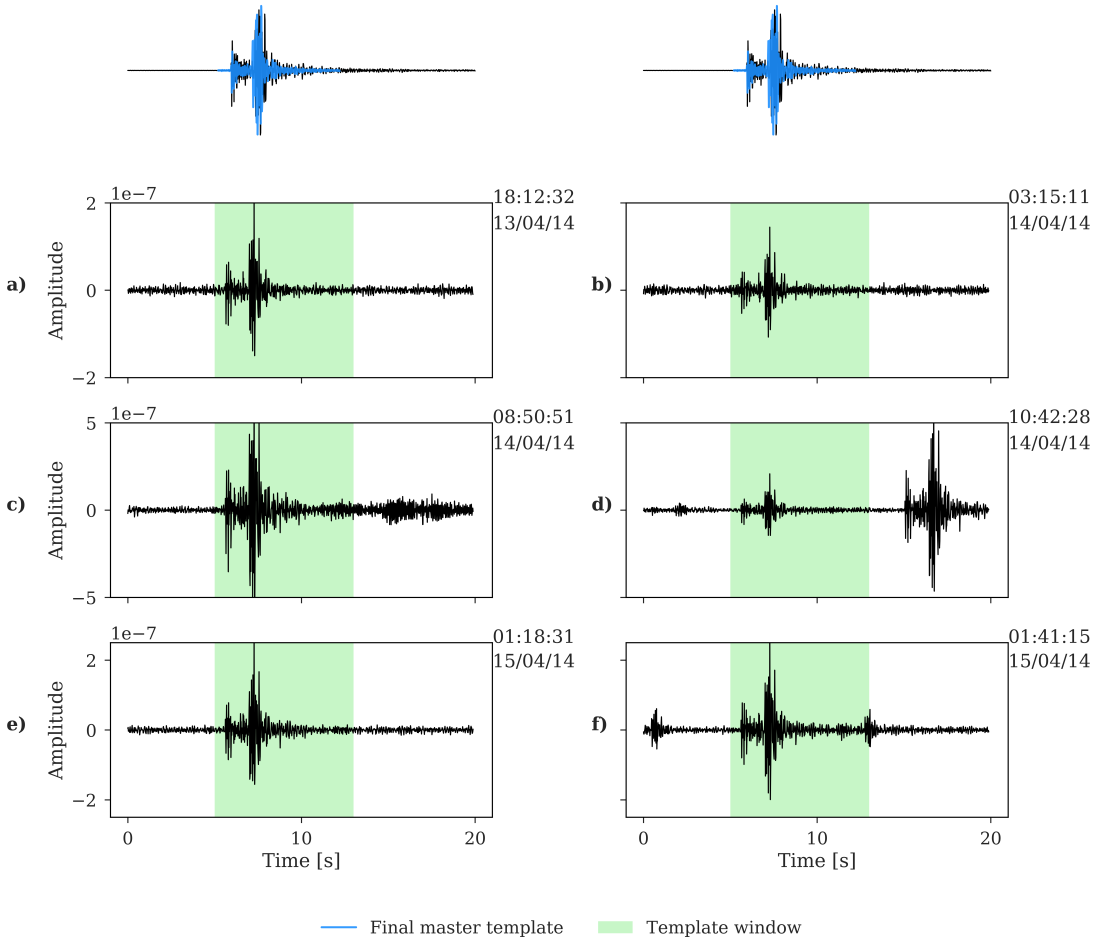

Figure 6.8: Comparison of six multiplets found from the multiplet matching method. The green box indicates the multiplet window. The horizontal waveforms are scaled to the same y-axis. The starting time and date of each multiplet window is shown in the upper right of each plot. The original template trace and final master template (blue) is shown twice in the upper row for both columns as reference.

The upper diagram shows the original template event, which is compared to the final master template event (blue) used in the multiplet matching method (from Step 7 of section 3.3.1). The original template event was recorded as M_L=1.6 in the SED catalogue, and occurred at 13:44 on 14/04/14, with an epicentre at 46.65°, 7.59°, in latitude and longitude, respectively. The window that defines the multiplet is shown

by the green box in Figure 6.8, with the time when this occurred on the seismometer shown in the upper right. The multiplets found by the final master template are shown in Figure 6.8a-f, where the green box indicates the multiplet window, which is aligned with the upper templates. I chose to show these particular multiplets, as they have a very high cross-correlation coefficient with each other (cross-correlation value > 0.9).

The multiplet in Figure 6.8a had an estimated magnitude, M^e, of -0.11, and the multiplet in Figure 6.8b had M^e=-0.19. In the second row of multiplets shown in Figures 6.8c and 6.8d, the former had M^e=0.38 and the latter M^e=-0.02. Finally, the third row of multiplets illustrated in Figures 6.8e and 6.8f had M^e=0.50 and M^e=-0.01, respectively.

6.2.3 Statistical Analysis

The statistical metrics for the events associated with the Diemtigen sequence are presented and discussed in this subsection. This includes a time series for the magnitude and inter-event times of the events, and the result of frequency-magnitude distributions, inter-event times and event rate variation. The SED and multiplet matching catalogues are both used as input, and the results compared.

First, I show the temporal evolution of the multiplets found by the multiplet matching method, as illustrated in Figure 6.9. The multiplet events are denoted by blue circles, with the known events from the SED catalogue shown in green triangles. The inter-event times (upper diagram), peak amplitude (middle diagram) and magnitude (lower diagram) are all included to reveal whether there were any patterns in this sequence.

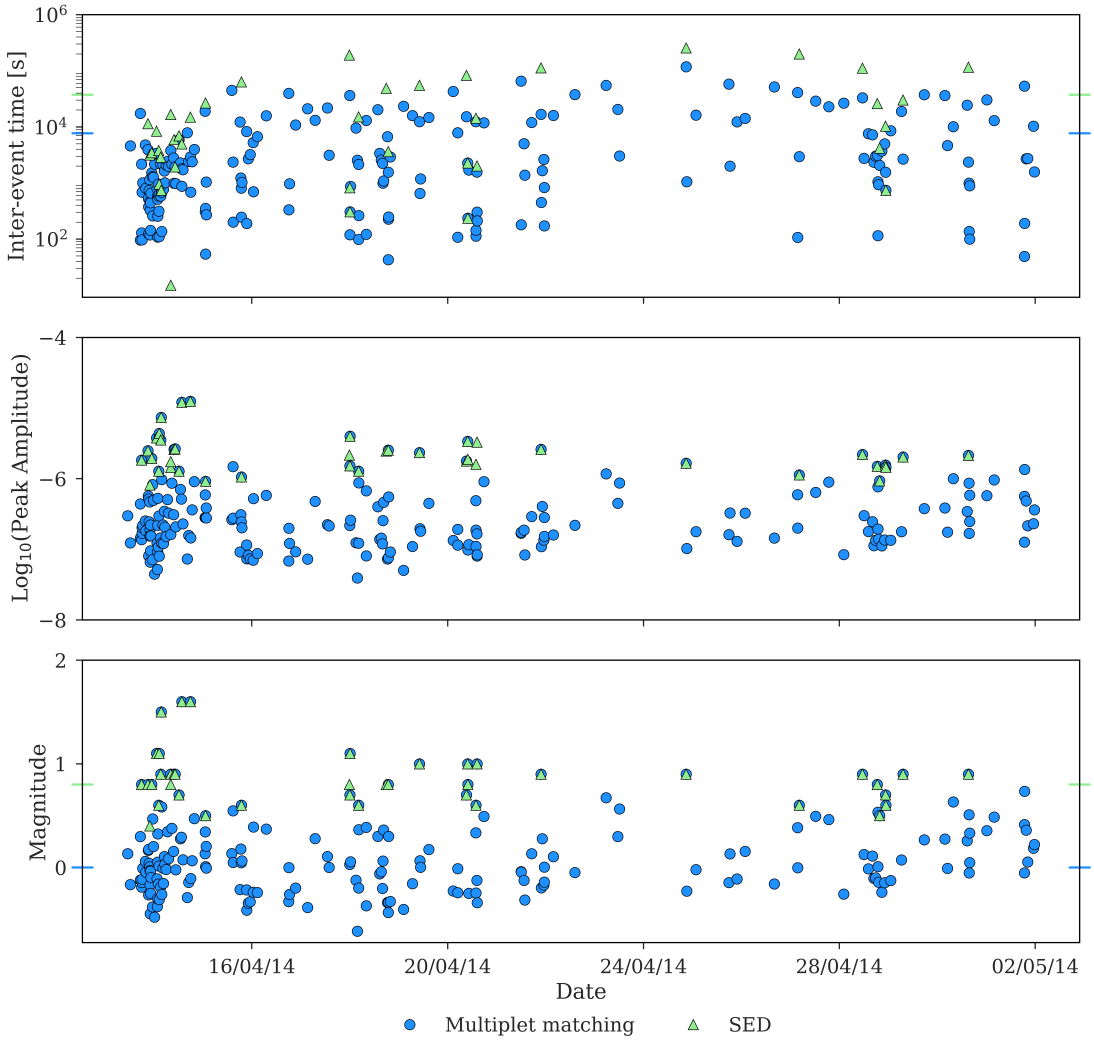

Figure 6.9: Time evolution of SED catalogue (green triangles) and events found by multiplet matching (blue circles), of their inter-event times (upper), peak amplitude (middle), and magnitude (lower). Coloured horizontal tick lines show average inter-event time (upper), and the magnitude of completeness, M_c, (lower) per catalogue.

The average inter-event times for the events found from the multiplet matching method (blue) and the SED catalogue (green) are shown by the horizontal tick lines in the top diagram, where the colour represents the catalogue in Figure 6.9. The majority of events in both the multiplet matching and SED catalogue accompanied the largest

events in this sequence, which occurred within the first few days. The average inter-event time is smaller for the multiplet matching catalogue, as many more events have been detected, particularly early on in the sequence. The SED catalogue is much more sparse, so its average inter-event time is much higher.

The middle plot of Figure 6.9 shows the peak amplitude of the multiplet matching and SED events. This is included as a check on the magnitudes calculated in the lower plot of Figure 6.9, as these should be proportional to one another. The magnitudes of the multiplets in the lower diagram are relatively small, with most having an estimated magnitude <1. The peak amplitude of the multiplets are proportional to the pattern seen by the magnitudes in the lower diagram, providing confidence in the estimated magnitude. The M_c for these two catalogues are shown by the horizontal tick lines on the two y-axes in the lower diagram, where the colour represents the catalogue used. This confirms that the multiplet matching catalogue contains many more lower magnitude events than the SED catalogue alone, hence the lower M_c.

The rates at which the multiplets are occurring appear to be reasonably stable, apart from the lead up to the relatively higher magnitude events (magnitudes 1.5-1.6) at the start of the time period studied. A zoom in on Figure 6.9 to around the time of these three earthquakes is illustrated in Figure 6.10, where their times are shown by red vertical dashed lines.

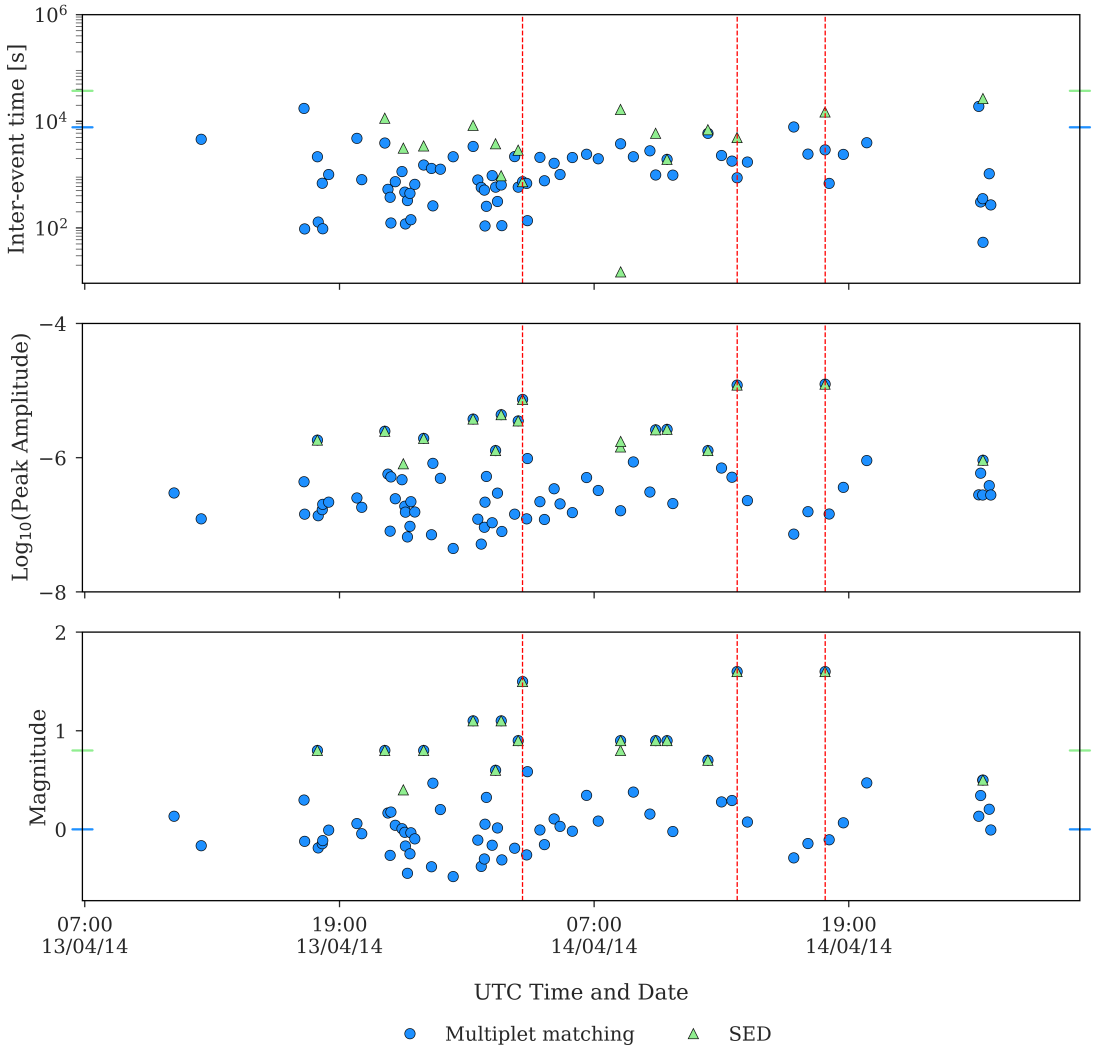

Figure 6.10: Time evolution of SED catalogue (green triangles) and events found by multiplet matching (blue circles), of their inter-event times (upper), peak amplitude (middle), and magnitude (lower). Coloured horizontal tick lines show average inter-event time (upper), and the magnitude of completeness, M_c, (lower) per catalogue.

The temporal evolution of the seismicity in this period shows the typical characteristics of an earthquake swarm, as there was no clear mainshock (Figure 6.10). However, Figure 6.10 shows that there was an increase in low-magnitude events prior to the first of the three largest earthquakes in this time period for the two catalogues. This could

be an indicator to some underlying nucleation mechanisms, which became the driver for this seismic swarm, in turn associated with a repeated rupture of the same patches, such as creep from temporary fluid overpressure (Diehl et al., 2015).

Next, I created a frequency-magnitude distribution of the multiplet matching (Figure 6.11a in blue) and SED (Figure 6.11b in green) event catalogues.

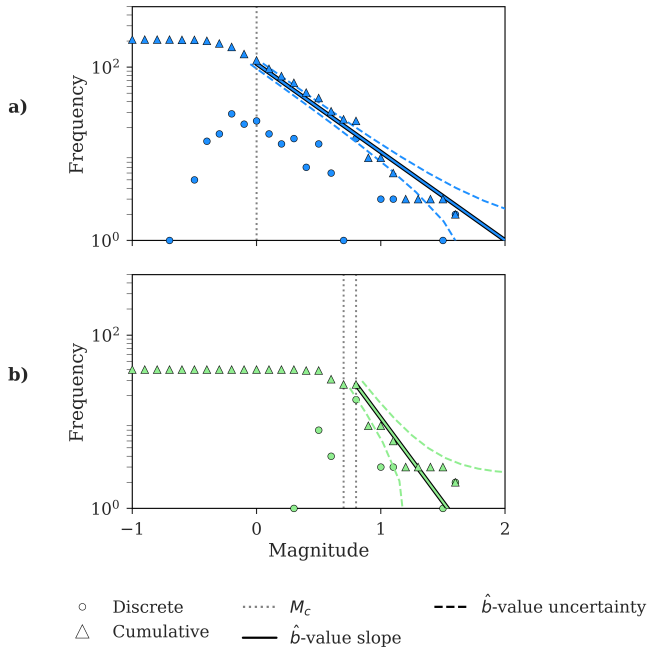

Figure 6.11: Comparison of the frequency-magnitude distributions for events in the multiplet matching (plot a in blue) and SED (plot b in green) catalogues. The discrete (filled circles) and triangles (filled triangles) frequencies are shown for both catalogues. The $\hat{b}$-value corresponding to each catalogue is shown by the filled line, where the colour matches the catalogue, and the dashed lines show the uncertainties on the slope. The grey dotted lines illustrate the different values of M_c calculated.

The grey dotted lines in Figure 6.11 illustrate the different values for the magnitude of completeness, M_c, which were estimated through the workflow in Roberts et al. (2015) (Figure 2.3), for each catalogue. The $\hat{b}$-value and its uncertainty, which were

then estimated from the chosen M_c using the MLE method (Equations 2.5 - 2.6). They are shown for each catalogue in Figure 6.11, where the solid line on each plot represents the MLE and dashed lines show the bounds of the uncertainty from the uncertainty in $\hat{b}$-value.

The results of the b-value stability (BVS) method are shown in Figure 6.12. In this case, the b-value stabilises (horizontal dot-dashed line) when b_{ave} is within one error of the b_{MLE}.

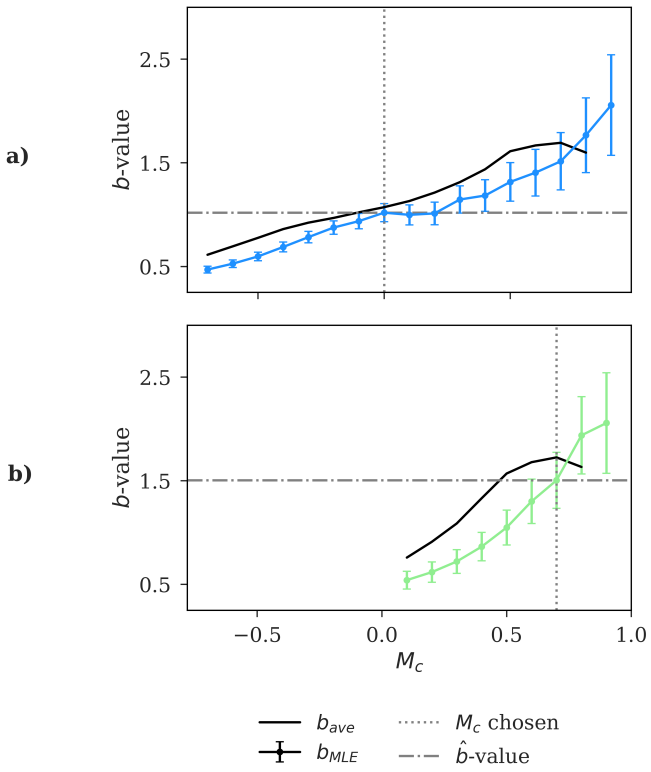

Figure 6.12: Comparison of b-value stability curves, showing the b-values for each magnitude of completeness, M_c, for the multiplet matching (plot a in blue) and the USGS (plot b in green) catalogues. The vertical dotted line shows the chosen M_c from this method, and the horizontal dashed line shows the b-value at this point. The M_c is chosen as when the average of the five successive b-values (black line) are within one error of the b-value.

A summary of the M_c and $\hat{b}$-value results from the BVS and the Maximum Curvature (MaxC) methods is shown in Tables 6.2 - 6.3.

	BVS	**MaxC**
M_c	0.0	0.0
$\hat{b}$-value	1.0 ± 0.074	1.0 ± 0.074

Table 6.2: The magnitude of completeness, M_c, for the b-value stability (BVS) and Maximum Curvature (MaxC) methods, and the $\hat{b}$-value plus uncertainty from the MLE (Maximum Likelihood Estimation) method (Equations 2.5-2.6), for the multiplet matching catalogue in Figure 6.11a for each estimate of M_c.

	BVS	**MaxC**
M_c	0.70	0.80
$\hat{b}$-value	1.5 ± 0.22	1.9 ± 0.39

Table 6.3: The magnitude of completeness, M_c, for the b-value stability (BVS) and Maximum Curvature (MaxC) methods, and the $\hat{b}$-value plus uncertainty from the MLE (Maximum Likelihood Estimation) method (Equations 2.5-2.6), for the SED catalogue in Figure 6.11b for each estimate of M_c.

Following Figure 2.3 of the workflow of Roberts et al. (2015), the results in Tables 6.2 illustrate that the simpler MaxC method is sufficient for the multiplet matching catalogue, as the M_c's agree within ± 0.1 and the b-value error is <0.25. In fact, all parameters are indepedent of whether BVS or MaxC is used in this case. Therefore, the M_c for the multiplet matching catalogue is 0.0, with a $\hat{b}$-value of 1.0 ± 0.074. For the SED catalogue, the BVS method is instead preferred as although the M_c's are within ± 0.1, which indicates an initial preference for the MaxC method, the error is >0.25. Hence, the BVS method is preferred as the error is <0.25 for this method. Therefore, the best estimate of M_c for the SED catalogue is 0.70, with a $\hat{b}$-value of 1.5 ± 0.22.

These values of M_c and $\hat{b}$-values were used to plot the best fit lines and uncertainty ranges for the frequencies in Figure 6.11.

The best fit line for the SED catalogue in Figure 6.11b shows a much steeper slope which underestimates the likelihood of the two M_L 1.6 events in this sequence, although they are not outside the uncertainty ranges shown. The $\hat{b}$-value calculated for the SED catalogue (1.5 ± 0.22) fits with the general b-value for Switzerland of 1.39, as estimated in Godano et al. (2014), however it is outwith the multiplet matching catalogue's $\hat{b}$-value of 1.0 ± 0.074. The best fit $\hat{b}$-value line in Figure 6.11a for the multiplet matching catalogue shows that this $\hat{b}$-value fits the data very well, except that it overestimates the likelihood of the largest events in this time period, however they are generally within the uncertainty ranges shown. In conclusion, the swarm data has a significantly smaller b-value for the multiplet matching catalogue, and one that agrees with that expected of tectonic seismicity of b=1.

Next, I examined the inter-event times of the multiplet matching (Figure 6.13a) and SED (Figure 6.13b) catalogues. These were compared with two known statistical distributions to model the processes associated with these events.

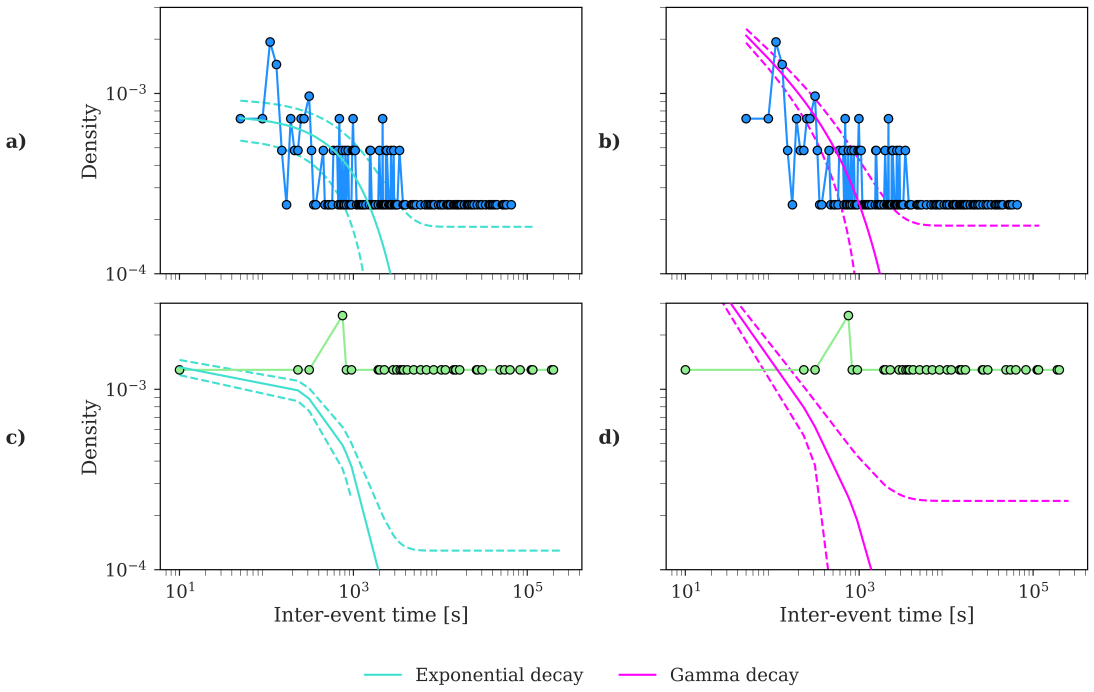

Figure 6.13: Comparison of multiplet matching (a, b) and SED (c, d) catalogues inter-event times, with gamma (pink) and exponential (cyan) distributions. Confidence intervals of 95% have been added to both distributions, and are shown by their corresponding colour and boundaries as dashed lines.

I include an exponential distribution (cyan) to test the null hypothesis that the inter-event times of earthquakes that are at least 15 seconds apart are a Poisson process, and a gamma distribution (pink) to test for correlated and uncorrelated event pairs, as seen in the ETAS model (Bak et al., 2002; Touati et al., 2009). The 95% confidence intervals for these distributions have also been added to Figure 6.13a-d to account for errors.

The multiplet matching catalogue in Figure 6.13a and b shows that both the exponential and gamma distributions fit the data well <3,000 seconds. The shortest inter-event times appear better modelled at <200 seconds by an exponential decay, and it provides a reasonable fit up to 3,000 seconds. The gamma distribution is best at modelling the short to mid inter-event times from around 200-2,000 seconds, but with a

significant number which lie outwith the confidence interval. This indicates that there is a mixture of uncorrelated and correlated event pairs within the multiplet matching catalogue. This mixture between two fits is likely due to the catalogue only containing the high-quality waveforms (cross-correlation >0.7), which has removed events which were not highly correlated. This has essentially taken out many events at different time windows, which has biased the inter-event time distributions.

The SED catalogue in Figure 6.13c and d shows that both the exponential and gamma distributions did not fit the inter-event time distributions well. The events occurred far apart in time and in no particular pattern apart from an increased probability of being around 800 seconds apart. This lack of a well-fitting model is most likely due to the sparsity of the catalogue.

To further analyse the distributions, I include the Akaike Information Criterion (AIC) from Equation 2.10 and Bayesian Information Criterion (BIC) from Equation 2.11 for both distributions as a measure of which statistical distribution was preferred. These criteria for the inter-event times are shown in Table 6.4.

	Multiplet matching method	**SED**
$AIC_{exponential-gamma}$	-1	-1
$BIC_{exponential-gamma}$	-59	-21

Table 6.4: The Akaike Information Criterion (AIC) from Equation 2.10 and Bayesian Information Criterion (BIC) from Equation 2.11 calculated for the exponential and gamma distributions in Figure 6.13 to measure which fits the inter-event times the best.

The resultant values in Table 6.4 indicate that based on the AIC and BIC, a preference for the exponential distribution best overall fits the multiplet matching and SED catalogues, with a very strong preference for the BIC for the exponential model.

Next, I examined the cumulative rate at which the multiplet matching (blue) and SED (green) events occurred in time, as illustrated in Figure 6.14.

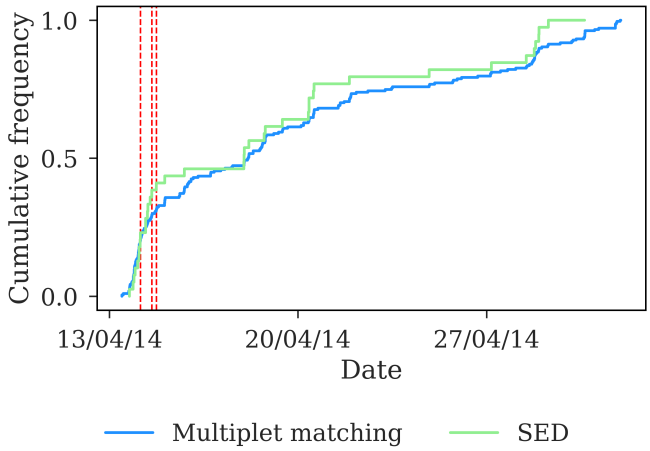

Figure 6.14: Comparison of multiplet matching (blue) and SED (green) normalised cumulative frequency of events to observe event rate.

The cumulative event rate in Figure 6.14 has been normalised for an easier comparison between the two catalogues. The rate of events in Figure 6.14 seems relatively unstable after an initial transient for the SED catalogue, with several points of significantly increased seismicity, particularly around the time of the three largest events early on in the sequence. Overall, the multiplet matching catalogue seems smoother and more stationary after the initial transient. The rate of the multiplet matching events follows the SED event rate closely, indicating that the driver behind the known SED events, could also be driving the low-magnitude events in the multiplet matching catalogue. The event rate can also be examined by giving weight to the event size, by observing the cumulative seismic moment, M_o, for the multiplet matching (blue) and SED (green) catalogues in Figure 6.15.

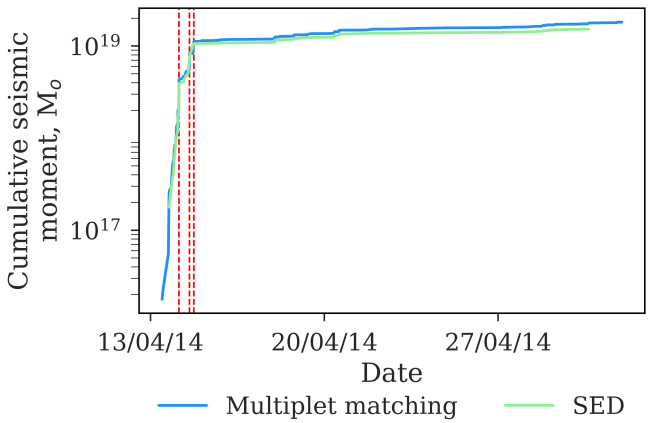

Figure 6.15: Comparison of multiplet matching (blue) and USGS (green) cumulative seismic moment of events.

Figure 6.15 indicates that the majority of M_o for the multiplet matching and SED catalogue occurred in the first few days of the time period studied during the transient swarm on Figure 6.14. There is a significant increase in event rate and cumulative moment during this time, and then a stable increase at a lower rate for the remainder of the catalogues. The curve for the multiplet matching catalogue begins to deviate from the SED catalogue but the difference is negligible on Figure 6.15 because the multiplet matching events are smaller. Although this seismicity was not associated with known faults prior to the start of this sequence, Diehl et al. (2015) found that it was approximately 4km away from the epicentre of the historic 1729 M5.2 Frutigen earthquake (Fäh et al., 2003), hence it is possible that the swarm is related to this earlier earthquake as long-lived aftershocks on persistent zones of weakness (Wang et al., 2017).

The events included in the multiplet matching catalogue are highly correlated with one another. This is consistent with the hypothesis that creep drives regular failure of the same fault patches, in turn producing repeated events with similar waveforms. This is indicative of the preslip model, where the multiplets are a part of an ongoing process. The use of the multiplet matching method in this sequence has produced a more

complete catalogue with significantly lower M_c, allowing for a clearer understanding of the driver behind this seismic swarm.

6.3 Mount St. Helens volcano, USA

6.3.1 Summary

Mount St. Helens is a volcano in the Cascade Range, located in southwestern Washington State, USA. It is the most active volcano in North America, with several recorded major explosive eruptions and many smaller eruptions taking place (Scott et al., 2008; Moran et al., 2008a). From late September 2004, the volcano had increasing seismic swarms with earthquakes occurring roughly once a minute, within 2km of the surface (Moran et al., 2008a; Chouet and Matoza, 2013). From October 2004, uplift began to grow steadily, with cracks being observed through December, leading to the formation of a new spine of lava (Poland et al., 2008).

To observe seismic signals that might be related to this steady growth, I downloaded a three day seismogram recorded at the HSR seismic station on the Pacific Northwest Seismic Network (PNSN) operated by the University of Washington (UW), located on the south ridge of the Mount St Helens volcano, USA from 15th - 18th December 2004, as this period showed a time of constant periodic events occurring within 1km of the surface. The locations of the HSR station and of the earthquakes recorded, are shown in Figure 6.16.

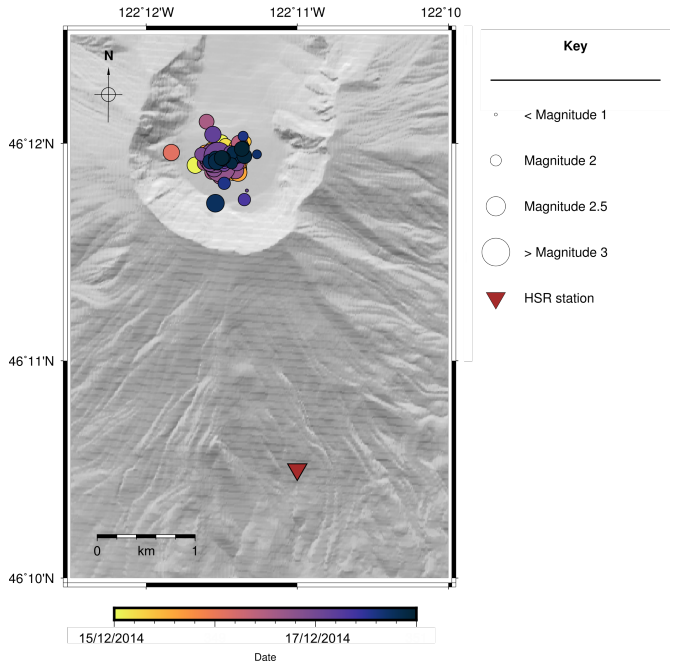

Figure 6.16: Illustration of the location of the HSR station (brown triangle), and the 97 earthquake events (coloured dots, where colour corresponds to date) in the PNSN catalogue for the seismicity observed near the Mount St. Helens volcano, USA, on 15th - 18th December 2004.

This timeframe covered the period reported by Poland et al. (2008) as when the steady uplift and any associated seismic activity were occurring. I band-pass filtered between 0Hz and 8Hz and downsampled the data to 25Hz after observing where the dominant frequencies were for the waveforms in a spectrogram. The full waveform data for this time period is illustrated in Figure 6.17.

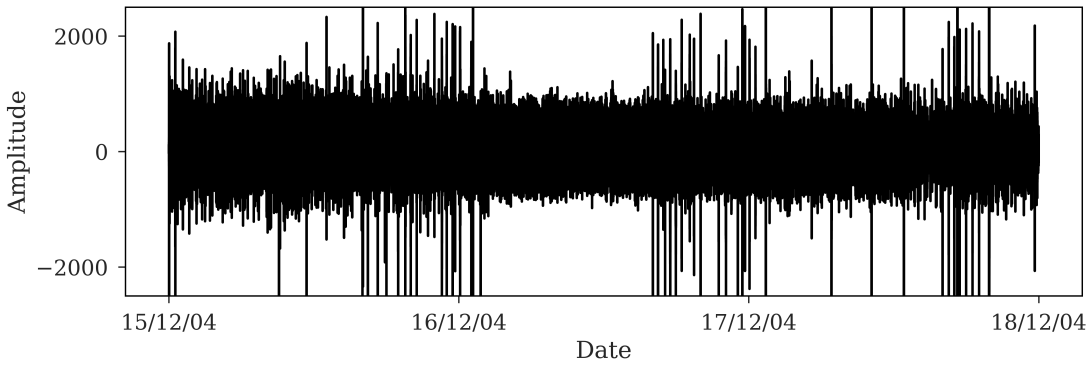

Figure 6.17: Illustration of the seismogram covering three days of data during a repetitive seismicity period near the Mount St. Helens volcano in USA. Data is from the Pacific Northwest Seismic Network, from the EHZ channel from the HSR station within the University of Washington network.

The events occurring in Figure 6.17 have previously been called 'drumbeat' earthquakes due to their highly repetitive nature and resemblance of the sound pattern that is produced from the beating of a drum (Moran et al., 2008a). An example of how repetitive these earthquakes were can be seen in the zoomed in version of Figure 6.17 in Figure 6.18, showing 20 minutes of repetitive seismicity with a steady 'beat' but varying signal amplitudes.

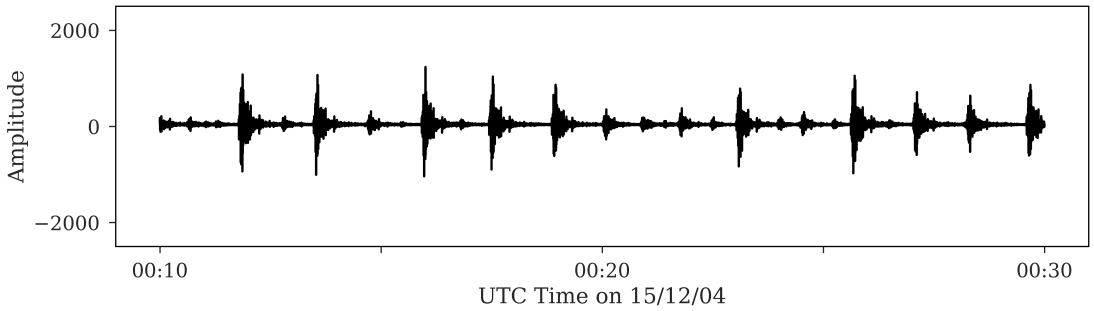

Figure 6.18: Zoomed in version of Figure 6.17, showing 20 minutes of repetitive seismicity, recorded from near the Mount St. Helens volcano in USA. Data is from the Pacific Northwest Seismic Network, from the EHZ channel from the HSR station within the University of Washington network.

6.3.2 Method

The PNSN catalogue contained 97 events in their catalogue during this three day period for this region, where their locations were shown in Figure 6.16, with the colour of the dots denoting the date and the size corresponding to the magnitude. In this case, I did not choose any template traces a priori because of the variety of possible template events. Instead, I applied the first pass z-detect method (described in section 3.3.1) as a starting point for finding similar events. I chose a window size of 20 seconds and a higher cross-correlation threshold of 0.7 due to the repetitive nature of these waveforms, and applied the iterative multiplet matching procedure of section 3.3. The runtime of this was approximately 1 hour on the supercomputer.

The multiplet matching method found 3,069 highly similar events (cross-correlation >0.7). An additional data cleaning step was used to remove all events within 30 seconds of each other to avoid any potential overlapping events, resulting in 2,966 unique multiplets. As a comparison between catalogues, the multiplet matching catalogue contained 83 of the 97 known events from the PNSN catalogue (which were picked by

an automatic phase-picked method). This meant that 14 events present in the PNSN catalogue were missing from the multiplet matching catalogue because of dissimilarity between the events and/or from several events being within the overlap range. The amount of events which were found, matching, missing and 'new' (i.e. events in the multiplet matching catalogue, but not in the PNSN catalogue) for both the multiplet matching and PNSN catalogues is summarised in Table 6.5.

Events	**Multiplet matching**	**PNSN**
Found	2,966	97
Matching	-	83
Missing	-	14
New	-	2,883

Table 6.5: Summary of the found, matching, missing and new events in the highly correlated multiplet matching and PNSN catalogues.

The similarity of the 2,966 multiplets can be seen in the stack plot in Figure 6.19, where the wave attributes are seen to be well aligned with one another in the lower diagram, and the summed waveform shown above.

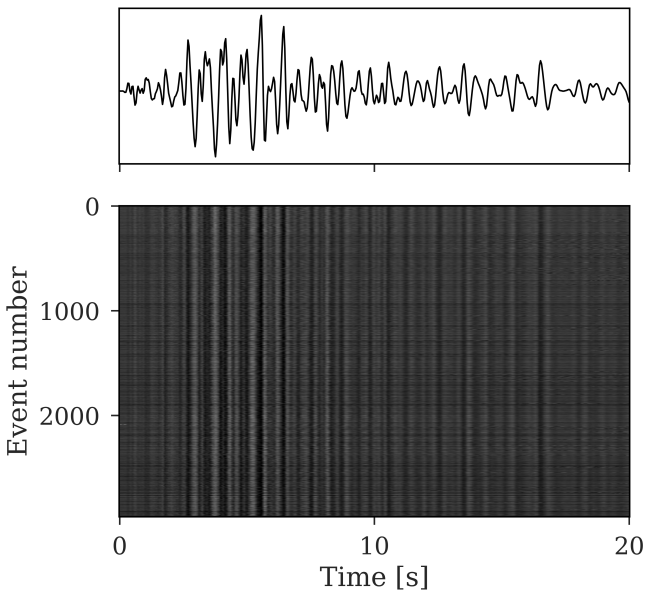

Figure 6.19: Normalised stack of the 2,966 multiplets found in the Mount St Helens dataset, with a cross-correlation threshold of 0.7. The summed waveform is shown in the upper plot, with the lower plot shows a greyscale image of all waveforms.

Figure 6.19 illustrates the wave attributes are very well aligned throughout this 20 second time window, confirming the high similarity of these waveforms to one another. In particular, the similarity in the coda part of the wave strongly indicates that they are sourced from the same region.

Once the events were identified by the multipet matching method through visual analysis, they were assigned estimated magnitudes using Equations 3.9 - 3.10 (described in section 3.4). The c value in Equation 3.9 was calculated using the data from the events in the PNSN catalogue which had a magnitude assigned by conventional methods, i.e. 'M_{new}' was known, and comparing them with the known magnitudes (M_{known} in Equation 3.9). I tested several values of c to find which gave the best estimation of the known magnitude, as illustrated in Figure 6.20.

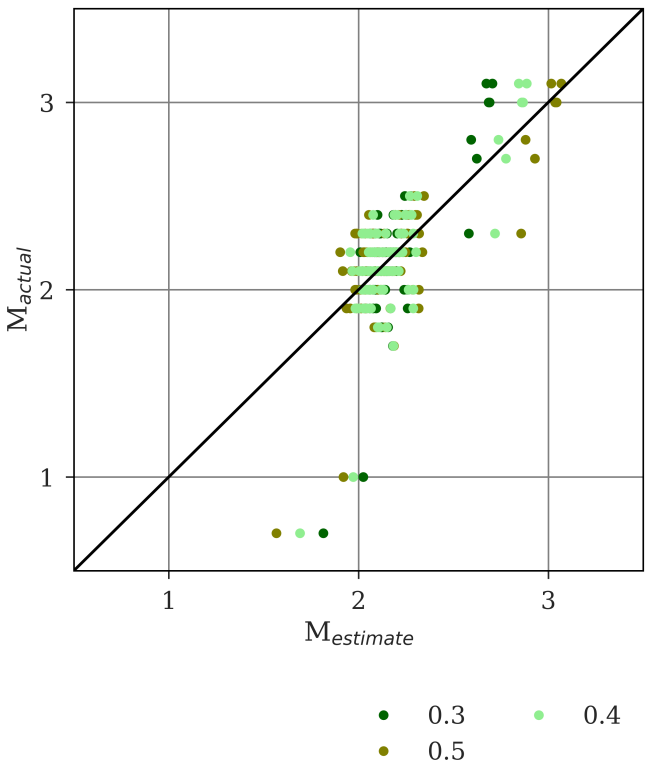

Figure 6.20: Illustration of working out c in Equations 3.9 - 3.10 to best estimate the magnitude of known template events from the PNSN catalogue. In this case, the best value of c was judged to be 0.4.

In this example, $c = 0.4$ gave the best estimate of the known magnitudes, shown as light green dots in Figure 6.20. This value of c was then used in Equations 3.9 - 3.10 to calculate the estimated magnitudes (M^e) of the new events.

An example of some of the waveforms of six multiplets which were identified from the multiplet matching method, are shown in Figure 6.21.

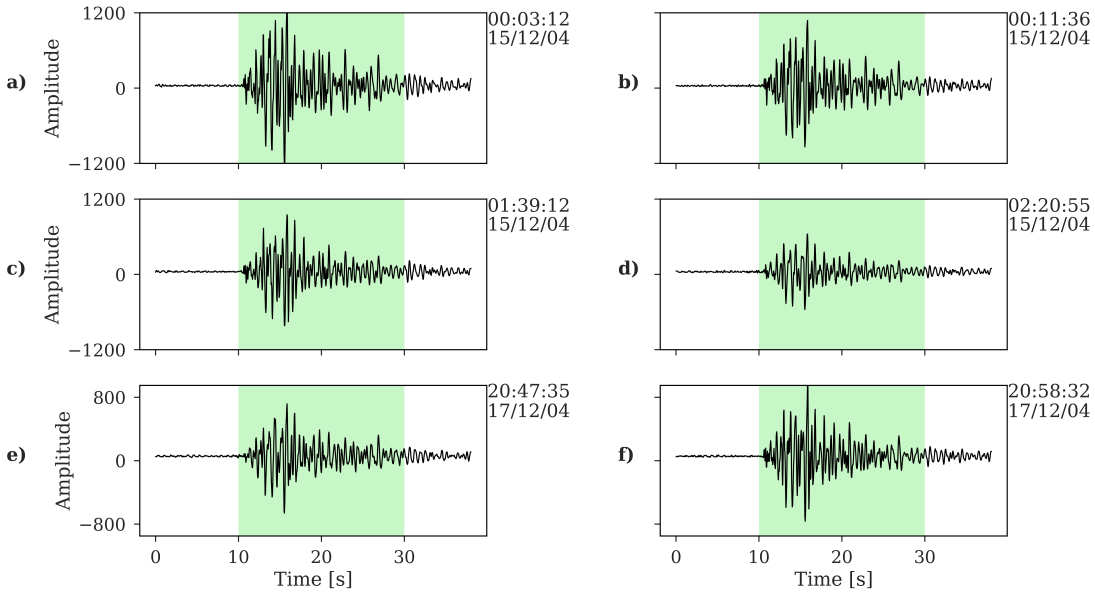

Figure 6.21: Comparison of six multiplets found from the multiplet matching method. The horizontal waveforms are scaled to the same y-axis. The starting time and date of each multiplet window (green box) is shown in the upper right of each plot.

The multiplets found by the multiplet matching method are shown in Figure 6.21a-f, where the green box indicates the multiplet window. They all have a cross-correlation value >0.9, thus they are all deemed to be very highly correlated with one another.

The multiplet in Figure 6.21a had M^e=1.9, and the multiplet in Figure 6.21b had M^e=2.1. In the second row of multiplets shown in Figures 6.21c and 6.21d, the former had M^e=2.1 and the latter M^e=1.9. Finally, the third row of multiplets illustrated in Figures 6.21e and 6.21f had M^e=1.9 and M^e=2.0, respectively.

6.3.3 Statistical Analysis

The statistical analyses of the multiplets found from the multiplet matching method for the Mount St Helens sequence will be presented and discussed here, following the

same protocol as the previous section. I will be comparing the results for the multiplet matching catalogue to the PNSN catalogue, herein shown by blue and green colours, respectively.

The temporal evolution of the multiplets found by the multiplet matching method is shown in Figure 6.22. The multiplets are denoted by blue circles, with the known events from the PNSN catalogue shown in green triangles. Figure 6.22 shows the inter-event times (upper diagram), peak amplitudes (middle diagram) and magnitudes (lower diagram), all on the same temporal scale.

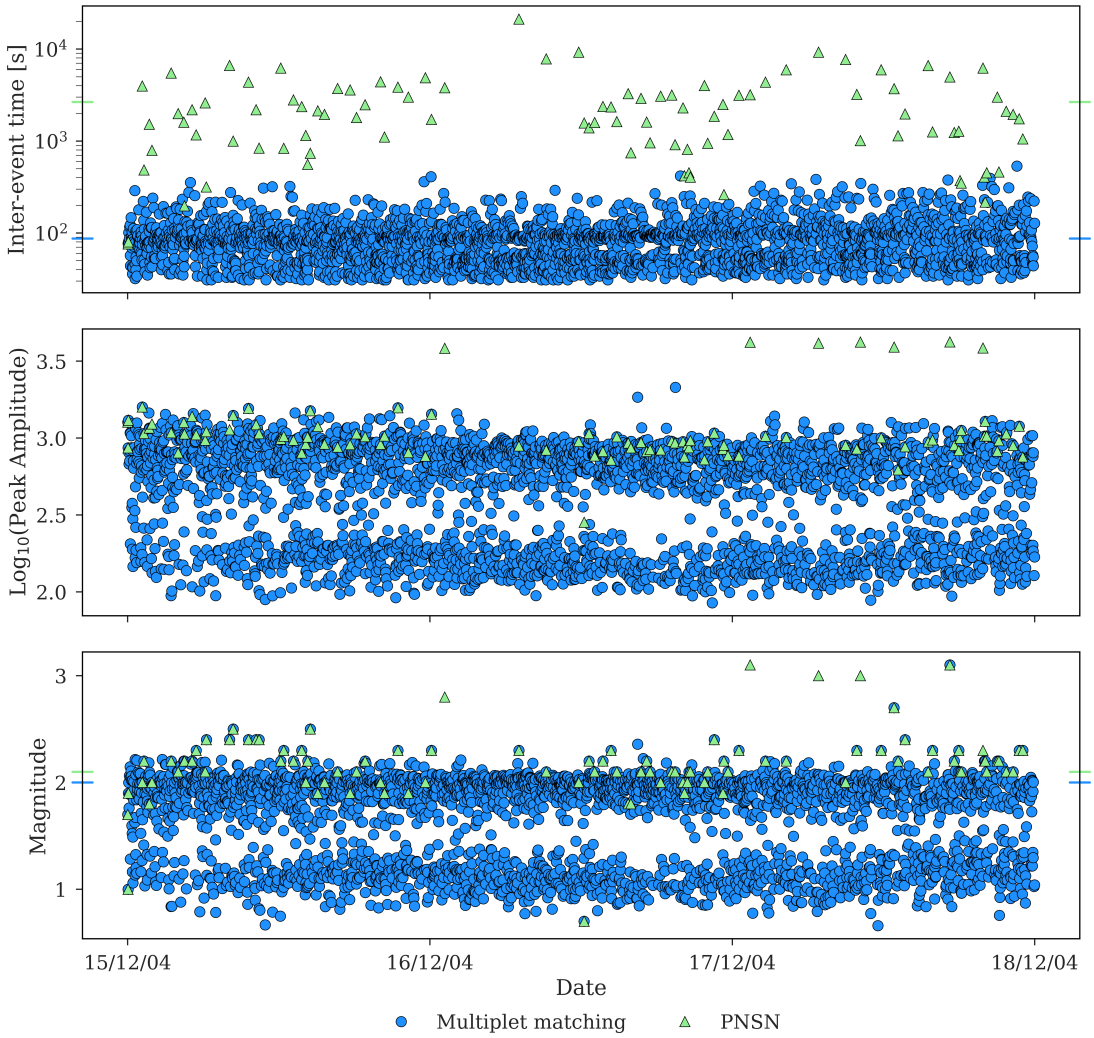

Figure 6.22: Time evolution of PNSN catalogue (green triangles) and events found by multiplet matching (blue circles). The upper shows the inter-event times, the middle plot shows the peak amplitudes of events, as a check on the precision of the magnitudes in the lower plot. Coloured horizontal tick lines show average inter-event time (upper), and the magnitude of completeness, M_c, (lower) per catalogue.

The inter-event times in the upper plot of Figure 6.22 shows that the multiplets are very periodic in time, and most occur within 200 seconds of one another, with a dominant inter-event time at around 90 seconds. This differs to the PNSN catalogue,

which shows a varied amount of inter-event times with no clear pattern or periodicity. The average inter-event times for the events found from the multiplet matching method (blue) and the PNSN (green) catalogues are shown by the coloured tick lines on the two y-axes in the top diagram, where the colour represents the catalogue in Figure 6.22. The values of M_c are calculated later in this section by the MaxC and BVS methods, and are shown by the coloured tick lines on the lower plot of Figure 6.22.

Figure 6.22 confirms the many new events found through the multiplet matching method, particularly those with a much lower magnitude than in the PNSN catalogue. The middle and lower plot of Figure 6.22 illustrate two dominant amplitudes. It is not uncommon to see 'drumbeat' seismicity restricted in magnitudes, but it is unusual to see such a separation at around $M = 1.5$ in Figure 6.22c. This could be due to: 1) an artefact of using one station, perhaps then causing an inappropriate selection of c from Figure 6.20, which is used in Equations 3.9 - 3.10, 2) the events were occurring in different locations, 3) more than one underlying process taking place, 4) the events being different types of seismicity (mixed polarities), or a combination of these. As the events in Figure 6.18 showed two varying amplitudes, it strongly indicates that there are either two populations or polarities of events. For waveforms to still appear to be similar, they must be located within one quarter a wavelength of each other, or approximately <400 metres (Geller and Mueller, 1980). Therefore, it is possible that this small difference in location equates to a small difference in amplitude, but still produce a similar waveform.

It is also possible that this could be combined with mixed first-motion polarities for these events, which is not uncommon with the effects of heterogeneity, and thus velocity contrast in the material, at Mount St. Helens (Thelen et al., 2008). This mixed polarity was previously seen for the intrusive magma body that intersected bounding faults during the late 1990s at Mount St. Helens (Musumeci et al., 2002), and for several events during the 2004-2006 eruptive activity due to reverse faulting on a north-striking, vertical or steeply dipping fault (Thelen et al., 2008). Harrington and Brodsky (2007)

also showed that not all of the events had the same polarity at all stations, suggesting that not all of the events found were occurring due to tensile cracks. To investigate this, I observed the first-motion arrivals in a stack plot, similar to Figure 6.19, shifting the time window back by several seconds, as shown in Figure 6.23.

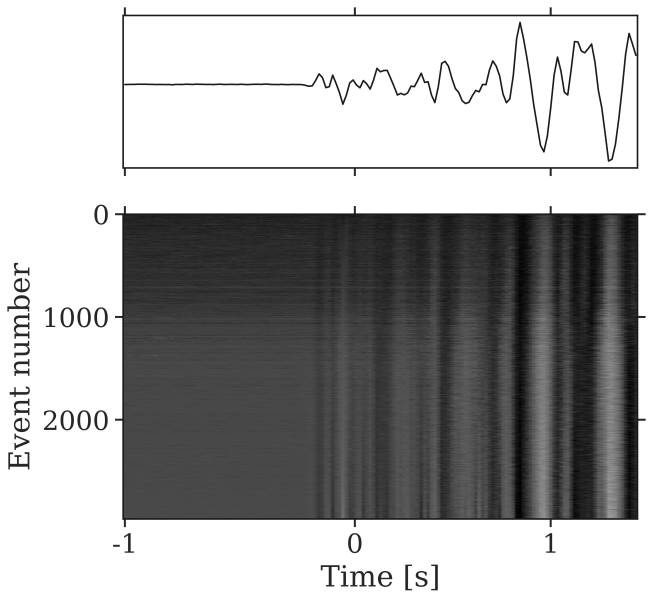

Figure 6.23: Normalised stack of the first-motion arrivals of the 2,966 multiplets found in the Mount St Helens dataset, with a cross-correlation threshold of 0.7. The summed waveform is shown in the upper plot, with the lower plot shows a greyscale image of all waveforms. The waveforms are in descending order from the normalised amplitude at the first-motion point in time.

From the ordering of amplitude of the waveforms in Figure 6.23, there is a distinct split of amplitudes, where the darker colours shows that there is more of a contribution of the earlier arrivals in the 'noisier' events (i.e. the smaller events) to the rest of the waveform. There is also not a considerable difference in the first-motion arrivals, which appear to be dilatational. This is confirmed with the study by Waite et al. (2008), where it was suggested that the dilatational first-motion signals at Mount St. Helens during this period indicated that the source could be the collapse of a crack

or a near-vertical single force (such as a magma plug stuck). However it is difficult to assign the first-motion arrivals on such an emergent waveform. An example of some of the smaller-magnitude waveforms of three multiplets which were identified from the multiplet matching method, are shown in Figure 6.24, to better examine the waveforms.

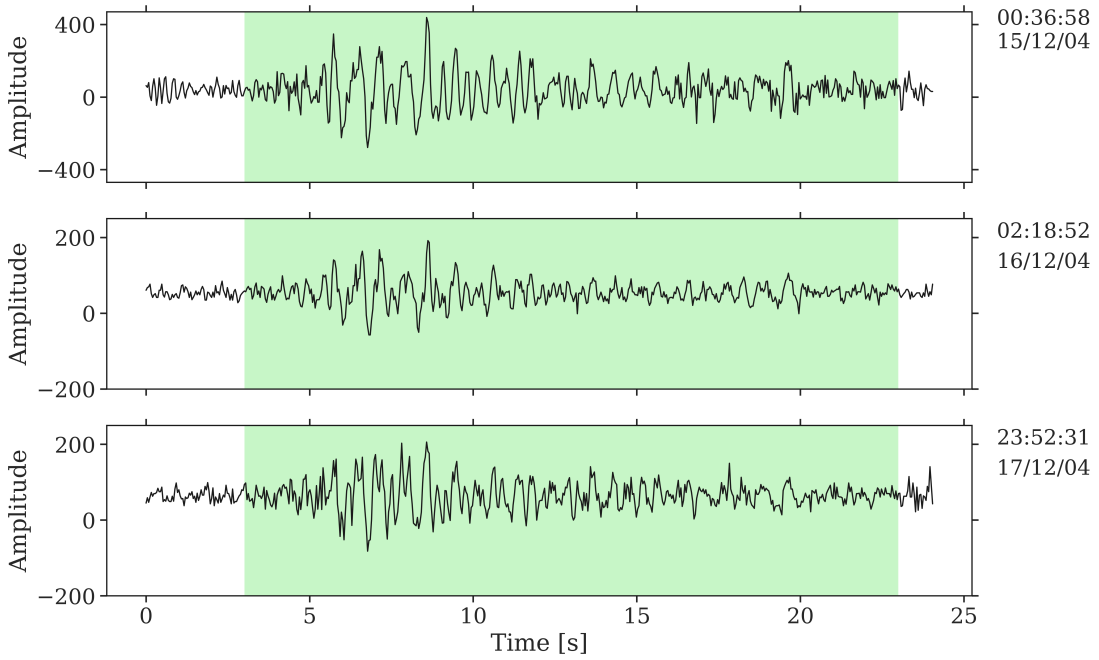

Figure 6.24: Comparison of three small-magnitude multiplets found from the multiplet matching method. The starting time and date of each multiplet window (green box) is shown in the upper right of each plot.

The multiplet in the upper plot of Figure 6.24a had M^e=1.7, the multiplet in the middle of Figure 6.24b had M^e=1.2, and the lower multiplet had M^e=1.3. The green box indicates the multiplet window. As seen by the y-axis in Figure 6.24, these are much smaller in amplitude than the larger amplitudes in Figure 6.21. As these multiplets have a much higher Signal-to-Noise ratio, their first motion arrivals are much harder to distinguish than those in Figure 6.21. Their onsets are much more emergent, possibly due to being more shallow, which could influence the magnitude estimation as being much smaller magnitude events than they actually are. This could indicate

that these smaller-magnitude events are the result of another process occurring, but have been grouped in with these larger-magnitude events due to their close proximity (thus appearing as similar waveforms). However as they were picked by the multiplet matching method, I will not filter these events out and continue with all the uniquely picked events in the multiplet matched catalogue.

Next, I examined a frequency-magnitude distribution of the multiplet matching event catalogue (Figure 6.25a in blue) and the PNSN event catalogue (Figure 6.25b in green).

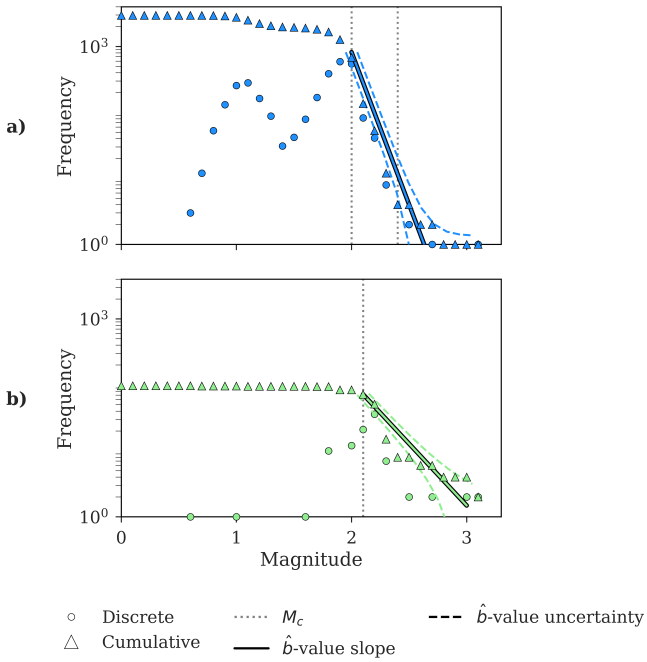

Figure 6.25: Comparison of the frequency-magnitude distributions for events in the multiplet matching (plot a in blue) and PNSN (plot b in green) catalogues. The discrete (filled circles) and cumulative (filled triangles) frequencies are shown for each catalogue. The $\hat{b}$-value corresponding to each catalogue is shown by the filled line, where the colour matches the catalogue, and the dashed lines show the uncertainties on the slope. The grey dotted lines illustrate the different values of M_c calculated.

The frequency-magnitude distribution of the multiplet matching event catalogue showed a two-peak magnitude distribution, similar to that of the analysis by Lahr et al. (1994) of the broad frequency-magnitude distribution of the 1989-1990 eruptions at Redoubt volcano. Lahr et al. (1994) had separated these events into VT, LP and hybrid events, all showing varying peaks. Also, Matoza et al. (2015) suggested that there were two sub-groups of events occurring - one group as a deep structure of cracks, and the other group as a shallow single sub-horizontal crack.

Although the seismicity at Mount St. Helens volcano does not follow Gutenberg-Richter statistics, I analysed Figure 6.25 in the same way as other cases in order to calculate the M_c. This was calculated using BVS, MaxC and Goodness-of-Fit Tests (GFT) methods, following the method in Roberts et al. (2015) (Figure 2.3). The summary of the BVS, MaxC and GFT methods are shown in Tables 6.6 - 6.7.

	BVS	**MaxC**	**GFT 90%**
M_c	2.4	2.0	2.0
$\hat{b}$-value	2.7 ± 1.0	4.6 ± 0.13	4.6 ± 0.13

Table 6.6: The magnitude of completeness, M_c, for the b-value stability (BVS), Maximum Curvature (MaxC) and GFT 90% methods, and the $\hat{b}$-value plus uncertainty from the MLE (Maximum Likelihood Estimation) method (Equations 2.5-2.6), for the multiplet matching catalogue in Figure 6.25a for each estimate of M_c.

	BVS	**MaxC**
M_c	2.1	2.1
$\hat{b}$-value	1.9 ± 0.22	1.9 ± 0.22

Table 6.7: The magnitude of completeness, M_c, for the b-value stability (BVS) and Maximum Curvature (MaxC) methods, and the $\hat{b}$-value plus uncertainty from the MLE (Maximum Likelihood Estimation) method (Equations 2.5-2.6), for the PNSN catalogue in Figure 6.25b for each estimate of M_c.

As a summary, the MaxC method chooses M_c based on the maximum curvature of the frequency-magnitude distributions from Figure 6.25, BVS instead chooses M_c based on when the b-value stabilises to when b_{ave} (the average for the next five successive $\hat{b}$-values) lies within the error of the b_{MLE} by incrementally increasing M_c. When the MaxC and BVS methods fail, the GFT method (from Wiemer and Wyss (2002)) is instead used. This method calculates the M_c for when 90% of the catalogue can be described by a power-law fit.

The MaxC method yielded the M_c as 2.1 for the PNSN catalogue, but chooses a lower M_c of 2.0 for the multiplet matching catalogue. This lower value of M_c then estimates the $\hat{b}$-value as 4.6 ± 0.13, which is irregularly high.

Next, I show the plots for the BVS method for the two catalogues in Figure 6.26.

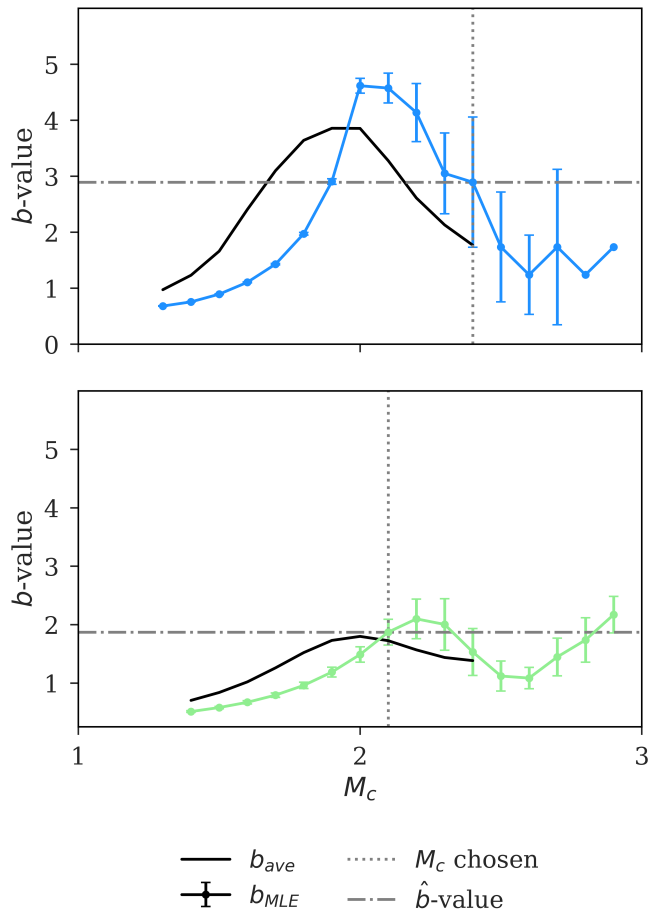

Figure 6.26: Comparison of b-value stability curves, showing the b-values for each magnitude of completeness, M_c, for the multiplet matching (upper plot in blue) and PNSN (lower plot in green) catalogues. The vertical dotted line shows the chosen M_c from this method, and the horizontal dashed line shows the b-value at this point. The M_c is chosen as when the average of the five successive b-values (black line) are within one error of the b-value.

The chosen M_c from the BVS method is shown by the vertical dotted line in Figure 6.26. The b-value at this M_c is illustrated as the horizontal dot-dashed line. The BVS method for the multiplet matching catalogue in the upper of Figure 6.26 shows that the choice of M_c=2.4 came from when the $\hat{b}$-value began to stabilise at 2.7, however

the error on this value (± 1.0) was very large. The PNSN catalogue had a much more stable choice for M_c of 2.1, as seen in the lower of Figure 6.26, with a $\hat{b}$-value of 1.9 ± 0.22, shown by the solid line in Figure 6.25b with error bands shown by the dashed lines. As this error is < 0.25, and the two M_c's for the MaxC and BVS method yield the same result, this M_c is accepted for the PNSN catalogue with the BVS method. This $\hat{b}$-value is still relatively high, however high b-values are expected in some volcanic regions due to the abundance of smaller magnitude events (Roberts et al., 2015), although the uncertainties here are too large to be definitive.

Following the method designed in Roberts et al. (2015) (Figure 2.3), the GFT 90% method (section 2.3.1) for choosing the M_c is accepted for the multiplet matching method. This is because although the difference between M_c's for the MaxC and BVS methods is <0.1, which would indicate that BVS is the better method, the $\hat{b}$-value error is >0.25. This then prompts the use of the GFT method in the workflow, whence M_c = 2.0. The $\hat{b}$-value at this M_c is estimated as 4.6 ± 0.13, which is shown by the solid line in Figure 6.25a, with the error bands shown by the dashed lines. This is still a fairly large $\hat{b}$-value and error, so it is not clear that this is a representative $\hat{b}$-value for this catalogue. The reason is that the bandwidth of complete observations is relatively narrow (one order of magnitude) and the multiplet matching has found more smaller events above M_L=2 than the PNSN catalogue.

Next, I observed the inter-event times of the two catalogues by comparing them with common statistical distributions used to model inter-event times in Figure 6.27, where the multiplet matching catalogue is in the upper plots in blue, and the PNSN catalogue is in the lower plots in green.

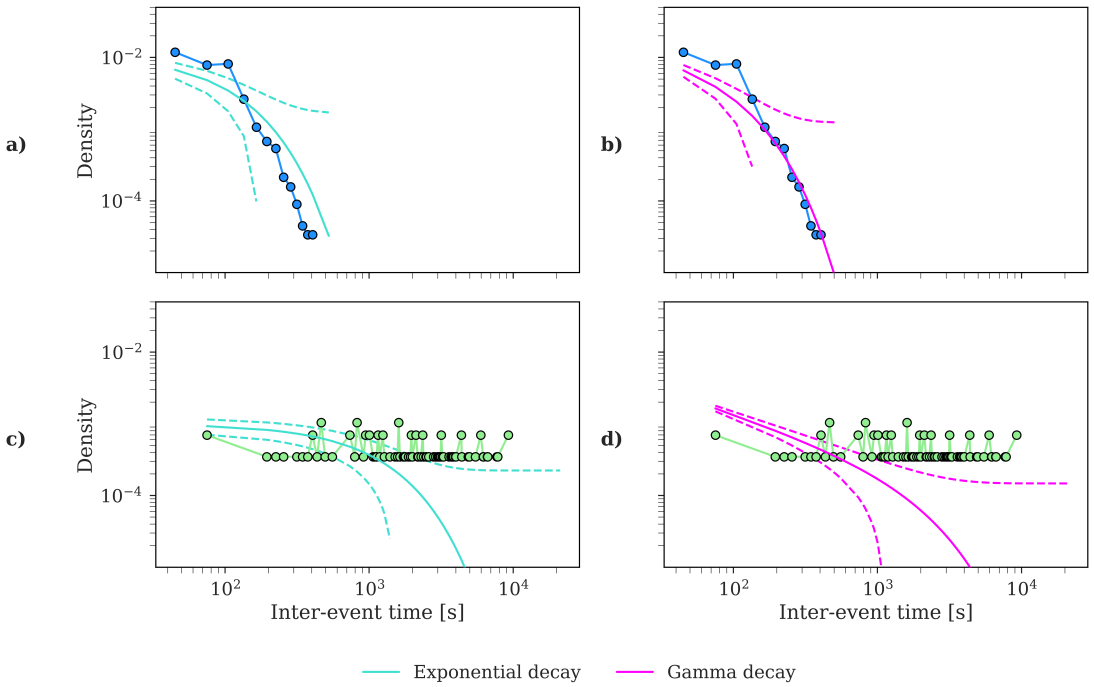

Figure 6.27: Comparison of multiplet matching (blue) and PNSN (green) catalogues inter-event times, shown by filled circles, with the null hypothesis of exponential (cyan) distributions shown in the left plots, and gamma (pink) and power law (orange) distributions in the right plots as solid lines. Confidence intervals of 95% are shown by dashed lines in corresponding colours.

The exponential (cyan) decay fits in the left plots of Figure 6.27(a,c), and gamma (pink) decay fits in the right plots in Figure 6.27(b,d) for the two catalogues inter-event times. The counts are normalised in Figure 6.27 to form a probability density, where it is weighted so that the integral of the density over the range, is 1. Further to this, the 95% confidence interval of the distributions are shown in their corresponding colour, with the bounds marked by a dashed line. While no obvious periodicity is seen here because of the small time bins, the multiplet matching catalogue has most of their events occurring at very short intervals, whereas the PNSN events are more spread out.

Figure 6.27a shows that the exponential model does not fit the shorter inter-event

times of the multiplet matching catalogue well. The fit becomes better when the inter-event times are >100 seconds, with most of the points lying within the confidence bands. This indicates that the events occurring >100 seconds apart may not be correlated to one another. This is consistent with the majority of the drumbeat events occurring within 100 seconds of one another, as seen in Iverson et al. (2006). Figure 6.27b shows a better fit of the mid to longer inter-event times with the gamma decay function, particularly >200 seconds. The gamma fit does not do well < 100 seconds in this case, with the points here lying outwith the confidence bands. This is likely due to the multiplet matching method removing overlapping events <30 seconds from one another, which lowers the density of the early bins. These results indicate that the multiplet matching method has picked up some correlated events, best modelled by a gamma function, as well as independent events (uncorrelated events), modelled with an exponential function. The inter-event times between 200 and 400 seconds, which fit both the exponential and gamma functions well, could also be described by a power-law distribution because of the cross-over of these two functions (Touati et al., 2009).

Figure 6.27c shows that the mid inter-event times of the PNSN catalogues inter-event time distribution matches an exponential model well from > 300 to < 2,000 seconds, indicating that the events in this time period are more likely to be independent to one another. Figure 6.27d does not have a well fitted gamma function for inter-event times, indicating that the events are not correlated.

A comparison can be made to the drumbeat seismicity at the Tungurahua volcano in Ecuador, where Bell et al. (2017) suggested that instead of the assumption that inter-event times require the same energy source for successive earthquakes, sources can instead switch between families and phases of activity, as well as evolve. Bell et al. (2017) noted that a particular period of drumbeat seismicity at Tungurahua was similar in nature to the drumbeat events at Mount St Helens on the dates observed in this thesis. This can be seen particularly the inter-event times in Figure 6.27, which look similar to the first phase of drumbeat seismicity at Tungurahua, which gives confidence

to these results. Also, Bell et al. (2017) observed some event amplitudes at Tungurahua that were much lower than other events in the same family, suggesting that there were both persistent and transient sources that were causing the drumbeat activity. This could also be a likely candidate for the two dominant amplitudes seen in Figure 6.22 and Figure 6.25.

The AIC from Equation 2.10 and BIC from Equation 2.11 were calculated for both inter-event time distributions as a measure of which statistical distribution was preferred as shown in Table 6.8.

	Multiplet matching method	**PNSN**
$AIC_{exponential-gamma}$	-1	-1
$BIC_{exponential-gamma}$	-6	-26

Table 6.8: The Akaike Information Criterion (AIC) from Equation 2.10 and Bayesian Information Criterion (BIC) from Equation 2.11 calculated for the Poisson and gamma distributions in Figure 6.27 to measure which fits the inter-event times the best.

The results in Table 6.8 indicate that based on the AIC and BIC, the exponential distribution best overall fits both the multiplet matching and PNSN catalogues. This result would suggest that overall, these are uncorrelated and independent events that are the result of random occurrence, thus failing to reject the null hypothesis that there is no causal pre-slip or cascade based on the inter-event times. This result of exponential inter-event times was also observed for the Tungurahua volcano by Bell et al. (2017), which exhibited similar drumbeat behaviour to the seismicity at Mount St Helens in this analysis.

Next, I examined the cumulative rate at which the multiplet matching (blue) and the PNSN (green) catalogue events occurred in time, in Figure 6.28.

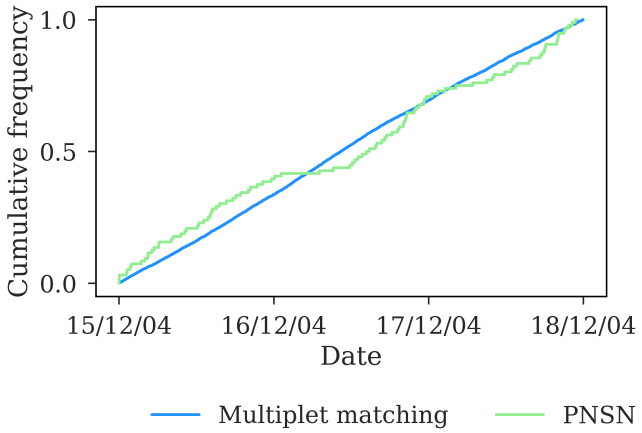

Figure 6.28: Comparison of multiplet matching (blue) and PNSN (green) normalised cumulative frequency of events to observe event rate.

The normalised cumulative rate of the multiplet matching catalogue in Figure 6.28 has 2,966 events, causing the event rate to appear much smoother than the PNSN catalogue, which only contains 97 events over this time period. This indicates a much more stationary underlying process, which is consistent with the understanding that drumbeat seismicity at Mount St Helens is the result of a persistent source mechanism (Iverson et al., 2006).

The cumulative seismic moment, M_o, for the multiplet matching and PNSN catalogue is shown in Figure 6.29, following the same protocol as in Figure 6.28. The results show a significant additional difference moment in the multiplet matching catalogue compared to the PNSN catalogue. Both catalogues follow a relatively stationary cumulative moment, which is typical from a stable event sequence.

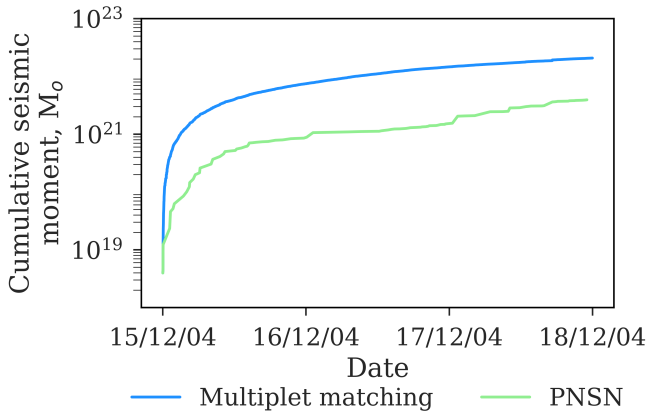

Figure 6.29: Cumulative seismic moment of multiplet matching (blue) and PNSN (green) events.

The results of the multiplet matching catalogue in Figure 6.29 agrees with the stable inter-event time and magnitude patterns seen in Figure 6.22. The high similarity between waveforms (Figure 6.19) strongly indicates that they are sourced from the same region (within <0.4 km), thus a stable source is likely to be the cause. This infers that a stable underlying mechanism, such as a steady rate of extrusion of several lava spines was taking place during this dome building period (Iverson et al., 2006; Thelen et al., 2008; Vallance et al., 2008). Waite et al. (2008) instead attributed the source that was driving the growing lava dome to be a resonating crack with a steady-supply of fluid causally-triggering the repeating events, which were consistent with collapse of the crack. It is not possible to distinguish a definitive source of the mechanism causing these events from this analysis alone. However, the short inter-event times imply that there is a rapid healing, loading, and reactivation of the source is required to produce the highly repetitive pattern seen, indicating that their occurrence is likely due to several different complex systems (Chouet and Matoza, 2013; Bell et al., 2018).

6.4 Nuugaatsiaq landslide, Greenland

6.4.1 Introduction

The Nuugaatsiaq landslide that occurred at 23:39 UTC on 17th June 2017 in the North-west of Greenland, producing the same energy as a M_L 4.2 earthquake (USGS, 2017). This landslide was chosen for analysis as Poli (2017) and Bell (2018) previously showed many similar waveforms preceding the landslide on the same day, that were picked up on the nearby seismic station, Nuugaatsiq (NUUG), on the Danish Seismological Network (DK). The location of the landslide (red dot) and the seismic station (brown triangle) are illustrated in Figure 6.30.

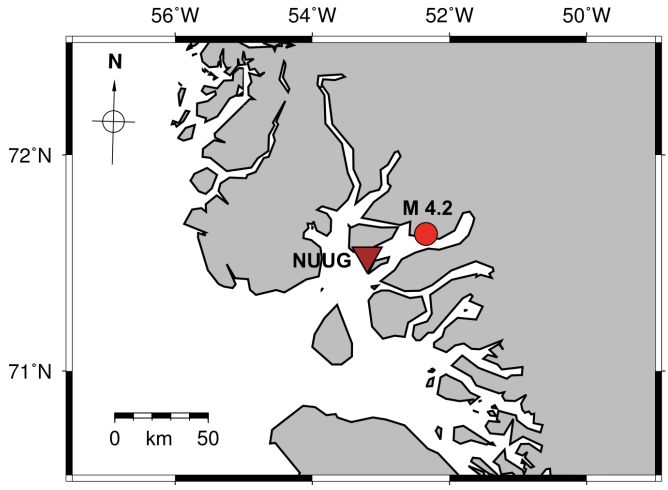

Figure 6.30: Illustration of seismometer (brown triangle) and landslide (red dot) locations.

The waveform data for the 17th June 2017 was downloaded from IRIS and bandpass filtered between 2Hz and 9Hz, as in Poli (2017). The day-long seismogram for this time period is illustrated in Figure 6.31, with the arrival time of the landslide on the NUUG station is shown by the red dashed vertical line.

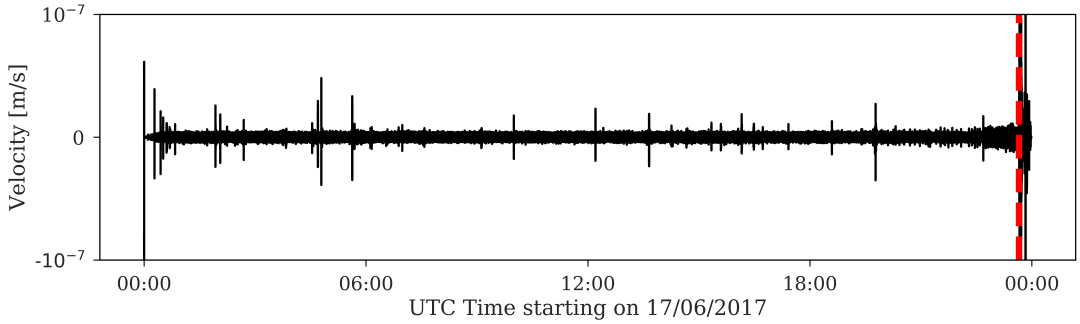

Figure 6.31: Illustration of the Nuugaatsiaq landslide sequence on 17th June 2017, with the red dashed vertical line showing the arrival time of the landslide at 23:40 UTC. This illustration has been clipped at $\pm 10^{-7}$ m/s to show smaller seismic signals prior to the landslide.

6.4.2 Method

The USGS catalogue contains only the landslide event for this time period. Thus I will be comparing the number of events found by the multiplet matching catalogue to those found in the Poli (2017) and Bell (2018) catalogues. The Poli (2017) catalogue was compiled in a similar way to the multiplet matching method. First, Poli (2017) used an arbitrary waveform and cross-correlated it with the entire seismogram, with a threshold level of eight times the Median Absolute Deviation (MAD) to produce an initial catalogue of 83 newly detected events. These were then stacked to define a new reference trace, which was again cross-correlated with the entire seismogram, resulting in 95 detected events.

The Bell (2018) catalogue was compiled through using a standard phase picking method to create an initial catalogue of detected events. These events were then cross-correlated with each other to find the highest correlating waveform, which Bell (2018) found was at 23:27:33 on 17th June 2017, to then become the template waveform (rather than the initial arbitrary choice in Poli (2017)). This template waveform was then cross-

correlated with the rest of the seismogram with a threshold level of 0.3, which amounted to 89 detected waveforms, including those in the initial phase-picked catalogue.

The difference between the number of detections in the Poli (2017) and Bell (2018) catalogues is likely due to the threshold sensitivity, as Bell (2018) found that lowering the cross-correlation threshold to 0.275 returned 92 detections, and increasing to 0.325 returned 87 detections. The cross-correlation detection threshold that Poli (2017) used was eight times the MAD of the cross-correlation output, however although the distinct number is not found, it appears to be around 0.3 in Figure 3 of Poli (2017). An additional reason for the difference in number of detections, is that Poli (2017) used an iterative approach (similar to the multiplet matching method proposed in this thesis) of reassigning the template trace to find events which were initially not detected by the first cross-correlation.

The multiplet matching method differs from the method used in Poli (2017), as it has an extra pass for finding more similar events (described in Steps 7-9 in section 3.3.1).

Here, the multiplet matching catalogue was constructed by initially using the highest correlated event, as in Bell (2018), as the original template trace, and detected 92 similar events, including the original template trace, using a correlation threshold of 0.39. The runtime of this was several minutes on a local computer. The similarity of the 92 multiplets can be seen in the stack plot in Figure 6.32, where the wave attributes are seen to be well aligned with one another in the lower diagram, and the summed waveform shown above.

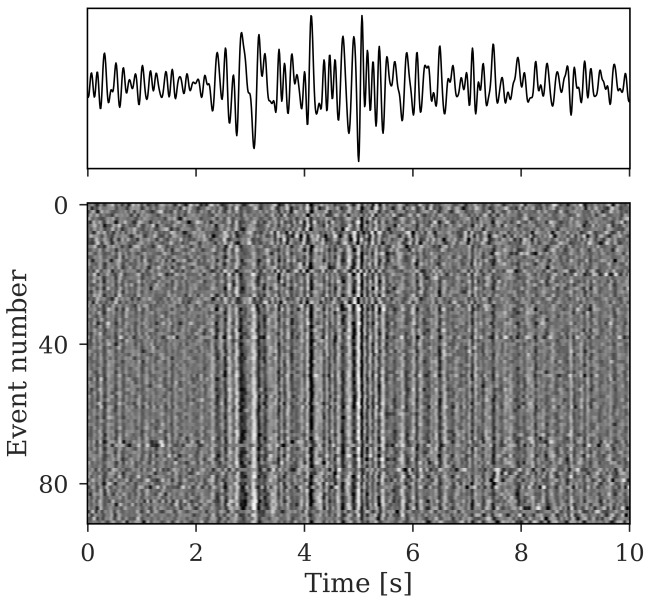

Figure 6.32: Normalised stack of the 92 multiplets found in the Nuugaatsiaq landslide dataset, with a cross-correlation threshold of eight times the Median Absolute Deviation, of 0.39. The summed waveform is shown in the upper plot, with the lower plot shows a greyscale image of all waveforms.

Figure 6.32 illustrates the wave attributes are well aligned throughout this 10 second time window, which further confirms the similarity of these waveforms to one another. In particular, the wave at 3-6 seconds is particularly well aligned. The tail part of the wave (>7 seconds) also seems reasonably aligned, which indicates that they are sourced from the same region. However, the events which occurred close to the point of failure were occurring up to four seconds apart, and so their seismograms were overlapping significantly. This meant that their waveforms were not as well aligned with the template within its window of 10 seconds. In this case, I chose to keep these overlapping segments in to preserve the events occurring closest to the failure time, at the expense of including events with significant differences especially towards the start and end times of the window.

For a comparison to the two other catalogues, the multiplet matching detection threshold of eight times the MAD in this case was found to be 0.39. When lowered to 0.30, the multiplet matching method yielded 194 detections (compared to 89 with a detection threshold of 0.30 in Bell (2018)). The stack plot of these events is shown in Figure 6.33.

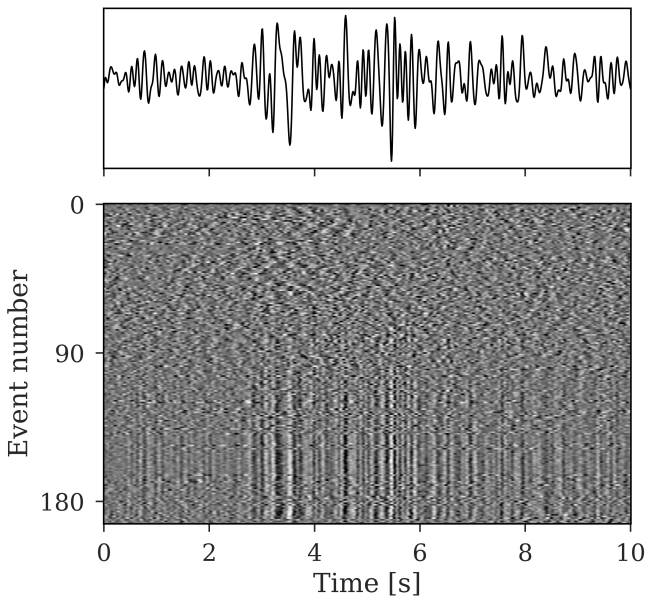

Figure 6.33: Normalised stack of the 192 multiplets found in the Nuugaatsiaq landslide dataset, with a cross-correlation threshold of 0.30. The summed waveform is shown in the upper plot, with the lower plot shows a greyscale image of all waveforms.

There is a noticeable degradation in the quality of the waveforms in Figure 6.33 compared to Figure 6.32, where the larger amplitude points of the wave (3-6 seconds) are not distinguishable. Hence, I will continue with the first catalogue seen in Figure 6.32, which contained 92 events, for the remainder of this analysis.

Once the events were identified, they were assigned estimated magnitudes using Equations 3.9 - 3.10. The landslide was the only event registered for this sequence with a 'magnitude' assigned, thus the value of c could not be accurately calculated as several

recorded magnitudes are required for this technique. Basing this on just one sample would therefore give a biased result, so the value of c will be set to 1, as this is the general scaling default for local magnitudes in other cases (Shelly et al., 2016b). This scaling relation was then applied to estimate the magnitudes for the new multiplets using Equations 3.9 - 3.10. These magnitudes are only for reference, and should not be taken with much confidence due to the use of the default scaling relation because of the lack of known events with assigned magnitudes in this sequence.

An example of the original and final template events, and some multiplets found in the preceding time to the landslide, are illustrated in Figure 6.34.

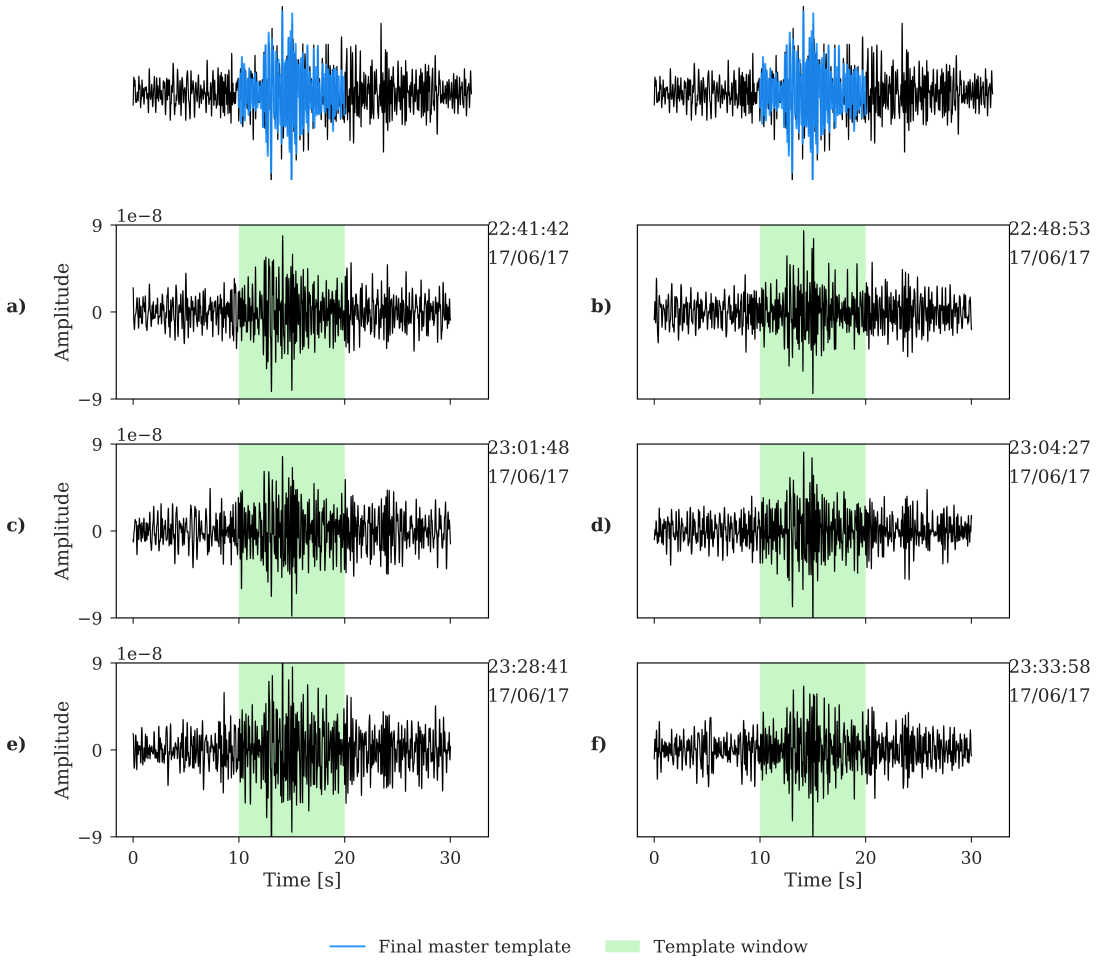

Figure 6.34: Illustration of original template and final master template events (upper) to the newly found multiplets from the multiplet matching method. The horizontal waveforms in a-f are multiplets of one another, and are scaled to the same y-axis. The UTC starting time of each multiplet is shown in the upper right of each plot. All the multiplets shown here occurred prior to the landslide at 23:29, and were found by the template in the upper plots.

In the two upper diagrams, the original template event is compared to the final master template event (blue) used in the multiplet matching method (from Step 7 of section 3.3.1). This template event occurred at 23:27:31, and had an estimated magnitude of -0.14 with the aforementioned method for estimating magnitudes. The

multiplets found by the final master template event are shown in Figure 6.21a-f, where the green box indicates the multiplet window, which is aligned with the upper templates. I chose to show these particular sets of multiplets as the horizontal waveforms are deemed highly correlated to one another as they have a cross-correlation value >0.7.

The multiplet in Figure 6.21a had an estimated M^e=-0.26, and another multiplet in Figure 6.21b had an estimated M^e=-0.33, with a cross-correlation value between the two seismograms of 0.78. In the second set of multiplets shown in Figures 6.21c and 6.21d, the former had an estimated M^e=-0.25 and the latter M^e=-0.27, and a cross-correlation value between the two seismograms of 0.84. Finally, the third set of multiplets illustrated in Figures 6.21e and 6.21f had an estimated M^e=-0.14 and M^e=-0.30, respectively, with a cross-correlation value between the two seismograms of 0.83.

6.4.3 Statistical Analysis

Here, the statistical metrics for the events associated with the Nuugaatsiaq landslide sequence will be presented and discussed, again the form of time series for the point process, frequency-magnitude distributions, inter-event times and event rate, all plotted with respect to the catastrophic failure for the multiplet matching catalogue (Figure 6.35).

The inter-event times are shown on the upper diagram, peak amplitudes in the middle as a check on the magnitudes in the lower diagram. The solitary green triangle represents the USGS catalogue event.

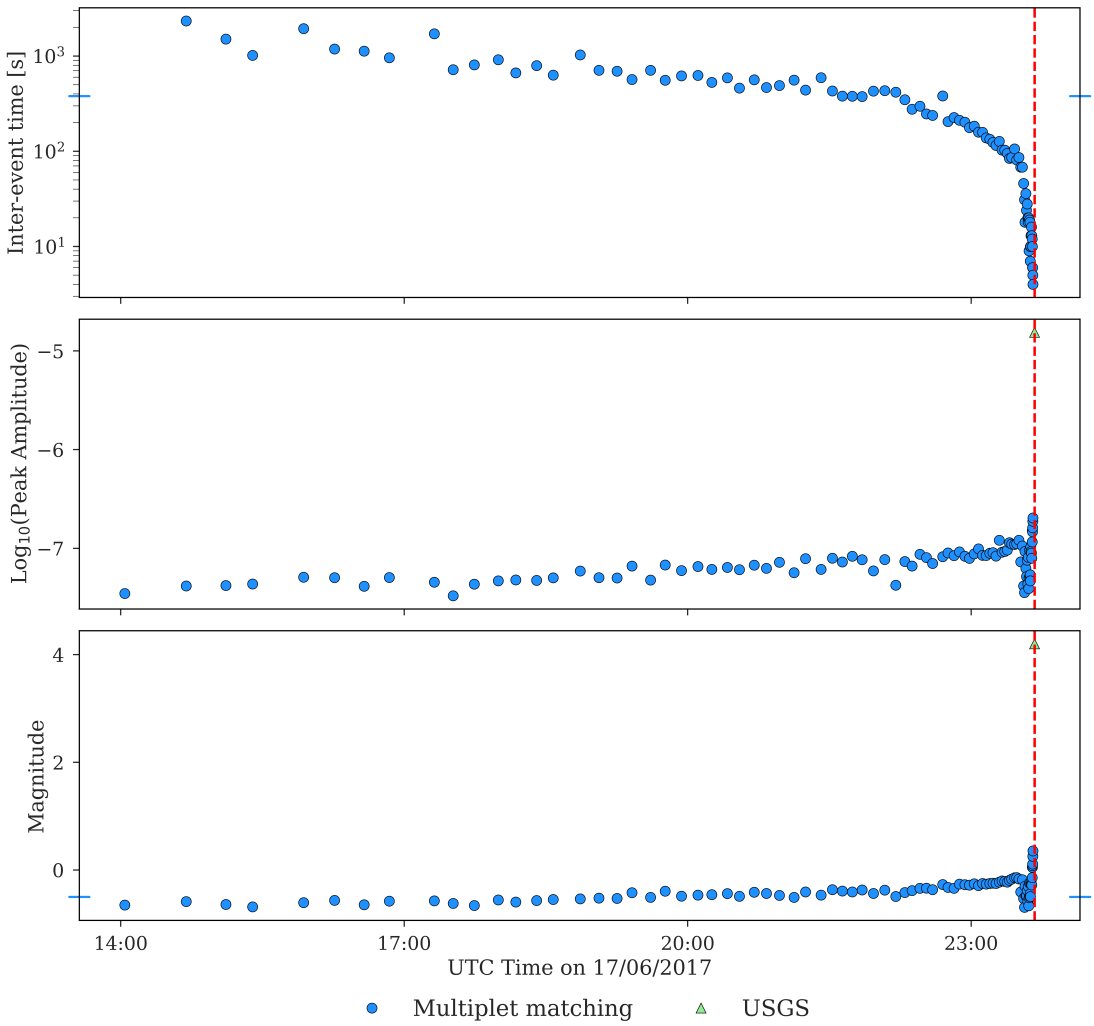

Figure 6.35: Time evolution of the events found by multiplet matching (blue circles) with their inter-event times (upper), peak amplitude (middle) and magnitude (lower). The landslide event was recorded by USGS (green triangle), with the arrival time denoted by a red vertical dashed line. The blue y-axes tick lines show average inter-event time (upper), and the magnitude of completeness, M_c, (lower).

The inter-event times in the upper plot of Figure 6.35 shows that the events detected by the multiplet matching method occurred closer in time prior to the landslide (red vertical dashed line). The multiplets began to occur at around 2,000 seconds apart,

before accelerating towards being within 10 seconds of one another prior to the failure. The average inter-event times for the multiplets found is shown by the blue tick lines on the two y-axes in the top diagram of Figure 6.35, and the M_c (calculated later in this section) is shown by the blue tick lines in the lower diagram.

The magnitudes of the multiplets in the lower plot of Figure 6.35 also shows an increase as failure approaches, which could be an indication of a creep-like event until the acceleration of the crack nucleation dominates the deformation of the bulk movement, resulting eventually in the landslide.

To observe the lead-up to landslide in more detail, a zoomed in version of the 30 minutes prior to the landslide is illustrated in Figure 6.36, following the same protocol as Figure 6.35.

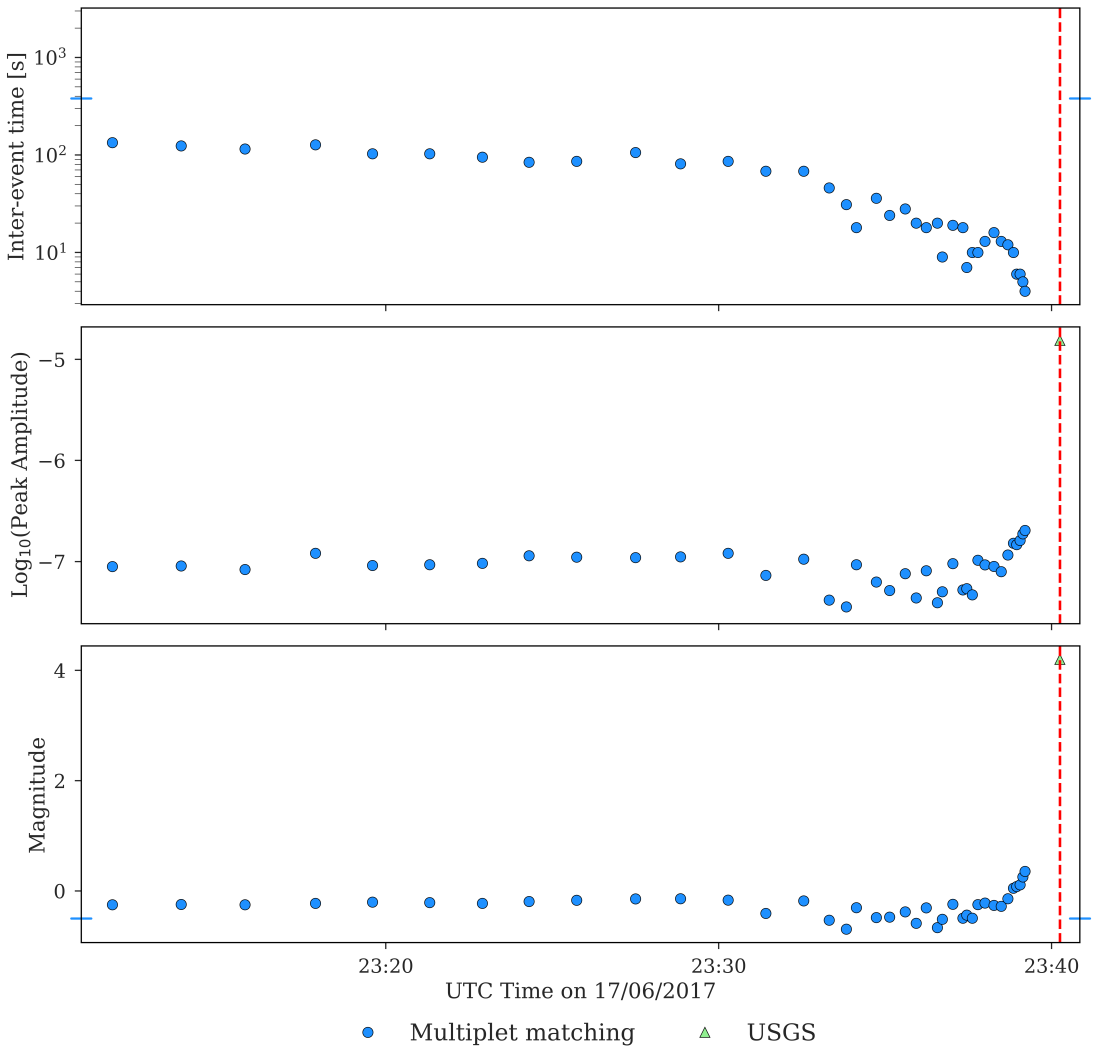

Figure 6.36: Time evolution of the events found by multiplet matching (blue circles) with their inter-event times (upper), peak amplitude (middle) and magnitude (lower), 30 minutes prior to the landslide event (recorded by USGS (green triangle), with the arrival time denoted by a red vertical dashed line). The blue y-axes tick lines show average inter-event time (upper), and the magnitude of completeness, M_c, (lower).

Figure 6.36 shows that the multiplet evolution was relatively stable in time, with events initially occurring approximately 100 seconds apart with an estimated M^e=-0.25, until around 23:35 UTC. After this point, the multiplets become much closer together

and their magnitudes generally increase until the last multiplet was detected at 23:39:12 with an M^e=0.31, one minute before the landslide occurred. This pattern could be an indication that the slow rock cracking (aseismic slip) was occurring, associated with acceleration of the deformation towards the time of the slope failure.

Next, I created a frequency-magnitude distribution of the multiplet matching catalogue, as illustrated in Figure 6.37.

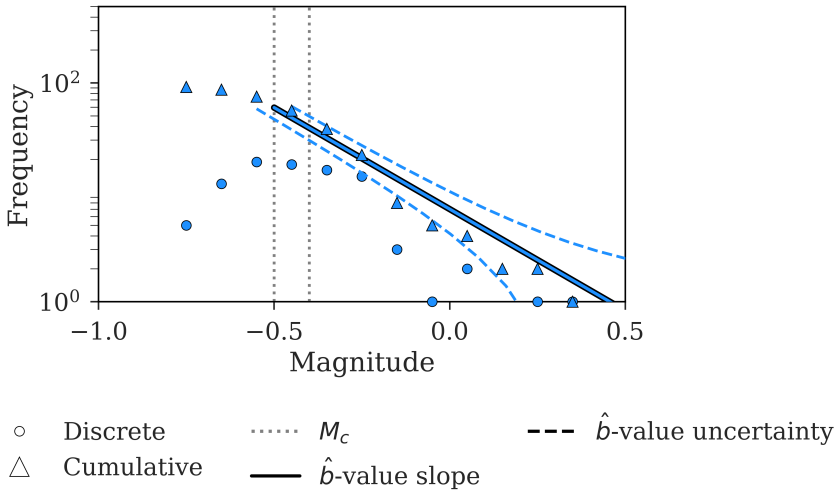

Figure 6.37: Multiplet matching frequency-magnitude distribution, where the discrete (filled circles) and triangles (filled triangles) frequencies are both shown. The $\hat{b}$-value corresponding is shown by the filled line, and the dashed lines show the uncertainties on the slope. The grey dotted lines illustrate the different values of M_c calculated.

I analysed Figure 6.37 in the same way as other cases in order to calculate M_c, and to examine the relative rate of occurrence of small and larger events. The grey dotted lines in Figure 6.37 represent the different values for the magnitude of completeness, M_c, which were estimated through the b-value stability (BVS) method and maximum curvature (MaxC) method (section 2.3.1). The $\hat{b}$-value and its uncertainties, which are estimated from the chosen M_c in MLE method from Equations 2.5 - 2.6), is shown in

Figure 6.37, by the solid line on each plot. The dashed lines show the bounds of the uncertainty on the $\hat{b}$-value.

The plot for the BVS method for the multiplet matching catalogue is shown in Figure 6.38.

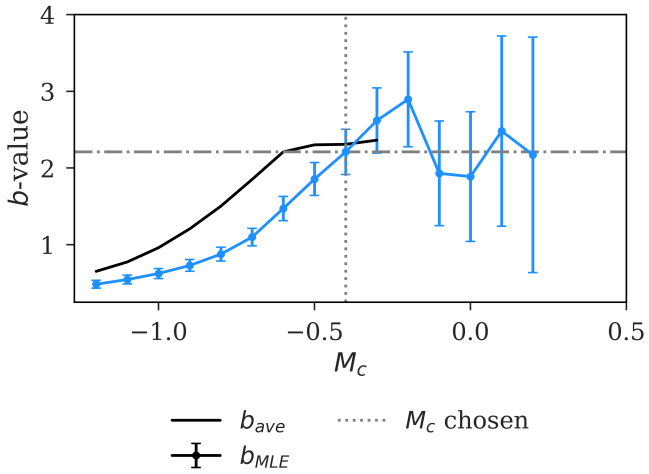

Figure 6.38: The b-value stability curve, showing the b-values for each magnitude of completeness, M_c, for the multiplet matching catalogue. The vertical dotted line shows the chosen M_c from this method, and the horizontal dashed line shows the b-value at this point. The M_c is chosen as when the average of the five successive b-values (black line) are within one error of the b-value.

The chosen M_c from the BVS method is shown by the vertical dotted line in Figure 6.38. The b-value at this M_c is illustrated as the horizontal dot-dashed line. The BVS method shows that the choice of M_c=-0.40 came from when the $\hat{b}$-value began to stabilise at 2.2, however the error on this value was very large due to the small number of data points.

The MaxC method estimated M_c = -0.50 for the multiplet matching catalogue with $\hat{b}$-value=1.9 $\pm$ 0.17 (estimated from the MLE method in Equations 2.5 - 2.6). Following

the workflow of Roberts et al. (2015) (Figure 2.3), as the two M_c's agree within $\pm$ 0.1, and the error is <0.25, the MaxC method is accepted. This value of M_c and the corresponding $\hat{b}$-value was used to plot the best fit line and uncertainty range for the frequencies in Figure 6.37. A summary of the M_c and $\hat{b}$-value results from the discussed methods is shown in Table 6.9.

	BVS	**MaxC**
M_c	-0.40	-0.50
$\hat{b}$-value	2.2 $\pm$ 0.25	1.9 $\pm$ 0.17

Table 6.9: The magnitude of completeness, M_c, for the b-value stability (BVS) and Maximum Curvature (MaxC) methods, and the $\hat{b}$-value plus uncertainty from the MLE (Maximum Likelihood Estimation) method (Equations 2.5-2.6), for the multiplet matching catalogue in Figure 6.37 for each estimate of M_c.

Next, I compared the inter-event times of the multiplet matching catalogue with two known statistical distributions, as illustrated in Figure 6.39, to better understand the processes of the events in the time prior to catastrophic failure.

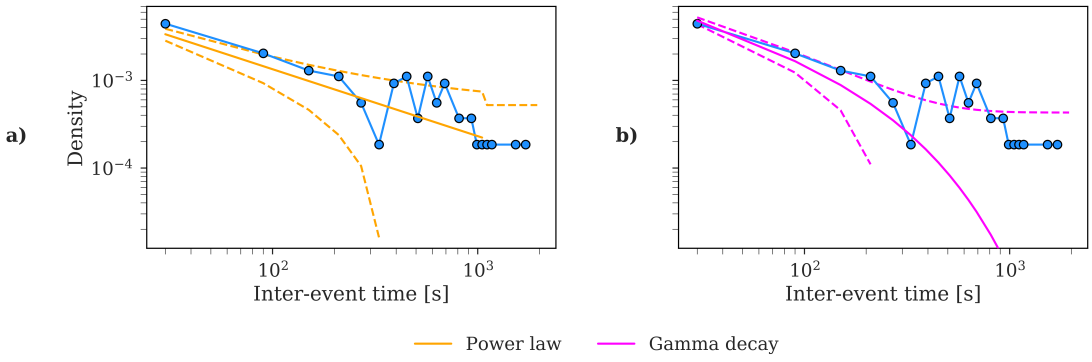

Figure 6.39: Comparison of multiplet matching inter-event times with a power law (orange) and gamma decay (pink) statistical models. Confidence intervals of 95% have been added to both distributions, and are shown by their corresponding colour and boundaries as dashed lines.

As discussed in section 2.3.1, the frequency of the inter-event times of accelerating events can follow a power-law distribution (Bell, 2018). A gamma distribution is also included as a model for interevent times which may follow a more generalised version of the Poisson distribution, resulting in a process that follows a gamma distribution (Touati et al., 2009). Further to this, the 95% confidence interval of the two distributions are shown in their corresponding colour, with the bounds marked by a dashed line.

Figure 6.39a shows that the pure power law distribution generally fits the inter-event times for the multiplet matching catalogue well, particularly in the 100-1,000 seconds region. The first binned inter-event time at <100 seconds occurs just outwith the confidence interval boundary, which indicates a higher density at the smaller inter-event times than the pure power law distribution would expect. However, Figure 6.39b shows that the inter-event times < 300 seconds could also be described by a gamma distribution, with the points within this region generally lying within the confidence bands. Applying this with the same theory for the tectonic settings, this indicates correlated event pairs at short inter-event times (Touati et al., 2009). Despite the gamma-type acceleration at <300 seconds, the inter-event times shown in Figure 6.39 as a whole agrees better with the power law distribution. This agrees with the results in Bell (2018), which also showed that a power-law distribution fit the inter-event times in this sequence better than an exponential and hyperbolic model.

To further analyse which distribution fits the inter-event times the best, I use the Akaike Information Criterion (AIC) from Equation 2.10 and Bayesian Information Criterion (BIC) from Equation 2.11 for both distributions for each catalogue (Table 6.10).

	Multiplet matching method
$AIC_{power-gamma}$	-2
$BIC_{power-gamma}$	-7

Table 6.10: The Akaike Information Criterion (AIC) from Equation 2.10 and Bayesian Information Criterion (BIC) from Equation 2.11 calculated for the Poisson and gamma distributions in Figure 6.39 to measure which fits the inter-event times prior to the landslide better.

The results in Table 6.10 indicate that the pure power law distribution is preferred by both the AIC and BIC for modelling the inter-event times for the multiplet matching catalogue. As the AIC is considered better for prediction, and the BIC is preferred for a consistent estimation of the underlying data generating process, it is promising that they both yield the same results. A power law fit indicates that the events were the result of slow creep through the repeated failure of asperity patches, suggesting that the preslip model best describes this situation.

Next, I observed the cumulative rate at which the multiplet matching catalogue events occurred in Figure 6.40, where the arrival time of the landslide is shown by the red vertical dashed line.

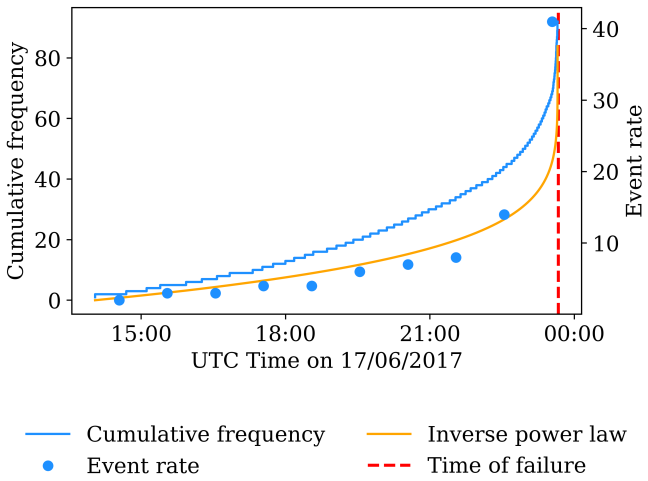

Figure 6.40: Multiplet matching cumulative frequency of events to observe event rate per hour, compared with an inverse power law model. The red vertical dashed line shows the arrival time of the landslide.

Figure 6.40 demonstrates the acceleration of the rate of multiplets to the failure. This represents the first time failure of the landslide, driven by the fracture growth. The rate of events per hour (blue dots) is fitted with an inverse power law model (orange line) accounting for Poisson counting errors on the event rate data, to illustrate the acceleration. However it should be noted that Bell et al. (2013) reported that this these fits could then be biased by the size of the bins prior to the failure time.

This acceleration confirms that this event rate is analogous to earthquake foreshock sequences, as it follows the reverse-time Omori law (Equation 2.14), where the rate p'=0.82, which is comparable to the rate of p'=0.71 calculated in Bell (2018). It would be beneficial to also apply Voight's relation (Equation 2.12) with the Failure Forecast Method (Cornelius and Voight, 1994) on this dataset, similar to that of (Bell, 2018), to test on the forecasting power of this result.

Each multiplet event increases the stress on the slope, which in turn drives this

increasing event rate until the catastrophic failure. The events can also be examined with the cumulative seismic moment, M_o, for the multiplet matching catalogue in Figure 6.41.

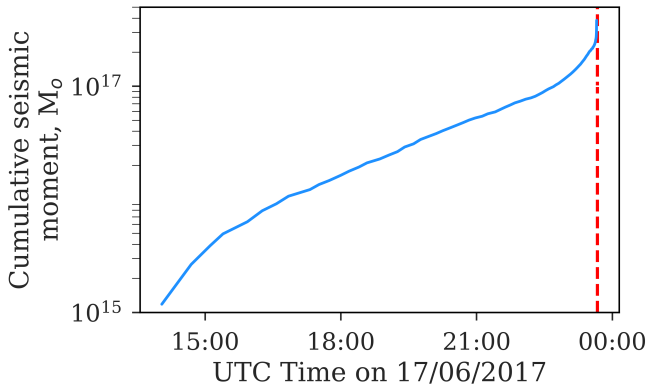

Figure 6.41: Cumulative seismic moment of multiplet matching events. The red vertical dashed line shows the time of the landslide.

The cumulative seismic moment in Figure 6.41 appears to look like the classic 3-stage creep-to-failure evolution of the moment release: I) deceleration, II) steady-state, and then III) accelerating creep (Main, 2000) due to the log-scale. However it is not possible to be fully confident in these results until the seismic moment has been reliably calculated. This does however give an indication that the utility of seismic events to characterise creep-type behaviours on a field-scale could be possible, confirming observations already made in a controlled laboratory setting by Heap et al. (2009, 2011), and ultimately gives confidence to forecast the failure time at the end of the process. The preslip nucleation hypothesis is most appropriate here from the indication that the events were caused by slip that reached a critical level where it was no longer stable and the eventual landslide occurred.

6.5 Results summary

In this chapter I described the results obtained from applying the multiplet matching method introduced in section 3.3 to three different settings: a tectonic setting featuring seismic swarms with no catastrophic failure (Diemtigen, Switzerland), during an eruptive volcanic period (Mount St Helens, USA), and prior to a large landslide (Nuugaatsiaq, Greenland). I observed the inter-event times, event rate and magnitudes of the found multiplets with respect to the rest of the catalogue.

The results showed that the events detected through the multiplet matching method in the Diemtigen sequence provide new insights on the underlying seismicity during the seismic swarm by lowering the M_c from 0.7 to -0.5 during this time period. There was a significant increase in cumulative seismic moment during the first few days in both the multiplet matching and SED catalogues, before the evolution became relatively steady, with the multiplet matching catalogue beginning to diverge as it contained many more events than the SED catalogue. However, as this was a seismic swarm sequence, the cumulative seismic moment in the steady-state phase was small. The initial increase indicates an underlying mechanism initiated and became the driver for the creep during this seismic swarm, which Diehl et al. (2015) suggested was either temporary fluid overpressure at the start of this sequence or some other sort of stress transfer which caused ruptures of several small fault segments. As the events in the multiplet matching catalogue were highly correlated with one another, this supports the theory that creep is the driver to what is causing the regular failure of the same fault patches which produces the highly similar low-magnitude waveforms. The multiplet matching method in this sequence has produced a more complete catalogue, and lowered the M_c significantly, allowing for a better understanding of the driver behind this seismic swarm. An obvious next step would be to observe the full seismic swarm sequence and to test different detection thresholds to include events which are less similar. Also, the

hypothesis that creep is the driver of this swarm could be further verified by observing temporal changes in the b-values.

The Mount St Helens sequence exhibited a very smooth and relatively stable event rate. In contrast, the cumulative seismic moment exhibited a smooth and clear transient involving a deceleration trend analogous to a primary creep process. The waveforms found were highly similar to one another, indicating that they were sourced from the same region. These factors agree with independent observations at Mount St Helens, that the steady rate of extrusion of several lava spines were causing these events, during the passive dome building period (Poland et al., 2008; Iverson et al., 2006; Thelen et al., 2008; Vallance et al., 2008).

Lastly, the results for the events detected through the multiplet matching method in the Nuugaatsiaq landslide sequence showed behaviour consistent with all three stages of the approach to failure driven by underlying creep processes. The multiplets detected had very similar waveforms, and initially occurred relatively stably, indicating the slow creep of the slope through the repeated failure of one (or multiple) asperity patch(es) was occurring. Approximately 10 minutes prior to the catastrophic failure, the inter-event times rapidly dropped and the magnitudes increased, hence increasing the cumulative seismic moment rate before eventual failure. The multiplet matching method enabled the nucleation of the landslide to be examined by tracking how the multiplets evolved with respect to the failure. A next step would be to include this type of analysis at other landslide points to provide insights into the occurrence of multiplets as precursors prior to other failures.

Chapter 7

Discussion

Throughout this thesis, I have produced and examined multiplet matching catalogues for different types of seismic sequence as a time series of events, and reviewed their statistical properties such as the frequency-magnitude relation, inter-event time distributions, event rates and cumulative release of seismic moment. In this chapter, I discuss the implications of the results within a broader context, and explore the degree to which this has generated new understanding from the competing hypotheses of pre-slip nucleation, triggered cascades, and random occurrence for different types of failure events.

In this discussion, I first explore the implications of the results discussed in chapters 5 and 6 from finding events through the multiplet matching method to current models for time-dependent deformation. Then, I examine how the multiplet pattern depends on the underlying processes that may control the evolving seismicity in each case. Finally, I consider some possible future extensions to the multiplet matching method discussed in this thesis, and further tests which could be completed.

7.1 Models for time-dependent behaviour

The multiplet matching method found over three times as many multiplets in the 2004 M_W 6.0 Parkfield and fourteen times as many in the 2014 M_W 8.2 Iquique earthquake sequences as the standard methods based on identifying events from the STA/LTA ratio alone (chapter 5). Their evolution in time was then compared to those obtained in other published catalogues using standard phase picking methods in the approach to their respective mainshocks.

In these two case studies the aim was to examine the potential of whole-waveform event detection to improve our understanding of nucleation-related precursors associated with repeater events located at the hypocentre of known mainshocks, and occurring prior to their origin times. Preslip nucleation itself occurs by a build up of localised, often predominantly aseismic, slip at the mainshock hypocentre (section 2.2.1). It is often associated with, or inferred from, repeated localised seismic slip from small events at the hypocentre occurring before the mainshock. More broadly, this discussion also examines the potential of new data to the time-dependent behaviour associated with transient or steady-state deformation processes that may or may not include nucleation-related precursors (e.g. Main (2000)). This included application to a seismic swarm, volcanic seismicity associated with effusive eruptions, and a slope failure resulting in an eventual landslide (chapter 6). I now consider each case study in this context, starting with the first two case studies.

7.1.1 Parkfield M_W 6.0 earthquake

The Parkfield segment is a unique portion of the San Andreas fault, located at the transition zone between a creeping section to the northwest, and the locked section to the southeast (Harris and Segall, 1987). Thus, it exhibits hybrid behaviour; creep occurs at

the surface, but locked asperities exist at seismogenic depths, resulting in brittle failure and significant earthquakes of similar characteristic size of M $\approx$ 6 (Harris and Segall, 1987; Murray and Langbein, 2006). The occurrence of multiplets on creeping faults has previously been used as an indicator of slip nucleation on small locked patches which are weaker than a larger locked region (Sammis and Rice, 2001). In this model, the patches fail many times before the larger region is ready to rupture, generating repeating events (Chen and Lapusta, 2009), and the small earthquakes that accompany the creep accumulate stress at the edges of the permanent asperity in this area (first identified by Harris and Segall (1987) and Malin et al. (1989)). Lengliné and Marsan (2009) and Twardzik et al. (2012) argue that the associated stress concentration activated the 2004 Parkfield earthquake.

The multiplet matching catalogue indicated an increase in the seismicity in the three hours prior to the Parkfield mainshock (section 5.2). This is confirmed by the observation that the eventual failure was preceded by an episode of aseismic deformation (Veedu and Barbot, 2016). These independent observations are consistent with the hypotheses of preslip reloading the asperities, and allows us to reject the null hypothesis that the events were random.

7.1.2 Iquique M_W 8.2 earthquake

There was no particular pattern in the seismicity in the two weeks prior to the M_W 8.2 mainshock in the Iquique sequence. Most of the information from the temporal evolution of multiplets showed behaviour that was consistent instead with transients associated with the triggering of large aftershocks of the previous M>6 earthquakes, with no accelerating cascade, rather than any precursory behaviour. Therefore this catalogue failed to reject the null hypothesis that these events were the result of random occurrence, as they could not be confidently described by the preslip or the cascade model.

Alternatively, Kato and Nakagawa (2014); Kato et al. (2016a); Socquet et al. (2017) previously found several slow slip events along the plate boundary fault in the 8 months prior to the M_W 8.2 earthquake. Their catalogue showed an increase in seismicity, aseismic slip, background seismicity and frequency of migrations from around 270 days before the mainshock. The multiplet matching catalogue obtained in section 5.3 started only two weeks prior to the mainshock, so unfortunately this longer-term pattern is not seen. The longer term studies show there is an initial large increase in cumulative seismic moment before the M_W 6.7 foreshock, likely due to an acceleration in the slow slip (Kato and Nakagawa, 2014; Kato et al., 2016a; Socquet et al., 2017). After this point, the seismic moment returned to a steady state of postseismic transients with afterslip inferred from the numerous foreshocks, consistent with ground deformation transients seen in geodesy studies (Ruiz et al., 2014; Schurr et al., 2014; Socquet et al., 2017). All of this occurred before the eventual dynamic rupture of the M_W 8.2 earthquake. These insights from other studies indicate that the Iquique sequence could be best modelled by a longer-term preslip hypothesis, as the larger aseismic nucleation process that was causing these slow slip events is the most likely underlying mechanism driving the timing of the mainshock. Although instead of a smoothly accelerating nucleation process, the activity took the form of several transients associated with creep deformation events. However, the information from the multiplet matching catalogue alone was not enough to reject the null hypothesis of no causal signal prior to the mainshock.

7.1.3 Diemtigen seismic swarm

The frequency of events in the phase-picked SED catalogue initially indicated the presence of three separate transients during the sequence (green line in Figure 6.14). However, improving the catalogue with the events detected with the multiplet matching method showed a more steady-state process, indicating a much more stationary or steady-state underlying process after the initial transient (blue line in Figure 6.14).

The multiplet matching method in this sequence produced a more complete catalogue, and lowered the M_c significantly. This improvement on the catalogue revealed an initial increase in cumulative seismic moment, consistent with a transient response to the onset of an underlying creep event during this seismic swarm. In an alternate hypothesis, Diehl et al. (2015) suggested this was due to temporary fluid overpressure developing at the start of this sequence or some other sort of stress transfer which caused ruptures of several small fault segments.

The events in the multiplet matching catalogue were highly correlated with one another, further indicating that creep was driving regular failure of the same fault patches, in turn producing repeated events with similar waveforms. Creep as the driver of this swarm could be further tested by observing temporal changes in the b-values attributed to varying loading rates (Wiemer and Wyss, 1997) and stress conditions (Wyss et al., 2004; Schorlemmer et al., 2004). Creep is indicative of the preslip model, where the multiplets found were a part of an ongoing process.

7.1.4 Mount St Helens volcanic activity

The Mount St Helens sequence showed a very smooth and relatively stationary event rate in the multiplet matching catalogue. The cumulative seismic moment also revealed a smooth and clear increase, directly analogous to a stable event process taking place. The null hypothesis that there is no causal pre-slip or cascade could not be rejected based on the study of the inter-event times, but overall, it is more likely that the events were independent to one another, and hence part of a random process.

Independent observations at Mount St Helens reported that during this period, there was a steady rate of extrusion of several lava spines that were causing these events during the passive dome building period (Poland et al., 2008; Iverson et al., 2006; Thelen et al., 2008; Vallance et al., 2008). In this case, the high similarity in events support

the hypothesis that a crack located at shallow depth was rapidly healing, loading, and reactivating the source at a steady-rate that was causally-triggering the events (Waite et al., 2008; Bell et al., 2018). Thus the events were correlated to a common underlying process rather than to each other.

7.1.5 Nuugaatsiaq landslide

The multiplets detected in the Nuugaatsiaq landslide sequence enabled the nucleation of the landslide to be examined by tracking how their properties evolved with respect to the eventual failure time. The tracking of the cumulative seismic moment clearly exhibited stages prior to failure expected from underlying creep processes, notable to those of steady-state followed by accelerating creep. However this inference depends on the moment calculated for these events from the estimated magnitude, and so requires further magnitude and moment characterisation for assurance. Overall the results are consistent with the preslip hypothesis.

The cumulative moment release curves were very smooth, and indistinguishable from illustrations of the evolution of strain in the three-stage creep model often shown in textbooks, in response to a step-change in otherwise constant applied stress. This observation is consistent with the physical model for creep by damage associated with time-dependent, sub-critical crack growth in the otherwise brittle field developed by Main (2000). This begun with the initial deceleration of the cumulative seismic moment indicative with a transient process, before reaching a steady-state of creep and then accelerating to failure. However it is unclear whether the initial deceleration is real, or the unintentional product of the magnitude estimation which is exaggerated by the log scale, and so this initial deceleration cannot be established confidently at this stage. Nonetheless, this analysis of the region would not have been possible without the inclusion of the events detected by the multiplet matching method, which confirmed the potential of the method to identify a representative population of seismic

events capable of characterising creep-type behaviours on a field scale. This supports the recommendation that having high-resolution seismic data in critical areas could help improve preparedness with forecasting the landslide hazard by monitoring of the evolution of events.

7.2 Areas for future work

The multiplet matching method introduced in section 3.3.1 provided a technique for detecting and identifying earthquakes with similar waveforms (multiplets) for a wide variety of tectonic settings and types of seismic sequence. There are several potential modifications and further tests to this method that could be considered in future work.

7.2.1 Improvements to the multiplet matching method

Due to time constraints, and the primacy given to examining many different types of seismic sequence in this thesis, I did not have time to implement the multiplet matching method using multiple stations. This would introduce a significant extra dimension in terms of spatial analysis of multiplets, and also establish whether the multiplets are truly repeating earthquakes in the sense that they have the same focal mechanism. Extra stations would also likely identify a greater number of candidate repeater events, and enhance the statistical analysis further.

The main advantage of using multiple stations would be to enhance the catalogues by providing locations and more accurate magnitude estimations, which would help in all examined case studies. In particular, it would reveal whether the magnitudes of the multiplets detected at Mount St Helens had two dominant amplitudes due to an unidentified artefact, events occurring in different locations, or if their size discrepancy indicated more than one underlying processes taking place. It was not possible to

distinguish two separately-driven populations that manifested in the bimodal behaviour observed. However, the waveforms were sufficiently similar, meaning that the events would be located within one quarter a wavelength of each other, or <400 metres (Geller and Mueller, 1980). Hence, obtaining the precise location and focal mechanism of these events would improve the understanding of their source, and whether they represent two separate underlying processes. Similarly, the spatial evolution of the detected seismicity prior to the Parkfield mainshock, could greatly assist in the understanding of the nucleation of this earthquake sequence.

The inclusion of additional stations would also negate the need for the preferential removal of overlapping events in the multiplet matching method, as their arrival times would differ on multiple stations. Refining the travel time picking across networks would also improve locations. This would be a great improvement in the method, as it would then include more events than previous tests, which influences factors such as the inter-event time distributions and event rates greatly. In this thesis, the analysis of the inter-event time distributions proved to be the least conclusive in particular.

Another modification would be to combine seismograms from several sources to compile a 'master' catalogue, which could include events which are both similar to one another (i.e. multiplets), and those that are not. They were treated independently in this thesis to analyse the events which were populating the same region, but there is no reason to not include them when examining other aspects of seismicity, for example the completeness of the catalogue.

7.2.2 Future applications

The detection and identification of events with the multiplet matching method in this thesis has provided new insight into the underlying processes that drive seismic sequences in several different settings. An interesting next step could be to observe

all the previously studied sequences on a longer timescale, allowing for an enhanced observation of their individual behaviours. This would be particularly interesting for the Iquique earthquake sequence, where an insight of the underlying seismicity both prior to and after the mainshock has been previously studied in Kato and Nakagawa (2014) and Socquet et al. (2017), thus could be built upon and compared with. Expanding the timeframe for the Diemtigen seismic swarm could also further assist in the role of analysing the driver of the swarm.

Additionally, investigating different families of multiplets in the same locations could also be done to examine stress changes associated with multiplets (De Meersman et al., 2009). This would have been particularly useful for the Mount St Helens study to determine whether several families of multiplets were taking place. Also, introducing more automated detected methods – for example, migration (Wagner et al., 2017) or machine learning methods (Yoon et al., 2015) could also be completed for a more advanced multiplet matching method.

Another obvious next step would be to apply the method on a larger scale of failures to get a measure of how many significant earthquake sequences have had a nucleation pattern prior to their mainshock. In the time available, I was able to only analyse behaviour prior to two mainshocks in two earthquake sequences. However I would have liked to applied this to the 1999 M_W 7.6 Izmit, Turkey earthquake sequence where Bouchon et al. (2011) and Ellsworth and Bulut (2018) saw opposing nucleation patterns prior to the mainshock, and the 2011 M_W 9.0 Tohoku-Oki (Japan) earthquake sequence, where Kato et al. (2012) found pronounced foreshock migration seismicity. Unfortunately, this was not possible in this thesis, as it proved impossible to obtain the datasets.

At the time of writing this thesis, a M_W 7.1 earthquake occurred near Ridgecrest in California, USA on 6th July 2019 with several moderately sized foreshocks as well as many aftershocks present (USGS, 2019). The epicentre of the mainshock was 250km

away from that of the Parkfield sequence, but it would be interesting to compare whether a similar pattern was observable in this sequence.

Chapter 8

Conclusions

The presence of multiplets in the seismic signal can help better understand the nucleation processes that may be occurring, which has implications for the forecasting of failure and associated risk management. In this thesis, I have explored how having a more complete catalogue of seismic events can be used to better the understanding of the behaviour associated with the underlying processes that drive seismicity in several different sequences through several different statistical metrics. For example, the finding of many multiplets in the Parkfield sequence strongly indicated that there was creep occurring. The combination of this result with other independent studies gave confidence to the use of multiplets as a mechanical support to infer underlying processes such as creep along major faults. In this thesis, I applied my method to two large-magnitude earthquake sequences, a seismic swarm with no clear mainshock, volcanic seismicity associated with an effusive eruption, and the failure of a slope that preceded a large landslide.

A method of iterative template matching was developed to detect previously unknown events with similar waveforms (referred to as 'multiplets') in seismic datasets. The multiplets found improved our understanding of nucleation-related precursors associated with events located close to, or at, the nucleation point of failure. This

method significantly improved the official event catalogues which use the common triggering approach alone to find events, with many new detections for the five separate case studies considered in this thesis.

This method evolved beyond existing methods used by other authors, as it adapted the master trace (i.e. the one searching for similar waveforms), based on previous multiplets found. The method was also versatile by allowing for a comparison in finding similar events in different seismic datasets, which few existing techniques can currently claim. Identifying newly found events in different types of failure sequences provided new insight into the understanding of the time-dependent behaviour associated with deformation processes that may or may not include nucleation-related precursors.

The new event catalogues for the five separate case studies showed several types of behaviour associated with failure. An increase in the number of relatively close together low-magnitude multiplets in the preceding time of the M_W 6.0 Parkfield mainshock implied a repeated rupture of the small locked patches, consistent with the occurrence of slip nucleation and creep on the fault, and thus being an appropriate candidate for the preslip hypothesis. Alternatively, the events detected in the M_W 8.2 Iquique earthquake sequence lowered the magnitude of completeness significantly. This revealed a steady-state pattern of the postseismic transients associated with creep deformation events, inferred from the numerous foreshocks occurring before the eventual dynamic rupture. However, the information revealed by the multiplet matching catalogue failed to reject the null hypothesis that the multiplets occurrence were random. A much more stationary or steady-state underlying process was observed after the initial transient during the Diemtigen seismic swarm, showing consistency with localised creep being the driver, also indicating the preslip hypothesis applies here. The null hypothesis that there was no causal pre-slip or cascade could not be rejected in the Mount St Helens dataset based on the study of the inter-event times. However, the multiplet matching catalogue indicated a stable seismic moment, consistent with the independent observations of a steady rate of extrusion of several lava spines which were causing these multiplets during

the passive dome building period. Lastly, the stages to failure driven by underlying creep processes, were clearly observed in the studied time period of the Nuugaatsiaq landslide. This behaviour is typically observed in the physical models for creep, of the damage associated with time-dependent, sub-critical crack growth in brittle materials, thus confirming the use of multiplets to characterise creep-like characteristics. This is indicative of the preslip nucleation hypothesis from the observation that the multiplets were caused by slip that then reached a critical level, resulting in the eventual landslide.

These analyses of five separate regions would not have been easily done without the inclusion of the events detected by the method introduced in this thesis. Considering multiplets in these cases confirmed the potential in understanding the nucleation behaviour of the underlying processes that drive seismicity in several different sequences.

Although the task of locating the hypocentre of the events still remains, several other characteristics studied in this thesis, including the temporal evolution of events prior to catastrophic failure, could be helpful in future analysis of similar sequences. Other features like the inter-event time distributions proved less useful in determining the characteristics for the tectonic-earthquake studies, because of the temporal proximity of some events. In some cases, the cumulative seismic moment was the most useful feature studied, as it revealed unknown deformation processes which were not initially apparent. For example, it was found that a repeated rupture of the same, or multiple, fault patches during creep does not necessarily result in a large rupture.

The method introduced in this thesis provided a simple approach to improving the current event catalogues by detecting previously unknown events by the similarity of their waveforms. Combining this with several different statistical analyses allowed for the nucleation characteristics to be examined in greater detail. Hence expanding the timescale on the failure sequences studied in this thesis would allow for further in-depth observations of their individual behaviours. These findings make the developed method

a promising technique for use in future research on addressing the current understanding associated with the seismicity for determining nucleation in different failure settings.

Bibliography

Akaike, H. (1974). A new look at the statistical model identification. *IEEE Transactions on Automatic Control*, 19(6):716–723.

Aki, K. (1965). Maximum likelihood estimate of b in the formula log N = a-bM and its confidence limits. *Bull. Earthq. Res. Inst., Tokyo Univ.*, 43:237–239.

Allstadt, K. (2013). Extracting source characteristics and dynamics of the August 2010 Mount Meager landslide from broadband seismograms. *Journal of Geophysical Research: Earth Surface*, 118(3):1472–1490.

Amelung, F. and King, G. (1997). Earthquake scaling laws for creeping and non-creeping faults. *Geophy*, 24(5):507–510.

Anderson, K., Lisowski, M., and Segall, P. (2010). Cyclic ground tilt associated with the 2004-2008 eruption of Mount St. Helens. *Journal of Geophysical Research: Solid Earth*, 115(11):1–29.

Angermann, D., Klotz, J., and Reigber, C. (1999). Space-Geodetic Estimation of the Nazca-South America Euler Vector. *Earth and Planetary Science Letters*, 171(3):329–334.

Anstey, N. A. (1964). Correlation Techniques - A Review. *Geophysical Prospecting*, 12(4):355–382.

Bak, P., Christensen, K., Danon, L., and Scanlon, T. (2002). Unified scaling law for earthquakes. *Physical Review Letters*, 88(17):1785011–1785014.

Bak, P., Tang, C., and Wiesenfeld, K. (1988). On self organized criticality. *Physical Review A*, 38(1):364–374.

Baker, J. W. (2013). Probabilistic Seismic Hazard Analysis. *White Paper Version 2.0.1*, page pp 79.

Bakun, W., Breckenridge, K., Bredehoeft, J., Burford, R., Ellsworth, W., Johnston, M. S., Jones, L., Lindh, A., Mortensen C., Mueller, R., Poley, C., Roeloffs, E., Schulz, S., Segall, P., and Thatcher, W. (1987). Parkfield, California, Earthquake Prediction Scenarios and Response Plans. Technical report, USGS.

Bakun, W. and Lindh, A. (1985). The Parkfield, California, Earthquake Prediction Experiment. *Science*, 229(4714):619–624.

Bakun, W. H. and McEvilly, T. V. (1984). Recurrence models and Parkfield, California, earthquakes. *Journal of Geophysical Research: Solid Earth*, 89(B5):3051–3058.

Barrett, S. A. and Beroza, G. C. (2014). An Empirical Approach to Subspace Detection. *Seismological Research Letters*, 85(3):594–600.

Belardinelli, M. E. (2003). Earthquake triggering by static and dynamic stress changes. *J. Geophys Res.*, 108:1–16.

Bell, A. F. (2018). Predictability of Landslide Timing From Quasi-Periodic Precursory Earthquakes. *Geophysical Research Letters*, 45(4):1860–1869.

Bell, A. F., Hernandez, S., Gaunt, H. E., Mothes, P., Ruiz, M., Sierra, D., and Aguaiza, S. (2017). The rise and fall of periodic 'drumbeat' seismicity at Tungurahua volcano, Ecuador. *Earth and Planetary Science Letters*, 475:58–70.

Bell, A. F. and Kilburn, C. R. (2012). Precursors to dyke-fed eruptions at basaltic volcanoes: Insights from patterns of volcano-tectonic seismicity at Kilauea volcano, Hawaii. *Bulletin of Volcanology*, 74:325–339.

Bell, A. F. and Kilburn, C. R. J. (2013). Trends in the aggregated rate of pre-eruptive volcano-tectonic seismicity at Kilauea volcano, Hawaii. *Bulletin of Volcanology*, 75(1):1–10.

Bell, A. F., Naylor, M., Heap, M. J., and Main, I. G. (2011). Forecasting volcanic eruptions and other material failure phenomena: An evaluation of the failure forecast method. *Geophysical Research Letters*, 38.

Bell, A. F., Naylor, M., Hernandez, S., Main, I. G., Gaunt, H. E., Mothes, P., and Ruiz, M. (2018). Volcanic Eruption Forecasts From Accelerating Rates of Drumbeat Long-Period Earthquakes. *Geophysical Research Letters*, 45.

Bell, A. F., Naylor, M., and Main, I. G. (2013). The limits of predictability of volcanic eruptions from accelerating rates of earthquakes. *Geophysical Journal International*, 194(3):1541–1553.

Benoit, J. and McNutt, S. (1996). Global volcanic earthquake swarms database and preliminary analysis of volcanic earthquake swarm duration.

Berberich, G., Berberich, M., Grumpe, A., Wöhler, C., and Schreiber, U. (2013). Early results of three-year monitoring of red wood ants' behavioral changes and their possible correlation with earthquake events. *Animals*, 3(1):63–84.

Berger, J. and Sax, R. L. (1980). Seismic Detectors: The State of the Art. Technical report, AFTAC Technical Report SSR-R-80-4588.

Beroza, G. C. and Ellsworth, W. L. (1996). Properties of the seismic nucleation phase. *Tectonophysics*, 261(1-3):209–227.

Beyreuther, M., Barsch, R., Krischer, L., Megies, T., Behr, Y., and Wassermann, J. (2010). ObsPy: A Python Toolbox for Seismology. *Seismological Research Letters*, 81(3):530–533.

Bommer, J. J., Oates, S., Cepeda, J. M., Lindholm, C., Bird, J., Torres, R., Marroquín,

G., and Rivas, J. (2006). Control of hazard due to seismicity induced by a hot fractured rock geothermal project. *Engineering Geology*, 83(4):287–306.

Borghi, A., Aoudia, A., Javed, F., and Barzaghi, R. (2016). Precursory slow-slip loaded the 2009 L'Aquila earthquake sequence. *Geophysical Journal International*, 205(2):776–784.

Bouchon, M., Durand, V., Marsan, D., Karabulut, H., and Schmittbuhl, J. (2013). The long precursory phase of most large interplate earthquakes. *Nature Geoscience*, 6(4):299–302.

Bouchon, M., Karabulut, H., Aktar, M., Ozalaybey, S., Schmittbuhl, J., and Bouin, M.-P. (2011). Extended nucleation of the 1999 Mw 7.6 Izmit earthquake. *Science (New York, N.Y.)*, 331(6019):877–880.

Boué, A., Lesage, P., Cortés, G., Valette, B., and Reyes-Dávila, G. (2015). Real-time eruption forecasting using the material Failure Forecast Method with a Bayesian approach. *Journal of Geophysical Research: Solid Earth*, 120:2143–2161.

Brantut, N., Heap, M. J., Meredith, P. G., and Baud, P. (2013). Time-dependent cracking and brittle creep in crustal rocks: A review. *Journal of Structural Geology*, 52(1):17–43.

Brown, J. R., Beroza, G. C., and Shelly, D. R. (2008). An autocorrelation method to detect low frequency earthquakes within tremor. *Geophysical Research Letters*, 35(16):1–5.

Bürgmann, R. (2018). The geophysics, geology and mechanics of slow fault slip. *Earth and Planetary Science Letters*, 495:112–134.

Burnham, K. P. and Anderson, D. R. (2004). Multimodel Inference: Understanding AIC and BIC in Model Selection. *Sociological Methods & Research*, 33(2):261–304.

Cailleau, B., Lafemina, P. C., and Dixon, T. H. (2007). Stress accumulation between

volcanoes : an explanation for intra-arc earthquakes in Nicaragua? *Geophys. J. Int.*, 169:1132–1138.

Cao, A. and Gao, S. S. (2002). Temporal variation of seismic b -values beneath northeastern Japan island arc . *Geophysical Research Letters*, 29(9):48–1–48–3.

Cesca, S., Grigoli, F., Heimann, S., Dahm, T., Kriegerowski, M., Sobiesiak, M., Tassara, C., and Olcay, M. (2016). The Mw 8.1 2014 Iquique, Chile, seismic sequence: a tale of foreshocks and aftershocks. *Geophysical Journal International*, 204(3):1766–1780.

Chambers, D., Boltz, M., Richardson, J., and Finley, S. (2017). Application of subspace detection on a surface seismic network monitoring a deep silver mine. *Deep Mining*, pages 141–154.

Chen, Q. F. and Wang, K. L. (2010). The 2008 Wenchuan Earthquake and Earthquake Prediction in China. *Bulletin of the Seismological Society of America*, 100(5B):2840–2857.

Chen, T. and Lapusta, N. (2009). Scaling of small repeating earthquakes explained by interaction of seismic and aseismic slip in a rate and state fault model. *Journal of Geophysical Research*, 114(B01311):1–12.

Chesley, C., LaFemina, P. C., Puskas, C., and Kobayashi, D. (2012). The 1707 Mw8.7 Hoei earthquake triggered the largest historical eruption of Mt. Fuji. *Geophysical Research Letters*, 39(24):6–10.

Chouet, B. A. and Matoza, R. S. (2013). A multi-decadal view of seismic methods for detecting precursors of magma movement and eruption. *Journal of Volcanology and Geothermal Research*, 252:108–175.

Cicerone, R. D., Ebel, J. E., and Britton, J. (2009). A systematic compilation of earthquake precursors. *Tectonophysics*, 476(3-4):371–396.

Cocco, M. and Rice, J. R. (2002). Pore pressure and poroelasticity effects in Coulomb stress analysis of earthquake interactions. *Journal of Geophysical Research*, 107(B2).

Cornelius, R. R. and Voight, B. (1994). Seismological aspects of the 1989-1990 eruption at Redoubt Volcano, Alaska: the Materials Failure Forecast Method (FFM) with RSAM and SSAM seismic data. *Journal of Volcanology and Geothermal Research*, 62(1-4):469–498.

Corral, Á. (2004). Long-Term Clustering , Scaling , and Universality in the Temporal Occurrence of Earthquakes. *Physical Review Letters*, 92(10):1–4.

Cutter, S. L., Ash, K. D., and Emrich, C. T. (2014). The geographies of community disaster resilience. *Global Environmental Change*, 29:65–77.

Dascalu, C., François, B., and Keita, O. (2009). A two-scale model for subcritical damage propagation. *International Journal of Solids and Structures*, 47:493–502.

De la Cruz-Reyna, S. and Reyes-Dávila, G. A. (2001). A model to describe precursory material-failure phenomena: applications to short-term forecasting at colima volcano, Mexico. *Bulletin of Volcanology*, 63(5):297–308.

De Meersman, K., Kendall, J. M., and van der Baan, M. (2009). The 1998 Valhall microseismic data set: An integrated study of relocated sources, seismic multiplets, and S-wave splitting. *Geophysics*, 74(5):B183–B195.

De Michele, M., Raucoules, D., Rolandone, F., Briole, P., Salichon, J., Lemoine, A., and Aochi, H. (2011). Spatiotemporal evolution of surface creep in the Parkfield region of the San Andreas Fault (1993-2004) from synthetic aperture radar. *Earth and Planetary Science Letters*, 308(1-2):141–150.

Deichmann, N. and Giardini, D. (2009). Earthquakes Induced by the stimulation of an enhanced geothermal system below Basel (Switzerland). *Seismological Research Letters*, 80(5):784–798.

Dhakal, A. S. and Sidle, R. C. (2004). Distributed simulations of landslides for different rainfall conditions. *Hydrological Processes*, 18(4):757–776.

Diehl, T., Deichmann, N., Clinton, J., Kästli, P., Cauzzi, C., Kraft, T., Behr, Y., Edwards, B., Guilhem, A., Korger, E., Hobiger, M., Haslinger, F., Fäh, D., and Wiemer, S. (2015). Earthquakes in Switzerland and surrounding regions during 2014. *Swiss Journal of Geosciences*, 108(2-3):425–443.

Dieterich, J. H. (1979). Modeling of rock friction 1. Experimental results and constitutive equations. *Journal of Geophysical Research: Solid Earth*, 84(B5):2161–2168.

Dieterich, J. H. (1992). Earthquake nucleation on faults with rate-and state-dependent strength. *Tectonophysics*, 211(1-4):115–134.

Dixon, T. H., Jiang, Y., Malservisi, R., McCaffrey, R., Voss, N., Protti, M., and Gonzalez, V. (2014). Earthquake and tsunami forecasts: Relation of slow slip events to subsequent earthquake rupture. *Proceedings of the National Academy of Sciences*, 111(48):17039–17044.

Dzurisin, D., Moran, S. C., Lisowski, M., Schilling, S. P., Anderson, K. R., and Werner, C. (2015). The 2004-2008 dome-building eruption at Mount St. Helens, Washington: epilogue. *Bulletin of Volcanology*, 77(10).

Earle, P. S. and Shearer, P. M. (1994). Characterization of Global Seismograms Using an Automatic-Picking Algorithm. *Bulletin of the New Zealand Society for Earthquake Engineering*, 84(2):366–376.

Ekström, G. and Stark, C. P. (2013). Simple Scaling of Catastrophic Landslide Dynamics. Supplementary Materials. *Science*, 339(6126):1416–1419.

Ellsworth, W. (2018). Personal communication.

Ellsworth, W. L. (1995). Characteristic Earthquakes and Long-Term Earthquake Forecasts: Implications of Central California Seismicity. In *Urban Disaster Mitigation: The Role of Engineering and Technology*, pages 1–14. Elsevier.

Ellsworth, W. L. (2013). Injection-Induced Earthquakes. *Science*, 341(July):1–8.

Ellsworth, W. L. and Beroza, G. C. (1995). Seismic Evidence for an Earthquake Nucleation Phase. *Science*, 268(5212):851–855.

Ellsworth, W. L. and Bulut, F. (2018). Nucleation of the 1999 Izmit earthquake by a triggered cascade of foreshocks. *Nature Geoscience*, 11(July):531–536.

Fäh, D., Giardini, D., Bay, F., Bernardi, F., Braunmiller, J., Deichmann, N., Furrer, M., Gantner, L., Gisler, M., Isenegger, I., Jimenez, M., Kästli, P., Koglin, R., Masciadri, V., Rutz, M., Scheidegger, C., Schibler, R., Schorlemmer, D., Schwarz-Zanetti, G., Steimen, S., Sellami, S., Wiemer, S., and Wossner, J. (2003). Earthquake Catalogue Of Switzerland (ECOS) and the related macroseismic database. *Eclogae Geologicae Helvetiae: Swiss Journal of Geosciences*, 96(2):219–236.

Fäh, D., Gisler, M., Jaggi, B., Kästli, P., Lutz, T., Masciadri, V., Matt, C., Mayer-Rosa, D., Rippmann, D., Schwarz-Zanetti, G., Tauber, J., and Wenk, T. (2009). The 1356 Basel earthquake: An interdisciplinary revision. *Geophysical Journal International*, 178(1):351–374.

Felzer, K. R., Abercrombie, R. E., and Ekstrom, G. (2004). A common origin for aftershocks and multiplets . *Bull. Seismol. Soc. Am.*, 94(1):88–99.

Field, E. H., Seligson, H. A., Gupta, N., Gupta, V., Jordan, T. H., and Campbell, K. W. (2005). Loss estimates for a Puente Hills blind-thrust earthquake in Los Angeles, California. *Earthquake Spectra*, 21(2):329–338.

Francis, P. and Oppenheimer, C. (2004). *Volcanoes*. Oxford University Press, Oxford, 2nd edition.

Freed, A. M. (2005). Earthquake Triggering By Static, Dynamic, and Postseismic Stress Transfer. *Annual Review of Earth and Planetary Sciences*, 33(1):335–367.

Gardner, J. and Knopoff, L. (1974). Is the sequence of earthquakes in Southern California, with aftershocks removed, Poissionian? *Bulletin of the Seismological Society of America*, 64(5):1363–1367.

Gariano, S. L. and Guzzetti, F. (2016). Landslides in a changing climate. *Earth-Science Reviews*, 162:227–252.

Geller, R. J. and Mueller, C. S. (1980). Four Similar Earthquakes in Central California. *Geophys. Res. Lett.*, 7(10):821–824.

Gibbons, S. J. and Ringdal, F. (2006). The detection of low magnitude seismic events using array-based waveform correlation. *Geophysical Journal International*, 165(1):149–166.

Godano, C., Lippiello, E., and De Arcangelis, L. (2014). Variability of the b value in the Gutenberg-Richter distribution. *Geophysical Journal International*, 199(3):1765–1771.

Goebel, T. H. and Brodsky, E. E. (2018). The spatial footprint of injection wells in a global compilation of induced earthquake sequences. *Science*, 361(6405):899–904.

Gomberg, J. (2018). Unsettled earthquake nucleation. *Nature Geoscience*, 11(July):463–464.

Grant, R. A. and Halliday, T. (2010). Predicting the unpredictable; evidence of pre-seismic anticipatory behaviour in the common toad. *Journal of Zoology*, 281:263–271.

Green, D. N. and Neuberg, J. (2006). Waveform classification of volcanic low-frequency earthquake swarms and its implication at Soufrière Hills Volcano, Montserrat. *Journal of Volcanology and Geothermal Research*, 153(1-2 SPEC. ISS.):51–63.

Gutenberg, B. and Richter, C. (1944). Frequency of Earthquakes in California. *Bulletin of the Seismological Society of America*, 34:185–188.

Hammer, C. and Neuberg, J. W. (2009). On the dynamical behaviour of low-frequency earthquake swarms prior to a dome collapse of Soufri\‘ere Hill volcano , Montserrat. *Geophys. Res. Lett.*, 36:1–3.

Handwerger, A. L., Rempel, A. W., Skarbek, R. M., Roering, J. J., and Hilley, G. E. (2016). Rate-weakening friction characterizes both slow sliding and catastrophic failure of landslides. *Proceedings of the National Academy of Sciences*, 113(37):10281–10286.

Hanks, T. C. and Kanamori, H. (1979). A Moment Magnitude Scale. *Journal of Geophysical Research*, 84(B5):2348–2350.

Harrington, R. M. and Brodsky, E. E. (2007). Volcanic hybrid earthquakes that are brittle-failure events. *Geophysical Research Letters*, 34(6).

Harris, D. B. (2006). Subspace Detectors: Theory. Technical report, Lawrence Livermore National Laboratory, Livermore, California.

Harris, R. A. and Segall, P. (1987). Detection of a locked zone at depth on the Parkfield, California, segment of the San Andreas fault (USA). *Journal of Geophysical Research*, 92(B8):7945–7962.

Heap, M. J., Baud, P., Meredith, P. G., Bell, A. F., and Main, I. G. (2009). Time-dependent brittle creep in darley dale sandstone. *Journal of Geophysical Research: Solid Earth*, 114(7).

Heap, M. J., Baud, P., Meredith, P. G., Vinciguerra, S., Bell, A. F., and Main, I. G. (2011). Brittle creep in basalt and its application to time-dependent volcano deformation. *Earth and Planetary Science Letters*, 307(1-2):71–82.

Helmstetter, A. and Sornette, D. (2002). Foreshocks Explained by Cascades of Triggered Seismicity. *Journal of Geophysical Research*, 108(B10):2457.

Hickman, S. and Langbein, J. (2004). The Parkfield Experiment - Capturing What Happens in an Earthquake. Technical report, USGS.

Hill, D. P., Reasenberg, P. a., Michael, A., Arabaz, W. J., Beroza, G., Brumbaugh, D., Brune, J. N., Castro, R., Davis, S., Ellsworth, W. L., Gomberg, J., Harmsen,

S., House, L., Jackson, S. M., Johnston, M. J. S., Jones, L., Keller, R., Malone, S., Munguia, L., Nava, S., Pechmann, J. C., Sanford, A., Simpson, R. W., Smith, R. B., Stark, M., Stickney, M., Vidal, A., Walter, S., Wong, V., and Zollweg, J. (1993). Seismicity Remotely Triggered by the Magnitude 7.3 Landers, California, Earthquake. *Science*, 260(June):1617–1623.

Hough, S. E. (2010). *Predicting the Unpredictable: The Tumultuous Science of Earthquake Prediction*. Princeton University Press, Princeton.

Husen, S., Kissling, E., and von Deschwanden, A. (2013). Induced seismicity during the construction of the Gotthard Base Tunnel, Switzerland: Hypocenter locations and source dimensions. *Journal of Seismology*, 17(1):63–81.

Ide, S., Shelly, D. R., and Beroza, G. C. (2007). Mechanism of deep low frequency earthquakes: Further evidence that deep non-volcanic tremor is generated by shear slip on the plate interface. *Geophysical Research Letters*, 34(3).

Iio, Y. (2009). Encyclopedia of Complexity and Systems Science. In Meyers, A. R., editor, *Encyclopedia of Complexity and Systems Science*, chapter Earthquake, pages 2538–2555. Springer New York, New York, NY.

Iverson, R. M. (2008). Dynamics of Seismogenic Volcanic Extrusion Resisted by a Solid Surface Plug , Mount St . Helens , 2004 – 2005. In Sherrod, D., Scott, W., and Stauffer, P., editors, *A Volcano Rekindled: The Renewed Eruption of Mount St. Helens 2004-2006, U.S. Geological Survey Professional Paper 1750*, chapter 21, pages 425–460. USGS.

Iverson, R. M., Dzurisin, D., Gardner, C. A., Gerlach, T. M., LaHusen, R. G., Lisowski, M., Major, J. J., Malone, S. D., Messerich, J. A., Moran, S. C., Pallister, J. S., Qamar, A. I., Schilling, S. P., and Vallance, J. W. (2006). Dynamics of seismogenic volcanic extrusion at Mount St Helens in 2004–05. *Nature*, 444(7118):439–443.

Jaeger, J., Cook, N., and Zimmerman, R. (2007). *Fundamentals of Rock Mechanics*. Blackwell Publishing, fourth edition.

Johanson, I. A., Fielding, E. J., Rolandone, F., and Bürgmann, R. (2006). Coseismic and postseismic slip of the 2004 Parkfield earthquake from space-geodetic data. *Bulletin of the Seismological Society of America*, 96(4 B).

Jones, L. M. and Molnar, P. (1979). Some characteristics of foreshocks and their possible relationship to earthquake prediction and premonitory slip on faults. *Journal of Geophysical Research*, 84(B7):3596.

Jordan, T. H. (2009). Earthquake system science: Potential for seismic risk reduction. *Scientia Iranica*, 16(5):351–366.

Jordan, T. H., Chen, Y. T., Gasparini, P., Madariaga, R., Main, I., Marzocchi, W., Papadopoulos, G., Sobolev, G., Yamaoka, K., and Zschau, J. (2011). Operational earthquake forecasting: State of knowledge and guidelines for utilization. *Annals of Geophysics*, 54(4):319–391.

Jordan, T. H., Marzocchi, W., Michael, A. J., and Gerstenberger, M. C. (2014). Operational Earthquake Forecasting Can Enhance Earthquake Preparedness. *Seismological Research Letters*, 85(5):955–959.

Jordan, T. H., McGuire, J. J., and Boettcher, M. S. (2004). Foreshocks and Short-Term Earthquake Predictability on East Pacific Rise Transform Faults. In *UJNR Meeting*.

Kanamori, H. (1983). Magnitude scale and quantification of earthquakes. *Tectonophysics*, 93(3-4):185–199.

Kanamori, H. and Given, J. W. (1982). Analysis of long-period waves excited by the May 18, 1980, eruption ofMount St. Helens— a terrestrial monopole? *Journal of Geophysical Research*, 87(B7):5422–5432.

Kato, A., Fukuda, J., Kumazawa, T., and Nakagawa, S. (2016a). Accelerated nucleation of the 2014 Iquique, Chile Mw 8.2 Earthquake. *Scientific Reports*, 6(April):24792.

Kato, A., Fukuda, J., Kumazawa, T., and Nakagawa, S. (2016b). Accelerated nucleation of the 2014 Iquique, Chile Mw 8.2 Earthquake. *Scientific Reports*, 6(April):1 – 9.

Kato, A. and Nakagawa, S. (2014). Multiple slow-slip events during a foreshock sequence of the 2014 Iquique, Chile Mw 8.1 earthquake. *Geophysical Research Letters*, 41:5420–5427.

Kato, A., Obara, K., Igarashi, I., Tsuruoka, H., Nakagawa, S., and Hirata, N. (2012). Propagation of Slow Slip Leading Up to the 2011 Mw 9.0 Tohoku-Oki Earthquake. *Science*, 335(2):705–708.

Kendall, J.-M., Butcher, A., Stork, A. L., Verdon, J. P., and Luckett, R. (2019). How big is a small earthquake? Challenges in determining microseismic magnitudes. *First Break*, 37(February):51–56.

Kendrick, J. E., Lavallée, Y., Hirose, T., Di Toro, G., Hornby, A. J., De Angelis, S., and Dingwell, D. B. (2014). Volcanic drumbeat seismicity caused by stick-slip motion and magmatic frictional melting. *Nature Geoscience*, 7(6):438–442.

Kilb, D. and Gomberg, J. (1999). The initial subevent of the 1994 Northridge, California, earthquake: Is earthquake size predictable? *Journal of Seismology*, 3(4):409–420.

Kilburn, C. R. (2003). Multiscale fracturing as a key to forecasting volcanic eruptions. *Journal of Volcanology and Geothermal Research*, 125(3-4):271–289.

Kilburn, C. R. and Petley, D. N. (2003). Forecasting giant, catastrophic slope collapse: Lessons from Vajont, Northern Italy. *Geomorphology*, 54(1-2):21–32.

Kilburn, C. R. J. (2018). Forecasting Volcanic Eruptions: Beyond the Failure Forecast Method. *Frontiers in Earth Science*, 6(133).

Kim, S.-H. and Das, M. P. (2013). Artificial Seismic Shadow Zone by Acoustic Metamaterials. *Modern Physics Letters B*, 27(20):1–4.

Krischer, L., Megies, T., Barsch, R., Beyreuther, M., Lecocq, T., Caudron, C., and Wassermann, J. (2015). ObsPy : a bridge for seismology into the scienti fi c Python ecosystem. *Computational Science & Discovery*, 8(1):1–17.

Lahr, J. C., Chouet, B. A., Stephens, C. D., Power, J. A., and Page, R. A. (1994). Earthquake classification, location, and error analysis in a volcanic environment: implications for the magmatic system of the 1989-1990 eruptions at redoubt volcano, Alaska. *Journal of Volcanology and Geothermal Research*, 62(1-4):137–151.

Lapusta, N. and Rice, J. R. (2003). Nucleation and early seismic propagation of small and large events in a crustal earthquake model. *Journal of Geophysical Research*, 108(B4):1–18.

Lengliné, O. and Marsan, D. (2009). Inferring the coseismic and postseismic stress changes caused by the 2004 Mw= 6 Parkfield earthquake from variations of recurrence times of microearthquakes. *Journal of Geophysical Research: Solid Earth*, 114(10):1–19.

Lewis, J. P. (1995). Fast Template Matching. *Vision Interface 95, Canadian Image Processing and Pattern Recognition Society*, pages 120–123.

Li, J. Z., Bai, Z. Q., Chen, W. S., Xia, Y. Q., Liu, Y. R., and Ren, Z. Q. (2003). Strong earthquakes can be predicted : a multidisciplinary method for strong earthquake prediction. *Natural Hazards And Earth System Sciences*, pages 703–712.

Lin, C. W., Liu, S. H., Lee, S. Y., and Liu, C. C. (2006). Impacts of the Chi-Chi earthquake on subsequent rainfall-induced landslides in central Taiwan. *Engineering Geology*, 86(2-3):87–101.

López-Comino, J. A. and Cesca, S. (2018). Source Complexity of an Injection Induced Event: The 2016 Mw5.1 Fairview, Oklahoma Earthquake. *Geophysical Research Letters*, 45(9):4025–4032.

Lott, D. F., Hart, B. L., and Howell, M. W. (1981). Retrospective studies of unusual animal behavior as an earthquake predictor. *Geophysical Research Letters*, 8(12):1203–1206.

Main, I. (1999). Is the reliable prediction of individual earthquakes a realistic scientific goal? *Nature*.

Main, I. (2017). Scale-model seismicity - Taking the rough with the smooth. *Geology*, 45(9):859–860.

Main, I. and Naylor, M. (2012). Extreme events and predictability of catastrophic failure in composite materials and in the Earth. *European Physical Journal: Special Topics*, 205:183–197.

Main, I. G. (2000). A damage mechanics model for power-law creep and earthquake aftershock and foreshock sequences. *Geophysical Journal International*, 142:151–161.

Main, I. G., Leonard, T., Papasouliotis, O., Hatton, C. G., and Meredith, P. G. (1999). One slope or two? Detecting statistically significant breaks of slope in geophysical data, with application to fracture scaling relationships. *Geophysical Research Letters*, 26(18):2801–2804.

Major, J. J., Scott, W. E., Driedger, C., and Dzurisin, D. (2005). Mount St. Helens Erupts Again Activity from September 2004 through March 2005. Technical Report April, USGS.

Malin, P. E., Blakeslee, S. N., Alvarez, M. G., and Martin, A. J. (1989). Microearthquake imaging of the Parkfield asperity. *Science*, 244(4904):557–560.

Marzocchi, W. and Sandri, L. (2003). A review and new insights on the estimation of the b-value and its uncertainty. *Annals of Geophysics*, 46(6):1271–1282.

Matoza, R. S., Chouet, B. A., Dawson, P. B., Shearer, P. M., Haney, M. M., Waite, G. P., Moran, S. C., and Mikesell, T. D. (2015). Source mechanism of small long-period events at Mount St. Helens in July 2005 using template matching, phase-weighted stacking, and full-waveform inversion. *Journal of Geophysical Research B: Solid Earth*, 120(9):6351–6364.

McNutt, S. R. (2002). Volcano Seismology and Monitoring for Eruptions. *International Geophysics*, 81:383–407.

Megies, T., Beyreuther, M., Barsch, R., Krischer, L., and Wassermann, J. (2011). ObsPy - what can it do for data centers and observatories? *Annals of Geophysics*, 54(1):47–58.

Meissner, R. (1982). *Deterministic Earthquake Prediction — Present Stage and Future Developments*, pages 563–575. Springer, Wiesbaden.

Mesimeri, M. and Karakostas, V. (2018). Repeating earthquakes in western Corinth Gulf (Greece): implications for aseismic slip near locked faults. *Geophysical Journal International*, 215(1):659–676.

Métois, M., Socquet, A., Vigny, C., Carrizo, D., Peyrat, S., Delorme, A., Maureira, E., Valderas-Bermejo, M.-C., and Ortega, I. (2013). Revisiting the North Chile seismic gap segmentation using GPS-derived interseismic coupling. *Geophysical Journal International*, 194(3):1283–1294.

Mignan, A. (2014). The debate on the prognostic value of earthquake foreshocks: A meta-analysis. *Scientific reports*, 4:4099.

Miller, A. D., Stewart, R. C., White, R. A., Luckett, R., Baptie, B. J., Aspinall, W. P., Latchman, J. L., Lynch, L. L., and Voight, B. (1998). Seismicity associated with dome growth and collapse at the Soufriere Hills Volcano, Montserrat. *Geophys. Res. Lett.*, 25(18):3401–3404.

Moran, S. C., Malone, S. D., Qamar, A. I., Thelen, W. A., Wright, A. K., and Caplan-Auerbach, J. (2008a). Seismicity Associated with Renewed Dome Building at Mount St. Helens, 2004-2005. In Sherrod, D., Scott, W., and Stauffer, P., editors, *A Volcano rekindled; the renewed eruption of Mount St. Helens, 2004-2006*, chapter 2, pages 27–60. USGS.

Moran, S. C., Matoza, R. S., Garcés, M. A., Hedlin, M. A. H., Bowers, D., Scott, W. E., Sherrod, D. R., and Vallance, J. W. (2008b). Seismic and acoustic recordings of an unusually large rockfall at Mount St. Helens, Washington. *Geophysical Research Letters*, 35(19):2–7.

Moran, S. C., Newhall, C., and Roman, D. C. (2011). Failed magmatic eruptions: Late-stage cessation of magma ascent. *Bulletin of Volcanology*, 73(2):115–122.

Moretti, L., Mangeney, A., Capdeville, Y., Stutzmann, E., Huggel, C., Schneider, D., and Bouchut, F. (2012). Numerical modeling of the Mount Steller landslide flow history and of the generated long period seismic waves. *Geophysical Research Letters*, 39(16):1–7.

Mukaka, M. M. (2012). Statistics Corner: A guide to appropriate use of Correlation coefficient in medical research. *Malawi Medical Journal*, 24(3):69–71.

Murray, J. and Langbein, J. (2006). Slip on the San Andreas fault at Parkfield, California, over two earthquake cycles, and the implications for seismic hazard. *Bulletin of the Seismological Society of America*, 96(4 B):283–303.

Musumeci, C., Gresta, S., and Malone, S. D. (2002). Magma system recharge of Mount St. Helens from precise relative hypocenter location of microearthquakes. *Journal of Geophysical Research: Solid Earth*, 107(B10):ESE 16–1–ESE 16–9.

Nadeau, R. M., Foxall, W., and McEvilly, T. (1995). Clustering and Periodic Recurrence of Microearthquakes on the San Andreas Fault at Parkfield, California. *Science*, 267(5197):503–507.

Nadeau, R. M. and Johnson, L. R. (1998). Seismological studies at Parkfield VI: moment release rates and estimates of source parameters for small repeating earthquakes. *Bulletin of the Seismological Society of America*, 88(3):790–814.

Naylor, M., Main, I. G., and Touati, S. (2009). Quantifying uncertainty in mean

earthquake interevent times for a finite sample. *Journal of Geophysical Research: Solid Earth*, 114(1):1–18.

Naylor, M., Orfanogiannaki, K., and Harte, D. (2010). Exploratory data analysis: magnitude, space, and time. Community Online Resource for Statistical Seismicity.

Neuberg, J. (2011). Earthquakes, Volcanogenic. In *Encyclopedia of Solid Earth Geophysics*, chapter Earthquake, pages 261–269. Springer.

Neuberg, J., Luckett, R., Baptie, B., and Olsen, K. (2000). Models of tremor and low-frequency earthquake swarms on Montserrat. *Journal of Volcanology and Geothermal Research*, 101(1-2):83–104.

Neuberg, J. W., Tuffen, H., Collier, L., Green, D., Powell, T., and Dingwell, D. (2006). The trigger mechanism of low-frequency earthquakes on Montserrat. *Journal of Volcanology and Geothermal Research*, 153(1-2 SPEC. ISS.):37–50.

Newhall, C. G., Costa, F., Ratdomopurbo, A., Venezky, D. Y., Widiwijayanti, C., Win, N. T. Z., Tan, K., and Fajiculay, E. (2017). WOVOdat – An online, growing library of worldwide volcanic unrest. *Journal of Volcanology and Geothermal Research*, 345:184–199.

Nyquist, H. (1928). Certain Topics in Telegraph Transmission Theory. *Transactions of the American Institute of Electrical Engineers*, 47(2):617–644.

Obara, K. (2002). Nonvolcanic deep tremor associated with subduction in southwest Japan. *Science*, 296(May):1679–1681.

Ogata, Y. (1988). Statistical models for earthquake occurrences and residual analysis for point processes. *Journal of The American Statistical Association*, 83(401):9–27.

Ogata, Y. (1992). Detection of precursory relative quiescence before great earthquakes through a statistical model. *Journal of Geophysical Research*, 97(B13):19845.

Ohnaka, M. (1992). Earthquake source nucleation: A physical model for short-term precursors. *Tectonophysics*, 211(1-4):149–178.

Ohnaka, M. and Kuwahara, Y. (1990). Characteristic features of local breakdown near a crack-tip in the transition zone from nucleation to unstable rupture during stick-slip shear failure. *Tectonophysics*, 175(1-3):197–220.

Oskin, B. (2013). Foreshocks Announce Future Earthquakes on Some Faults. *Live Science*.

Pagliuca, N. M., Badiali, L., Cattaneo, M., Ciraba, H., Delladio, A., Demartin, M., Garcia, A., Lisi, A., Lukaya, F., Marchetti, A., Monachesi, G., Mavonga, A., Sgroi, T., and Tedesco, D. (2009). Preliminary results from seismic monitoring at Nyiragongo Volcano (Democratic Republic of Congo) through telemetered seismic network, Goma volcanological observatory. *Bollettino di Geofisica Teorica ed Applicata*, 50(2):117–127.

Papazachos, B. (1975). Foreshocks and earthquake prediction. *Tectonophysics*, 28(4):213–226.

Peng, Z. and Zhao, P. (2009). Migration of early aftershocks following the 2004 Parkfield earthquake. *Nature Geoscience*, 2(12):877–881.

Petersen, B. M. D., Mueller, C. S., Moschetti, M. P., Hoover, S. M., Rubinstein, J. L., Andrea, L., Michael, A. J., Ellsworth, W. L., Mcgarr, A. F., Holland, A. A., Anderson, J. G., Jewell, S., and Survey, U. S. G. (2015). Incorporating Induced Seismicity in the 2014 United States National Seismic Hazard Model — Results of 2014 Workshop and Sensitivity Studies. *USGS Open File Report*, 2015-1070:75.

Petersen, M. D., Cao, T., Campbell, K. W., and Frankel, A. D. (2007). Time-independent and Time-dependent Seismic Hazard Assessment for the State of California: Uniform California Earthquake Rupture Forecast Model 1.0. *Seismological Research Letters*, 78(1):99–109.

Petersen, T. (2007). Swarms of repeating long-period earthquakes at Shishaldin Volcano, Alaska, 2001-2004. *Journal of Volcanology and Geothermal Research*, 166(3-4):177–192.

Petley, D. N., Higuchi, T., Petley, D. J., Bulmer, M. H., and Carey, J. (2005). Development of progressive landslide failure in cohesive materials. *Geology*, 33(3):201–204.

Poland, M. P., Dzurisin, D., LaHusen, R. G., Major, J. J., Lapcewich, D., Endo, E. T., Gooding, D. J., Schilling, S. P., and Janda, C. G. (2008). Remote Camera Observations of Lava Dome Growth at Mount St. Helens, Washington. In Sherrod, D. R., Scott, W. E., and Stauffer, P. H., editors, *A Volcano Rekindled: The Renewed Eruption of Mount St. Helens, 2004–2006*, pages 225–236. USGS.

Poli, P. (2017). Creep and slip: Seismic precursors to the Nuugaatsiaq landslide (Greenland). *Geophysical Research Letters*, pages 1–5.

Porter, R. T., Striolo, A., Mahgerefteh, H., and Faure Walker, J. (2019). Addressing the risks of induced seismicity in subsurface energy operations. *Wiley Interdisciplinary Reviews: Energy and Environment*, 8(2):1–18.

Power, J. A. and Lalla, D. J. (2010). Seismic Observations of Augustine Volcano , Alaska. In Power, J., Coombs, M., and Freymueller, J., editors, *The 2006 Eruption of Augustine Volcano, Alaska*, chapter 1, pages 1970–2007. USGS.

Prejean, S. G. and Hill, D. P. (2011). Earthquakes, Dynamic Triggering of. In Meyers, R., editor, *Extreme Environmental Events*, chapter Earthquake, pages 425–446. Springer, New York, NY.

Proakis, J. G. and Manolakis, D. G. (1996). *Digital Signal Processing: Principles, Algorithms, and Applications*. Prentice-Hall, third edit edition.

Radiguet, M., Cotton, F., Vergnolle, M., Campillo, M., Walpersdorf, A., Cotte, N., and Kostoglodov, V. (2012). Slow slip events and strain accumulation in the Guerrero gap, Mexico. *Journal of Geophysical Research: Solid Earth*, 117(4):1–13.

Raleigh, C. B., Bennett, G., Craig, H., Hanks, T., and Molnar, P. (1977). Prediction of the Haicheng earthquake. *Eos*, 58:236–272.

Reasenberg, P. and Simpson, R. W. (1992). Response of Regional Seismicity to the Static Stress Change Produced by the Loma Prieta Earthquake. *Science*, 255(5052):1687–1690.

Reiter, L. (1991). *Earthquake hazard analysis issues and insights*, volume 20. Columbia University Press, New York.

Richter, C. (1935). An Instrumental Earthquake Magnitude Scale. *Bull. Seismol. Soc. Am.*, 25(1).

Roberts, N. S., Bell, A. F., and Main, I. G. (2015). Are volcanic seismic b-values high, and if so when? *Journal of Volcanology and Geothermal Research*, 308:127–141.

Rodriguez, B., Labson, V., Stanley, W., and Sampson, J. (2004). Deep Geoelectrical Structure of the Loma Prieta Region. In Wells, R., editor, *The Loma Prieta, California, earthquake of October 17, 1989: earthquake occurrence*, pages 81 – 106. USGS.

Rogers, G. and Dragert, H. (2003). Episodic Tremor and Slip on the Cascadia Subduction Zone : The. *Science*, 300(5627):1942–1944.

Roland, E. and Mcguire, J. J. (2009). Earthquake swarms on transform faults. *Geophys. J. Int.*, 178:1677–1690.

Rong, K., Yoon, C. E., Bergen, K. J., Elezabi, H., Bailis, P., Levis, P., and Beroza, G. C. (2018). Locality-Sensitive Hashing for Earthquake Detection: A Case Study Scaling Data-Driven Science. *Proceedings of the VLDB Endowment*, 11(11).

Ross, Z. E., Trugman, D. T., Hauksson, E., and Shearer, P. M. (2019). Searching for hidden earthquakes in Southern California. *Science*, 364(May):767–771.

Rubinstein, J. L. and Ellsworth, W. L. (2010). Precise estimation of repeating earthquake moment: Example from parkfield, california. *Bulletin of the Seismological Society of America*, 100(5 A):1952–1961.

Rubinstein, J. L., Vidale, J. E., Gomberg, J., Bodin, P., Creager, K. C., and Malone, S. D. (2007). Non-volcanic tremor driven by large transient shear stresses. *Nature*, 448(7153):579–582.

Ruina, A. (1983). Slip instability and state variable friction laws. *Journal of Geophysical Research*, 88(B12):10359–10370.

Ruiz, S., Metois, M., Fuenzalida, A., Ruiz, J., Leyton, F., Grandin, R., Vigny, C., Madariaga, R., and Campos, J. (2014). Intense foreshocks and a slow slip event preceded the 2014 Iquique Mw 8.1 earthquake. *Science (New York, N.Y.)*, 345(6201):1165–1169.

Sammis, C. G. and Rice, J. (2001). Repeating Earthquakes as Low-Stress-Drop Events at a Border between Locked and Creeping Fault Patches. *Bulletin of the Seismological Society of America*, 91(3):532–537.

Sammis, C. G. and Sornette, D. (2002). Positive feedback, memory, and the predictability of earthquakes. *Proceedings of the National Academy of Sciences*, 99(Supplement 1):2501–2508.

Schaff, D. (2010). Improvements to detection capability by cross-correlating for similar events: a case study of the 1999 Xiuyan, China, sequence and synthetic sensitivity tests. *Geophysical Journal International*, 180:829–846.

Schick, R. (1981). Source Mechanism of Volcanic Tremor. *Bulletin Volcanologique*, 44(3):491–497.

Scholz, C. H. (1998). Earthquakes and friction laws. *Nature*, 391(6662):37–42.

Schorlemmer, D., Wiemer, S., and Wyss, M. (2004). Earthquake statistics at Parkfield: 1. Stationarity of b values. *Journal of Geophysical Research: Solid Earth*, 109(12):1–17.

Schurr, B., Asch, G., Hainzl, S., Bedford, J., Hoechner, A., Palo, M., Wang, R., Moreno, M., Bartsch, M., Zhang, Y., Oncken, O., Tilmann, F., Dahm, T., Victor,

P., Barrientos, S., and Vilotte, J.-P. (2014). Gradual unlocking of plate boundary controlled initiation of the 2014 Iquique earthquake. *Nature*, 512(7514):299–302.

Schwarz, G. (1978). Estimating the Dimension of a Model. *The Annals of Statistics*, 6(2):461–464.

Scott, W. E., Sherrod, D. R., and Gardner, C. A. (2008). Overview of the 2004 to 2006, and continuing, eruption of Mount St. Helens, Washington. In Sherrod, D., Scott, W., and Stauffer, P., editors, *A Volcano Rekindled: The Renewed Eruption of Mount St. Helens, 2004-2006, U.S. Geological Survey Professional Paper 1750*, chapter 1, pages 3–22. USGS.

Scuderi, M. M., Collettini, C., and Marone, C. (2017). Frictional stability and earthquake triggering during fluid pressure stimulation of an experimental fault. *Earth and Planetary Science Letters*, 477:84–96.

Seif, S., Mignan, A., Zechar, J. D., Werner, M. J., and Wiemer, S. (2017). Estimating ETAS: The effects of truncation, missing data, and model assumptions. *Journal of Geophysical Research: Solid Earth*, 122(1):449–469.

Shannon, C. (1998). Communication In The Presence Of Noise (Republished). *Proceedings of the IEEE*, 86(2):447–457.

Sheldon, H. A. and Micklethwaite, S. (2007). Damage and permeability around faults: Implications for mineralization. *Geology*, 35(10):903–906.

Shelly, D. R., Beroza, G. C., and Ide, S. (2007). Non-volcanic tremor and low-frequency earthquake swarms. *Nature*, 446(7133):305–307.

Shelly, D. R., Ellsworth, W. L., and Hill, D. P. (2016a). Fluid-faulting evolution in high definition: Connecting fault structure and frequency-magnitude variations during the 2014 Long Valley Caldera, California, earthquake swarm. *Journal of Geophysical Research : Solid Earth*, 121:1776–1795.

Shelly, D. R., Hardebeck, J. L., Ellsworth, W. L., and Hill, D. P. (2016b). A new strategy for earthquake focal mechanisms using waveform-correlation-derived relative polarities and cluster analysis: Application to the 2014 Long Valley Caldera earthquake swarm. *Journal of Geophysical Research: Solid Earth*, 121(12):8622–8641.

Shelly, D. R., Peng, Z., Hill, D. P., and Aiken, C. (2011). Triggered creep as a possible mechanism for delayed dynamic triggering of tremor and earthquakes. *Nature Geoscience*, 4(6):384–388.

Shi, Y. and Bolt, B. (1982). The Standard Error of the Magnitude-Frequency b Value. *Bulletin of the Seismological Society of America*, 72(5):1677–1687.

Sidle, R. C., Bougeret, J.-l., Bebout, G. E., Fesen, C. G., Friedrichs, C. T., Haese, R. R., Berry, W., Minschwaner, K. R., Nyblade, A., Strobel, D., and Wang, C. (2006). *Landslides Processes , Prediction, and Land Use*. American Geophysical Union, Washington D.C.

Silver, P. G. and Valettesilver, N. J. (1992). Detection of Hydrothermal Precursors to Large California Earthquakes. *Science*, 257(September):437–441.

Sobisevich, L. E., Rogozhin, E. A., Sobisevich, A. L., Shen, T., and Liu, Z. (2017). Instrumental observations of geomagnetic disturbances prior to seismic events in several regions of China. *Seismic Instruments*, 53(1):28–45.

Socquet, A., Piña Valdes, J., Jara, J., Cotton, F., Walpersdorf, A., Cotte, N., Specht, S., Ortega-Culaciati, F., Carrizo, D., and Norabuena, E. (2017). An 8-month slow slip event triggers progressive nucleation of the 2014 Chile megathrust. *Geophysical Research Letters*, pages 4046–4053.

Sornette, D. (2002). Predictability of catastrophic events: material rupture, earthquakes, turbulence, financial crashes and human birth. *Proceedings of the National Academy of Sciences*, 99.

Sornette, D. (2009). Dragon-Kings, Black Swans and the Prediction of Crises. *International Journal of Terraspace Science and Engineering*, 2(1):1–18.

Sović, I., Šariri, K., and Živčić, M. (2013). High frequency microseismic noise as possible earthquake precursor. *Research in Geophysics*, 3:2.

Stix, J. and de Moor, J. M. (2018). Understanding and forecasting phreatic eruptions driven by magmatic degassing. *Earth, Planets and Space*, 70(1).

Tape, C., Holtkamp, S., Silwal, V., Hawthorne, J., Kaneko, Y., Ampuero, J. P., Ji, C., Ruppert, N., Smith, K., and West, M. E. (2018). Earthquake nucleation and fault slip complexity in the lower crust of central Alaska. *Nature Geoscience*, 11(July 2018):536–541.

Thelen, W., Malone, S., and West, M. (2011). Multiplets: Their behavior and utility at dacitic and andesitic volcanic centers. *Journal of Geophysical Research: Solid Earth*, 116(8):1–16.

Thelen, W., West, M., and Senyukov, S. (2010). Seismic characterization of the fall 2007 eruptive sequence at Bezymianny Volcano, Russia. *Journal of Volcanology and Geothermal Research*, 194(4):201–213.

Thelen, W. A., Allstadt, K., De Angelis, S., Malone, S. D., Moran, S. C., and Vidale, J. (2013). Shallow repeating seismic events under an alpine glacier at Mount Rainier, Washington, USA. *Journal of Glaciology*, 59(214):345–356.

Thelen, W. A., Crosson, R. S., and Creager, K. C. (2008). Absolute and Relative Location of Earthquakes at Mount St. Helens, Washington, Using Continuous Data: Implications for Magmatic Processes. In Sherrod, D., Scott, W., and Stauffer, P., editors, *A Volcano Rekindled: The Renewed Eruption of Mount St. Helens 2004-2006, U.S. Geological Survey Professional Paper 1750*, chapter 4, pages 71–95. USGS.

Thurber, C., Zhang, H., Waldhauser, F., Hardebeck, J., Michael, A., and Eberhart-Phillips, D. (2006). Three-dimensional compressional wavespeed model, earthquake

relocations, and focal mechanisms for the Parkfield, California, region. *Bulletin of the Seismological Society of America*, 96(4 B).

Touati, S., Naylor, M., and Main, I. G. (2009). Origin and nonuniversality of the earthquake interevent time distribution. *Physical Review Letters*, 102(16):1–4.

Townend, J. and Zoback, M. D. (2000). How faulting keeps the crust strong. *Geology*, 28(5):399–402.

Trnkoczy, A. (2012). Understanding and parameter setting of STA/LTA trigger algorithm. In Bormann, P., editor, *New Manual of Seismological Observatory Practice 2 (NMSOP-2)*, pages 1–20. Potsdam.

Tsunogai, U. and Wakita, H. (1996). Anomalous Changes in Groundwater Chemistry. Possible Precursors of the 1995 Hyogo-ken Nanbu Earthquake, Japan. *Journal of Physics of the Earth*, 44(4):381–390.

Twardzik, C., Madariaga, R., Das, S., and Custódio, S. (2012). Robust features of the source process for the 2004 Parkfield, California, earthquake from strong-motion seismograms. *Geophysical Journal International*, 191(3):1245–1254.

Uchida, N. and Bürgmann, R. (2019). Repeating Earthquakes. *Annual Review of Earth and Planetary Sciences*, 47:305–332.

Udias, A., Madariaga, R., and Buforn, E. (2014). *Source Mechanisms of Earthquakes*. Cambridge University Press, Cambridge.

USGS (2017). M 4.2 Landslide - 107km N of Uummannaq, Greenland.

USGS (2019). M 7.1 - 2019 Ridgecrest Earthquake Sequence.

Utsu, T., Ogata, Y., and Matsu'ura, R. (1995). The Centenary a Decay of the Omori Formula Activity for Law of Aftershock Activity. *J. Phys. Earth*, 43:1–33.

Uyeda, S., Kamogawa, M., and Tanaka, H. (2009). Analysis of electrical activity and seismicity in the natural time domain for the volcanic-seismic swarm activity

in 2000 in the Izu Island region, Japan. *Journal of Geophysical Research: Solid Earth*, 114(2):4–13.

Vallance, J., Schneider, D., and Schilling, S. (2008). Growth of the 2004-2006 Lava-Dome Complex at Mount St. Helens, Washington. *A Volcano Rekindled: The Renewed Eruption of Mount St. Helens 2004-2006, U.S. Geological Survey Professional Paper 1750*, pages 169–208.

van den Ende, M. P., Chen, J., Ampuero, J. P., and Niemeijer, A. R. (2018). A comparison between rate-and-state friction and microphysical models, based on numerical simulations of fault slip. *Tectonophysics*, 733(July 2017):273–295.

Varotsos, P., Alexopoulos, K., and Lazaridou, M. (1993). Latest aspects of earthquake prediction in Greece based on seismic electric signals, II. *Tectonophysics*, 224(1-3):1–37.

Varotsos, P., Alexopoulos, K., Nomicos, K., and Lazaridou, M. (1988). Official earthquake prediction procedure in Greece. *Tectonophysics*, 152(3-4):193–196.

Vasseur, J., Wadsworth, F. B., Heap, M. J., Main, I. G., Lavallée, Y., and Dingwell, D. B. (2017). Does an inter-flaw length control the accuracy of rupture forecasting in geological materials? *Earth and Planetary Science Letters*, 475:181–189.

Veedu, D. M. and Barbot, S. (2016). The Parkfield tremors reveal slow and fast ruptures on the same asperity. *Nature*, 532(7599):361–365.

Vere-Jones, D. (1976). A Branching Model for Crack Propagation. *PAGEOPH*, 114:711–725.

Viesca, R. C. and Rice, J. R. (2012). Nucleation of slip-weakening rupture instability in landslides by localized increase of pore pressure. *Journal of Geophysical Research: Solid Earth*, 117(3):1–21.

Voight, B. (1978). *Rockslides and Avalanches: 1. Natural phenomena*. Elsevier Scientific Publishing Company, Amsterdam.

Voight, B. (1988). A method for the prediction of volcanic eruptions. *Nature*, 332(10):125–130.

Voss, N., Dixon, T. H., Liu, Z., Malservisi, R., Protti, M., and Schwartz, S. (2018). Do slow slip events trigger large and great megathrust earthquakes? *Science Advances*, 4(10):1–6.

Vuan, A., Sugan, M., Amati, G., and Kato, A. (2018). Improving the detection of low-magnitude seismicity preceding the Mw6.3 L'Aquila earthquake: Development of a scalable code based on the cross correlation of template earthquakes. *Bulletin of the Seismological Society of America*, 108(1):471–480.

Wagner, F., Tryggvason, A., Roberts, R., Lund, B., and Gudmundsson (2017). Automatic seismic event detection using migration and stacking: A performance and parameter study in Hengill, southwest Iceland. *Geophysical Journal International*, 209(3):1866–1877.

Waite, G. P., Chouet, B. A., and Dawson, P. B. (2008). Eruption dynamics at Mount St . Helens imaged from broadband seismic waveforms : Interaction of the shallow magmatic and hydrothermal systems. *Journal of Geophysical Research*, 113(B02305):1–22.

Wang, J., Main, I. G., and Musson, R. M. W. (2017). Earthquake clustering in modern seismicity and its relationship with strong historical earthquakes around Beijing , China with strong historical earthquakes around Beijing , China. *Geophys. J. Int.*, 211:1005–1018.

Wang, K., Chen, Q.-F., Sun, S., and Wang, A. (2006). Predicting the 1975 Haicheng Earthquake. *Bulletin of the Seismological Society of America*, 96(3):757–795.

Wang, K. and Rogers, G. C. (2014). Earthquake Preparedness Should Not Fluctuate on a Daily or Weekly Basis. *Seismological Research Letters*, 85(3):569–571.

Whiteley, J. S., Chambers, J. E., Uhlemann, S., Wilkinson, P. B., and Kendall, J. M. (2019). Geophysical Monitoring of Moisture-Induced Landslides: A Review. *Reviews of Geophysics*, 57(1):106–145.

Wiemer, S. and Wyss, M. (1997). Mapping the frequency-magnitude distribution in asperities: An improved technique to calculate recurrence times? *Journal of Geophysical Research*, 102(3):15,115 15,128.

Wiemer, S. and Wyss, M. (2000). Minimum Magnitude of Completeness in Earthquake Catalogs : Examples from Alaska , the Western United States , and Japan. *Bulletin of the Seismological Society of America*, 90(4):859–869.

Wiemer, S. and Wyss, M. (2002). Mapping spatial variability of the frequency-magnitude distribution of earthquakes. *Advances in Geophysics*, 45:259–V.

Withers, M., Aster, R., Young, C., Beiriger, J., Harris, M., Moore, S., and Trujillo, J. (1998). A comparison of select trigger algorithms for automated global seismic phase and event detection. *Bulletin of the Seismological Society of America*, 88(1):95–106.

Woessner, J. and Wiemer, S. (2005). Assessing the quality of earthquake catalogues: Estimating the magnitude of completeness and its uncertainty. *Bulletin of the Seismological Society of America*, 95(2):684–698.

Woith, H., Petersen, G. M., Hainzl, S., and Dahm, T. (2018). Review : Can Animals Predict Earthquakes ? *Bull. Seismol. Soc. Am.*, 108(3A):1031–1045.

Wong, J., Han, L., Bancroft, J. C., and Stewart, R. R. (2009). Automatic time picking of first arrivals on noisy microseismic data. In *CSEG Microseismic Workshop*. University of Calgary, CREWES.

Wyss, M., Sammis, C. G., Nadeau, R. M., and Wiemer, S. (2004). Fractal Dimension and b-Value on Creeping and Locked Patches of the San Fractal Dimension and b -Value on Creeping and Locked Patches of the San Andreas Fault near Parkfield , California. *Bulletin of the Seismological Society of America*, 94(2):410–421.

Yamada, M., Kumagai, H., Matsushi, Y., and Matsuzawa, T. (2013). Dynamic landslide processes revealed by broadband seismic records. *Geophysical Research Letters*, 40(12):2998–3002.

Yamada, M., Mangeney, A., Matsushi, Y., and Matsuzawa, T. (2018). Estimation of dynamic friction and movement history of large landslides. *Landslides*, 15(10):1963–1974.

Yamada, M., Mori, J., and Matsushi, Y. (2016). Possible stick-slip behavior before the Rausu landslide inferred from repeating seismic events. *Geophysical Research Letters*, 43(17):9038–9044.

Yamaguchi, J., Naoi, M., Nakatani, M., Moriya, H., Igarashi, T., Murakami, O., Yabe, Y., Durrheim, R., and Ogasawara, H. (2018). Emergence and disappearance of very small repeating earthquakes on a geological fault in a gold mine in South Africa. *Tectonophysics*, 747-748(November 2017):318–326.

Yamashita, T. and Ohnaka, M. (1991). Nucleation process of unstable rupture in the brittle regime - a theoretical approach based on experimentally inferred relations. *Journal of Geophysical Research-Solid Earth and Planets*, 96(B5):8351–8367.

Yamauchi, H., Uchiyama, H., Ohtani, N., and Ohta, M. (2014). Unusual Animal Behavior Preceding the 2011 Earthquake off the Pacific Coast of Tohoku, Japan: A Way to Predict the Approach of Large Earthquakes. *Animals*, 4(March 2011):131–145.

Yoon, C. E., Huang, Y., Ellsworth, W. L., and Beroza, G. C. (2017). Seismicity During the Initial Stages of the Guy-Greenbrier, Arkansas, Earthquake Sequence. *Journal of Geophysical Research: Solid Earth*, 122(11):9253–9274.

Yoon, C. E., O'Reilly, O., Bergen, K. J., and Beroza, G. C. (2015). Earthquake detection through computationally efficient similarity search. *Science Advances*, 1(December):1–14.

Zaliapin, I. and Ben-Zion, Y. (2016). Discriminating characteristics of tectonic and human-induced seismicity. *Bulletin of the Seismological Society of America*, 106(3):846–859.